

# **Strategies for Producing Bulk Nanocrystalline Al-Mg Alloys by Cryogenic Milling and SPS Consolidation**

**Bamidele Akinrinlola**

Department of Mining and Materials Engineering  
McGill University, Montreal

January 2018

A thesis submitted to McGill University in partial fulfillment of the requirements of the  
degree of Doctor of Philosophy in Engineering

©Bamidele Akinrinlola 2018



## Abstract

In bulk nanostructured (NS) materials produced by powder metallurgy routes, adequate consolidation of the NS powders typically requires high temperature application for extended periods of time. This increases the likelihood of grain growth in the nanocrystalline material and therefore loss in strength and hardness. Spark Plasma Sintering (SPS), with short sintering cycles and mechanisms peculiar to the process, reduces grain growth and improves consolidation of milled powders compared to conventional processes. Multi-stage SPS is investigated for sintering cryomilled NS Al-Mg powders to improve the consolidation while minimizing the grain growth. The effects of change in powder composition, i.e.: microalloying, on the grain growth in cryomilled Al-Mg alloys are also studied.

Improved consolidation of cryomilled Al powders was obtained under two-stage (TSS) versus one-stage (OSS) sintering processes. With properly selected parameters  $T_1$  and  $T_2$  (TSS:  $T_1 > T_2$ ,  $t_1 < t_2$ ) a two-stage sintering process allowed for enhanced sintering while avoiding excessive grain growth. The increased duration of the second hold (from 5 to 20 minutes) marginally increased the Weibull Modulus (from 23 to 25). The best sintering schedule for milled Al 5356 was determined as the 500 TSS-20 schedule (i.e.: 500 °C for 1 minute + 350 °C for 20 minutes). Minimal grain growth occurred during the TSS regime, with  $68 \pm 46$  nm after one-stage and  $73 \pm 46$  nm after two-stage sintering.

Al-Mg-Er powders – final compositions of Al-4.65Mg-0.08Er (0.1 Er) and Al-4.48Mg-0.44Er (0.5 Er) – were investigated. Prolonged cryomilling for 30 hours resulted in substantial oxygen contamination in the final milled powders, ~8 and ~13 wt.% in 0.1 Er and 0.5 Er, respectively. Grain growth was observed at 180 °C in the 0.1 Er powder, but the as milled grain size of ~20 nm was maintained till 400 °C ( $0.8 T_m$ ) in the 0.5 Er powders. Evidence of nanoscale  $L1_2$  structured  $Al_3Er$  precipitation was not observed by X-ray or electron diffraction. Crystalline oxides (spinel) were observed for powders annealed at 500 °C and higher.

Densification and consolidation of the milled Al-Mg-Er powders with TSS processes was dependent on the sintering temperature, maximum pressure, and heating rate. Consolidation was improved under a heating rate of  $300\text{ }^{\circ}\text{C}\cdot\text{min}^{-1}$  and maximum pressure of 60 MPa during the 550 TSS 20 schedule (i.e.:  $550\text{ }^{\circ}\text{C}$  for 0.5 minute +  $350\text{ }^{\circ}\text{C}$  for 20 minutes). Average grain size was  $86 \pm 52\text{ nm}$  and  $50 \pm 21\text{ nm}$  in the 0.1 Er and 0.5 Er samples, respectively, after the 550 TSS 20 schedule. Crystalline oxide formation (spinel) during sintering was dependent on the powder composition and selection of  $T_1$ . Oxide particles of Al-Mg-Er-Fe-O, Al-Mg-Er-Fe-O-N, and Al-Mg-O-N content were observed in the 0.5 Er powders sintered at  $550\text{ }^{\circ}\text{C}$ .

Three-stage sintering (MSS:  $T_1 < T_2 < T_3$ ) improved the consolidation of cryomilled 0.1 Er powder compared to results from the two-stage sintering process (TSS:  $T_1 > T_2$ ). Higher fracture strength and hardness were obtained with samples from MSS schedules versus TSS schedules. MSS samples also exhibited smaller standard deviations ( $\sim 20\text{ nm}$ ) in fracture strength, hardness, and nanocrystalline grain size. Best results were obtained with the 350 MSS 5 condition (i.e.:  $350\text{ }^{\circ}\text{C}$  for 10 minutes +  $450\text{ }^{\circ}\text{C}$  for 5 minutes +  $500\text{ }^{\circ}\text{C}$  for 5 minutes). MSS sintering schedules limited the average grain growth to  $\sim 60\text{ nm}$ , compared to  $\sim 70\text{ nm}$  after TSS sintering. Clusters of Er and Ti were observed in TSS samples. Nanoscale precipitation of Al-Fe and Al-Fe-Ni phases were observed in MSS samples after 30 minutes of sintering.

## Resume

Dans le cas de matériaux nanocristallins (NC) massifs produits par métallurgie des poudres, une consolidation adéquate de ces poudres requiert généralement l'utilisation de hautes températures pendant de longues périodes de temps. Cela augmente la probabilité de croissance de grains au sein de matériaux NC, ce qui mène à une diminution de la résistance et de dureté du matériau. Le frittage par décharge plasma (FDP) réduit la croissance des grains et améliore la consolidation des poudres broyées par rapport aux procédés de frittage classiques. Le FDP à plusieurs étapes a ainsi été mis en œuvre pour le frittage de poudres NC d'Al-Mg broyées cryogéniquement pour améliorer la consolidation des poudres, tout en minimisant la croissance des grains. Les effets de la composition des poudres sur la croissance des grains dans les alliages d'Al-Mg broyés cryogéniquement ont également été étudiés.

En sélectionnant adéquatement les paramètres  $T_1$  et  $T_2$  (F2E:  $T_1 > T_2$ ,  $t_1 < t_2$ ), le processus de frittage en deux étapes a permis d'améliorer la consolidation obtenue tout en évitant une croissance excessive des grains. La durée accrue de la deuxième étape (de 5 à 20 minutes) du cycle a légèrement augmenté le module Weibull (de 23 à 25). Le meilleur cycle de frittage pour l'Al 5356 broyé a ainsi été déterminé comme étant un cycle à 500 °C pendant 1 minute suivi d'une seconde étape à 350 °C pendant 20 minutes. Une croissance des grains minimale a été observée pendant le cycle F2E, avec une taille de grains de  $68 \pm 46$  nm après la première étape et  $73 \pm 46$  nm après la seconde étape.

Des poudres d'alliage d'Al-Mg-Er dont les compositions finales étaient Al-4.65Mg-0.08Er (0.1 Er) et Al-4.48Mg-0.44Er (0.5 Er) ont été analysées. Un broyage prolongé de 30 heures a mené en oxygène au sein des poudres finales, ~8% et ~13% en poids pour les poudres 0.1 Er et 0.5 Er, respectivement. Une croissance des grains a été observée à 180 °C au sein de la poudre 0.1 Er, alors qu'une taille des grains broyés d'environ 20 nm a été maintenue jusqu'à 400 °C ( $0.8 T_m$ ) au sein de la poudre 0.5 Er. La précipitation de la phase  $L_{12}$  d' $Al_3Er$  à l'échelle nanométrique n'a cependant pas été observée. Des oxydes cristallins (spinelle) au sein des poudres recuites à 500 °C et plus ont néanmoins été mis en évidence.

La densification et consolidation des poudres broyées d'Al-Mg-Er via des procédés de F2E a ainsi été améliorée en utilisant une vitesse de chauffage de  $300\text{ °C min}^{-1}$  et une pression maximale de 60 MPa au cours du cycle de frittage à  $550\text{ °C}$  pendant 0.5 minute suivi d'une seconde étape à  $350\text{ °C}$  pendant 20 minutes. La taille moyenne des grains a  $86 \pm 52\text{ nm}$  et  $50 \pm 21\text{ nm}$  au sein des poudres 0.1 Er et 0.5 Er, respectivement, après ce cycle de frittage. La formation d'oxyde cristallin (spinelle) pendant le frittage dépendait de la composition de la poudre et de la température  $T_1$  sélectionnée.

Le frittage en trois étapes (F3E:  $T_1 < T_2 < T_3$ ) a amélioré la consolidation de la poudre 0.1 Er broyée cryogéniquement par rapport aux résultats obtenus lors du processus de F2E ( $T_1 > T_2$ ). Une plus grande résistance à la fracture et dureté ont été obtenues avec des échantillons issus de F3E par rapport à ceux de provenant de F2E. Les échantillons produits via F3E ont également présenté des écarts-types de résistance à la fracture, dureté et taille des grains nanocristallins plus petits. Les meilleurs résultats ont été obtenus en utilisant un cycle de  $350\text{ °C}$  pendant 10 minutes, suivi d'une seconde étape de  $450\text{ °C}$  pendant 5 minutes et d'une troisième étape de  $500\text{ °C}$  pendant 5 minutes. Les cycles de frittage F3E ont également limité la croissance moyenne des grains à  $\sim 60\text{ nm}$ , par rapport à  $\sim 70\text{ nm}$  après un cycle de F2E. Par ailleurs, des agrégats d'Er et de Ti ont été observés au sein d'échantillons préparés par F2E. De même, la précipitation de phases nanométriques d'Al-Fe et d'Al-Fe-Ni a été observée au sein d'échantillons de F3E après 30 minutes de frittage.

To God, my mother Lanre, my sisters Seni and Funlayo,  
and my family who support and encourage me in each new endeavour

To the memory of my grandparents  
Silvanus Olatunde and Agnes Modupeola Williams

## Acknowledgements

I would like to extend my gratitude to my thesis supervisor, Prof. Mathieu Brochu for giving me the opportunity to work on this research project and to grow and challenge myself as an engineer and researcher. I would also like to thank both my supervisors Prof. Mathieu Broch and Prof. Raynald Gauvin for their guidance during the course of this work. In addition, I would like to express my gratitude to McGill, FQRNT, and REGAL for extending financial support to this project.

I am grateful to Prof. Carl Blais at Laval University for providing assistance by producing the customized atomized powders. I am also grateful to SGS Canada for their assistance with analyzing the oxide content of the powders used in this study. I would like to thank Ranjan Roy and Andrew Golsztajn for their assistance with chemical analysis of my samples. I would also like to offer many thanks to Nicolas Brodusch and David Liu for all their help with electron microscopy. I would like to thank Francois-Johan Chassaing and Jason Milligan for their assistance with production and characterization of Al-Mg-Er materials and cryomilling of conventional Al alloy powders, respectively. I would also like to use this opportunity to thank Barbara Hanley, Florence Paray, Monique Riendeau, Raymond Langlois, Robert Paquette, and Pierre Vermette for their assistance over the years.

Last but not least I would like to thank my fellow graduate students who have helped and encouraged me, especially Amrita Yasin, Neslihan Alpay, Phillipe Hendrix, David Walker, Jose Alberto Muniz, Abhi Ghosh, Andrew Walker, Jason Milligan, Mert Celikin, David Heard, Dong-Geun Kim, Sriraman Rajagopalan, and Manas Paliwal.

## Preface and Contribution of Authors

This research work investigated strategies for producing bulk nanostructured Al-Mg alloys by powder metallurgy techniques. Bulk nanocrystalline Al-Mg alloys were produced using multi-stage SPS consolidation of cryomilled powders, with temperatures ranging from  $0.6T_m$  to  $0.9T_m$ . These results are presented in a monograph style thesis and experimental results are presented in Chapters 4 through 7.

A version of Chapter 4 has been published [Akinrinlola B, Gauvin R, Brochu M (2012) Improving the mechanical reliability of cryomilled Al-Mg alloy using a two-stage spark plasma sintering cycle, *Scripta Materialia* 66:455-458]. I was responsible for collecting and analyzing the data, as well as manuscript composition. Vintilla R was involved in the early stages of concept development. Gauvin R provided expertise on the electron microscopy work. Brochu M was the supervising author and oversaw the concept development and manuscript composition.

A version of Chapter 5 has been published [Akinrinlola B, Gauvin R, Blais C, Brochu M (2017) Thermal stability of cryomilled Al-Mg-Er powders, *Journal of Nanomaterials* 2017:6348569 17p. doi:10.1155/2017/6348569]. I was responsible for concept development, collecting and analyzing the data, as well as manuscript composition. Blais C supplied technical assistance with production of the Al-Mg-Er powders. Gauvin R provided expertise on the electron microscopy work. Brochu M was the supervising author and oversaw the concept development and manuscript composition.

Concerning the works presented in Chapters 6 and 7, I was responsible for the concept development, collecting and analyzing the data, as well as manuscript composition. Blais C supplied technical assistance with production of the Al-Mg-Er powders. Gauvin R provided expertise on the electron microscopy work. Brochu M was the supervising author and supplied technical and scientific advice and editing of the manuscript.

Figures in Chapters 1 and 2 are used with permission from pertinent sources.

## Table of Contents

Abstract.....	ii
Resume.....	iv
Acknowledgements.....	vii
Preface and Contribution of Authors.....	viii
Table of Contents.....	ix
List of Figures.....	xiii
List of Tables.....	xix
List of Abbreviations.....	xx
List of Symbols.....	xxii
Chapter 1 : Introduction.....	1
Background.....	1
Objectives.....	4
References.....	5
Chapter 2 Literature Review.....	7
2.1. Alloy systems.....	7
2.1.1. Aluminum-Magnesium alloys.....	7
2.1.2. Aluminum-Magnesium-Erbium alloys.....	9
2.2. Grain boundaries and grain growth.....	11
2.3. Nanocrystalline materials.....	14
2.4. Grain growth in nanocrystalline systems.....	17
2.5. Bulk nanocrystalline materials by PM.....	20
2.5.1. Cryomilling.....	20
2.5.2. Spark Plasma Sintering.....	22
2.6. Bulk nanocrystalline cryomilled Al-Mg alloys.....	25
2.6.1. ODS Al alloys by mechanical alloying (MA).....	25
2.6.2. Cryomilled Al-Mg powders.....	27
2.6.3. Grain growth in cryomilled Al-Mg alloys.....	29
2.6.4. Microstructure of bulk cryomilled nanostructured Al-Mg.....	30
2.6.5. Mechanical properties of bulk cryomilled Al-Mg.....	32
2.7. References.....	34

Chapter 3 Experimental Methodology .....	48
3.1. Powder production and characterization.....	48
3.1.1. Atomized powders .....	48
3.1.2. Cryomilled powders .....	50
3.2. Bulk sintered samples.....	52
3.2.1. Spark Plasma Sintering .....	52
3.2.2. Sintering parameters .....	53
3.3. Properties of bulk sintered samples.....	55
3.3.1. Density .....	55
3.3.2. Microhardness .....	56
3.3.3. Flexural/Bend Strength.....	56
3.4. Analysis methods.....	57
3.4.1. Differential scanning calorimetry.....	57
3.4.2. X-ray Diffraction.....	57
3.4.3. X-ray Photoelectron Spectroscopy (XPS).....	58
3.4.4. Microscopy methods.....	59
3.5. References .....	60
Chapter 4 Improving Consolidation of Cryomilled Al 5356 Alloy Using a Two-Stage (TSS) SPS Sintering Cycle.....	61
4.1. Introduction .....	61
4.2. Background.....	61
4.3. Phases in the sintered bulks .....	62
4.4. Microstructure and grain size.....	64
4.5. Grain growth during sintering.....	67
4.6. Consolidation improvement and Weibull modulus analysis .....	69
4.7. Summary .....	71
4.8. References .....	72
Chapter 5 Investigating the Thermal Stability of Cryomilled Al-Mg-Er Powders .....	75
5.1. Introduction .....	75
5.2. Background.....	75
5.3. Al-Mg-Er powders .....	76
5.3.1. Atomized Al-Mg-Er powders.....	76
5.3.2. Cryomilled powders .....	80

5.4. DSC analysis of milled Al-Mg-Er powders .....	85
5.5. Annealing behavior of 0.1 Er powder .....	87
5.5.1. XRD results of 0.1 Er powder .....	87
5.5.2. TEM results of 0.1 Er powder .....	90
5.6. Annealing behavior of 0.5 Er powder .....	94
5.6.1. XRD results of 0.5 Er powder .....	94
5.6.2. TEM results of 0.5 Er powder .....	97
5.7. Grain size stability .....	99
5.7.1. Activation energy for grain growth .....	100
5.7.2. Er effect on grain growth .....	101
5.7.3. Oxide contributions to grain size control .....	102
5.8. Possible Er contributions to oxidation behaviour .....	104
5.9. Summary .....	106
5.10. References .....	107
<b>Chapter 6 Consolidation of Cryomilled Al-Mg-Er Powders by Two-Stage (TSS) SPS Sintering Processes .....</b>	<b>112</b>
6.1. Introduction .....	112
6.2. Phases in sintered Al-Mg-Er compacts .....	112
6.2.1. XRD results .....	112
6.2.2. TEM results .....	115
6.3. Microstructure and grain size distribution .....	120
6.4. Grain growth during consolidation .....	124
6.5. Effect of heating rate on consolidation .....	129
6.6. Summary .....	138
6.7. References .....	139
<b>Chapter 7 Multi-stage SPS Processing of 0.1 Er Cryomilled Powder .....</b>	<b>143</b>
7.1. Introduction .....	143
7.2. Background .....	143
7.3. Phases in sintered samples .....	145
7.3.1. XRD results .....	145
7.3.2. TEM results .....	146
7.4. Microstructure and grain size analysis .....	155
7.5. Grain growth during consolidation .....	158

7.6. Consolidation in multi-stage sintered samples .....	161
7.7. Summary .....	164
7.8. References .....	165
Chapter 8 Summary, Contributions, and Future Work .....	169
8.1. Summary .....	169
8.2. Contributions to original knowledge .....	170
8.3. Recommendations for future work .....	171

## List of Figures

Figure 1.1 Improvement in tensile strength with grain refinement. Taken from ref. [1.6].	2
Figure 2.1 Aluminum-Magnesium binary phase diagram. Taken from ref. [2.1].	8
Figure 2.2 Concentration profiles across the matrix/precipitate interface for Al-0.06 Zr-0.04 Sc-0.02 Er alloys aged at 400 °C for (a) 0.5 h and (b) 64 days; inset images are APT reconstructions of the corresponding precipitate. Images are from ref. [2.24].	10
Figure 2.3 (a,b) HRTEM micrographs of precipitates in Al-0.06 Zr-0.03 Er after 768 h at 400 °C with diffractograms of the regions indicated shown in (b). Images are taken from ref. [2.27].	11
Figure 2.4 Changes in grain boundary energy with misorientation between [001] directions for (a) [100] tilt boundaries and (b) [110] tilt boundaries in Al. Taken from ref. [2.36].	13
Figure 2.5 Structure of nanocrystalline material: unfilled circles are atoms in the GB regions. Taken from ref. [2.40].	15
Figure 2.6 Schematic for critical distance for a dislocation pile up $L_c$ taken from ref. [2.54].	17
Figure 2.7 (a) Nanocrystalline Al stability map plotting elastic enthalpy versus the enthalpy of mixing for stabilizing solutes (red dots) and other solutes (black dots) in the system; (b) Table of stabilizing solutes (red dots). Taken from ref. [2.76].	20
Figure 2.8 Schematic of a cryomill set-up.	21
Figure 2.9 Formation of nanostructure during mechanical milling process, reproduced from ref. [2.78].	22
Figure 2.10 Mass transport mechanisms that contribute to sintering and neck growth, taken from ref. [2.90].	23
Figure 2.11 Schematic of an SPS apparatus, taken from ref. [2.90].	24
Figure 2.12 As milled microstructure in Al-7.6 at.% Mg powders taken from ref. [2.84].	29
Figure 2.13 Grain growth in SPS consolidated Al 5083: (a) UFG structure after SPS consolidation at 400 °C for 3 mins under 100 MPa; (b) Bands of coarser UFGs; (c) grain size distribution in SPS material. Images taken from ref. [2.136].	31

Figure 2.14 Typical dislocation structures observed after SPS consolidation of cryomilled nanocrystalline Al 5083 powders. Taken from ref. [2.136].	32
Figure 2.15 (a) Increasing ductility with tailored bimodal microstructure in bulk cryomilled Al 5083, taken from ref. [2.135]; (b) Propagation of a microcrack in a nanostructured material with a bimodal lamellar structure, taken from ref. [2.52].	34
Figure 3.1 SEM micrographs of the atomized powders - (a) 0.1 Er and (b) 0.5 Er; Particle size distributions from sieve analysis for (c) 0.1 Er and (d) 0.5 Er.	49
Figure 3.2 Union Process Attrition mills used for the cryomilling experiments: (a) 1-S mill; (b) HD-01 mill.	50
Figure 3.3 SEM micrograph of the cryomilled Al 5356 powder.	51
Figure 3.4 SEM micrographs of the cryomilled powders: (a) 0.1 Er, (b) 0.5 Er; Particle size distributions for (c) 0.1 Er and (d) 0.5 Er.	52
Figure 3.5 Thermal Thermal Technology LLC 10-3 SPS apparatus.	53
Figure 3.6 Schematics of sintering schedules (a) TSS and (b) MSS.	55
Figure 4.1 Phase identification after milling of Al 5356 powder with W standard.	63
Figure 4.2 Phase identification after sintering: XRD spectra of 500 OSS, 500 TSS 5 and 500 TSS 20 samples with a Si standard. Peaks have been normalized.	63
Figure 4.3 STEM images (a,b) showing dislocation structures (dashed black arrows), Al-Mg-Cr precipitates (white arrows), and Al-Mg-Cr-Ti precipitates (red arrows) observed in 500 TSS 20 sample. EDS microanalysis (c, d, e) of precipitates/areas indicated in (a) and (b).	64
Figure 4.4 TEM micrographs and SAED patterns showing nanocrystalline structure of the SPS pucks: (a) BF image of a 500 OSS sample; (b) BF image of a 500 TSS 20 sample; (c) SAED pattern of the 500 OSS region shown in (a); (d) SAED pattern of the 500 TSS 20 region shown in (b).	65
Figure 4.5 Bimodal microstructure observed in 500 TSS 20 sample with (a) coarse grains with dislocation structures microstructure and (b) lamellar-type grains.	67
Figure 4.6 Grain size distribution after 500 OSS (average grain size = $68 \pm 46$ nm; 300 grains) and 500 TSS 20 sintering conditions (average grain size = $73 \pm 46$ nm; 319 grains).	67
Figure 4.7 Grain size estimations for TSS schedules.	68

Figure 4.8 Weibull modulus plots for 500 OSS (m = 13; n = 28), 500 TSS 5 (m = 23; n = 12) and 500 TSS 20 (m = 25; n = 18) conditions.....	70
Figure 4.9 Calculated densification curve for the 500 TSS 20 sample .....	71
Figure 5.1 XRD spectra of atomized Al-Mg-Er powders.....	78
Figure 5.2 BSE images of atomized Al-Mg-Er powders: (a) 0.1 Er powder; (b) 0.5 Er powder with inset showing micro-scale segregation; (c) some nanoscale features in 0.5 Er powder; (d) EDS element line scan analysis from inset in (b) showing Mg and Er distribution.....	79
Figure 5.3 30 h milled powders with supersaturated $\alpha$ -Al phase after milling (a); nanocrystalline grains as shown in Bright field TEM images of 0.1 Er (b) and 0.5 Er (c), both with inset SAED patterns taken from the areas shown; and the grain size distributions obtained from TEM image analysis (d). The nanocrystalline $\alpha$ -Al phase is indicated by the blue arcs.....	82
Figure 5.4 XPS analysis of the oxide film on 0.1 Er (a – c) and 0.5 Er (d – f) powders: Al2p peaks (a,d); O1s peaks (b,e); valence region with Shirley background subtracted (c,f).....	84
Figure 5.5 HRTEM images of (a) 0.1 Er and (b) 0.5 Er powders showing the oxide film (indicated by arrows) and the crystalline Al matrix: $d \approx 0.232$ nm ( $d_{111} = 0.2338$ nm) and $d \approx 0.128$ nm ( $d_{311} = 0.1221$ nm).....	85
Figure 5.6 DSC traces (solid lines) and TG traces (dotted lines) of 0.1 Er and 0.5 Er powders at heating rate of $10 \text{ K} \cdot \text{min}^{-1}$ under flowing Ar: exothermic events A and B, and endothermic event C. ....	85
Figure 5.7 XRD patterns of the annealed 0.1 Er powders with major phases labelled; 25 to 60 Deg. 2-Theta inset shows minor crystalline oxide peaks.....	89
Figure 5.8 Grain size distributions obtained from TEM image analysis for selected 0.1 Er annealed powders. D is the largest grain size observed at temperature.....	91
Figure 5.9 TEM images of 0.1 Er powder annealed at 150 °C (a), 180 °C (b,c), 330 °C (d,e) and 500 °C (f,g); top row – nanocrystalline regions; bottom row - abnormal grain growth. Nanocrystalline $\alpha$ -Al phase is indexed with the blue arcs. ....	92
Figure 5.10 Indexed SAED patterns from the large grained regions shown in the previous figure: Al grains viewed from (a) $B = [103]$ direction at 180 °C, (b) $B = [112]$	

direction at 330 °C, and (c) B = [121] direction at 500 °C; (d) second phase particles observed in powders annealed at 330 °C. The small circles indicate the spot diffraction pattern and rings (indicated by arrows) are produced by nanoscale phases in the imaged regions..... 93

Figure 5.11 STEM-EDS analysis of some nanoscale phases observed in the powders annealed at 330 °C. .... 94

Figure 5.12 XRD patterns of the annealed 0.5 Er powders with major phases labelled; 25 to 60 Deg. 2-Theta inset showing minor crystalline oxide peaks ..... 95

Figure 5.13 Grain size distribution obtained from TEM image analysis for selected 0.5 Er annealed powders. D is the largest grain size observed at temperature. .... 98

Figure 5.14 Nanocrystalline grains after annealing of 0.5 Er powders at 150 °C (a) and 250 °C (b). Nanocrystalline  $\alpha$ -Al phase is indexed with blue arcs ..... 98

Figure 5.15 TEM images of the 0.5Er powders after various anneals: nanocrystalline regions after annealing at 400 °C (a); the onset of abnormal grain growth at 450 °C (b); grain growth at 500 °C (c) with corresponding diffraction pattern (d). Nanocrystalline  $\alpha$ -Al and  $MgAl_2O_4$  are indicated by the blue and red arcs, respectively ..... 99

Figure 6.1 XRD spectra of samples sintered by TSS schedules for 0.1 Er (a, b) and 0.5 Er (c, d): full spectra (a, c) and close up of small peaks (b, d). Peaks are normalized. 114

Figure 6.2 X-ray spectrums taken from the nanocrystalline (blue line) and coarse grained (orange line) in the 0.1 Er 550 TSS 20 sample..... 116

Figure 6.3 Typical results from sintered 0.1 Er samples (a,b – 500 TSS 20; c,d – 550 TSS 20): bimodal microstructure (a,c). Typical SAED patterns taken from the nanocrystalline regions (b,d). SAED patterns are indexed as  $\alpha$ -Al (blue arcs) and  $MgAl_2O_4$  (red arcs) phases. .... 117

Figure 6.4 Microstructure in sintered 0.5 Er pucks (a,b – 500 TSS 20\*; c,d – 550 TSS 20): bimodal microstructure (a,c). Typical SAED patterns taken from nanocrystalline regions (b,d). SAED patterns are indexed as  $\alpha$ -Al (blue arcs),  $MgAl_2O_4$  (red arcs), and  $\gamma$ - $Al_2O_3$  (orange arc). .... 118

Figure 6.5 X-ray elemental maps of 0.5 Er 550 TSS 20 sample showing distribution of Mg, Er, and Fe solutes in the sintered sample. .... 119

Figure 6.6 X-ray spectrum and TEM image of Al-Mg-Er-Fe-O particle from Region A 119

Figure 6.7 X-ray spectrums and HRTEM images of Al-Mg-Er-Fe-O-N particles from (a) Region B and (b) Region C .....	120
Figure 6.8 X-ray spectrum and HRTEM image of Al-Mg-O-N particles from Region D	120
Figure 6.9 Grain size distribution in TSS sintered Al 5356, 0.1 Er and 0.5 Er samples	123
Figure 6.10 Dark field and bright field images of the microstructure in the 0.1 Er 500 TSS 20 (a,d), 0.1 Er 550 TSS 20 (b, e) and 0.5 Er 550 TSS 20 (c,f).....	124
Figure 6.11 Estimated boundary mobilities .....	128
Figure 6.12 Estimated and experimental grain growth during TSS schedules .....	129
Figure 6.13 Densification curves for (a) 500 TSS 20 and (b) 550 TSS 20 processes; (c) 0.1 Er and 0.5 Er powders.....	132
Figure 6.14 (a) SPS temperature profiles and (b) SPS current profiles during TSS sintering of 0.5 Er powders.....	133
Figure 6.15 Temperature profiles (a,b) and fitted densification curves (c,d) obtained for 500 TSS 20 (left column) and 550 TSS 20 (right column) sintering of 0.5 Er powders	136
Figure 7.1 (a) XRD spectra of the TSS and MSS sintered samples; (b) close-up of minor peaks in XRD spectra. Peaks have been normalized.....	146
Figure 7.2 X-ray spectrums taken from nanocrystalline and coarse-grained regions of (a) 500 TSS 20 and (b) 350 MSS 5 samples showing distribution of solute elements.	147
Figure 7.3 TEM analysis of phases in the 350 MSS 5 sample: (a) nanocrystalline region imaged in BF mode; (b) corresponding diffraction pattern from area shown in (a) indexed with colored arcs – Al (blue) and $MgAl_2O_4$ (red); coarse grain imaged in DF (c) and BF (d) mode with inset SAED pattern indexed as Al from $B = [121]$ direction. ....	148
Figure 7.4 X-ray elemental maps of the 350 MSS 5 sample showing higher concentrations of Mg and O in the nanocrystalline regions. X-ray spectrum collected from the mapping area showing the elements present.....	149
Figure 7.5 X-ray elemental maps of the 350 MSS 10 sample showing higher concentrations of Mg and O within the nanocrystalline regions. X-ray spectrum collected from the mapping area showing the elements present.....	151
Figure 7.6 X-ray elemental maps of a nanocrystalline region in the 350 MSS 10 sample showing Fe and Ni rich clusters of ~ 300 nm size suggesting the presence of Al-Fe-Ni	

precipitates. X-ray spectrum collected from the mapping area showing the elements present. ....	152
Figure 7.7 X-ray elemental maps of a nanocrystalline region in the 350 MSS 10 sample showing clusters of Mg and O atoms. Fe and Ni rich clusters of ~ 200 nm size suggest the presence of nanoscale Al-Fe-Ni precipitate. X-ray spectrum collected from the mapping area shows the elements present. ....	153
Figure 7.8 X-ray elemental maps of the 500 TSS 20 sample showing higher concentrations of Mg and O in the nanocrystalline regions and possible clustering of Er and Ti atoms. X-ray spectrum collected from mapping area showing the elements present. ....	154
Figure 7.9 As sintered microstructure of 350 MSS 5 (first row), 350 MSS 10 (second row) and 500 TSS 20 (third row): Bimodal microstructure in sintered samples (a,d,g); BF images of nanocrystalline regions (b,e,h); corresponding SAED patterns (c,f,i) indexed with colored arcs – Al (blue arcs) and MgAl <sub>2</sub> O <sub>4</sub> (red arcs) phases. ....	157
Figure 7.10 TEM grain size distributions in TSS and MSS sintered samples.....	158
Figure 7.11 Estimation of grain growth during the TSS and MSS schedules using Burke's model with estimated boundary mobility $m_b$ .....	161
Figure 7.12 Plotted densification curves for the (a) MSS and (b) TSS schedules .....	163

## List of Tables

Table 1.1 Properties of coarse-grained, UFG, and NS Al-Mg alloys .....	4
Table 2.1 Cryomilled Al and Al-Mg alloys.....	28
Table 2.2 Properties of bulk Al-Mg and bulk NS Al-Mg by cryomilling.....	33
Table 3.1 Composition of atomized Al-Mg-Er powders .....	49
Table 3.2 Composition of 30 h milled Al-Mg-Er powders (wt.%) .....	52
Table 3.3 Sintering parameters for OSS, TSS and MSS schedules.....	54
Table 4.1 Summary of XRD analysis obtained from milled and consolidated samples.	65
Table 4.2 Mechanical properties obtained from OSS and TSS consolidated samples..	69
Table 5.1 Composition of atomized and 30 hour milled powders (wt.%).....	77
Table 5.2 XRD results for atomized and 30 hour milled powders.....	79
Table 5.3 Oxide composition from XPS peak analysis .....	84
Table 5.4 XRD results and TEM grain size for the 0.1 Er annealed powders.....	90
Table 5.5 XRD results and TEM grain size for the 0.5 Er annealed powders.....	96
Table 5.6 Volume fraction of nanoscale oxides and Zener limit grain size .....	103
Table 6.1 XRD peak analysis for milled powders and sintered bulks .....	114
Table 6.2 Grain size and micro-strain data.....	121
Table 6.3 Mechanical properties of sintered samples .....	130
Table 6.4 Aluminum material properties used for the model .....	137
Table 7.1 XRD results for milled powders and sintered pucks .....	146
Table 7.2 Grain size and microstrain data .....	155
Table 7.3 Diffusion data for boundary mobility calculations.....	161
Table 7.4 Properties of Multi-stage SPS sintered bulks .....	162

## List of Abbreviations

Abbreviation	Full meaning
BF	Bright field
BSE	Back-scattered electron
CIP	Cold Isostatic Pressing
DF	Dark field
DSC	Differential scanning calorimetry
ECAP	Equal Channel Angular Pressing
EDS	Energy Dispersive Spectroscopy
FAST	Field Assisted Sintering Technique
FCC	Face centered cubic structure
FWHM	Full-width half maximum
GB	Grain boundary
HAGB	High angle grain boundary
HIP	Hot Isostatic Pressing
HP	Hot Pressing
HPT	High-Pressure Torsion
HRTEM	High-resolution transmission electron microscopy
ICP	Inductively Couple Plasma
IGA	Instrumental Gas Analysis
MA	Mechanical alloying
MSS	Multi-stage sintering
NS	Nanostructured
ODS	Oxide-dispersion strengthened
OSS	One-stage sintering
PECS	Pulsed-Electric Current Sintering
PM	Powder metallurgy

RE	Rare earth
RQC	Routine Quality Control
SAED	Selected area electron diffraction
SEM	Scanning electron microscopy
SPD	Severe plastic deformation
SPS	Spark Plasma Sintering
TEM	Transmission electron microscopy
TG	Thermogravimetric
TGA	Thermogravimetric analysis
TM	Transition metal
TSS	Two-stage sintering
UFG	Ultra-fine grained
XPS	X-ray Photoelectron Spectroscopy
XRD	X-ray Diffraction

## List of Symbols

Symbol	Meaning
Å	Angstrom
b	Burger's vector of a dislocation
$d_{\min}$	minimum grain size obtained by milling
D	grain size
$D_0$	initial grain size
$D_{\max}$	maximum grain size
$D_{\text{Zener}}$	Zener limit grain size
f	volume fraction of second phase particles
$\Delta H_{\text{seg}}^{\text{elastic}}$	Elastic Enthalpy
$\Delta H_{\text{mix}}$	Enthalpy of Mixing
L12	cubic crystal structure, Pm3m space group
$L_c$	critical equilibrium distance between two edge dislocations
$m_b$	grain boundary mobility
m	Weibull modulus
n	grain growth exponent
nm	nanometer
P	driving force for grain growth
$P_{\text{Zener}}$	Zener drag force
Q	activation energy
r	radius of second phase particles
T	Temperature
$T_m$	melting Temperature
$\mu\text{m}$	micrometer
V	grain boundary velocity

## Chapter 1 : Introduction

### Background

Due to a variety of properties such as low density, corrosion resistance, strength, recyclability, formability, ductility and conductivity, aluminum alloys are highly valuable metals and are widely used in a variety of sectors such as transport, construction, packaging, electrical and domestic industries. Aluminum by itself has poor mechanical properties, but can be strengthened by precipitation hardening, solid solution strengthening, or strain hardening [1.1]. Heat-treatable Al alloys (i.e.: precipitation hardening) are the highest strength Al alloys, which include the 2xxx (Al-Cu/Al-Cu-Mg), 6xxx (Al-Mg-Si), and 7xxx (Al-Zn-Mg-Cu) series. Series 1xxx (Al-Fe-Si), 3xxx (Al-Mn), 4xxx (Al-Si) and 5xxx (Al-Mg) are classified as non-heat treatable alloys (i.e.: solid solution strengthened); mid-strength alloys are found in the 3xxx and 5xxx series. Significant improvement in strength of Al alloys can be obtained by grain size refinement as shown in Figure 1.1, where tensile strength of nanostructured Al alloys can potentially reach three times that of the strongest conventional Al alloys. Markets for nanostructured metals exist in many product sectors where superior strength, strength-to-weight ratio and fatigue life are important design parameters [1.2]. High strength nanostructured Al alloys have potential for commercial use in the electronics, automotive and aerospace industries [1.3-1.5].

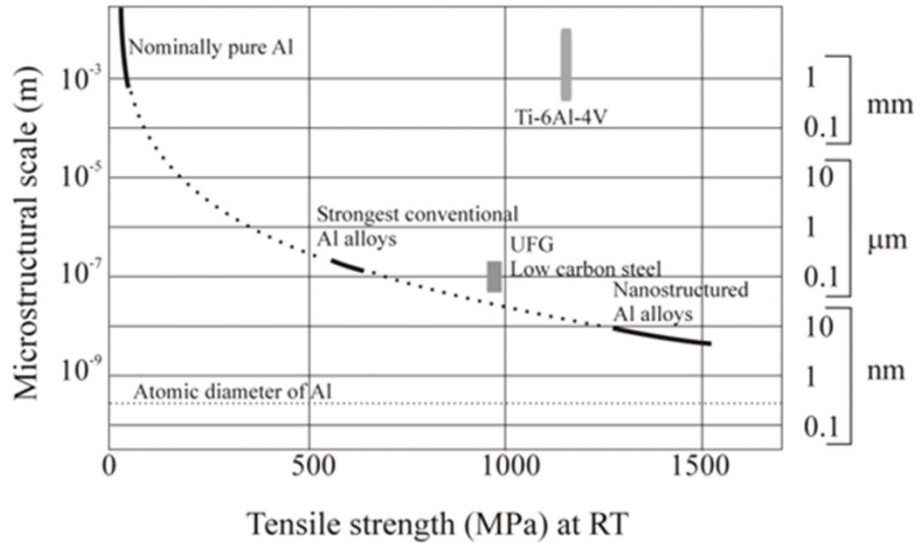


Figure 1.1 Improvement in tensile strength with grain refinement. Taken from ref. [1.6].

As the grain size is refined below 1  $\mu\text{m}$ , the microstructure enters the ultra-fine grained (UFG) regime (100 nm – 1  $\mu\text{m}$ ) and the nanocrystalline regime (< 100 nm). Solids of bulk dimensions (micron to meter length scales) composed of structural elements (i.e.: crystallites) of nanometer-scale size are referred to as nanocrystalline or nanostructured (NS) materials [1.7]. Many bulk NS materials are produced by “two-step” methods which involve synthesis of nanoscale particulates or NS powders followed by consolidation into bulk samples. Bulk NS Al materials produced by the powder metallurgy (PM) route typically involve production of nanocrystalline powders by cryomilling followed by consolidation with thermo-mechanical/pressure-assisted processes such as Hot Pressing (HP), Hot or Cold Isostatic Pressing (HIP/CIP), extrusion, and current assisted sintering processes such as Spark Plasma Sintering (SPS). Cryomilling is mechanical alloying or milling carried out at cryogenic temperatures and is a cyclic severe plastic deformation (SPD) process that produces the nanocrystalline structure inside the powders [1.8].

Much research effort has been expended into the development of bulk NS 5xxx alloys. The 5xxx series Al-Mg alloys are important for use in buildings (i.e.: architecture sheets, scaffolding), automotive parts (i.e.: chassis components, press-formed body parts) and marine applications (i.e.: ship building, platforms). 5xxx series alloys offer the best combination of strength and corrosion resistance of all the Al-alloys. These alloys

also have the added benefit of simultaneous strength improvement and weight reduction with increasing Mg addition, i.e.: improved strength-to-weight ratio. In bulk NS materials produced by PM routes, the final microstructure and properties of the material depend on both the parameters for powder production and powder consolidation. Several methods have been used to consolidate NS Al 5083 powders such as CIP, HIP, and SPS as shown in Table 1.1. Compared to the conventional Al 5083 alloy, bimodal, UFG, and NS Al 5083 exhibit significant improvement in strength and hardness, but reduced ductility. Tensile yield strength increases by a factor of ~4.5 for bulk NS Al 5083 compared to conventional polycrystalline Al 5083 alloys. The creation of artifacts (i.e.: porosity, microcracks, insufficient bonding between particles) during processing is one of the main factors that limits ductility in bulk NS materials [1.9]. In bulk NS materials with similar average grain size (~30 nm), the ductility is dependent on the consolidation method where ~ 9% elongation is obtained with in-situ consolidation versus ~2% elongation after CIP and extrusion.

Adequate consolidation of the milled powder typically requires high temperature application for extended periods of time. This increases the likelihood of grain growth. The average grain size reported is typically in the UFG range after thermo-mechanical processing while cryomilled Al-Mg powders typically have an average grain size of ~ 20 nm after milling [1.10]. The strength benefits in bulk NS materials increase with decreasing grain size, from ~300 MPa for a bimodal microstructure [1.11] to 620 - 690 MPa for NS/UFG bulks [1.9, 1.10, 1.12]. To take advantage of the strength improvements from grain size refinement, it would be beneficial to retain the nanocrystalline structure after powder consolidation. Although grain sizes in the UFG range have been reported after SPS consolidation (Table 1.1), an average grain size as low as 51 nm was also reported for cryomilled Al 5083 sintered by SPS [1.13]. Compared to the conventional pressure-assisted sintering processes, the SPS process provides rapid sintering through the simultaneous application of current and pressure. Due to the short sintering cycle, SPS is beneficial for the consolidation of thermally sensitive materials and can be advantageous for retaining nanostructures during consolidation.

Table 1.1 Properties of coarse-grained, UFG, and NS Al-Mg alloys

Alloy	Condition	Grain size (nm)	Ultimate Tensile Stress (MPa)	Yield Strength <sup>a</sup> (MPa)	Elongation to failure (%)
<b>Polycrystalline Al 5083 [1.9]</b>		55·10 <sup>3</sup>	285	145	19
<b>Bimodal Al 5083 [1.11]</b>	Cryomilled; HIP and extrusion	Bimodal (nm - μm)	462	334	8.4
<b>NS Al 5083 [1.14,1.15]</b>	Cryomilled; SPS	192	-	~ 560 (700 <sup>b</sup> )	
<b>NS Al-7.5Mg [1.10]</b>	Cryomilled; HIP and extrusion	100 - 300	847	641	1.4
<b>NS Al 5083 [1.12]</b>	Cryomilled; CIP and extrusion	30	740	690	1.5
<b>NS Al 5083 [1.9]</b>	Cryomilled; in-situ consolidation	26	742	620	8.5

<sup>a</sup>0.2% offset; <sup>b</sup>Compressive stress

## Objectives

This thesis focuses on the production of bulk NS Al-Mg alloys by a “two-step” approach using PM techniques. The NS precursors are produced by cryomilling of atomized pre-alloyed powders, followed by consolidation via SPS. The goal of the thesis is to retain the average grain size of the material in the nano regime, i.e.: below 100 nm, while achieving densification and consolidation of the powders. Two routes are investigated to accomplish this goal – (1) testing of consolidation parameters in SPS (i.e.: multi-stage

sintering), and (2) changing the alloy composition to improve the thermal stability of the powders (i.e.: microalloying with Er). The remainder of the thesis is laid out as follows:

- Chapter 3 provides the experimental procedures and characterization techniques employed for the synthesis and characterization of the powder and bulk materials studied, as well as details on the materials and equipment used.
- Chapter 4 shows the benefits of using a two-stage (TSS) versus one-stage (OSS) SPS sintering schedule for minimizing grain growth while improving the consolidation of typical cryomilled Al 5356 alloy powders.
- Chapter 5 explores the thermal stability of cryomilled Al-5Mg powders microalloyed with Er (0.1 wt.%, 0.5 wt.%)
- Chapter 6 examines the grain growth and consolidation behaviour of the cryomilled Al-Mg-Er powders processed by two-stage sintering processes.
- Chapter 7 investigates the consolidation and grain growth behaviour of Al-Mg-Er alloys (0.1 wt.% Er) when subjected to two-stage (TSS) versus three-stage (MSS) sintering processes.

## References

- 1.1. Hatch JE (1984) Properties of commercial wrought alloys. In: Aluminum: Properties and Physical Metallurgy. ASM, Metals Park, OH, pp 351-378.
- 1.2. Lowe TC, Zhu YT (2003) Commercialization of nanostructured metals produced by severe plastic deformation processing, *Advanced Engineering Materials* 5:373-378.
- 1.3. Lowe TC (2009) Commercializing bulk nanostructured metals and alloys. In: Zehetbauer MJ, Zhu YT (eds) *Bulk Nanostructured Materials*. WILEY-VCH Verlag GmbH & Co. KGaA, Weinheim, pp 673-686.
- 1.4. Azushima A, Kopp R, Korhonen A, *et al.* (2008) Severe plastic deformation (SPD) processes for metals, *CIRP Annals - Manufacturing Technology* 57:716–735.

- 1.5. Valiev RZ, Sabirov I, Zhilyaev AP, Langdon TG (2012) Bulk nanostructured metals for innovative applications, *Journal of Materials* 64:1134-1142.
- 1.6. Perepezko JH, Hebert RJ (2002) Amorphous aluminum alloys—synthesis and stability, *Journal of Materials* 54:34–39.
- 1.7. Gleiter, H (1995) Nanostructured materials: state of the art and perspectives, *Nanostructured Materials* 6:3-14.
- 1.8. Fetch HJ (1995) Nanostructure formation by mechanical attrition, *Nanostructured Materials* 6:33-42.
- 1.9. Youssef KM, Scattergood RO, Murty KL, Koch CC (2006) Nanocrystalline Al–Mg alloy with ultrahigh strength and good ductility, *Scripta Materialia* 54:251-256.
- 1.10. Witkin D, Le Z, Rodriguez R *et al.* (2003) Al–Mg alloy engineered with bimodal grain size for high strength and increased ductility, *Scripta Materialia* 49:297-302.
- 1.11. Tellkamp VL, Lavernia EJ, Melmed A (2001) Mechanical behavior and microstructure of a thermally stable bulk nanostructured Al alloy, *Metallurgical and Materials Transactions A* 32: 2335-2343.
- 1.12. Han BQ, Mohamed FA, Lavernia EJ (2004) Deformation mechanisms and ductility of nanostructured Al alloys, *MRS Proceedings* 821: P9.1
- 1.13. Ye J, Ajdelsztajn L, Schoenung JM (2006) Bulk nanocrystalline aluminum 5083 alloy fabricated by a novel technique: Cryomilling and spark plasma sintering, *Metallurgical and Materials Transactions A* 37:2569-2579.
- 1.14. Xiong Y, Liu D, Li Y *et al.* (2012) Spark plasma sintering of cryomilled nanocrystalline Al alloy - part I: microstructure evolution, *Metallurgical and Materials Transactions A* 43:327-339.
- 1.15. Liu D, Xiong Y, Topping TD *et al.* (2012) Spark plasma sintering of cryomilled nanocrystalline Al alloy - part II: influence of processing conditions on densification and properties, *Metallurgical and Materials Transactions A* 43:340-350.

## Chapter 2 Literature Review

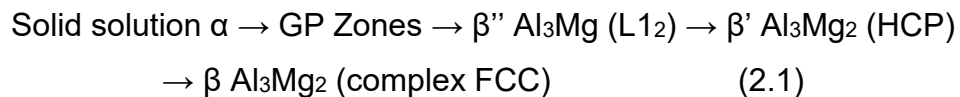
### 2.1. Alloy systems

The material system studied in this work is the Al-5%Mg system, microalloyed with Er (0.1, 0.5), in wt.%. In this section a brief introduction to Al-Mg alloys and microalloying of Al-Mg alloys with Er is presented.

#### 2.1.1. Aluminum-Magnesium alloys

The Aluminum-Magnesium binary system is an eutectic system with the eutectic located at 38.2 at.% Mg at 723 K (450 °C), as illustrated in the phase diagram in Figure 2.1. Mg has limited solubility in Al at room temperature (< 1 at.%) with highest solubility of 18.9 at.% at the eutectic temperature [2.1]. However, non-equilibrium processing of Al-Mg alloys can produce a supersaturated  $\alpha$ -Al solid solution. Clark *et al.* [2.2] were able to extend the solubility of Mg in Al up to 14.1 at.% by mechanical alloying at ambient temperatures; while Calka *et al.* [2.3] reported extended solubility limits of Mg in Al up to 18% and 45% in Al70Mg30 and Al50Mg systems, respectively, after mechanical attrition at ambient temperature. The most recognized phases in the binary Al-Mg system are  $\alpha$ -Al,  $\beta$ -Al<sub>3</sub>Mg<sub>2</sub> (40.3 at.% Mg),  $\gamma$ -Al<sub>12</sub>Mg<sub>17</sub> (44.54 – 50.58 at.% Mg),  $\epsilon$  (42 at.% Mg), and  $\delta$ -Mg [2.1].

In Al-rich compositions, studies in binary Al-Mg alloys showed the precipitation sequence of the  $\beta$  phase to be [2.4-2.6]:



With higher Mg content (> 3 wt.%) there is an increased susceptibility to grain boundary precipitation of the intermetallic  $\beta$ -Al<sub>3</sub>Mg<sub>2</sub> phase and subsequent intergranular corrosion. The intergranular  $\beta$  phase corrodes preferentially compared to the Al matrix in many environments, leading to intergranular corrosion and stress corrosion cracking [2.7]. A recent study showed that the degree of  $\beta$  phase

precipitation is dependent on the grain boundary misorientation angle, adjacent grain boundary planes and the grain boundary types with the misorientation angle being the most important factor [2.8].

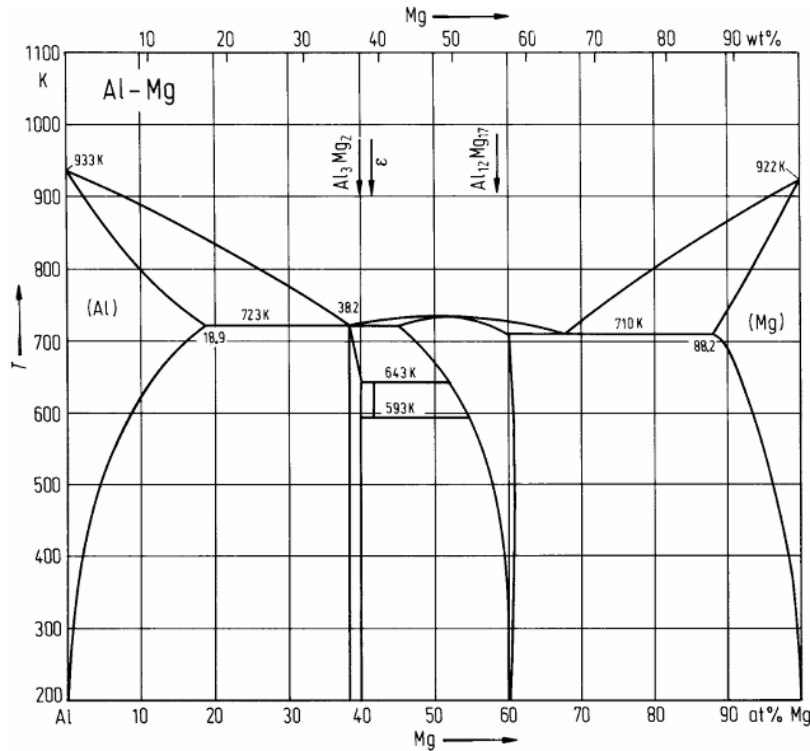


Figure 2.1 Aluminum-Magnesium binary phase diagram. Taken from ref. [2.1].

Aluminum alloys with Mg as the main alloying element ( $Mg < 6 \text{ wt.}\%$ ) are classified as the 5xxx series alloys. Due to the strength, good formability, weldability, corrosion resistance, and anodizing ability the 5xxx series alloys have been used in many outdoor applications [2.9]. They offer the best combination of strength and corrosion resistance of all the Al-alloys. Wrought 5xxx series alloys are mid strength Al alloys, typically lower than the 2xxx (Al-Cu-Mg), 6xxx (Al-Si-Mg), and 7xxx (Al-Zn-Mg-Cu) precipitation hardenable alloys. As non-heat treatable alloys, strengthening of the 5xxx series is mainly obtained from solid solution strengthening by the Mg solutes, dispersion strengthening and/or strain hardening [2.9]. Second phase forming elements, such as Mn and Cr, are added to Al-Mg in order to improve the resistance to recovery and recrystallization processes. Some of the phases found in cast 5xxx alloys may include:  $Mg_2Si$ ,  $Al_3Mg_2$ ,  $Al_{18}Mg_3Cr_2$ ,  $Al_{12}(Fe,Cr)_3Si$ , and  $AlMn$  [2.9]. These precipitates and dispersoids pin the grain boundaries and inhibit recrystallization processes [2.9].

### 2.1.2. Aluminum-Magnesium-Erbium alloys

Over the past few decades research on microalloying of aluminum alloys with rare earth metals (i.e.: Nd, Er, Sc, etc.) has been increasingly studied [2.10-2.15]. These rare earth (RE) additions modify the microstructure and improve the mechanical properties of the alloys. Of the possibilities, additions of Er and Sc have been most widely studied [2.11, 2.16-2.21], with Sc being the most effective addition by weight. A review of literature on Sc in Al alloys was conducted by Royset and Ryum [2.11]. Extensive research has established that decomposition of the Al–Sc solid solution leads to a dispersion of homogeneously nucleated precipitates of  $L_{12}$  structure, which can produce significant age hardening [2.11]. The  $Al_3Sc$  dispersoids and precipitates can also stabilize the grain structure of the alloys and prevent recrystallization after deformation by pinning grain and subgrain boundaries [2.11]. However, the widespread use of Sc is limited by its high price due to the significant cost increase in industrial applications.

To reduce costs, microalloying with Sc in combination with other  $L_{12}$  forming elements has been studied [2.22 – 2.24]. In the work by Knipling *et al.* [2.25], the  $Al_3M$  trialuminide cubic  $L_{12}$  forming elements in Al are given as Lanthanides (Ln) Sc, Er, Tm, Yb, Lu and transition metals (TMs) Ti, Zr, Hf. Complex alloying of Al-Sc with TMs or REs produce  $Al_3(Sc,RE,TM)$  type phases. Shorter incubation time, higher volume fraction and enhanced coarsening resistance are observed with the  $Al_3(Sc,RE,TM)$  type precipitates when compared to simple  $Al_3Sc$  phase precipitation [2.22-2.24]. These  $Al_3(Sc,RE,TM)$  type phases are core-shell/multi-shell precipitates, examples of which are given in Figure 2.2. The precipitates are typically layered according to the diffusivity of each element in Al, with the slowest diffusing element in the outermost shell. Segregation near the  $Al_3Sc$  phases has also been observed in ternary Al-Mg-Sc alloys. Mg segregates to the Al/ $Al_3Sc$  interface and Mg atoms have also been detected in the precipitate cores [2.26].

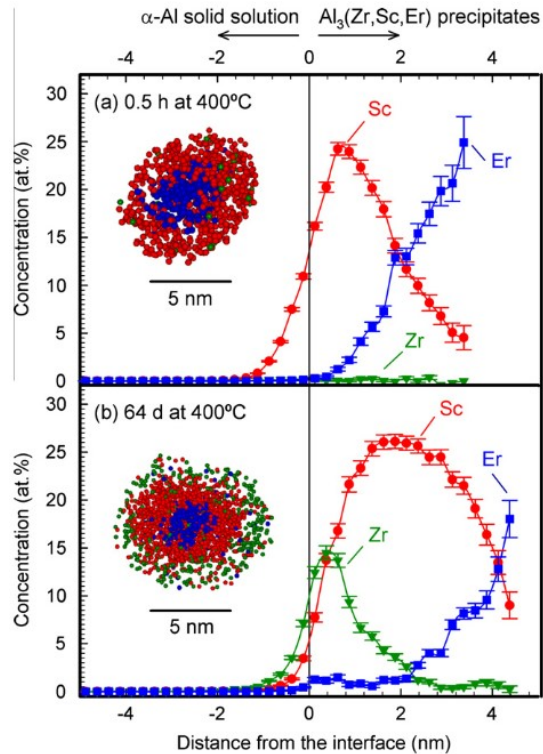


**Figure 2.2** Concentration profiles across the matrix/precipitate interface for Al-0.06 Zr-0.04 Sc-0.02 Er alloys aged at 400 °C for (a) 0.5 h and (b) 64 days; inset images are APT reconstructions of the corresponding precipitate. Images are from ref. [2.24].

By comparison, Er is a promising microalloying addition to Al alloys as it is much cheaper than Sc (i.e.: about 50% of the cost per kg). Like the results in Al-Sc-TM/RE alloys, complex alloying in Al-Er systems also produce core-shell precipitates, with layering according to the diffusivity of each element in Al. The  $L_{12}$  structured Al-Er-Zr precipitates obtained after annealing an Al-Er-Zr alloy at 400 °C exhibited an Er-rich core and Zr-rich outer shell as shown in Figure 2.3 [2.27]. Saccone *et al.* [2.28] and Cacciamani *et al.* [2.29] have carried out detailed experimental and thermodynamic investigations of the ternary Al-Mg-Er system. A variety of compounds were determined in the alloys annealed up to 35 days including -  $(Al,Mg)Er$ ,  $(Al,Mg)_2Er$ ,  $\gamma-(Al,Mg)$ ,  $(Al,Mg)_2Er_3$ ,  $(Al,Mg)Er_2$ ,  $(Al,Mg)_3Er$ ,  $\beta-(Al,Mg)$ ,  $(Al,Mg)_{24}Er_5$ , Er, Mg and Al phases [2.28]. The following phases were determined for a ternary Al-rich Al-Mg-Er alloy, with composition of 78.9 at.% Al, 12.6 at.% Mg and 8.5 at.% Er, annealed for 20 days –  $(Al_{1-x}Mg_x)_3Er$  of  $L_{12}$  structure, FCC Al solid solution and a ternary compound  $\tau$  of  $Al_{66.7}Er_{10}Mg_{23.3}$  stoichiometry with the hexagonal hP12-MgZn<sub>2</sub> structure [2.28].

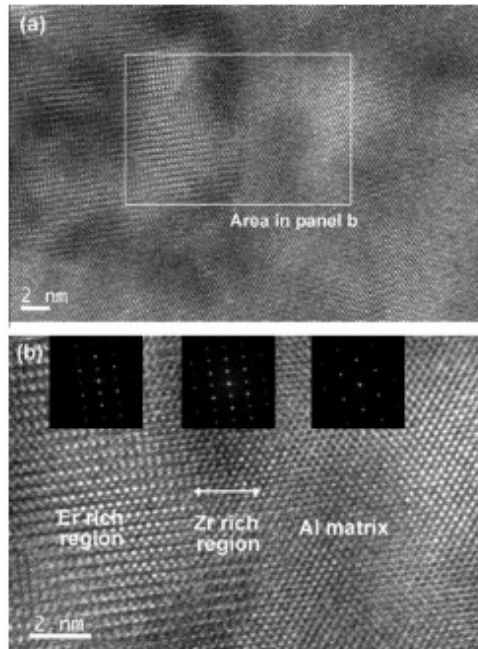


Figure 2.3 (a,b) HRTEM micrographs of precipitates in Al-0.06 Zr-0.03 Er after 768 h at 400 °C with diffractograms of the regions indicated shown in (b). Images are taken from ref. [2.27].

Nie and colleagues [2.16-2.21] have carried out intensive research on the influence of Er on the microstructure and mechanical properties of various aluminum alloys. The effect of microalloying of Er with 5xxx series alloy was extensively investigated [2.21]. Nie *et al.* found that an Er addition of 0.4% gave the best balance of tensile strength and ductility (438 MPa and 9.6%). Precipitation of the  $Al_3Er$  phase delayed recrystallization, leading to an onset temperature about 50 °C higher than that of the Er free Al-5Mg alloy [2.21].

## 2.2. Grain boundaries and grain growth

A grain boundary is an interface which separates crystals possessing the same composition and crystal structure but having different orientations in space [2.30]. The lattices of any two grains can be matched by rotating one of the grains through an appropriate angle about one axis [2.30]. There are two types of simple boundaries – tilt and twist boundaries. A tilt boundary forms when the axis of rotation is parallel to the

grain boundary plane, while a twist boundary is formed when the axis of rotation is perpendicular to the grain boundary plane [2.30].

When the misorientation between the grains is small the boundary can be considered as an array of dislocations. Burger [2.31] as well as Read and Shockley [2.32,2.33] proposed dislocation models of crystal grain boundaries. At low angles of misorientation, the grain boundary energy is dependent on the degree of misorientation and increases as predicted by the dislocation model [2.32,2.33]. For simple dislocation arrays

$$\frac{b}{d} = 2 \sin\left(\frac{\theta}{2}\right) \approx \theta \quad (2.2)$$

where:  $d$  is the spacing between dislocations,  $b$  is the Burger's vector of the dislocations, and  $\theta$  is the angle of boundary misorientation [2.30,2.32]. When  $\theta$  exceeds  $15^\circ$ , smaller spacing between the dislocations leads to overlapping of dislocation cores and the grain boundary energy becomes almost independent of misorientation [2.34]. At  $\theta > 15^\circ$  the boundary is known as a random high-angle grain boundary (HAGB) and is associated with relatively high energy. The energy of a HAGB can be approximated as  $\gamma_{gb} \cong \frac{1}{3} \gamma_{sv}$  [2.34]. For Al the surface energy is  $\gamma_{sv} = 1.08 \text{ J} \cdot \text{m}^{-2}$  and the grain boundary energy is  $\gamma_{gb} = 0.324 \text{ J} \cdot \text{m}^{-2}$  [2.35].

Special grain boundaries can occur at particular misorientations and boundary planes when two crystal lattices can be fit together with relatively little distortion [2.30]. Special HAGBs have significantly lower energies than random boundaries. Relative grain boundary energies in Al from the work of [2.36] are shown in Figure 2.4. For [100] tilt boundaries the boundary energy ceases to change with increasing misorientation between [001] directions when  $\theta > 15^\circ$  (Figure 2.4(a)), while several minima in boundary energy are observed at special grain boundaries at specific misorientations between [001] directions for [110] tilt boundaries (Figure 2.4(b)). The simplest special HAGB is between two twins, which occurs on the {111} plane at a misorientation of  $70.5^\circ$  about a  $\langle 110 \rangle$  axis for FCC metals [2.34].

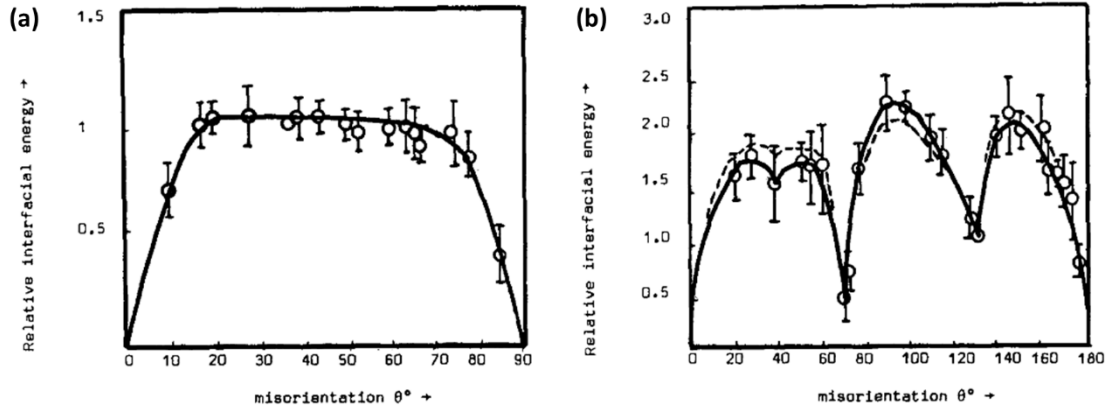


Figure 2.4 Changes in grain boundary energy with misorientation between [001] directions for (a) [100] tilt boundaries and (b) [110] tilt boundaries in Al. Taken from ref. [2.36].

Grain boundary migration at higher temperatures increases the mean grain size and reduces the total grain boundary energy. This is known as grain growth or grain coarsening and occurs in metals at temperatures above  $\sim 0.5 T_m$  [2.30]. The grain boundary velocity  $V$  during grain growth is proportional to the driving force  $P$  and the grain boundary mobility  $m_b$  [2.30]

$$V = m_b P \quad (2.3)$$

Grain growth kinetics can be described by assuming that the grain diameter  $D$ , proportional to the radius of curvature  $R$  ( $R = \alpha D$ ), changes proportionally to the average growth rate ( $V = \beta \frac{dD}{dt}$ ) [2.30]. Taking the driving force for grain growth as

$$P = \frac{2\gamma}{R} = \frac{2\gamma}{\alpha D} \quad (2.4)$$

equation 2.3 can be written as

$$\beta \frac{dD}{dt} = m_b \frac{2\gamma}{\alpha D} \quad (2.5)$$

which after integration becomes

$$D^2 - D_0^2 = \left[ \frac{2m_b\gamma}{\alpha\beta} \right] t = K_1 t \quad (2.6)$$

where:  $D_0$  is the initial grain size at time  $t = 0$  [2.30]. Experimentally, it is observed that grain growth is better approximated as

$$D = K_2 t^n \quad (2.7)$$

where  $n$  is typically less than 0.5 [2.30]. It has been suggested that changes in the boundary mobility, arising from solute drag effects, contribute to these changes observed in  $n$  [2.37].

### 2.3. Nanocrystalline materials

Nanomaterials are defined as materials with dimensions in the nanometer range, i.e.: below 100 nm. According to Gleiter [2.38] nanomaterials can be divided into three categories:

- (1) materials and/or devices with reduced dimensions such as nanoparticles, thin wires or thin films
- (2) Materials and/or devices with nanometer-sized microstructure limited to thin surface regions of a bulk material
- (3) Solids of bulk dimensions (micron to meter length scales) with nanometer-sized microstructure referred to as nanocrystalline or nanostructured (NS) materials. There are two subgroups: solids where the atomic structure and/or chemical composition varies throughout the material on the atomic scale, i.e.: glasses, gels or supersaturated solid solutions; and bulk materials made of nanometer sized building units, such as grains.

Production of nanomaterials can be classified under two general approaches: bottom-up and top-down methods. Bottom-up methods involve the assembly of atoms or molecules into nanoscale clusters and include methods such as inert gas condensation and electrodeposition [2.39]. The top-down approach involves deformation of micron to meter sized material to create nanometer-scale grains within the material; this includes severe plastic deformation (SPD) methods [2.40]. The recent review by Langdon [2.41] provides a good overview on SPD processing of metals, while the review by Sabirov *et al.* [2.42] on bulk NS Al alloys by SPD is also a good source for a more in-depth information on this topic.

Alterations in size, atomic structure and composition can produce major changes in the optical, mechanical, chemical, electrical, thermal, and diffusive properties of NS materials [2.39,2.40]. Changes in atomic structure result from the increased density of lattice defects (i.e.: incoherent interfaces, vacancies, etc.). Chemical composition changes can occur due to the altered behavior of equilibrium-immiscible solutes in nanocrystalline systems [2.43]. A solid-sphere representation of the nanocrystalline structure developed by Gleiter [2.40] is presented in Figure 2.5, where the unfilled circles represent the grain boundary atoms and the filled circles are the matrix atoms in the material. Gleiter [2.40] proposed that as the grain size decreases below 10 nm there is a significant increase in the volume fraction of the grain boundary, also known as the interphase volume, to over 50% in the material. As such, the atomic structure, chemical composition, thickness, etc. of the boundary regions are important to the properties of NS materials.

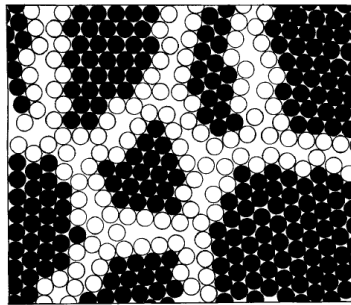


**Figure 2.5 Structure of nanocrystalline material: unfilled circles are atoms in the GB regions. Taken from ref. [2.40].**

Various researchers have reported that the structure of grain boundaries at the nanoscale differ from that of conventional polycrystalline materials. Reports on the structure of the grain boundaries in nanocrystalline materials have varied. It has been proposed that the interface regions (i.e.: grain boundaries) exhibit an atomic arrangement without short- or long-range order, possessing a “frozen-gas” like structure [2.44]. The grain boundary structure has also been likened to an isotropic, disordered, cement-like phase which may be characterized by its average width, reduced density and increased energy density [2.45]. It is proposed that the grain boundaries also possess relatively uniform thickness and energy [2.45]. Experimental results and molecular dynamics simulations suggest that for metal NS materials the low-

temperature atomic structures of the grain boundaries differ from those in coarse polycrystals mainly by the rigid body translations due to changing constraint conditions from neighboring grains [2.39]. In ultrafine grained (UFG) materials produced by SPD, a variety of grain boundaries have been observed depending on the method of SPD processing, including high- and low-angle, special and random, equilibrium and “non-equilibrium” grain boundaries [2.46,2.47]. “Non-equilibrium” grain boundaries are grain boundaries with excess energies and long-range stresses due to the presence of excess grain boundary dislocations [2.46]. possess a high-level of elastic stresses, dislocations, facets and steps [2.48]. These “non-equilibrium” grain boundaries have been shown to have a significant effect on transport properties of UFG materials [2.47,2.48].

The reduction in grain size affects material properties such as ductility, strength, and hardness. At fine grain sizes the small grains cannot support dislocation storage and dislocations are absorbed at the grain boundaries. This leads to a low rate of strain hardening and low strain rate, and limited elongations before failure [2.49]. Some strategies used to overcome this ductility issue in fine-grained materials include short temperature anneals after SPD [2.50], use of bimodal microstructures [2.51,2.52], nanoscale growth twins [2.53], and dispersion of nanoparticles or nanoscale precipitates [2.53] to name a few. The well-known Hall-Petch relation

$$\sigma_y = \sigma_0 + k_y D^{-1/2} \quad (2.8)$$

illustrates that the yield stress  $\sigma_y$  is a function of the lattice friction stress  $\sigma_0$ , a constant of yielding  $k_y$  and the grain size  $D$ . The Hall-Petch relation predicts an increase in yield strength and hardness with decreasing grain size of the material. However, a breakdown of the Hall-Petch relation has been observed below a threshold grain size in nanocrystalline materials.

Nieh and Wadsworth [2.54] have proposed that nanocrystalline materials exhibit an inverse Hall-Petch relation depending on the grain size with respect to  $L_c$ , the critical distance for a dislocation pile-up.  $L_c$  is illustrated in the schematic of Figure 2.6 and defined below in equation 2.9

$$L_c = \frac{3Gb}{\pi(1-\nu)H} \quad (2.9)$$

where: G is the shear modulus,  $\nu$  is the Poisson's ratio and H is the hardness of the material. Therefore, the threshold grain size for the Hall-Petch breakdown could be material dependent. When the grain size d is smaller than  $L_c$  dislocation pile-up will not occur and the Hall-Petch relation will break down [2.54]. Others have suggested that strength may fall below Hall-Petch predictions for crystallite sizes below  $\sim 20$  nm due to grain boundary sliding [2.55], modulus softening by high volume fraction of grain boundaries [2.56], increasing contribution of triple junctions to ductility [2.57], or a transition to glass-like plasticity [2.58].

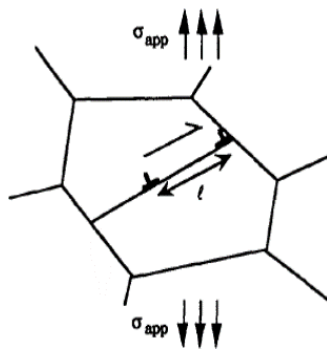


Figure 2.6 Schematic for critical distance for a dislocation pile up  $L_c$  taken from ref. [2.54].

## 2.4. Grain growth in nanocrystalline systems

Due to the large volume of grain boundary areas, there is a large driving force for grain growth in NS materials. However, literature shows that grain size stability in nanocrystalline metal systems is dependent on the route of production, largely due to the presence of impurities/solute in the systems. Grain size stability in nanocrystalline systems can be analyzed via kinetic or thermodynamic approaches. In the kinetic approach, various mechanisms can inhibit grain boundary mobility including porosity drag [2.59], solute drag [2.60], second phase drag [2.61], and triple and quadruple junction drag [2.62 – 2.64]. With the thermodynamic approach, the driving force for grain growth is reduced by lowering the grain boundary energy due to solute segregation to the grain boundary regions [2.65-2.67]. Recent reviews on the thermal stability in

nanocrystalline systems have been done by Koch *et al.* [2.68,2.69], Kalidindi *et al.* [2.70], and Andrievski [2.71].

Second phase particles will exert a Zener pinning force  $P_{Zener}$  on a moving boundary restricting its motion [2.72]. For a volume fraction  $f$  of particles with radius  $r$  the restraining force (per unit area of boundary) opposing the driving force for grain growth can be approximated as

$$P_{Zener} = \frac{3f\gamma}{2r} \quad (2.10)$$

When the driving force becomes insufficient to overcome the drag forces exerted by the particles, the grain growth will stagnate resulting in a maximum grain size defined by [2.72]:

$$D_{max} = \frac{4r}{3f} \quad (2.11)$$

Second phase drag was observed in a study on the thermal stability of cryomilled Fe-10 wt.% Al conducted by Perez *et al.* [2.73]. They found that a grain size of 20 nm was maintained after annealing up to 500 °C, and grain growth to 50 nm after annealing at 1100 °C. The grain size stability was attributed to the presence of nanoscale Al<sub>2</sub>O<sub>3</sub> and AlN dispersoids introduced during the milling process. Solute and second phase drag was also observed in an Al<sub>93</sub>Fe<sub>3</sub>Cr<sub>2</sub>Ti<sub>2</sub> alloy prepared by mechanical alloying [2.74]. The as-milled alloy was an Al solid solution. After annealing at various temperatures, a variety of intermetallic compounds with Cr, Fe, or Ti precipitated, followed by grain growth. No grain growth was observed at temperatures up to ~ 300 °C with the grain size distribution from TEM analysis reported as 6 – 45 nm. The authors attributed the inhibition of grain growth to solute drag on the grain boundaries at the lower annealing temperatures and pinning of the boundaries by the nanoscale intermetallic precipitates at higher temperatures.

Binary systems which may exhibit thermodynamic stability by solute segregation to grain boundaries were recently examined by Murdoch and Schuh [2.75] and Darling *et al.* [2.76]. Murdoch and Schuh [2.75] used a Miedema-type model for the estimation of grain boundary segregation enthalpies for ~2500 alloys to make predictions about

nanocrystalline stability. Both elastic and chemical contributions are taken into consideration for the calculation of the segregation enthalpies. In the model of Darling *et al.* [2.76] grain boundary energy was derived and studied for over 1000 binary systems (52 solutes and 44 solvents) including Ni, Cu, Al, and Fe based systems. For their predictions, a thermodynamically stable nanocrystalline system is obtained only when solute segregation results in reduction of the grain boundary energy to zero, not just a reduction in grain boundary energy as observed in the Ni-W system [2.67]. Predicted conditions for nanocrystalline thermal stability from the model were in good agreement with previously reported experimental results for the Fe-Zr system [2.76]. Darling *et al.* state that other factors such as second phase precipitation, solubility limit and grain boundary embrittlement must also be taken into consideration for nanocrystalline alloy design [2.76]. However, a recent study in the nanocrystalline Cu-Zr system [2.77] shows that Dillon-Harmer grain boundary complexions can also play a role in thermal stability of nanocrystalline systems and should also be taken into consideration.

General observations for the stabilized systems as determined by Darling *et al.*'s [2.76] model are as follows:

- (1) The solutes which have positive enthalpy of mixing in the systems tend to be better candidates for nanocrystalline structure stability. However, many of the predicted stabilizers have been previously suggested as grain boundary embrittling agents.
- (2) A positive enthalpy of mixing is not an essential requirement for stability
- (3) In some systems, most solutes have a negative enthalpy of mixing and so the thermodynamic stability of the nanocrystalline structure is limited

A nanocrystalline Al stability map from ref. [2.76] is shown in Figure 2.7. Stabilizing solutes (red dots), and other solutes requiring more than 10 at.% addition (black dots) are shown in the figure. The size of the stabilizing solutes (red dots) corresponds to the magnitude of the minimum solute concentration required to stabilize a grain size of 25 nm. The figure shows that the best candidates have an enthalpy of mixing range  $\Delta H_{mix} = -25 \text{ to } 25 \text{ kJ} \cdot \text{mol}^{-1}$  and an elastic enthalpy range of  $\Delta H_{seg}^{elastic} = -25 \text{ to } -$

$100 \text{ kJ} \cdot \text{mol}^{-1}$ . Stabilizing solutes for binary Al systems are listed in the table in Figure 2.7.

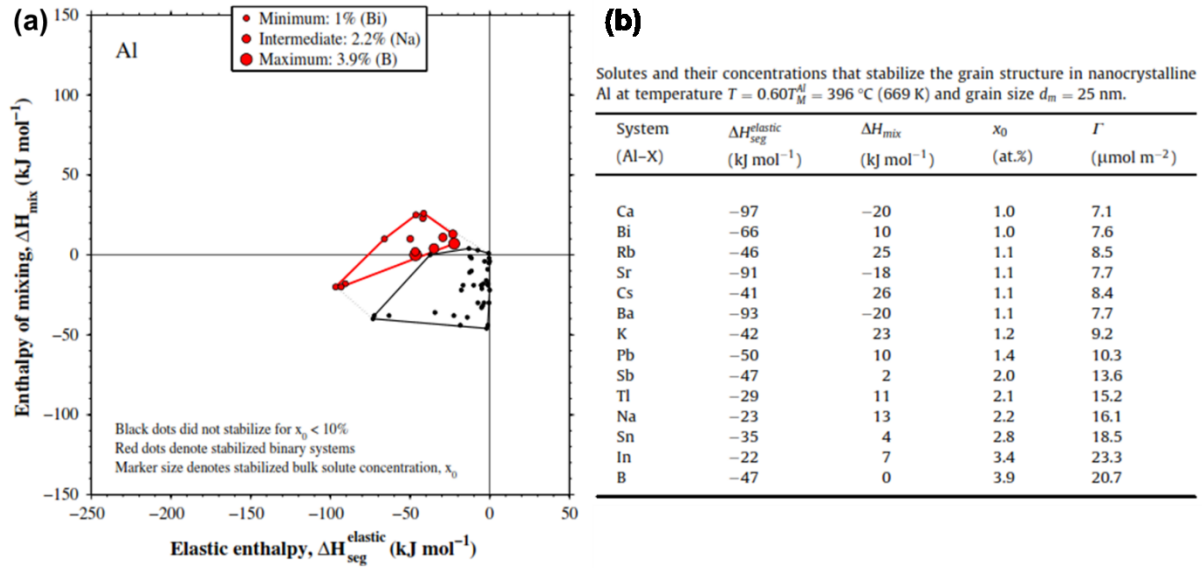


Figure 2.7 (a) Nanocrystalline Al stability map plotting elastic enthalpy versus the enthalpy of mixing for stabilizing solutes (red dots) and other solutes (black dots) in the system; (b) Table of stabilizing solutes (red dots). Taken from ref. [2.76].

## 2.5. Bulk nanocrystalline materials by PM

Bulk nanocrystalline materials are typically fabricated by two-step methods involving the production of NS powders which are then consolidated into a bulk material. In this thesis, the NS powders are produced by the cryomilling process followed by consolidation utilizing the SPS process. In this section a brief introduction to cryomilling and SPS processes are given.

### 2.5.1. Cryomilling

Mechanical attrition, i.e. mechanical milling, is a method of grain refinement by cyclic severe plastic deformation usually carried out at ambient temperatures. Mechanical milling can create various non-equilibrium conditions in the processed metal powders including supersaturated solid solution phase [2.2, 2.3], nanocrystallinity [2.78],

intermetallic phases [2.79], and amorphization [2.80]. Cryomilling is a variation of mechanical milling which is carried out under cryogenic conditions, often in a liquid nitrogen medium. A schematic of the milling process is shown in Figure 2.8, where powders and milling media (steel balls) are placed in a stainless-steel vial.

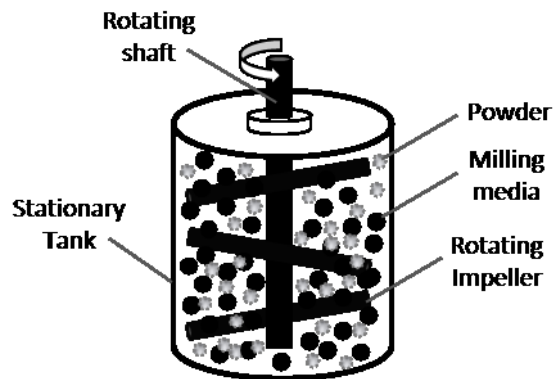


Figure 2.8 Schematic of a cryomill set-up.

Repeated fracturing and welding of the particles during milling leads to a final steady-state particle size and a refined nanocrystalline structure in the powders. The most widely accepted mechanism of nanostructure formation during ball milling was defined by Fetch [2.78] as a three stage process:

- (1) the deformation is localized in shear bands which consist of an array of high dislocation density;
- (2) at a particular strain level, the dislocations annihilate and recombine to form sub-grains or cells in the nanometer range with low angle grain boundaries;
- (3) grain rotation leads to randomly oriented grains with high angle grain boundaries.

This process is illustrated in Figure 2.9. At steady state deformation there is a balance between dislocation creation and recovery in the system, therefore the minimum grain size ( $d_{\min}$ ) obtainable by milling is determined by the competition between deformation during milling and recovery behaviour of the material [2.81]. As shown with Eq. 2.9, there is a critical equilibrium distance between two edge dislocations,  $L_c$ , dependent on the material parameters. Eckert [2.82] has shown that for metals synthesized by mechanical attrition, there is a linear relationship between the minimum grain size,  $d_{\min}$ , and  $L_c$ . The equilibrium distance between two dislocations in Al is calculated as  $\sim 10.5$

nm [2.82]. However, the minimum grain size reported for milled Al alloys in literature is typically  $\sim 25 \text{ nm} \approx 2L_c$  [2.83-2.85].

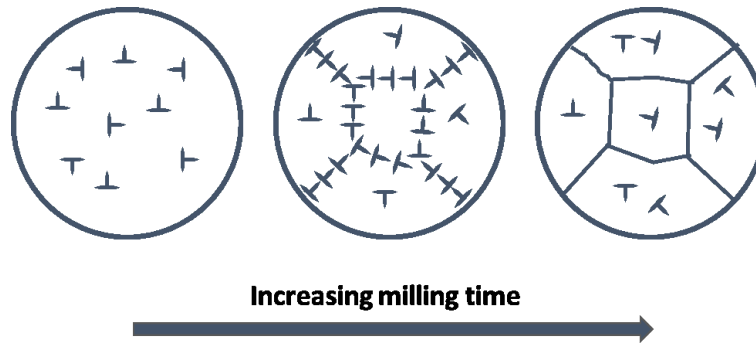


Figure 2.9 Formation of nanostructure during mechanical milling process, reproduced from ref. [2.78].

The use of nitrogen helps to limit oxidation of the new surfaces generated during milling as well as prevent recrystallization during milling [2.86]. Cryomilling also incorporates nitrogen and oxygen into the powders resulting in the formation of nanoscale nitrides ( $\text{AlN}$ ), oxides and oxynitrides which can increase the thermal stability of the powders by Zener pinning [2.87,2.88]. Luton *et al.* [2.87,2.88] identified the nature of dispersoids introduced into Al powders during the cryomilling process and reported that aluminum oxy-nitride particles of 2 – 10 nm in size [2.87], and platelets of aluminum-nitrogen and aluminum-oxygen content, a few atomic layers thick and 10 – 15 nm in two-dimensions [2.88], were formed in cryomilled oxide dispersion strengthened (ODS) Al powders. The reader is directed to the comprehensive review of the mechanical alloying and milling process by Suryanarayana [2.86] for more details on the cryomilling process.

### 2.5.2. Spark Plasma Sintering

Sintering is the bonding of powder particles at high temperatures through solid-state or liquid-phase processes. Solid-state sintering occurs via solid-state atomic transport events, while liquid-phase sintering involves the formation of a liquid phase which bonds the particles together upon cooling [2.89]. Particle bonding occurs by neck growth at particle contacts and sintering is driven by elimination of the surface energy associated with small particles and occurs by atomic motion [2.89]. Sintering transport mechanisms, as shown in Figure 2.10, can be categorized as surface and bulk transport

mechanisms, and are differentiated by the origin of the transported atoms [2.89]. Surface transport relocates atoms from the surface of the particles to the neck region but contributes minimally to densification of the powder compact (mechanisms 1 & 2 in Figure 2.10) [2.89]. Bulk transport moves atoms from the grain boundary and bulk regions to the neck region (mechanisms 3 & 4 in Figure 2.10). Bulk transport plays a significant role in densification [2.89]. Surface transport dominates at lower temperatures, while bulk transport dominates at higher temperatures [2.89].

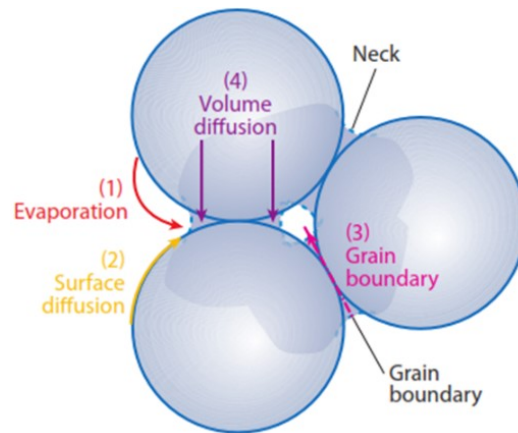


**Figure 2.10 Mass transport mechanisms that contribute to sintering and neck growth, taken from ref. [2.90].**

SPS is a sintering technique where the consolidation of powders occurs under the simultaneous application of current and pressure. Current-activated pressure-assisted consolidation methods are known by monikers such as SPS, field-assisted sintering technique (FAST), and pulsed-electric current sintering (PECS) among others. SPS has been used for the consolidation of various materials such as metal matrix composites [2.91], nanocrystalline ceramic powders [2.92], and various nanocrystalline Al and Al alloy powders [2.93-2.98]. The use of current facilitates rapid sintering at lower temperatures than conventional processes such as HP [2.90]. Reviews on current and pressure assisted sintering processes over the years include the work of Garay [2.90], Omori [2.99], Tokita [2.100], and Munir *et al.* [2.101].

A schematic of the SPS set-up is shown in Figure 2.11. The powders are placed in a die (typically graphite) and heating is achieved by passing a current (typically pulsed DC) through the die and powder bed while pressure is applied. Heating of the

powder compact is generated internally due to resistive heating between the die parts; heating is also generated inside the powder bed for conductive materials. Densification during SPS has been attributed to plastic yielding, viscous flow, creep and diffusion mechanisms [2.102]. Olevsky and Froyen [2.103] offered a list of densification mechanisms which can be classified under thermal and non-thermal effects. Thermal effects include non-uniform local and macroscopic temperature distributions which can produce conditions for thermal diffusion, local melting at inter-particle contacts and thermal stresses leading to dislocation creep [2.103]. Non-thermal effects can include electroplasticity, electromagnetic effects and dielectric breakdown of oxide films [2.103].

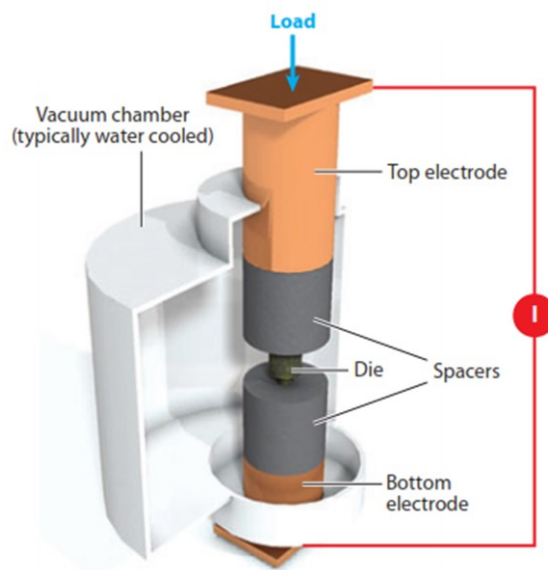


Figure 2.11 Schematic of an SPS apparatus, taken from ref. [2.90].

The internal heating provided by the current application allows fast heating rates to be used,  $\sim 100 - 600$  °C/min [2.90]. Fast heating rates help densification by bypassing temperature ranges where non-densifying diffusive mechanisms (i.e.: surface transport) are active in order to promote particle sintering instead of coarsening [2.104]. In addition to heating, the current is also proposed to create plasma in the powder bed during sintering. Depending on the temperature, spark discharges in micro-gaps between powder particles are proposed to melt and sputter material and form necks between particles [2.105]. The plasma is also proposed to have surface cleaning effects leading to sintering enhancement [2.99, 2.106-2.108]. Although the presence of plasma during SPS has been doubted by some due to the lack of clear experimental evidence

[2.109,2.110], its presence has been advocated for by many researchers [2.99, 2.107,2.108]. In the recent work by Zhang *et al.* [2.105], sub-micron necks between powder particles of Ti and Cu were cited as proof of the occurrence of spark discharges in micro-gaps between powder particles during SPS sintering. Current effects during SPS are also proposed to produce electromigration. Electromigration is mass transport in metals which are stressed under high current densities [2.111]. Typically, current densities of  $j > 10^3$  are required for significant effects of electromigration to be observed. However, using a series of tests with graphite foils Frei *et al.* [2.112] showed that current effects during SPS do have significant effect upon neck growth on Cu spheres as well as enhancing other surface effects, suggesting that electromigration-style effects may be operative at the current densities utilized during SPS.

## **2.6. Bulk nanocrystalline cryomilled Al-Mg alloys**

In this section, a brief review of bulk NS Al-Mg materials produced from cryomilled powders is presented. Firstly, a brief introduction on (alumina) oxide dispersion strengthened (ODS) Al alloys produced by mechanical alloying is presented. The remainder of the section is then dedicated to bulk NS Al-Mg materials produced by cryomilling.

### **2.6.1. ODS Al alloys by mechanical alloying (MA)**

ODS alloys are produced by PM techniques typically consisting of powder production, followed by cold compaction and sintering. The bulk is then subjected to some form of hot working procedure to obtain a dense alloy with suitable mechanical properties [2.113]. The mechanical milling/alloying process is used to incorporate oxide and carbide dispersoids into the powders. The mechanical alloying technique was initially invented and developed in the 1960s by Benjamin and his co-workers at the International Nickel Company (INCO) to produce ODS nickel-based superalloys. Adaptation of the process to the development of ODS Al alloys began later in the decade. Benjamin has provided an overview of the process in [2.114].

$\text{Al}_2\text{O}_3$  is the main oxide addition to Al-based ODS Al alloys. Incorporation of the alumina oxides into an Al-based matrix can occur via in situ and ex situ routes [2.115]. Ex-situ oxide addition involves incorporation of alumina particles into the powders by the milling process. In-situ processes involve reactive milling where the alumina dispersoids are created during milling due to reactions within the powders, i.e.: reduction reactions between metal oxides – such as CuO [2.116] and ZnO [2.117] – and aluminum. Milling processes such as cryomilling can also lead to oxide dispersion strengthening by nanoscale alumina and aluminum oxynitride particles when the milling is performed in a liquid nitrogen medium [2.87, 2.88]. A variety of Al-based ODS alloys with  $\text{Al}_2\text{O}_3$  have been investigated including Al-Cu [2.116], Al-Cu-Mn-Mg [2.118], Al-Mg [2.119,2.120], and Al-Si-Mg [2.121] alloys. The  $\text{Al}_2\text{O}_3$  content investigated has varied from 5 – 50 vol.% [2.118, 2.121, 2.122]. Commercially produced ODS Al based alloys include IncoMAP Al-9052 (Al-Mg), Al-905XL (Al-Mg-Li), and AL-9021 (Al-Cu-Mg) alloys with tensile yield strength ranging from 380 – 469 MPa and elongation between 9 – 13% [2.113].

The volume fraction, particle size and distribution of the  $\text{Al}_2\text{O}_3$  phases affects the compaction, densification, and mechanical properties of the ODS Al- $\text{Al}_2\text{O}_3$  alloys. As the oxide particle size decreases or the oxide volume fraction increases, green and sintered density generally decrease [2.123,2.124] while mechanical properties such as hardness and tensile strength increase [2.125-2.127]. In the study by Razavi-Tousi *et al.* [2.123], reducing the  $\text{Al}_2\text{O}_3$  particle size from sub-micron to nanoscale dimensions reduced the powder particle size after milling and influenced the final density of cold compacted powders. The increase of nanoscale  $\text{Al}_2\text{O}_3$  content from 1 to 7 vol.% resulted in decreased cold compaction density from 89% to 79% under 1 GPa [2.123]. At higher volume fractions, agglomeration of the oxide particles can hinder densification and also reduce their strengthening effects. In the work of Tabandeh *et al.* [2.127] a mixture of nanoscale (35 nm) and submicron (0.3  $\mu\text{m}$ )  $\text{Al}_2\text{O}_3$  particles, total of 10 wt.%, were milled with Al powders (45  $\mu\text{m}$ ) in various ratios - 2:8, 3:7, 4:6, 5:5, 6:4. Increase of the nanoscale oxide content produced an increase in strength up to 4 wt.% addition, after which a decrease in strength was observed. Decrease in strength was attributed to

agglomeration of the oxide nanoparticles and subsequent formation of a continuous brittle phase along the grain boundaries [2.127].

Grain growth in Al-Al<sub>2</sub>O<sub>3</sub> ODS alloys during consolidation is hindered by the presence of the nanoscale Al<sub>2</sub>O<sub>3</sub>, as well as other compounds and impurity elements that may be present in the alloy [2.120,2.123,2.128]. Increasing volume fraction of the oxide content improves grain size control in the UFG and nanoscale regime in ODS Al alloys. Addition of 0.4 wt.% Al<sub>2</sub>O<sub>3</sub> to an Al-5Mg alloy reduced the grain size in the fine-grained regions from 700 nm to 300 nm after spark plasma sintering at 550 °C [2.120]. While the addition of 12 wt.% alumina in AA 6061 minimized nanoscale grain growth during consolidation; grain size grew from 38 nm in the milled powder to 77 nm after conventional sintering [2.128].

### **2.6.2. Cryomilled Al-Mg powders**

Cryomilling is a variation of mechanical milling which is carried out under cryogenic conditions, often in a liquid nitrogen medium. Cryomilling studies have been carried out on a variety of Al-Mg compositions, including binary Al-Mg systems [2.84], ternary systems such as Al-Mg-Sc [2.85], and commercial Al 5083 alloys [2.129]. In literature, milling is often carried out in Szegvari attritor mills with an average duration of 8 hours, typically after which a heterogeneous microstructure is observed. Similar results are often obtained in the cryomilled Al-Mg powders. The average nanocrystalline grain sizes after 8 hours of milling are presented in Table 2.1. The grain sizes reported are between 22-26 nm, approximately twice the equilibrium distance  $L_c$  between two dislocations in a pile-up, as defined in the previous section.

The mechanisms of deformation and nanocrystalline grain formation in Al and Al alloy powders during cryomilling have been studied extensively [2.83-2.85]. The formation of the nanocrystalline high angle grain boundaries in Al and Al-Mg alloys was attributed to a grain subdivision mechanism occurring during the milling process, similar to heavily cold-rolled materials [2.83,2.85]. Two types of representative nanostructures are typically observed: a random dispersion of equiaxed grains with an average diameter ~ 25 nm and, less frequently, a lamellar structure 100 to 200 nm long with an

average width similar to the average grain size [2.84,2.85]. In some instances small crystallites with a dimension of less than 10 nm are also observed [2.84].

Representative images of the microstructure obtained are shown in Figure 2.12 from the results of Liao *et al.* in cryomilled Al-7.6 at.% Mg [2.84]. A microstrain of  $0.16 \pm 0.03$  was reported for Al, while  $0.20 \pm 0.03$  and  $0.23 \pm 0.03$  were reported for an Al-7.5Mg and Al-7.5Mg-0.3Sc powders, respectively [2.83,2.85]. Similar as-milled conditions have been reported for Al powders milled at ambient temperatures [2.130]; an average grain size of 25 nm and microstrain of  $\sim 0.16$  are obtained after 100 hours of milling [2.130].

**Table 2.1 Cryomilled Al and Al-Mg alloys**

Sample	Milling time (h)	D (nm)	$\langle e^2 \rangle^{1/2}$	T (K)	Mill	Ref
<b>Al</b>	> 100	~ 25	~ 0.16	298	Szegvari	[2.130]
<b>Al</b>	8	$26 \pm 2$	$0.16 \pm 0.03$	90	Szegvari	[2.83]
<b>Al-7.5Mg</b>	8	$22 \pm 2$	$0.20 \pm 0.03$	90	Szegvari	[2.85]
<b>Al-7.5Mg-0.3Sc</b>	8	$26 \pm 2$	$0.23 \pm 0.03$	90	Szegvari	[2.85]

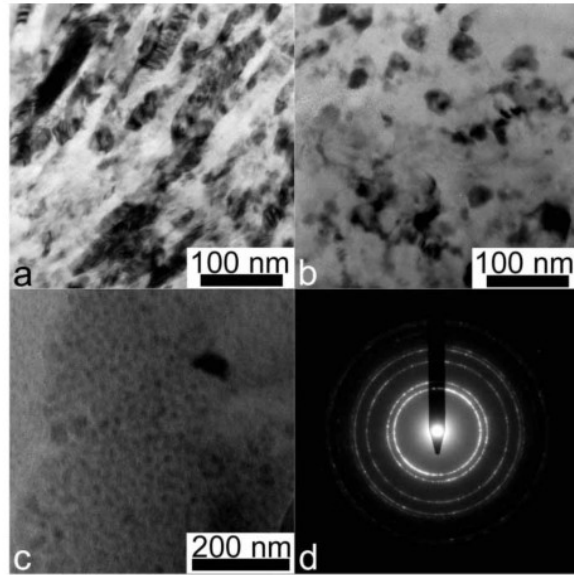


Figure 2.12 As milled microstructure in Al-7.6 at.% Mg powders taken from ref. [2.84].

### 2.6.3. Grain growth in cryomilled Al-Mg alloys

Cryomilled Al-Mg powders possess a thermally meta-stable microstructure which is subject to grain growth at elevated temperatures. Thermal stability of these microstructures has been attributed to the presence of impurities/solutes and dispersoids which help inhibit grain boundary mobility [2.131, 2.132]. Due to pinning forces during grain growth, the grain growth exponent  $n$  deviates from 0.5 [2.131, 2.132]. The grain growth can not be predicted by the traditional kinetic equations, in which case the Burke's model for grain growth [2.133] is used to deduce the activation energy,  $Q$ :

$$\frac{D_0 - D}{D_{max}} + \ln \left( \frac{D_{max} - D_0}{D_{max} - D} \right) = \frac{kt}{D_{max}^2} \quad (2.12)$$

Differentiating equation 2.12 leads to the basic growth rate equation expressed as

$$\frac{dD}{dt} = k \left( \frac{1}{D} - \frac{1}{D_{max}} \right) \quad (2.13)$$

showing that the rate of grain growth is controlled by the difference between the limiting grain size  $D_{max}$  and the instantaneous average grain size  $D$ .

Typically for milled Al and Al-Mg systems there are two defined grain growth regimes: low-temperature region and high-temperature region, each with corresponding activation energy  $Q$ . In milled Al-7.6Mg powders the activation energies determined from DSC measurements were  $\sim 120 \text{ kJ}\cdot\text{mol}^{-1}$  for recovery and  $\sim 190 \text{ kJ}\cdot\text{mol}^{-1}$  for recrystallization events [2.134]. Whereas in cryomilled Al 5083 (powder & bulk samples) lower temperature  $Q$  was associated with the reordering of grain boundaries and ranged from  $5 - 25 \text{ kJ}\cdot\text{mol}^{-1}$ , while higher temperature  $Q$  values were reported as ranging from  $124 - 142 \text{ kJ}\cdot\text{mol}^{-1}$  [2.129, 2.132].

#### **2.6.4. Microstructure of bulk cryomilled nanostructured Al-Mg**

The final microstructure of the material depends not only on the milling parameters, but also on the methods used to consolidate the powders. Several pressure-assisted processes such as HIP, CIP, SPS, and extrusion have been used to consolidate the nanostructured powders. The consolidation of the milled powder usually requires high temperatures for extended periods of time, leading to grain growth. The average grain size in the consolidated bulk is typically reported in the UFG range after thermo-mechanical processing. An average grain size of  $100 - 300 \text{ nm}$  was reported for milled Al-7.6Mg [2.135], while an average grain size of  $305 \text{ nm}$  was reported for milled Al 5083 [2.132] when consolidated by HIP and extrusion methods. An average grain size of  $192 \text{ nm}$  was reported for milled Al 5083 consolidated at  $400 \text{ }^\circ\text{C}$  under  $100 \text{ MPa}$  by SPS process [2.136], although an average grain size of  $51 \text{ nm}$  has also been reported for milled Al 5083 consolidated by SPS [2.96].

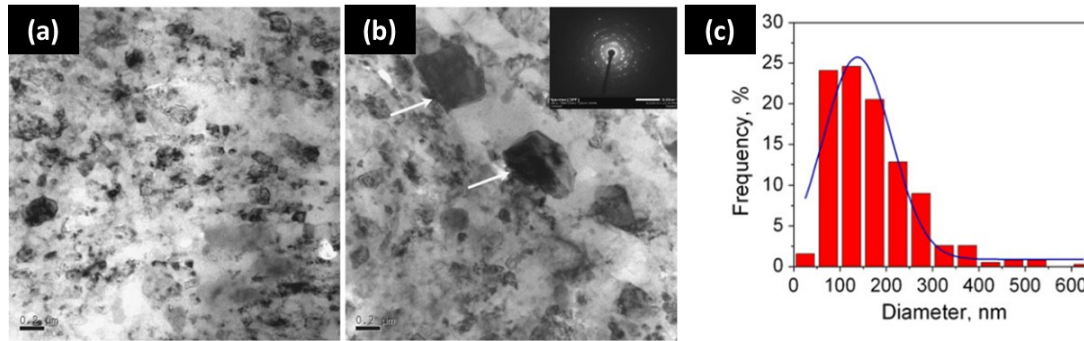


**Figure 2.13** Grain growth in SPS consolidated Al 5083: (a) UFG structure after SPS consolidation at 400 °C for 3 mins under 100 MPa; (b) Bands of coarser UFGs; (c) grain size distribution in SPS material. Images taken from ref. [2.136].

A bimodal microstructure is typically obtained after consolidation of cryomilled Al alloy powders with a small fraction of micron-sized grains located within a nanocrystalline/UFG grain matrix. In the case of HIP consolidation, the micron-sized grains formed at the triple-point areas between the nano-grained prior powder particle areas and are attributed to diffusional processes [2.137]. Non-uniform current density, temperature and pressure distributions in the powder bed during SPS can result in localized conditions at particle-particle contacts that can promote abnormal grain growth by enhanced atomic diffusion, local melting or grain rotation and coalescence under high pressure ( $\geq 300$  MPa) [2.136,2.138]. For milled Al 5083 powders, consolidation at a high pressure (i.e.: 500 MPa) in SPS results in grain coarsening via a combination of thermally activated grain boundary (GB) migration, stress-coupled GB migration and grain rotation-induced grain coalescence [2.138]. However, for sintering processes carried out at 100 MPa, grain growth was generally attributed to thermally activated grain boundary migration [2.138]. An example of the microstructure obtained after SPS consolidation of a milled Al 5083 alloy is shown in Figure 2.13 taken from the results of Y Xiong *et al.* [2.136] on SPS consolidation of cryomilled Al 5083. The figure shows nanocrystalline and UFG microstructures obtained after sintering (Figure 2.13(a)), bands of coarse UFGs (Figure 2.13(b)) [2.136] and the grain size distribution determined for the compact (Figure 2.13(c)). Residual dislocations are also often observed in the sintered microstructure in the form of dislocation networks, walls, and tangles in the coarser UFGs (see Figure 2.14). Similar microstructure was also observed in cryomilled Al 5083 consolidated by HIP and extrusion [2.132].

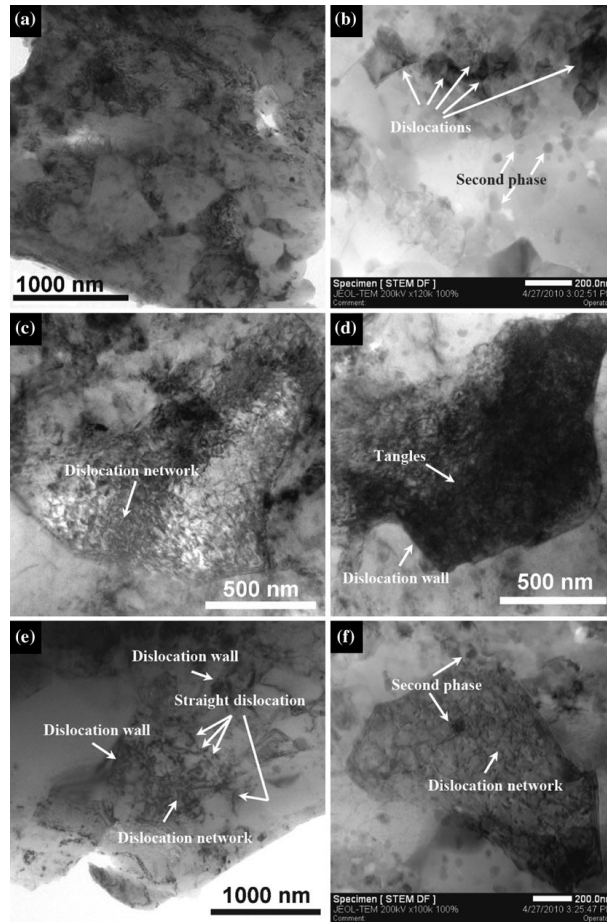


Figure 2.14 Typical dislocation structures observed after SPS consolidation of cryomilled nanocrystalline Al 5083 powders. Taken from ref. [2.136].

### 2.6.5. Mechanical properties of bulk cryomilled Al-Mg

Increased strength and hardness but reduced ductility is obtained with bulk cryomilled Al-Mg alloys compared to conventional Al 5083 as observed in Table 2.2. Conventional polycrystalline Al 5083 has a yield strength of 145 MPa and 19% elongation [2.139]. A bulk NS Al-7.5Mg material, produced by cryomilling with consolidation by HIP and extrusion, has a yield strength of 641 MPa with elongation of only 1.4% [2.135]. While bulk NS Al 5083 has similar yield strength and elongation of 690 MPa and 1.5%, respectively [2.140]. An SPS consolidated milled Al 5083 has a minimum yield strength of 560 MPa when sintered at 400 °C under 100 MPa [2.141].

Ductility enhancement in bulk cryomilled Al-7.5Mg alloy has been realized by a bimodal microstructure design achieved by mixing atomized and cryomilled powders. The effects of additions of atomized powders at 15% and 30% is shown in Figure 2.15(a) taken from [2.135]. The results show a correlation between elongation and the proportion of un-milled powder. As the proportion of un-milled powder is increased to 15% and 30%, the yield strength decreases from 641 MPa to 630 MPa and 554 MPa, respectively, but the elongation increases from 1.4% to 2.4% and 5.4 %, respectively [2.135]. Toughness enhancement with bimodal microstructures was explained by Han *et al.* with a model of crack bridging and delamination as shown in Figure 2.15(b) [2.52]. Under tensile deformation, microcracks will nucleate in the nanostructured regions and propagate along the grain boundaries. Submicron grains will retard crack propagation by blunting the crack and/or by delamination of interfaces between the submicron and nanocrystalline grained areas. The tensile ductility is enhanced by the delamination of interfaces and necking deformation in ductile submicron grained regions.

**Table 2.2 Properties of bulk Al-Mg and bulk NS Al-Mg by cryomilling**

<b>Alloy</b>	<b>Condition</b>	<b>Ultimate Tensile Strength (MPa)</b>	<b>Yield Strength<sup>a</sup> (MPa)</b>	<b>Elongation to failure (%)</b>	<b>Grain size (nm)</b>
<b>Polycrystalline Al 5083 [2.139]</b>	-	285	145	19	55·10 <sup>3</sup>
<b>Al-7.5Mg [2.135]</b>	Cryomilling + HIP & extrusion	847	641	1.4	100 – 300
<b>Nano Al 5083 [2.140]</b>	Cryomiling + CIP & extrusion	740	690	1.5	30
<b>Nano Al 5083 [2.136, 2.141]</b>	Cryomilling + SPS	-	~ 560	~32 <sup>b</sup>	192

<sup>a</sup>0.2% offset; <sup>b</sup>Compressive testing

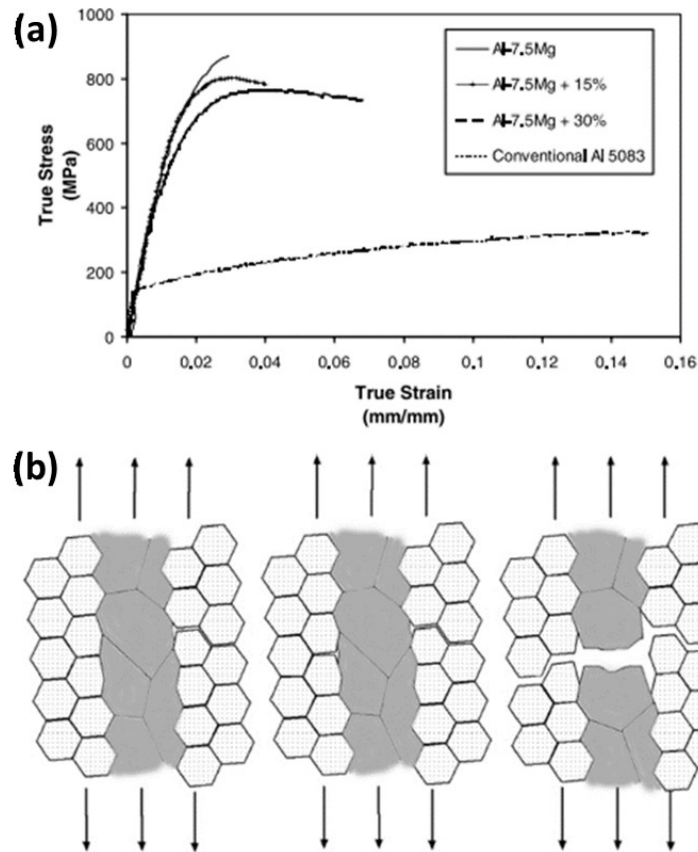


Figure 2.15 (a) Increasing ductility with tailored bimodal microstructure in bulk cryomilled Al 5083, taken from ref. [2.135]; (b) Propagation of a microcrack in a nanostructured material with a bimodal lamellar structure, taken from ref. [2.52].

## 2.7. References

- 2.1. Predel B (1991) Al-Mg (Aluminum-Magnesium). In: 'Phase equilibria, crystallographic and thermodynamic data of binary alloys', Landolt-Börnstein - Group IV Physical Chemistry, Volume 5a:1-9
- 2.2. Clark CR, Suryanarayana C, Froes FH (1995) Solid solubility extension in binary aluminum and magnesium alloys by mechanical alloying. International Conference & Exhibition on Powder Metallurgy & Particulate Materials. Seattle: WA.

- 2.3. Calka A, Kaczmarek W, Williams JS (1993) Extended solid solubility in ball-milled Al-Mg alloys, *Journal of Materials Science* 28:15-18.
- 2.4. Starink MJ, Zahra AM (1997) Low-temperature decomposition of Al-Mg alloys: Guinier-Preston zones and L<sub>12</sub> ordered precipitates, *Philosophical Magazine A* 76:701-714.
- 2.5. Starink MJ, Zahra AM (1998)  $\beta'$  and  $\beta$  precipitation in an Al-Mg alloy studied by DSC and TEM, *Acta Materialia* 46:3381-3397.
- 2.6. Yassar RS, Field DP, Weiland H (2005) The effect of predeformation on the  $\beta''$  and  $\beta'$  precipitates and the role of Q' phase in an Al-Mg-Si alloy: AA6022. *Scripta Materialia* 53:299-303.
- 2.7. Jones RH, Baer DR, Danielson MJ, Vetrano JS (2001) Role of Mg in the stress corrosion cracking of an Al-Mg alloy, *Metallurgical and Materials Transactions A* 32:1699-1711.
- 2.8. Yan J, Heckman NM, Velasco L, Hodge AM (2016) Improve sensitization and corrosion resistance of an Al-Mg alloy by optimization of grain boundaries, *Scientific Reports* 6:26870 1-10.
- 2.9. Hatch JE (Ed.), *Aluminum: Properties and Physical Metallurgy*, ASM, Metals Park, OH, 1984
- 2.10. Zhang J, Zhao JJ, Zuo RL (2015) Microstructure and mechanical properties of micro-alloying modified Al-Mg alloys, *International Conference on Power Electronics and Energy Engineering* 2015:153-156.
- 2.11. Royset J, Ryum N, Scandium in aluminum alloys, *International Materials Reviews* 50 (2005) 19-44.
- 2.12. Li HZ, Wang HJ, Liang XP *et al.* (2012) Effect of Sc and Nd on the microstructure and mechanical properties of Al-Mg-Mn Alloy, *Journal of Materials Engineering and Performance* 21:83-88.

- 2.13. Liu ZX, Li ZJ, Wang MX, Weng YG (2008) Effect of complex alloying of Sc, Zr and Ti on the microstructure and mechanical properties of Al-5Mg alloys, *Materials Science and Engineering A* 483-484:120-122.
- 2.14. Chen Q, Pan QL, Wang Y *et al.* (2012) Microstructure and mechanical properties of Al-5.8Mg-Mn-Sc-Zr alloy after annealing treatment, *Journal of Central South University of Technology* 19:1785–1790.
- 2.15. Rosalbino F, Angelini E, De Negri S *et al.* (2003) Influence of the rare earth content on the electrochemical behaviour of Al–Mg–Er alloys, *Intermetallics* 11:435–44.
- 2.16. Nie ZR, Fu JB, Zou JX *et al.* (2004) Advanced aluminum alloys containing rare-earth erbium, *Materials Forum* 28:197-201.
- 2.17. Nie Z, Jin T, Fu J *et al.* (2002) Research on rare earth in aluminum, *Materials Science Forum* 396-402:1731-1736.
- 2.18. Xu G, Mou S, Yang J *et al.* (2006) Effect of trace rare earth element Er on Al-Zn-Mg alloy, *Transactions of Nonferrous Metals Society of China* 16:598-603.
- 2.19. Wen SP, Xing ZB, Huang H *et al.* (2009) The effect of erbium on the microstructure and mechanical properties of Al–Mg–Mn–Zr alloy, *Materials Science and Engineering A* 516:42-49.
- 2.20. Lin S, Nie Z, Huang H, Li B (2010) Annealing behaviour of a modified 5083 aluminum alloy, *Materials Design* 31:1607-1612.
- 2.21. Nie ZR, Li BL, Wang W *et al.* (2007) Study on the Erbium strengthened aluminum alloy, *Materials Science Forum* 546:623-628.
- 2.22. Karnesky RA, Dunand DC, Seidman DN (2009) Evolution of nanoscale precipitates in Al microalloyed with Sc and Er, *Acta Materialia* 57:4022-4031.
- 2.23. Krug ME, Werber A, Dunand DC, Seidman DN (2010) Core–shell nanoscale precipitates in Al–0.06 at.% Sc microalloyed with Tb, Ho, Tm or Lu, *Acta Materialia* 58:134-145.

- 2.24. Booth-Morrison C, Dunand DC, Seidman DN (2011) Coarsening resistance at 400 °C of precipitation-strengthened Al–Zr–Sc–Er alloys, *Acta Materialia* 59:7029-7042.
- 2.25. Knipling KE, Dunand DC, Seidman DN (2006) Criteria for developing castable, creep-resistant aluminium-based alloys – A review, *Z Metallkd.* 97:246–265.
- 2.26. Marquis EA, Seidman DN (2004) Nanostructural evolution of Al<sub>3</sub>Sc precipitates in an Al–Sc–Mg alloy by three-dimensional atom probe microscopy, *Surface and Interface Analysis* 36:559–563.
- 2.27. Li H, Bin J, Liu J *et al.* (2012) Precipitation evolution and coarsening resistance at 400 °C of Al microalloyed with Zr and Er, *Scripta Materialia* 67:73-76.
- 2.28. Saccone A, Cacciamani G, De Negri S, Ferro R (2002) The Al-Er-Mg ternary system part I: experimental investigation, *Journal of Phase Equilibria* 23:29-37.
- 2.29. Cacciamani G, Saccone A, De Negri S, Ferro R (2002) The Al-Er-Mg ternary system part II: thermodynamic modeling, *Journal of Phase Equilibria* 23:37-50
- 2.30. Gottstein G, Shvindlerman LS (2010) Grain boundary migration in metals, CRC Press, Boca Raton.
- 2.31. Burger JM (1940) Geometrical considerations concerning the structural irregularities to be assumed in a crystal, *Proceedings of the Physical Society* 52:23-33
- 2.32. Shockley W, Read WT (1949) Quantitative predictions from dislocation models of crystal grain boundaries, *Physical Review* 75:692.
- 2.33. Read WT, Shockley W (1950) Dislocation models of crystal grain boundaries, *Physical Review* 78:275-289.
- 2.34. Porter DA, Easterling KE, Sherif MY (2009) *Phase Transformations in Metals and Alloys*, CRC Press, Boca Raton.
- 2.35. Murr LE (1975) *Interfacial phenomena in metals and alloys*, Addison-Wesley, London.

- 2.36. Hasson G, Goux C (1971) Interfacial energies of tilt boundaries in aluminum: experimental and theoretical determination, *Scripta Metallurgica* 5:889-894.
- 2.37. Hu H, Rath BB (1970) On the time exponent in isothermal grain growth, *Metallurgical Transactions* 1:3181-3184.
- 2.38. Gleiter H (1995) Nanostructured materials: state of the art and perspectives, *Nanostructured Materials* 6:3-14.
- 2.39. Gleiter H (2000) Nanostructured Materials: basic concepts and microstructure, *Acta Materialia* 48:1-29.
- 2.40. Gleiter H (1989) Nanocrystalline materials. *Progress in Materials Science* 33:223-315.
- 2.41. Langdon TG (2013) Twenty-five years of ultrafine-grained materials: Achieving exceptional properties through grain refinement, *Acta Materialia* 61:7035–7059.
- 2.42. Sabirov I, Murashkin MYu, Valiev RZ (2013) Nanostructured aluminium alloys produced by severe plastic deformation: New horizons in development, *Materials Science and Engineering A* 560:1-24.
- 2.43. Herr U, Jing J, Gonser U, Gleiter H (1990) Alloy effects in consolidated binary mixtures of nanometer-sized crystals, *Solid State Communications* 76:197-202.
- 2.44. Zhu X, Birringer R, Herr U, Gleiter H (1987) X-ray diffraction studies of the structure of nanometer-sized crystalline materials, *Physical Review B* 35:9085-9090.
- 2.45. Phillpot SR, Wolf D, Gleiter H (1995) A structural model for grain boundaries in nanocrystalline materials, *Scripta Metallurgica et Materialia* 33:1245–1251.
- 2.46. Valiev RZ, Islamgaliev RK, Alexandrov IV (2000) Bulk nanostructured materials from severe plastic deformation, *Progress in Materials Science* 45:103-189.
- 2.47. Valiev RZ, Murashkin MYu, Semenova IP (2010) Grain boundaries and mechanical properties of ultrafine-grained metals, *Metallurgical and Materials Transactions A* 41:816-822.

- 2.48. Kolobov YuR, Grabovetskaya GP, Ivanov MB, Zhilyaev AP, Valiev RZ (2001) Grain boundary diffusion characteristics of nanostructured nickel, *Scripta Materialia* 44:873-878
- 2.49. Wang YM, Ma E (2004) Strain hardening, strain rate sensitivity, and ductility of nanostructured metals, *Materials Science and Engineering A* 375–377:46–52
- 2.50. Kumar P, Kawasaki M, Langdon TG (2016) Overcoming the paradox of strength and ductility in ultrafine-grained materials at low temperatures, *Journal of Materials Science* 51:7-18.
- 2.51. Witkin D, Le Z, Rodriguez R, Nutt S, Lavernia E (2003) Al–Mg alloy engineered with bimodal grain size for high strength and increased ductility, *Scripta Materialia* 49:297-302.
- 2.52. Han BQ, Lee Z, Witkin D, Nutt SR, Lavernia EJ (2005) Deformation behaviour of biomodal nanostructured 5083 Al alloys, *Metallurgical and Materials Transactions A* 36:957-965.
- 2.53. Ma E (2006) Eight routes to improve the tensile ductility of bulk nanostructured metals and alloys, *The Journal of the Minerals, Metals & Materials Society* 58:49-53
- 2.54. Nieh TG, Wadsworth J (1991) Hall-Petch relation in nanocrystalline solids, *Scripta Metallurgica et Materialia* 25:955-958.
- 2.55. Wang N, Wang Z, Aust K, Erb U (1997) Room temperature creep behaviour of nanocrystalline nickel produced by an electrodeposition technique, *Materials Science and Engineering A* 237:150-158.
- 2.56. Weertman JR (1993) Hall-Petch strengthening in nanocrystalline metals, *Materials Science and Engineering A* 166:161-167.
- 2.57. Palumbo G, Erb U, Aust KT (1990) Triple line disclination effects on the mechanical behaviour of materials, *Scripta Metallurgica et Materialia*. 24:2347-2350.
- 2.58. Trelewicz JR, Schuh CA (2007) The Hall–Petch breakdown in nanocrystalline metals: a crossover to glass-like deformation, *Acta Materialia* 55:5948–5958.

- 2.59. Hofler HJ, Averbach RS (1990) Grain growth in nanocrystalline TiO<sub>2</sub> and its relation to Vickers hardness and fracture toughness, *Scripta Metallurgica et Materialia* 24:2401-2406.
- 2.60. Mehta SC, Smith DA, Erb U (1995) Study of grain growth in electrodeposited nanocrystalline nickel-1.2 wt.% phosphorus alloy, *Materials Science and Engineering A* 204:227-232.
- 2.61. Michels A, Krill CE, Ehrhardt H, Birringer R, Wu DT (1999) Modelling the influence of grain-size-dependent solute drag on the kinetics of grain growth in nanocrystalline materials, *Acta Materialia*. 47:2143-2152.
- 2.62. Gottstein G, Shvindlerman LS (2005) A novel concept to determine the mobility of grain boundary quadruple junctions, *Scripta Materialia* 52:863–866.
- 2.63. Novikov VYu (2008) Impact of grain boundary junctions on grain growth in polycrystals with different grain sizes, *Materials Letters* 62:2067–2069.
- 2.64. Zhao B, Gottstein G, Shvindlerman LS (2011) Triple junction effects in solids, *Acta Materialia* 59:3510–3518.
- 2.65. Kirchheim R (2002) Grain coarsening inhibited by solute segregation, *Acta Materialia* 50:413-419.
- 2.66. Liu F, Kirchheim R (2004) Nano-scale grain growth inhibited by reducing grain boundary energy through solute segregation, *Journal of Crystal Growth* 264:385-391.
- 2.67. Detor AJ, Schuh CA (2007) Grain boundary segregation, chemical ordering and stability of nanocrystalline alloys: Atomistic computer simulations in the Ni–W system, *Acta Materialia* 55:4221–4232.
- 2.68. Koch CC, Scattergood RO, Darling KA, Semones JE (2008) Stabilization of nanocrystalline grain sizes by solute additions, *Journal of Materials Science* 43:7264–7272
- 2.69. Koch CC, Scattergood RO, Saber M, Kotan H (2013) High temperature stabilization of nanocrystalline grain size: Thermodynamic versus kinetic strategies, *Journal of Materials Research* 28:1785-1791.

- 2.70. Kalidindi AR, Chookajorn T, Schuh CA (2015) Nanocrystalline materials at equilibrium: A thermodynamic review, *Journal of the Minerals, Metals and Materials Society* 67:2834-2843.
- 2.71. Andrievski RA (2014) Review of thermal stability of nanomaterials, *Journal of Materials Science* 49:1449–1460.
- 2.72. C. S. Smith (1949) *Trans. AIME.* 9:5.
- 2.73. Perez RJ, Huang B, Lavernia EJ (1996) Thermal stability of nanocrystalline Fe-10 wt.% Al produced by cryogenic mechanical alloying, *Nanostructured Materials* 7:565-512.
- 2.74. Shaw L, Luo H, Villegas J, Miracle D (2003) Thermal stability of nanostructured  $Al_{93}Fe_3Cr_2Ti_2$  alloys prepared via mechanical alloying, *Acta Materialia* 51:2647-2663.
- 2.75. Murdoch HA, Schuh CA (2013) Estimation of grain boundary segregation enthalpy and its role in stable nanocrystalline alloy design. *Journal of Materials Research* 28: 2154-2163
- 2.76. Darling KA, Tschopp MA, VanLeeuwen BK *et al.* (2014) Mitigating grain growth in binary nanocrystalline alloys through solute selection based on thermodynamic stability maps, *Computational Materials Science* 84:255-266.
- 2.77. Khalajhedayati A, Rupert TJ (2015) High-temperature stability and grain boundary complexion formation in a nanocrystalline Cu-Zr alloy, *Journal of Materials* 67:2788-2801.
- 2.78. Fetch HJ (1995) Nanostructure formation by mechanical attrition. *Nanostructured Materials* 6:33-42.
- 2.79. Koch CC, Whittenberger JD (1996) Mechanical milling/alloying of intermetallics, *Intermetallics* 4:339-355.

- 2.80. Mukherjee D, Ande V, Manna R, Murty BS, Mukhopadhyay NK (2010) Formation of nanostructured and amorphous  $\beta$ -Al<sub>3</sub>Mg<sub>2</sub> based alloys by rapid solidification and mechanical milling, *Materials Science and Engineering A* 527:5078-5083.
- 2.81. Eckert J, Holzer JC, Krill CE III, Johnson WL (1992) Structural and thermodynamic properties of nanocrystalline fee metals prepared by mechanical attrition, *Journal of Materials Research* 7:1751-1761.
- 2.82. Eckert J (1995) Relationships governing the grain size of nanocrystalline metals and alloys, *Nanostructured Materials* 6:413-416.
- 2.83. Zhou F, Witkin D, Nutt SR, Lavernia EJ (2004) Formation of nanostructure in Al produced by a low-energy ball milling at cryogenic temperature. *Materials Science and Engineering A* 375-377:917-921.
- 2.84. Liao XZ, Huang JY, Zhu YT, Zhou F, Lavernia EJ (2003) Nanostructures and deformation mechanisms in a cryogenically ballmilled Al-Mg alloy, *Philosophical Magazine* 83:3065-3075
- 2.85. Zhou F, Nutt SR, Bampton CC, Lavernia EJ (2003) Nanostructure in an Al-Mg-Sc alloy processed by low-energy ball milling at cryogenic temperatures, *Metallurgical and Materials Transactions A* 34:1985-1992.
- 2.86. Suryanarayana C (2001) Mechanical alloying and milling, *Progress in Materials Science* 46:1-184.
- 2.87. Luton MJ, Jayanth CS, Disko MM, Matras S, Vallone J (1988) Cryomilling of Nano-Phase Dispersion Strengthened Aluminum. *MRS Proc* 132:79.
- 2.88. Susegg O, Hellum E, Olsen A, Luton MJ (1993) HREM study of dispersoids in cryomilled oxide dispersion strengthened materials, *Philosophical Magazine A*, 68:2, 367-380.
- 2.89. German RM (2005) Sintering Concepts, In: *Powder Metallurgy & Particulate Materials Processing*, MPIF, New Jersey, p.219-260.
- 2.90. Garay JE (2010) Current-activated, pressure-assisted densification of materials *Annual Review of Materials Research* 40:445–468

- 2.91. Saheb N, Iqbal Z, Khalil A *et al.* (2012) Spark plasma sintering of metals and metal matrix nanocomposites: A Review, *Journal of Nanomaterials* 2012:18-30.
- 2.92. Chaim R (2007) Densification mechanisms in spark plasma sintering of nanocrystalline ceramics, *Materials Science and Engineering A* 443:25–32.
- 2.93. Zuniga A, Ajdelsztajn L, Lavernia EJ (2006) Spark plasma sintering of a nanocrystalline Al-Cu-Mg-Fe-Ni-Sc alloy, *Metallurgical and Materials Transactions A* 37:1343-1352.
- 2.94. Rana JK, Sivaprahasam D, Raju KS, Sarma VS (2009) Microstructure and mechanical properties of nanocrystalline high strength Al–Mg–Si (AA6061) alloy by high energy ball milling and spark plasma sintering, *Materials Science and Engineering A* 527:292–296.
- 2.95. Chen H, Tao K, Yang B, Zhang J (2009) Nanostructured Al-Zn-Mg-Cu alloy synthesized by cryomilling and spark plasma sintering, *Transactions of the Nonferrous Metals Society of China* 19:1110-1115.
- 2.96. Ye J, Ajdelsztajn L, Schoenung JM (2006) Bulk nanocrystalline aluminum 5083 alloy fabricated by a novel technique: Cryomilling and Spark Plasma Sintering, *Metallurgical and Materials Transactions A* 37:2569-2579.
- 2.97. Sasaki TT, Mukai T, Hono K (2007) A high-strength bulk nanocrystalline Al–Fe alloy processed by mechanical alloying and spark plasma sintering, *Scripta Materialia* 57:189-192.
- 2.98. Kubota M (2007) Properties of nano-structured pure Al produced by mechanical grinding and spark plasma sintering, *Journal of Alloys and Compounds* 434–435:294–297
- 2.99. Omori M (2000) Sintering, consolidation, reaction and crystal growth by the spark plasma system (SPS), *Materials Science and Engineering A* 287:183-188.
- 2.100. Tokita M, Mechanism of Spark Plasma Sintering (SPS), Sumimoto Coal Mining Company, Ltd: Japan.
- 2.101. Munir ZA, Anselmi-Tamburini U, Ohyanagi M (2006) The effect of electric field and pressure on the synthesis and consolidation of materials: A review of the spark plasma sintering method, *Journal of Materials Science* 41:763–777.

- 2.102. Ye J, Ajdelsztajn L, Schoenung JM (2006) Bulk nanocrystalline aluminum 5083 alloy fabricated by a novel technique: Cryomilling and Spark Plasma Sintering, *Metallurgical and Materials Transactions A* 37:2569-2579.
- 2.103. Olevsky EA, Froyen L (2009) Impact of thermal diffusion on densification during SPS. *Journal of the American Ceramics Society* 92:S122–S132
- 2.104. Olevsky EA, Kandukuri S, Froyen L (2007) Consolidation enhancement in spark-plasma sintering: Impact of high heating rates, *Journal of Applied Physics* 102:114913 1-12.
- 2.105. Zhang ZH, Liu ZF, Lu JF, Shen XB *et al.* (2014) The sintering mechanism in spark plasma sintering – Proof of the occurrence of spark discharge, *Scripta Materialia* 81:56-59.
- 2.106. Xie G, Ohashi O, Yamaguchi N, Wang A (2003) Effect of surface oxide films on the properties of pulse electric-current sintered metal powders, *Metallurgical and Materials Transactions A* 34:2655-2661.
- 2.107. Groza JR, Garcia M, Schneider JA (2001) Surface effects in field assisted sintering, *Journal of Materials Research* 16:286-292.
- 2.108. Groza JR, Zavaliangos A (2000) Sintering activation by external electrical field, *Materials Science and Engineering A* 287:171-177.
- 2.109. Hulbert DM, Anders A, Andersson J *et al.* (2009) A discussion on the absence of plasma in spark plasma sintering. *Scripta Materialia* 60:835-838.
- 2.110. Hulbert DM, Anders A, Dudina DV *et al.* (2008) The absence of plasma in "spark plasma sintering". *Journal of Applied Physics* 104:033305-1 – 033305-7.
- 2.111. Black JR (1969) Electromigration - A brief survey and some recent results. *Electron Devices, IEEE Transactions* 16:338-347.
- 2.112. Frei JM, Anselmi-Tamburini U, Munir ZA (2007) Current Effects on Neck Growth in the Sintering of Copper Spheres to Copper Plates by the Pulsed Electric Current Method, *J. Appl. Phys.* 101:114914-1 – 114914-8.

- 2.113. Weber JH (1993) Dispersion-Strengthened Aluminum Alloy, In: Mechanical Properties of Metallic composites, CRC Press, p.269 -292.
- 2.114. Benjamin JS (1976) Mechanical Alloying, Scientific American 234:40-48.
- 2.115. Suryanarayana S, Al-Aqeeli N (2013) Mechanically alloyed nanocomposites, Progress in Materials Science 58:383-502.
- 2.116. Arami H, Simchi A (2007) Reactive milling synthesis of nanocrystalline Al-Cu Al<sub>2</sub>O<sub>3</sub> nanocomposite, Materials Science and Engineering A 464:225-232.
- 2.117. Tavoosi M, Karimzadeh F, Enayati MH (2008) Fabrication of Al-Zn:α-Al<sub>2</sub>O<sub>3</sub> nanocomposite by mechanical alloying, Materials Letters 62:282-285.
- 2.118. Ozdemir I, Ahnens S, Mucklich S, Wielage B (2008) Nanocrystalline Al-Al<sub>2</sub>O<sub>3</sub> and SiCp composites produced by high-energy ball milling, Journal of Materials Processing Technology 205:111-118
- 2.119. Wagih A (2014) Effect of milling time on morphology and microstructure of Al-Mg:Al<sub>2</sub>O<sub>3</sub> nanocomposite powder produced by mechanical alloying, International Journal of Advances in Engineering Sciences 4:1-7.
- 2.120. Babu NK, Kallip K, Leparoux M *et al.* (2016) Influence of microstructure and strengthening mechanism of AlMg5-Al<sub>2</sub>O<sub>3</sub> nanocomposites prepared via spark plasma sintering, Materials and Design 95:534-544
- 2.121. Asgharzadeh H, Simchi A, Kim HS (2010) In situ synthesis of nanocrystalline Al6063 matrix nanocomposite powder via reactive mechanical alloying, Materials Science and Engineering A 527:4897-4905.
- 2.122. Prabhu B, Suryanarayana C, An L, Vaidyanathan R (2006) Synthesis and characterization of high volume fraction Al-Al<sub>2</sub>O<sub>3</sub> nanocomposite powders by high-energy milling, Materials Science and Engineering A 425:192-200.
- 2.123. Razavi-Tousi SS, Yazdani-Rad R, Manafi SA (2011) Effect of volume fraction and particle size of alumina reinforcement on compaction and densification

- behaviour of Al-Al<sub>2</sub>O<sub>3</sub> nanocomposites, *Materials Science and Engineering A* 528:1105-1110.
- 2.124. Saheb N, Khan MS, Hakeem AS (2015) Effect of Processing on Mechanically Alloyed and Spark Plasma Sintered Al-Al<sub>2</sub>O<sub>3</sub> Nanocomposites, *Journal of Nanomaterials* 1-13
- 2.125. Kang YC, Chan SLI (2004) Tensile properties of nanometric Al<sub>2</sub>O<sub>3</sub> particulate-reinforced aluminum matrix composites, *Materials Chemistry and Physics* 85:438-443.
- 2.126. Prabhu B. Microstructural and mechanical characterization of Al–Al<sub>2</sub>O<sub>3</sub> nanocomposites synthesized by high-energy milling. M.S. Thesis, University of Central Florida, Orlando, FL, USA, 2005
- 2.127. Tabandeh Khorshid M, Jenabali Jahromi SA, Moshksar MM (2010) Mechanical properties of tri-modal Al matrix composites reinforced by nano- and submicron-sized Al<sub>2</sub>O<sub>3</sub> particulates developed by wet attrition milling and hot extrusion, *Materials and Design* 1-16.
- 2.128. Sivasankaran S, Sivaprasad K, Narayanasamy R, Satyanarayana PV (2011) X-ray peak broadening analysis of AA 6061 100-x –x wt% Al<sub>2</sub>O<sub>3</sub> nanocomposite prepared by mechanical alloying, *Materials Characterization* 62:661-672.
- 2.129. Tellkamp VL, Dallek S, Cheng D, Lavernia EJ (2001) Grain growth behaviour of a nanostructured 5083 Al-Mg alloy, *Journal of Materials Research* 16:938-944.
- 2.130. Oleszak D, Shingu PH (1996) Nanocrystalline metals prepared by low energy ball milling, *Journal of Applied Physics* 79:2975-2980.
- 2.131. Zhou F, Lee J, Lavernia EJ (2001) Grain growth kinetics of a mechanically milled nanocrystalline Al, *Scripta Materialia* 44:2013-2017.
- 2.132. Roy I, Chauhan M, Lavernia EJ, Mohamed FA (2006) Thermal Stability in Bulk Cryomilled Ultrafine-Grained 5083 Al Alloy, *Metallurgical and Materials Transactions A* 37:721-730.

- 2.133. Burke JE (1949) Some factors affecting the rate of grain growth in metals, Transactions of the Metallurgical Society. AIME 180:73–91.
- 2.134. Zhou F, Liao XZ, Zhu YT, Dallek S, Lavernia EJ (2003) Microstructural evolution during recovery and recrystallization of a nanocrystalline Al-Mg alloy prepared by cryogenic ball milling, Acta Materialia 51:2777-2791.
- 2.135. Witkin D, Le Z, Rodriguez R, Nutt S, Lavernia E (2003) Al–Mg alloy engineered with bimodal grain size for high strength and increased ductility, Scripta Materialia 49:297-302.
- 2.136. Xiong Y, Liu D, Li Y *et al.* (2012) Spark plasma sintering of cryomilled nanocrystalline Al alloy - Part I: Microstructure evolution, Metallurgical and Materials Transactions A 43:327-339.
- 2.137. Tang F, Hagiwara M, Schoenung JM (2005) Formation of coarse-grained interparticle regions during hot isostatic pressing of nanocrystalline powder, Scripta Materialia 53:619-624.
- 2.138. Liu D, Wen H, Zhang D *et al.* (2014) Stress-enhanced grain growth in a nanostructured aluminium alloy during spark plasma sintering, Philosophical Magazine Letters 94:741-748.
- 2.139. Youssef KM, Scattergood RO, Murty KL, Koch CC (2006) Nanocrystalline Al–Mg alloy with ultrahigh strength and good ductility, Scripta Materialia 54:251-256.
- 2.140. Han BQ, Mohamed FA, Lavernia EJ. (2004) Mater Res Soc Symp Proc 821:P9.1.1.
- 2.141. Liu D, Xiong Y, Topping TD *et al.* (2012) Spark plasma sintering of cryomilled nanocrystalline Al alloy - Part II: Influence of processing conditions on densification and properties, Metallurgical and Materials Transactions A 43:340-350.

## Chapter 3 Experimental Methodology

### 3.1. Powder production and characterization

#### 3.1.1. Atomized powders

In this study, Al-5Mg alloys were used. Commercial Al 5356 powder was selected as a reference, while custom Al-5Mg-Er powders were produced for the study. Commercial gas atomized Al 5356 powder (-325 mesh) has a general composition range given as: 4.5 – 5.5 % Mg; 0.4 % Fe; 0.25 % Si; 0.1 % Zn; 0.1 % Cu; 0.06 – 0.2 % Cr, Mn, Ti; in wt.%. Ternary compositions of Al-Mg-Er were cast for this research. Pure aluminum was heated to 700 °C in a SiC crucible and pure Mg and Er were added to achieve the desired compositions. The melt was then heated to 720 °C prior to casting into graphite molds of 2 cm diameter by 10 cm length. Sections of the cast rods were removed, from top and bottom areas, for testing to verify the composition. The composition of the cast rods was determined with the Inductively Coupled Plasma (ICP) technique using the Thermo Scientific iCAP 6500 Duo ICP-AES instrument. Standards containing Al, Mg and Er elements at 1 ppm, 10 ppm and 100 ppm concentrations were mixed and used for the analysis. Lines for the Er, Al and Mg were chosen to reduce chances of interference from other elemental signals. When the correct composition range was achieved, the cast rods were then sent for atomization by the rotative electrode method at Laval University. Approximately 250 – 300 g of cast material was sent for each composition.

The composition of the received atomized Al-Mg-Er powders was verified by ICP. In addition to the previous Al, Mg and Er standards, the Fisher Scientific Standard Routine Quality Control 1 (RQC 1) solution was used to determine the level of trace impurities in the powders. The composition of the atomized powders is presented in Table 3.1. The powder compositions were determined as Al-5.29Mg-0.12Er and Al-5.4Mg-0.55Er; hereafter these compositions will be referred to as 0.1 Er and 0.5 Er, respectively. In addition to the main alloying elements, dilute concentrations of Ti and Tl are measured in the 0.1 Er powder. The concentration of impurity elements is reduced in the 0.5 Er powder, possibly due to Er increase reducing the solid solubility of the other elements.

**Table 3.1 Composition of atomized Al-Mg-Er powders**

Element	Mg	Er	Ti	Fe	Ni	Tl	Si	Sb	Zn
0.1 Er	5.29	0.12	0.19	0.07	0.01	0.15	0.07	0.05	0.04
0.5 Er	5.40	0.55	0.06	0.04	0.00	0.04	0.07	0.01	0.02

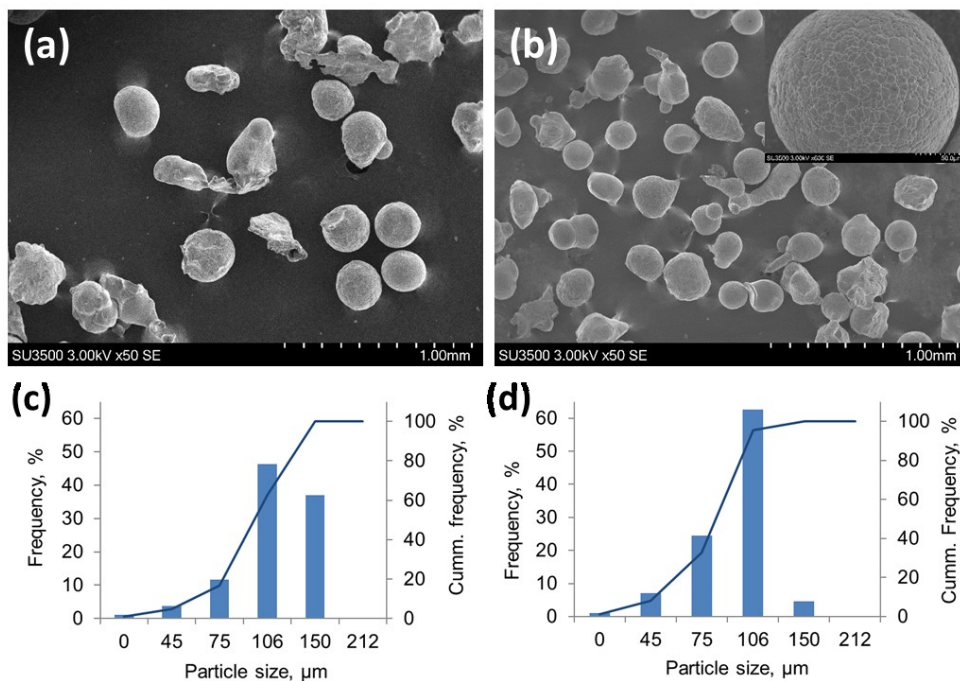


**Figure 3.1 SEM micrographs of the atomized powders - (a) 0.1 Er and (b) 0.5 Er; Particle size distributions from sieve analysis for (c) 0.1 Er and (d) 0.5 Er.**

The oxide content of the powders was also determined by Instrumental Gas Analysis (IGA) provided by SGS Canada Inc following ASTM E1019-08/ASTM E1447-09 standards. The oxygen content was determined as 0.5 wt.% and 0.2 wt.% for the 0.1 Er and 0.5 Er powders, respectively. The particle size distribution of the atomized powders was determined by sieve analysis and is presented in Figure 3.1, along with SEM micrographs of the powders. Both atomized powders had mode particle sizes of

106-150  $\mu\text{m}$ . Powders below 212  $\mu\text{m}$  were selected for further use in this study, and the spherical morphology of both powder compositions can be observed in Figure 3.1.

### 3.1.2. Cryomilled powders

Both the commercial Al 5356 powder and custom Al-5Mg-Er powders were cryomilled using Union Process attrition mills in stainless steel vials. Stainless steel balls, with a diameter of 4.85 mm, were used as grinding media and a ball to powder weight ratio of 32:1 was used. To prevent adhesion of the powder to the milling media and vessel, and to control the fracturing events, 0.25 wt.% of stearic acid ( $\text{CH}_3(\text{CH}_2)_{16}\text{COH}$ ) was added as a process control agent. Liquid nitrogen was continuously added to the vial by either an automatic feed or manually to maintain a constant slurry during milling, and to maintain the temperature at  $-196\text{ }^\circ\text{C}$ .

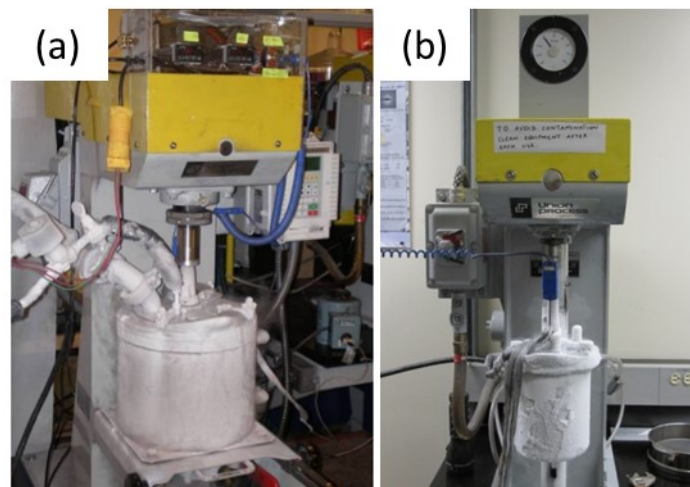


Figure 3.2 Union Process Attrition mills used for the cryomilling experiments: (a) 1-S mill; (b) HD-01 mill

The Al 5356 powder was cryomilled using a Union Process 1-S attrition mill (Figure 3.2(a)) at a speed of 180 rpm with the liquid nitrogen continuously added to the vial by an automatic feed. The powder was milled for 7 hours resulting in an average particle size of 10 to 50  $\mu\text{m}$  and equiaxed powder morphology after milling (see Figure 3.3). The custom Al-Mg-Er powders were cryogenically milled in a Union Process HD-01 Lab Attritor (Figure. 3.2(b)) at a speed of 300 rpm with the liquid nitrogen manually added to the vial. Due to the large starting size of these powder particles ( $< 212\text{ } \mu\text{m}$ ),

the Al-Mg-Er powders were milled for 30 hours in 2 stages. A previous cryomilling study on Al 2024 powder with similar particle size distribution indicated equiaxed powder particles were obtained after 18 hours of milling [3.1], so a similar time frame was used in this study. The particle morphology of the milled Al-Mg-Er powders was observed with SEM and the size distribution was also measured using a HORIBA LA-920 particle size analyzer. The powder was suspended in a fluid medium (i.e.: isopropanol) and a laser was used to measure the largest dimension of the powder particle. The particle size distribution of the milled powders is shown in Figure 3.4 along with SEM images of the powder showing the final equiaxed morphology. Mean particle size was 9.9  $\mu\text{m}$  and 7.9  $\mu\text{m}$  for 0.1 Er and 0.5 Er, respectively.

After milling, the composition of the Al-Mg-Er powders was determined by ICP and IGA with the same methods as detailed in Section 3.1.1 for the atomized powders. Oxygen concentration in the milled powders was also analyzed by SGS Canada Inc. by IGA. 8.4 wt.% and 13 wt.% of oxygen was determined for the 0.1 Er and 0.5 Er powders, respectively. The significant oxygen levels in the final powders are attributed to oxygen pick up in situ and after the cryomilling process. The composition of the milled powders is listed in Table 3.2. Changes in Mg and Er composition after milling the 0.1 Er powders fall within the measurement uncertainty of the ICP technique. However, the decrease in Mg and Er content after milling in the 0.5 Er powder is likely due to oxidation during milling. Fe, Ni, and Cr content increase in both powders as a result of contamination from the milling equipment.

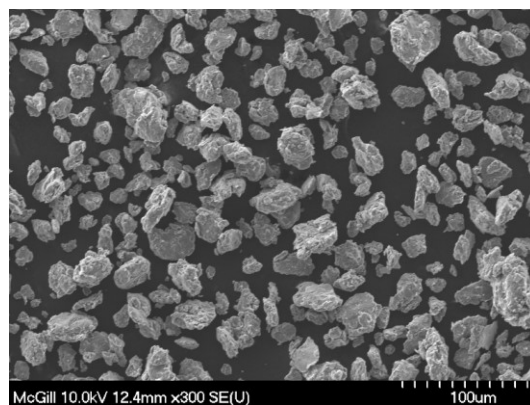


Figure 3.3 SEM micrograph of the cryomilled Al 5356 powder

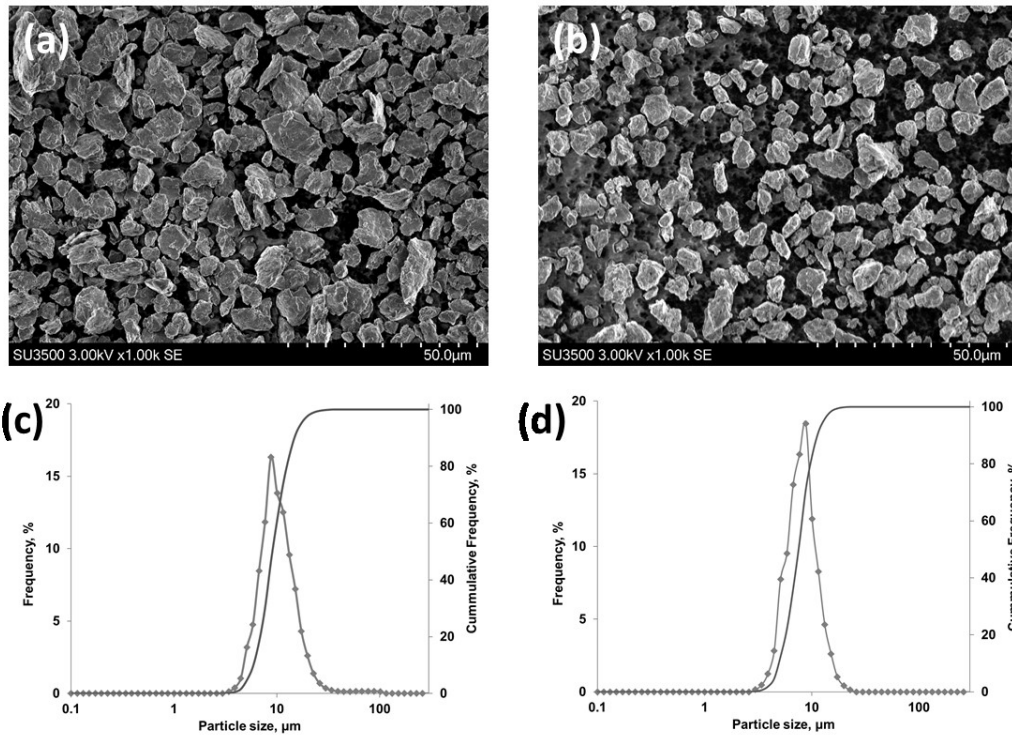


Figure 3.4 SEM micrographs of the cryomilled powders: (a) 0.1 Er, (b) 0.5 Er; Particle size distributions for (c) 0.1 Er and (d) 0.5 Er.

Table 3.2 Composition of 30 h milled Al-Mg-Er powders (wt.%)

Element	Mg	Er	Ti	Fe	Ni	TI	Si	Sb	Zn	Cr
0.1 Er	4.65	0.08	0.26	0.39	0.17	0.06	0.05	0.03	0.02	0.04
0.5 Er	4.48	0.44	0.01	0.16	0.03	0.00	0.05	0.01	0.02	0.03

## 3.2. Bulk sintered samples

### 3.2.1. Spark Plasma Sintering

The cryomilled powders were sintered in an ISO-Carb 85 graphite die using a Spark Plasma Sintering apparatus (Thermal Technology LLC Model 10 Series – 10-3) as

shown in Figure 3.5. The 10-3 model has a capability of 10 tons of force and 3000 amp power supply, pulsed DC current. The set temperature and pressure applied during the process are controlled through the PID controller, located in the control cabinet. Hydraulic rams, also controlled by the PID controller, regulate the pressure applied to the graphite die. The sample temperature was continuously read by the controller, while the applied voltage and current were adjusted to match the set point temperature. The sample temperature was measured using a thermocouple located in a hole drilled in the lower punch to 2 mm from the surface of the sample. The sintering process was carried out under vacuum conditions. A 20 mm diameter die set-up was used.



Figure 3.5 Thermal Technology LLC 10-3 SPS apparatus

### 3.2.2. Sintering parameters

Improved sintering of ceramic powder systems has been observed with multi-stage sintering processes using both conventional and novel powder metallurgy processes [3.2, 3.3]. In this study, multiple stage sintering processes are applied to the metal nanocrystalline Al-Mg system. Sintering schedules tested were one-stage sintering (OSS), two-stage sintering (TSS) and three-stage sintering (MSS) processes.

Temperatures ranging from 350 °C to 550 °C were selected with holding times varied from 0.5 to 20 minutes. The solidus temperature in the Al-5Mg system is approximately 580 °C, but the maximum  $T_1$  temperature was selected as 550 °C to remain in the solid-state sintering regime. Minimum sintering temperature was selected as 350 °C to ensure significant diffusion was active.

**Table 3.3 Sintering parameters for OSS, TSS and MSS schedules**

Sintering Schedule	T <sub>1</sub> , t <sub>1</sub>	T <sub>2</sub> , t <sub>2</sub>	T <sub>3</sub> , t <sub>3</sub>
500 OSS	500 °C, 1 minute	-	-
500 TSS 5	500 °C, 1 minute	350 °C, 5 minutes	-
500 TSS 20	500 °C, 1 minute	350 °C, 20 minutes	-
550 TSS 20	550 °C, 0.5 minute	350 °C, 20 minutes	-
350 MSS 5	350 °C, 10 minutes	450 °C, 5 minutes	500 °C, 5 minutes
350 MSS 10	350 °C, 10 minutes	450 °C, 10 minutes	500 °C, 10 minutes

For TSS cycles  $T_1 > T_2$ , while for the MSS cycles  $T_1 < T_2 < T_3$ . In OSS and MSS schedules typical SPS processing parameters of  $100 \text{ }^\circ\text{C}\cdot\text{min}^{-1}$  and maximum pressure of 50 MPa were used. For the TSS schedules, pressures of 50 and 60 MPa and heating rates of 100 and  $300 \text{ }^\circ\text{C}\cdot\text{min}^{-1}$  were used. A maximum pressure of 60 MPa was applied due to the structural limitations of the graphite die. In both the OSS and TSS cycles the pressure is low at the beginning (10 MPa) and increased to 50 or 60 MPa during the ramping segment to  $T_1$ . In the MSS schedules pressure was increased from 10 MPa to 50 MPa during the first ramping segment to  $T_1$  and held constant for the duration of the cycle. Sintering temperature and times for the different schedules are detailed in Table 3.3. OSS cycles consist of a hold at  $T_1$  temperature for a short duration  $t_1$ . The TSS cycle was composed of the OSS cycle with an additional hold at 350 °C ( $T_2 = 0.6T_m$ ) for durations of 5 and 20 minutes. For the TSS schedules,  $T_1$  was selected as 500 °C ( $T_1 = 0.9T_m$ ) or 550 °C ( $T_1 = 0.97T_m$ ), where  $T_m$  is the melting temperature. MSS sintering

temperatures were selected as 350 °C ( $T_1 = 0.6T_m$ ), 450 °C ( $T_2 = 0.8T_m$ ), and 500 °C ( $T_3 = 0.9T_m$ ); holding times were varied from 5 to 10 minutes. The TSS and MSS sintering cycles are illustrated in Figure 3.6.

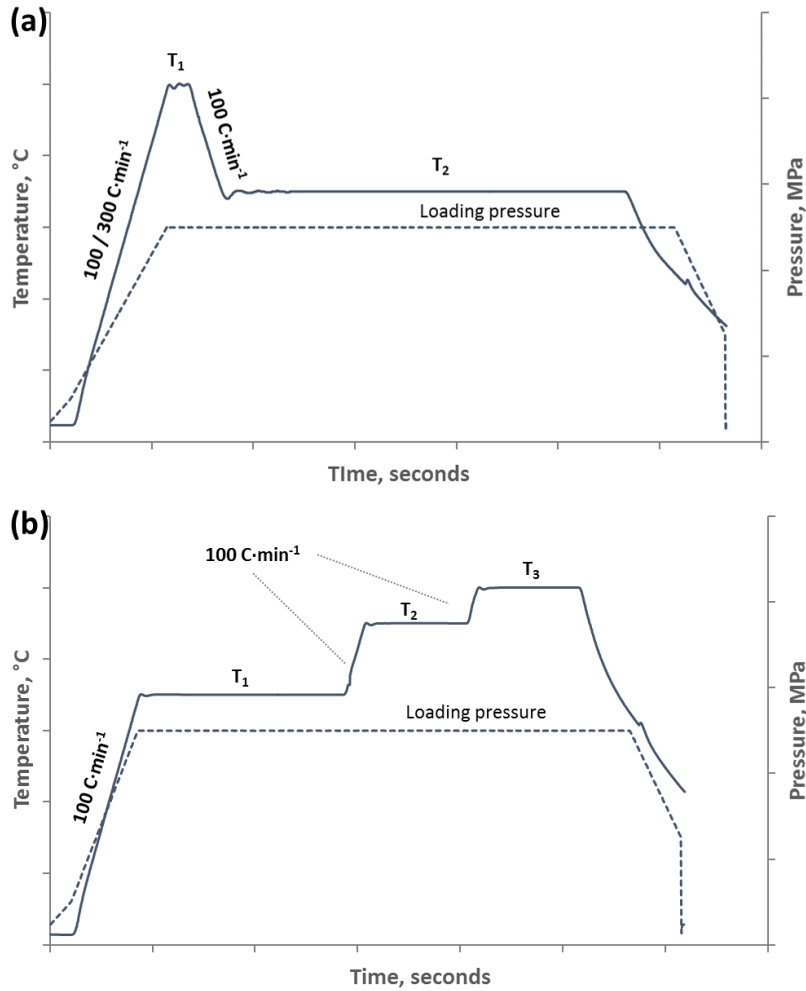


Figure 3.6 Schematics of sintering schedules (a) TSS and (b) MSS

### 3.3. Properties of bulk sintered samples

#### 3.3.1. Density

The density of the SPS samples was measured by either the Archimedes method or image analysis of micrographs. For image analysis, five fields were taken randomly through the microstructure and were analyzed to determine the area porosity. The density was calculated using the Archimedes method as shown in the equation 3.1

$$\theta = \frac{m_a \theta_w}{m_{ao} - (m_{wo} - m_{wire})} \quad (3.1)$$

where: the density  $\theta$  is a function of the mass of the sample in air  $m_a$ , the density of the water  $\theta_w$ , the mass of the sample impregnated with oil weighed in air  $m_{ao}$ , the mass of the sample impregnated with oil weighed in water  $m_{wo}$ , and the mass of the wire used to suspended the sample in the water  $m_{wire}$ . The density of the water was taken as the value at ambient temperature. A minimum of three samples were produced at each condition to verify the measured density of the samples.

### 3.3.2. Microhardness

Microhardness tests were selected to test the consolidation of the sintered samples. Cross sections of the samples were mounted, ground and polished using 320 grit SiC grinding paper, followed by 9  $\mu\text{m}$ , 3  $\mu\text{m}$ , 1  $\mu\text{m}$  diamond suspension and polishing on Buehler Vibromet auto-polisher for 4 - 12 hours. The Vicker's hardness of the samples was measured using a Clark Microhardness CM-100AT indenter, using a 50 gf load. The hardness values reported are an average of at least 10 indents per sample condition.

### 3.3.3. Flexural/Bend Strength

The flexural strength of the consolidated samples was determined with 3-point bending tests. The bending tests were performed at room temperature on a universal testing machine Tinius Olsen H25K-S with a crosshead loading speed of 10  $\text{mm}\cdot\text{min}^{-1}$  and a support span of 18.8 mm. An average of 3:2 ratio of width to thickness was used for each sample. The flexural strength  $\sigma$  of the samples can be calculated using equation 3.2

$$\sigma = \frac{3F_B L}{2wt^2} \quad (3.2)$$

where:  $\sigma$  is the flexural strength,  $F_B$  is the failure load,  $L$  is the span distance, and  $w$  and  $t$  are the sample width and thickness, respectively.

The flexural strain of the sample during testing can also be measured by equation 3.3

$$\varepsilon_{flex} = \frac{6Dt}{L^2} \quad (3.3)$$

where:  $\varepsilon_{flex}$  is the flexural strain and  $D$  is the maximum deflection at the center of the beam.

### 3.4. Analysis methods

#### 3.4.1. Differential scanning calorimetry

Differential scanning calorimetry (DSC) and thermo-gravimetric analysis (TGA) of the cryomilled Al-Mg-Er powders was performed with the NETZSCH Simultaneous Thermal Analyzer STA 449 F3 instrument. Linear scans from 30 °C – 750 °C at 10 K·min<sup>-1</sup> were run on samples in alumina crucibles; empty crucible of Al<sub>2</sub>O<sub>3</sub> were used as reference. Sample mass of powders was up to 40 mg, and the scans were run under argon atmosphere. Linear DSC scans were also obtained from samples ( $\approx$  15 mg) run in alumina crucibles at 5 – 40 K·min<sup>-1</sup> from 30 °C – 630 °C under flowing nitrogen atmosphere in a STARe DSC + TGA instrument. The as milled powders were annealed under flowing Argon in the DSC + TGA instrument. Powder samples were placed in alumina crucibles and heated to the desired temperatures at a rate of 10 K·min<sup>-1</sup>, isothermally held for one hour, and then cooled to room temperature.

#### 3.4.2. X-ray Diffraction

A Philips PW1710/00 Cu-K $\alpha$  source ( $\lambda = 1.5406 \text{ \AA}$ ) diffractometer operated at 40 mA and 20 kV was used to generate the X-ray Diffraction (XRD) patterns, with a step size of 0.02 °2 $\theta$ ·s<sup>-1</sup>. Alfa Aeser atomized pure Al powder (7 – 15  $\mu\text{m}$  particle size) was annealed under Ar atmosphere at 500 °C for 2 hours and used as the reference powder for peak analysis. For the cryomilled Al-Mg-Er powders, XRD peak de-convolutions were done with a Pearson VII function. Asymmetrical peaks, obtained by a split Pearson VII function with equal full width-half maximum (FWHM) values, were used to analyze the reference Al powders, while symmetric peaks were used for all milled powders. Reduced chi-square was used to assess the peak fitting. For the bulk samples, calculation of full-width at half-maximum (FWHM) were performed by linear regression analysis of the peaks. Phases present in the powders were identified with the

PANalytical X'Pert HighScore software. The lattice parameter of the powders was calculated from the peak positions with the XLAT program, a least squares program for the precise refinement of cell constants and is available online [3.4], using Si powder as standard. The average grain size and strain in the powders were determined with the Method of Integral Breadths, using the FWHM values in place of the integral breadths after [3.5] as shown in equation 3.4

$$\frac{\delta^2(2\theta)}{\tan^2\theta_0} = \frac{K\lambda}{L} \left[ \frac{\delta(2\theta)}{\tan\theta_0 \sin\theta_0} \right] + 16e^2, \quad (3.4)$$

where:  $\delta$  is the corrected full width at half maximum breadths (in radians), peak  $\theta_0$  is the position of the analyzed peak maximum,  $\lambda$  is the wavelength,  $L$  is the grain size and  $e$  is the micro strain. At least four Al reflections were used for the calculations.

Correction of the XRD peak width is performed with equation 3.5

$$\delta(2\theta) = B \left( 1 - \frac{b^2}{B^2} \right) (rad), \quad (3.5)$$

where:  $B$  and  $b$  are the full widths at half maximum breadths (in radians) of the same Bragg peak from the XRD scan. Peak broadening due to lattice effects is approximated by a Gaussian function, whereas crystallite size effects are approximated by a Cauchy function in this method. The XRD spectrum is processed by removal of background signal and stripping of the  $K_{\alpha 2}$  peaks before peak analysis.

### 3.4.3. X-ray Photoelectron Spectroscopy (XPS)

X-ray photoelectron spectra were collected using the Thermo Scientific™ K-Alpha™ XPS spectrometer with an Al  $K\alpha$  1486.6 eV excitation source in a vacuum ( $< 5 \cdot 10^{-7}$  mbar) at room temperature. The X-ray angle of incidence was  $30^\circ$  and the electron take-off angle is  $90^\circ$ . A minimum X-ray spot size of  $40 \mu\text{m}$  was used. 8 scans were used for the valence, survey and high resolution scans (i.e.: Al2p, Mg1s, Er4d, Er4p, C1s, O1s). A pass energy of 200 eV was used for the survey, while a pass energy of 50 eV was used for the valence and high resolution scans. The milled powders were compacted into thin (1 – 2 mm thick) 2 cm diameter discs with a hydraulic press. The pressed powder was placed in a vacuum chamber for at least 24 hours before being transferred to a

desiccator where the sample was stored until XPS analysis. The binding energies  $E_b$  were measured relative to the binding energy of C1s electrons on the sample surface accepted at 284.8 eV. Peak analysis was done using Shirley background removal.

#### **3.4.4. Microscopy methods**

Analysis of the nanostructure was done with scanning and transmission electron microscopes (SEM/TEM): Hitachi SU3500, Hitachi SU8000, Philips CM200, and Tecnai G2 F20 instruments. TEM powder samples were prepared by dispersion of powders on a TEM Cu grid, and STEM samples by mounting of powders in epoxy followed by preparation by ion-beam milling. TEM samples from SPS compacts were prepared by cutting thin sections (250 – 500  $\mu\text{m}$ ) from the sintered samples and mechanical thinning to thickness of 100 – 150  $\mu\text{m}$ . 3 mm discs were punched and then the discs were prepared by either dimpling or electropolishing. For the Al 5356 compacts, the sample was electropolished to perforation with a 15 vol.% nitric acid in methanol solution at 20 V and -30 °C. Final sample preparation was performed with ion milling on the Gatan 656 PIPS system, at low voltage under dual beam condition with the stage cooled by liquid nitrogen to ~165 °C. For the Al-Mg-Er samples, the 100 - 125  $\mu\text{m}$  discs were dimpled (on one or both sides) down to a thickness less than 20  $\mu\text{m}$  with the Gatan 656 Dimple Grinder system. Perforation of the sample was obtained by ion milling on the Gatan 656 PIPS system, under dual beam condition with the stage cooled by liquid nitrogen to ~165 °C. Starting conditions of beam voltage at 4 keV with milling angle of 6 - 8 degrees (top and bottom) until perforation.

Bright field (BF) and dark field (DF) images were used to obtain the grain size distributions using an area analysis method and the average measurement from at least 300 grains at each condition. Energy dispersive X-ray spectroscopy (EDS) analysis and selected area electron diffraction (SAED) patterns were used to determine phases.

### 3.5. References

- 3.1. Vintila R, Milligan J, Drew RAL, Brochu M (2009) Formation of nanostructures and solid solubility extension in cryomilled Al-Cu and Al-Si powders, *Canadian Metallurgical Quarterly* 48:33-44.
- 3.2. Ma J, Zhu S, Ouyang C (2011) Two-step hot-pressing sintering of nanocomposite WC-MgO compacts, *Journal of the European Ceramic Society* 31:1927-1935.
- 3.3. Reddy KM, Kumar N, Basu B (2010) Innovative multi-stage spark plasma sintering to obtain strong and tough ultrafine-grained ceramics, *Scripta Materialia* 62:435-438.
- 3.4. Rupp B (1988) XLAT - Least squares refinement of cell constants, *Scripta Metallurgica* 22, 1. [http://www.ruppweb.org/new\\_comp/xlat\\_new.htm](http://www.ruppweb.org/new_comp/xlat_new.htm)
- 3.5. Varin RA, Bystrzycki J, Calka A (1999) Effect of annealing on the microstructure, ordering and microhardness of ball milled cubic (L<sub>12</sub>) titanium trialuminide intermetallic powder, *Intermetallics* 7:785-796.

## Chapter 4 Improving Consolidation of Cryomilled Al 5356 Alloy Using a Two-Stage (TSS) SPS Sintering Cycle

### 4.1. Introduction

Nanostructured aluminum materials have improved mechanical properties due to the refined grain structure [4.1,4.2]. However, the high pressures and temperatures required for adequate consolidation of nanostructured powders often leads to grain growth in the final bulk product. Previous studies on nanostructured cryomilled Al-Mg alloy powders show that significant grain growth often occurs during consolidation with methods such as extrusion [4.3] and hot isostatic pressing (HIP) [4.4,4.5]. SPS, a pressure-assisted pulse current sintering process, allows fast fabrication of bulk materials from powders using fast heating rates and short sintering time thereby limiting the average grain growth compared to other pressure-assisted consolidation processes [4.6,4.7].

While longer sintering duration at higher temperatures improves consolidation, shorter time is preferred to minimize grain growth. The objective of this first chapter was to improve the consolidation of sintered nanostructured materials while also minimizing the grain growth during processing. This was achieved by utilizing a two-stage SPS sintering schedule (TSS). Improvements in consolidation of cryomilled Al 5356 powders were evaluated by the mechanical properties and by Weibull modulus analysis for fracture of brittle materials. The grain size was determined by XRD and TEM techniques. Results showed that a TSS process with longer second stage hold (i.e.: 20 minutes) resulted in almost doubling of the Weibull modulus and minimal grain growth when compared to one-stage sintering by SPS.

### 4.2. Background

In order to improve the consolidation of bulk nanostructured materials, a two-stage SPS sintering procedure is utilized, taking advantage of the rapid densification and minimal grain growth possible during consolidation of nanostructured powders [4.8–4.11]. Multi-

stage SPS sintering has been investigated with various ceramic materials [4.12,4.13], but to the best of the author's knowledge there are no reported studies on this sintering technique with metallic materials. Ma *et al.* [4.14] consolidated nano-composite WC-MgO with a two-step hot-pressing process, using a sintering profile similar to the one presented here. However, the process here utilizes an SPS sintering system and much shorter sintering durations, i.e. minutes instead of hours. The concept investigated is to densify a powder bed and initiate sintering at a high temperature with a short hold, followed by a second hold at a lower temperature to continue particle sintering but not further grain growth. Sintering of milled Al 5356 powders by the OSS and TSS schedules is presented in this chapter. Details of the sintering parameters for the OSS and TSS cycles can be found in Chapter 3. The powder compact is initially held at 500 °C ( $T_1 = 0.78T_m$ , where  $T_m$  is the melting temperature). The temperature is then dropped to 350 °C ( $T_2 = 0.53T_m$ ) to further continue sintering, reducing the quantity of internal defects.

### 4.3. Phases in the sintered bulks

Akin to previous studies in cryomilling of Al and Al alloy powders [4.10,4.11,4.15,4.16], a supersaturated  $\alpha$ -Al solid solution was formed in the powders during milling (Figure 4.1) with a final lattice parameter of 4.0636 Å. Assuming the lattice expansion is attributed solely to dissolved Mg the solid solution was estimated at 4.7 wt.% Mg, which agrees with the findings of [4.17]. After sintering,  $\beta$ -Al<sub>3</sub>Mg<sub>2</sub> and Al<sub>18</sub>Mg<sub>3</sub>Cr<sub>2</sub> peaks were observed in addition to the  $\alpha$ -Al peaks in the XRD spectra irrespective of OSS or TSS sintering condition (Figure 4.2). The presence of these phases is likely due to solid solution breakdown during sintering. STEM images of the 500 TSS 20 condition, presented in Figure 4.3 (a and b), revealed second phase precipitates located within grains and at grain boundaries. EDS microanalysis revealed precipitates of Al-Mg, Al-Mg-Cr, and Al-Mg-Cr-Ti composition within an  $\alpha$ -Al solid solution with Mg, Si, and Zn (Figure 4.3 c – e). Due to the absence of Al<sub>18</sub>Mg<sub>3</sub>Ti<sub>2</sub> peaks in the XRD spectra, the Al-Mg-Cr-Ti precipitates are thought to be the Al<sub>18</sub>Mg<sub>3</sub>(Cr,Ti)<sub>2</sub> phase, with Ti substituting for Cr sites.

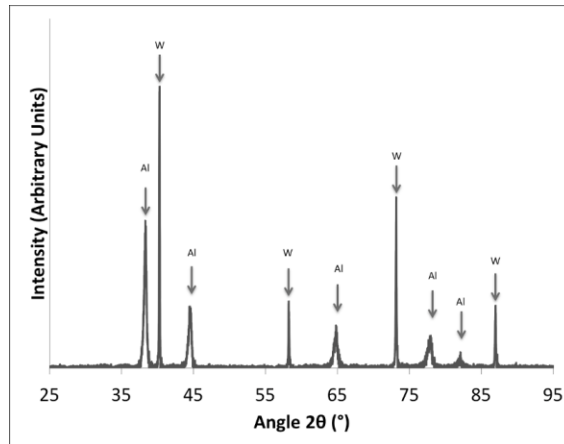


Figure 4.1 Phase identification after milling of Al 5356 powder with W standard.

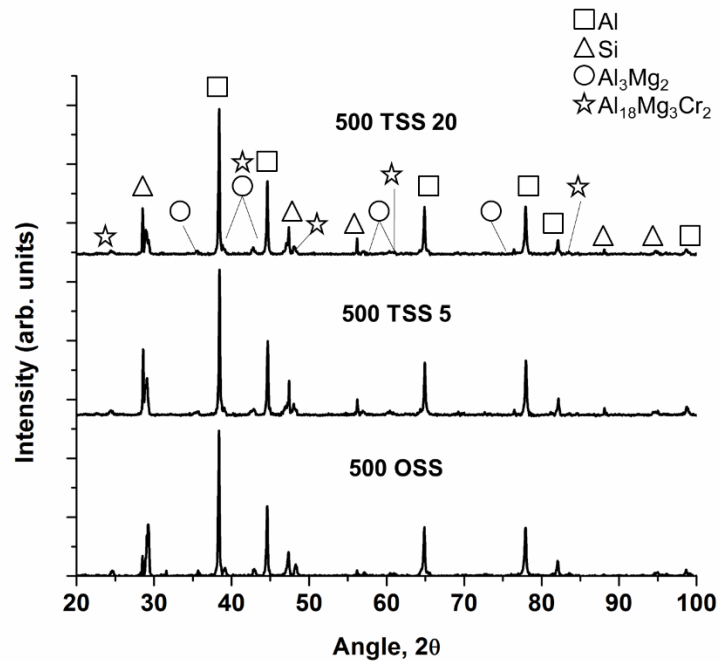


Figure 4.2 Phase identification after sintering: XRD spectra of 500 OSS, 500 TSS 5 and 500 TSS 20 samples with a Si standard. Peaks have been normalized.

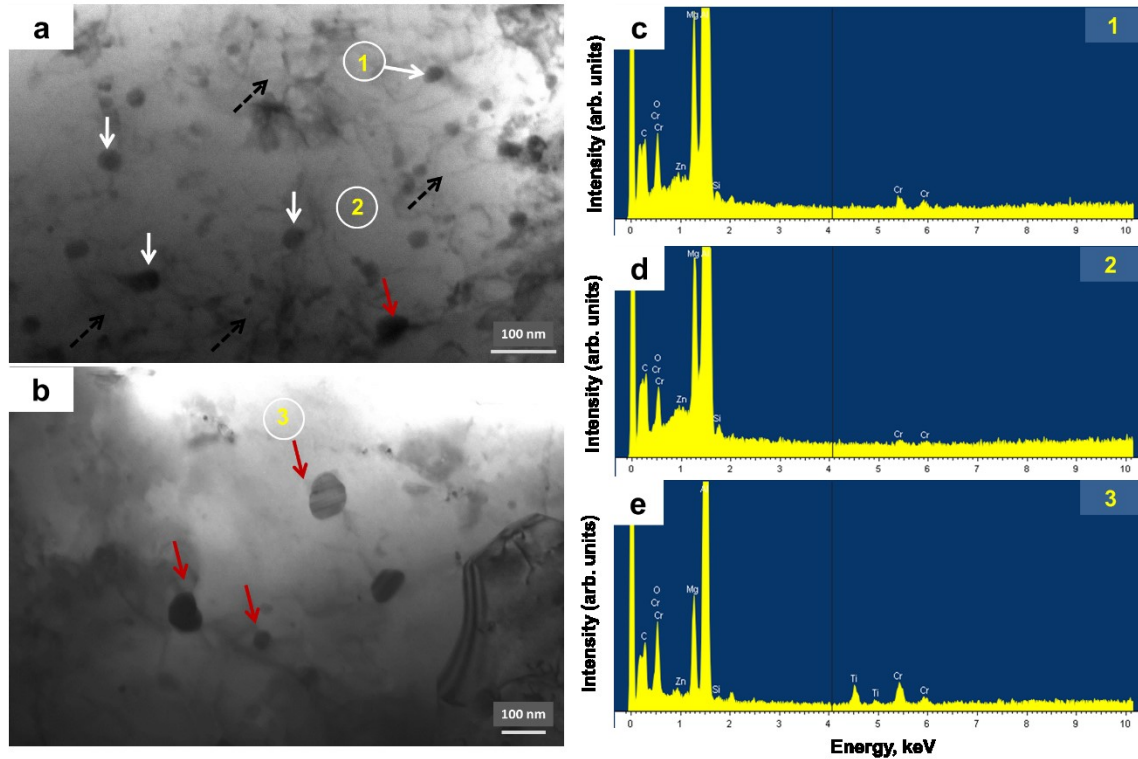


Figure 4.3 STEM images (a,b) showing dislocation structures (dashed black arrows), Al-Mg-Cr precipitates (white arrows), and Al-Mg-Cr-Ti precipitates (red arrows) observed in 500 TSS 20 sample. EDS microanalysis (c, d, e) of precipitates/areas indicated in (a) and (b).

#### 4.4. Microstructure and grain size

The average grain size and micro-strain in the cryomilled powder and sintered bulks is determined from XRD peak analysis. These results are presented in Table 4.1. The average grain size is also determined from TEM image analysis. The grain size and micro-strain in the cryomilled powder were determined to be 29 nm and 0.14 %, respectively, comparable to values reported for milled Al and Al alloys [4.10,4.15,4.16,4.18]. Upon SPS consolidation, the micro-strain in the powders decreased during sintering to 0.06 %, similar to a micro-strain value of 0.08% reported for cryomilled Al-Mg powders after annealing [4.16]. Average grain sizes of 97 nm and 91 nm from XRD peak analysis were obtained after the OSS and both TSS conditions, respectively. These values are similar within measurement error. TEM bright field (BF) images of the microstructure, with corresponding selected area diffraction (SAD)

patterns, were collected after sintering as shown in Figure 4.4; these images are taken from the nanocrystalline regions of the 500 OSS and 500 TSS 20 samples. The continuous ring patterns are indicative of the nanocrystalline structure and are indexed as the  $\alpha$ -Al phase indicated by the blue arcs in Figure 4.4.

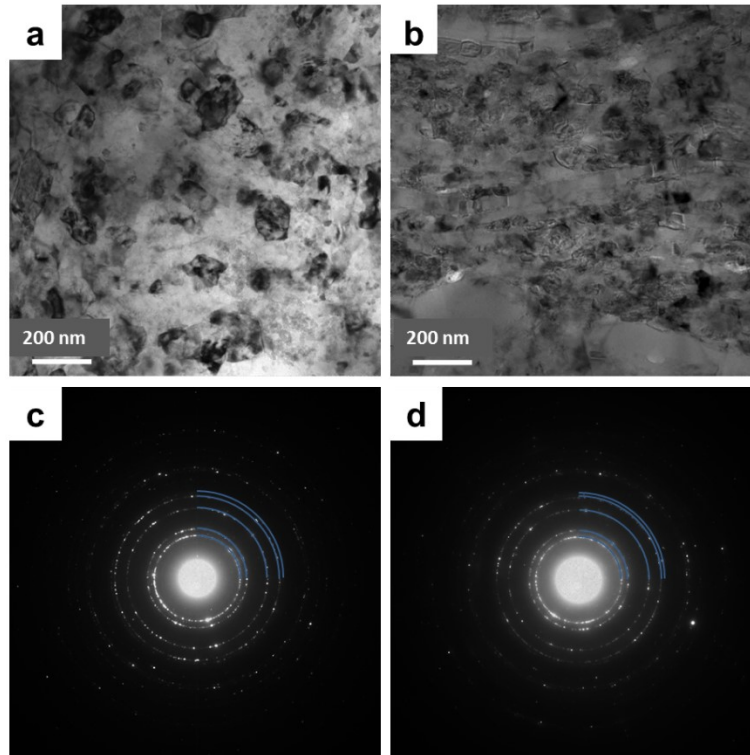


Figure 4.4 TEM micrographs and SAED patterns showing nanocrystalline structure of the SPS pucks: (a) BF image of a 500 OSS sample; (b) BF image of a 500 TSS 20 sample; (c) SAED pattern of the 500 OSS region shown in (a); (d) SAED pattern of the 500 TSS 20 region shown in (b).

Table 4.1 Summary of XRD analysis obtained from milled and consolidated samples.

Condition	Grain size (XRD)	Micro-strain	Corr. Coeff. ( $R^2$ )
Cryomilled powder	29 nm	0.14 %	0.873
500 OSS	97 nm	0.06 %	0.960
500 TSS 5	91 nm	0.06 %	0.850
500 TSS 20	91 nm	0.07 %	0.870

Previous researchers have reported a bimodal microstructure in SPS consolidated cryomilled Al powders [4.9–4.11] and similar results were observed in this system (Figure 4.5). Small regions of coarse grains ( $> 500$  nm) were sporadically observed within a matrix of nano-grains in all sintered samples. Regions of dislocation structures survived consolidation similar to reports by Roy *et al.* [4.19] on bulk Al 5083 consolidated by hot-isostatic pressing (HIP) and extrusion of cryomilled powders. Various dislocation structures were observed for both OSS and TSS samples including - dislocation networks, dislocation substructures and dislocations trapped within grains (Figure 4.5(a)). Samples also showed interactions between second phase precipitates and dislocation networks (Figure 4.3(a)). Evidence of recrystallization during consolidation was also observed. Grain size distribution determined for the 500 OSS and 500 TSS 20 conditions are presented in Figure 4.6. 80% of the measured grains in the 500 OSS sample were finer than 100 nm with an average grain size of  $68 \pm 46$  nm. Under similar one-stage SPS sintering conditions, the average grain size in the fine-grained regions of sintered Al alloys was reported as between 100 - 150 nm [4.9,4.10]. After a 20 minute hold at  $T_2$ , 80% of the measured grains were still finer than 100 nm with an average grain size of  $73 \pm 46$  nm. These results are in agreement with XRD measurements and confirmed that no significant grain growth occurred during sintering at  $T_2$ . The fine grain size contributes to the strength of the sintered material via the Hall-Petch relationship, while dislocation hardening and solid solution strengthening could also have an effect.

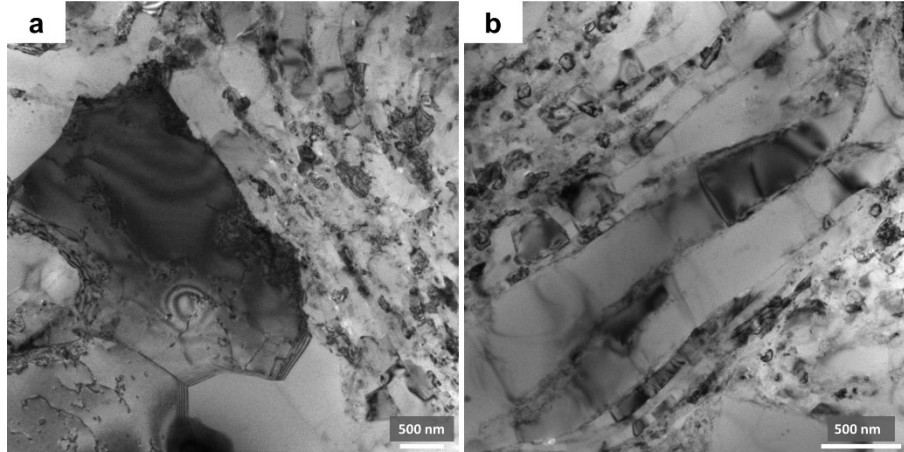


Figure 4.5 Bimodal microstructure observed in 500 TSS 20 sample with (a) coarse grains with dislocation structures microstructure and (b) lamellar-type grains.

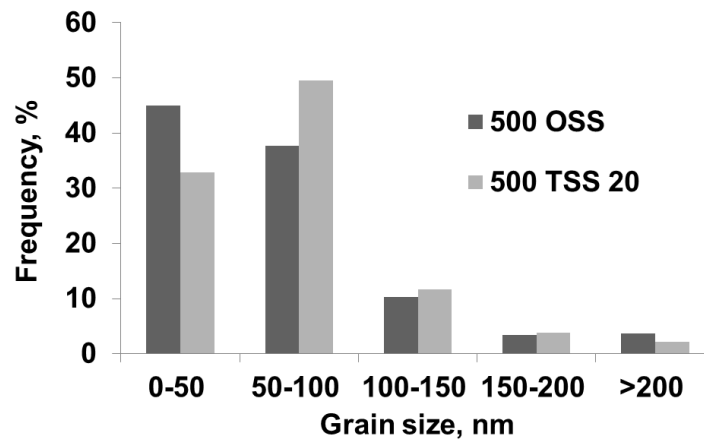


Figure 4.6 Grain size distribution after 500 OSS (average grain size =  $68 \pm 46$  nm; 300 grains) and 500 TSS 20 sintering conditions (average grain size =  $73 \pm 46$  nm; 319 grains).

#### 4.5. Grain growth during sintering

Selection of  $T_2$  was based on the consideration of recrystallization, grain growth and surface diffusion during sintering at lower temperatures. The recovery and recrystallization behavior of a cryomilled Al-7.6Mg (at.%) alloy was recently studied by Zhou *et al.* [4.16] where a recrystallization temperature of 327 °C and activation energy of 190 kJ·mol<sup>-1</sup> were determined. Activation energies and grain growth parameters were

selected for the 300 – 500 °C range from the studies of Zhou *et al.* on grain growth in a cryomilled Al powder [4.20]. The grain growth in this system was estimated from Eq. 4.1

$$D^{1/n} - D_0^{1/n} = kt \quad (4.1)$$

where:  $D_0$  and  $D$  are the initial and final grain size after an isothermal period  $t$ ,  $k$  is a temperature dependent constant and  $n$  is a constant. The activation energies were taken as  $Q = 112 \text{ kJ}\cdot\text{mol}^{-1}$  at 500 °C and  $Q = 79 \text{ kJ}\cdot\text{mol}^{-1}$  at 350 °C, while  $n$  was selected as  $n = 0.28$  for the 500 °C soak and  $n = 0.05$  for the 300 – 450 °C hold. Lastly, the activation energy for surface diffusion at lower temperatures was taken as  $142 \text{ kJ}\cdot\text{mol}^{-1}$  [4.21]. Based on eq. (4.1), after one minute of sintering at 500 °C, the predicted grain size was calculated as 50 nm, considering no growth during the heating stages or field effect contributions. Using 50 nm as the starting grain size for the  $T_2$  hold, calculations showed negligible grain growth (50 nm) as illustrated in Fig 4.7. The experimental results validated this inhibition of grain growth. Although the activation energy for surface diffusion is higher than that of grain growth at  $T_2$ , grain growth can be kinetically inhibited while surface diffusion can occur.

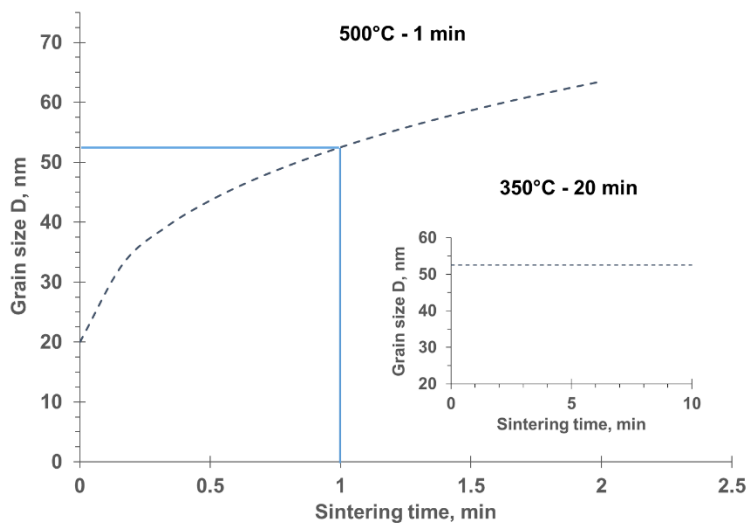


Figure 4.7 Grain size estimations for TSS schedules

#### 4.6. Consolidation improvement and Weibull modulus analysis

The mechanical properties of the sintered bulks from OSS and TSS cycles are compiled in Table 4.2. Upon consolidation, the density of the samples was determined via image analysis. A density of 95% is obtained after the OSS schedule, which increased to a maximum of 98% with the TSS schedules. The mechanical behavior of the samples was assessed by micro-hardness tests and flexural strength was determined with three-point bending tests. High hardness and flexural strength were achieved at 163 HV and 829 MPa, respectively. The hardness values are comparable to that of dense SPS consolidated cryomilled Al 5083 with hardness of  $165 \pm 6$  HV [4.11]. As shown in Table 4.2, using the 95% confidence criteria, no significant changes were observed in both hardness and flexural strength with the different sintering conditions. The improvement in material reliability resulting from the second sintering stage is reflected by the increase in Weibull modulus  $m$ . Assuming the scatter of a brittle material's fracture strengths follows a Weibull distribution, the strength reliability can be predicted from the empirically determined constant  $m$  [4.22]. As shown in Figure 4.8,  $m$  was determined graphically from the plot slope and increased with the hold at  $T_2$ , from a value of 13 for 500 OSS to a maximum of 25 at 500 TSS 20.

**Table 4.2 Mechanical properties obtained from OSS and TSS consolidated samples.**

<b>Condition</b>	<b>Vickers hardness (HV<sub>50gf</sub>)</b>	<b>3-point flexural strength (MPa)</b>	<b>Weibull modulus, <math>m</math></b>
<b>500 OSS</b>	$161 \pm 7$	$829 \pm 65$	13
<b>500 TSS 5</b>	$157 \pm 11$	$799 \pm 39$	23
<b>500 TSS 20</b>	$163 \pm 6$	$829 \pm 65$	25

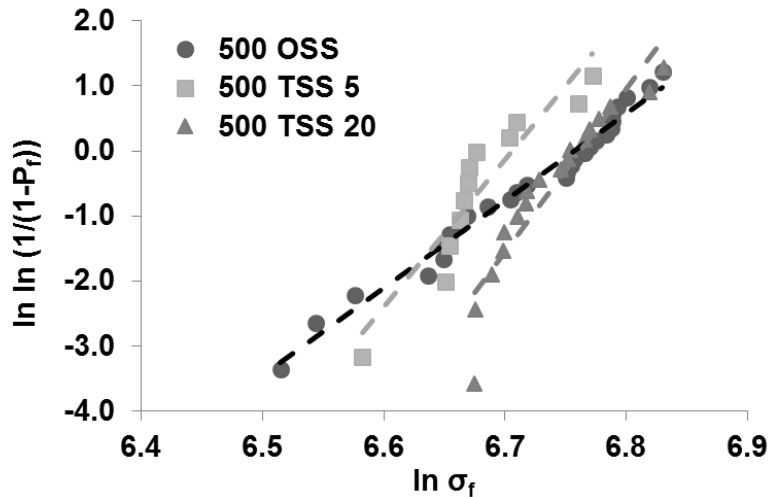


Figure 4.8 Weibull modulus plots for 500 OSS ( $m = 13$ ;  $n = 28$ ), 500 TSS 5 ( $m = 23$ ;  $n = 12$ ) and 500 TSS 20 ( $m = 25$ ;  $n = 18$ ) conditions.

In thermally sensitive materials high temperatures enhance sintering and densification, but also promote grain growth [4.23]. Therefore, the initial sintering temperature  $T_1$  was selected to ensure maximum densification in a short time. While the specific densification mechanisms during SPS are still under debate, they have been likened to those active during hot pressing [4.24]. It is proposed that Joule heating effects, i.e.: high local temperatures at particle contacts, enhance plastic yielding and contribute to densification during the initial stages of sintering [4.11,4.25]. Ye *et al.* [4.11] examined the possible densification mechanisms during consolidation of cryomilled Al 5083 by SPS. It was determined that plastic yielding dominated densification during the initial heating stages, but power law creep and diffusion dominated during the latter heating stages and during the isothermal hold. It is proposed that similar densification mechanisms were active in this system during sintering at  $T_1$ .

TSS densification curves confirmed macroscopic densification was completed after the  $T_1$  hold (Figure 4.9), but microscopic increase in inter-particle bonding (neck length growth) occurred via surface diffusion which was reflected by the increase in  $m$  during the  $T_2$  hold. Jayatilaka and Trustrum [4.26] showed that  $m$  can be related to the flaw size distribution in a material - the variability of defect size being greater for smaller values of  $m$  where a large crack/defect is more likely to be present. Weibull modulus of  $m = 20$  is often taken as the lower limit for a material in order to have sufficient

mechanical reliability and  $m > 20$  will give narrow distribution of fracture strength; typically  $m > 30$  for ductile metals. The doubling of  $m$  from OSS to TSS schedules indicates the TSS procedure definitely contributes to the elimination of large inter-particle flaws left after the OSS consolidation. Such internal flaws are known to affect the fracture behavior of sintered materials. However, the small gain in  $m$  after prolonged sintering at  $T_2$  suggests that surface diffusion contributions to improving particle consolidation are initially important, but rapidly decrease in effectiveness with advanced neck growth at final sintering stages. It is generally accepted that surface diffusion, acting alone, affects sintering due to the formation of strong interfaces, and a reduction in curvature-related driving forces with no major contribution to densification.

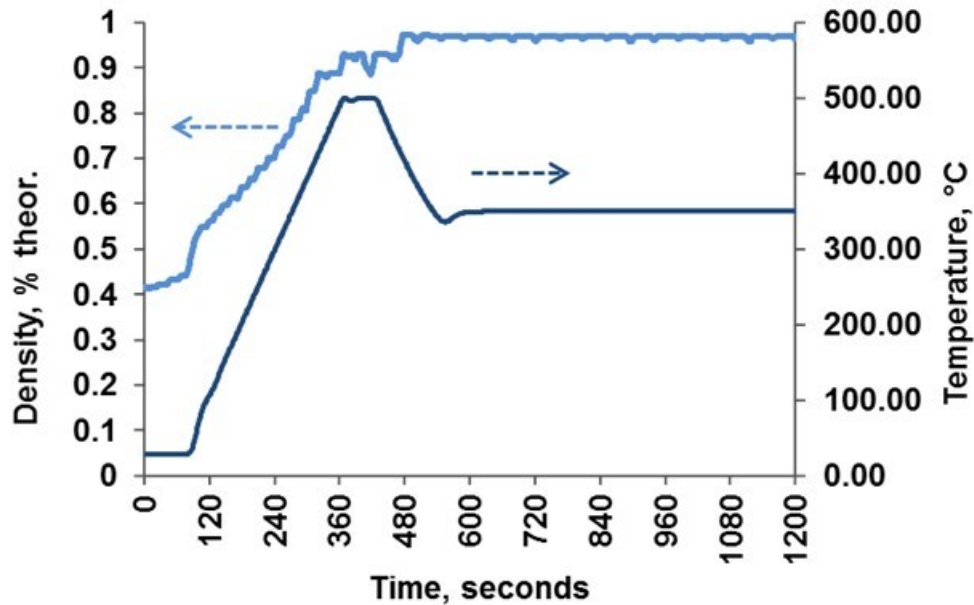


Figure 4.9 Calculated densification curve for the 500 TSS 20 sample

#### 4.7. Summary

The effect of using the TSS versus OSS sintering schedules on the consolidation of cryomilled Al-Mg powders was studied. TSS schedules, with properly selected parameters  $T_1$  and  $T_2$ , allowed for enhanced sintering while avoiding excessive grain growth. An average grain size of 70 nm was maintained in a Al 5356 alloy after over 20

minutes of sintering by SPS. Flexural strengths of ~800 MPa and hardness of ~160 HV were achieved for the three tested sintering conditions. The use of a two-stage sintering cycle did not influence the hardness and flexural strength, but consolidation of the bulk improved with time in the TSS regime shown by the doubling in fracture strength distribution statistic (Weibull modulus  $m$ ) from 13 to 25. The increased duration of the second hold (from 5 to 20 minutes) marginally increased the Weibull Modulus, from 23 to 25. Improvement in the consolidation was attributed to improved inter-particle cohesion via surface diffusion during the hold at  $T_2$ .

#### 4.8. References

- 4.1. A.S. Khan, B. Farrokh, L. Takacs (2008) Effect of grain refinement on mechanical properties of ball milled bulk aluminum, *Materials Science and Engineering A* 489:77-84.
- 4.2. M.A. Meyers, A. Mishra, D.J. Benson (2006) Mechanical properties of nanocrystalline materials, *Progress in Materials Science* 51:427-556.
- 4.3. Park YS, Chung KH, Kim NJ, Lavernia EJ (2004) Microstructural investigation of nanocrystalline bulk Al-Mg alloy fabricated by cryomilling and extrusion, *Materials Science and Engineering A* 374:211-216.
- 4.4. Roy I, Chauhan M, Lavernia EJ, Mohamed FA (2006) Thermal Stability in Bulk Cryomilled Ultrafine-Grained 5083 Al Alloy, *Metallurgical and Materials Transactions A* 37:721-730.
- 4.5. Lucadamo G, Yang NYC, San Marchi C, Lavernia EJ (2006) Microstructure characterization in cryomilled Al 5083, *Materials Science and Engineering A* 430:230–241.
- 4.6. Ye J, Ajdelsztajn L, Schoenung J (2006) Bulk Nanocrystalline Aluminum 5083 Alloy Fabricated by a Novel Technique: Cryomilling and Spark Plasma Sintering, *Metallurgical and Materials Transactions A* 37:2569-2579.

- 4.7. Rana JK, Sivaprahasam D, Raju KS, Sarma VS (2009) Microstructure and mechanical properties of nanocrystalline high strength Al-Mg-Si (AA6061) alloy by high energy ball milling and spark plasma sintering, *Materials Science and Engineering A* 527:292-296.
- 4.8. Kubota M (2007) Properties of nano-structured pure Al produced by mechanical grinding and spark plasma sintering *Journal of Alloys and Compounds* 434-435:294-297.
- 4.9. Zuniga A, Ajdelsztajn L, Lavernia EJ (2006) Spark Plasma Sintering of an Al-Cu-Mg-Fe-Ni-Sc alloy, *Metallurgical and Materials Transactions A* 37:1343-1352.
- 4.10. Chen H, Taq K, Yang B, Zhang J (2009) Nanostructured Al-Zn-Mg-Cu alloy synthesized by cryomilling and spark plasma sintering, *Transactions of Nonferrous Metals Society of China* 19:1110-1115.
- 4.11. Ye J, Ajdelsztajn L, Schoenung JM (2006) Bulk Nanocrystalline Aluminum 5083 Alloy Fabricated by a Novel Technique: Cryomilling and Spark Plasma Sintering, *Metallurgical and Materials Transactions A* 37:2569-2579.
- 4.12. Reddy KM, Kumar N, Basu B (2010) Innovative multi-stage spark plasma sintering to obtain strong and tough ultrafine-grained ceramics, *Scripta Materialia* 62:435-438.
- 4.13. Jain D, Reddy KM, Mukhopadhyay A, Basu B (2010) Achieving uniform microstructure and superior mechanical properties in ultrafine grained  $TiB_2$ - $TiSi_2$  composites using innovative multi stage spark plasma sintering, *Materials Science and Engineering A* 528:200-207.
- 4.14. Ma J, Zhu S, Ouyang C (2011) Two-step hot-pressing sintering of nanocomposite WC-MgO compacts, *Journal of the European Ceramic Society* 31:1927-1935.
- 4.15. Zhou F, Rodriguez R, Lavernia EJ (2002) Thermally Stable Nanocrystalline Al-Mg Alloy Powders Produced by Cryomilling, *Materials Science Forum* 386-388:409-414.

- 4.16. Zhou F, Liao XZ, Zhu YT *et al.* (2003) Microstructural evolution during recovery and recrystallization of a nanocrystalline Al-Mg alloy prepared by cryogenic ball milling, *Acta Materialia* 51:2777-2791.
- 4.17. Murray J (1982) Al-Mg, *Bulletin of Alloy Phase Diagrams* 3:60.
- 4.18. Zhou F, Witkin D, Nutt SR, Lavernia EJ (2004) Formation of nanostructure in Al produced by a low-energy ball milling at cryogenic temperature, *Materials Science and Engineering A* 375-377:917-921.
- 4.19. Roy I, Chauhan M, Lavernia EJ, Mohamed FA (2006) Thermal Stability in Bulk Cryomilled Ultrafine-Grained 5083 Al Alloy, *Metallurgical and Materials Transactions A* 37:721-730.
- 4.20. Zhou F, Lee J, Lavernia EJ (2001) Grain growth kinetics of a mechanically milled nanocrystalline Al, *Scripta Materialia* 44:2013-2017.
- 4.21. German RM: *Powder Metallurgy & Particulate Materials Processing*, MPIF, New Jersey, 2005.
- 4.22. Weibull W (1951) A statistical distribution function of wide applicability, *Journal of applied mechanics* 18:293-297.
- 4.23. Vintila R, Charest A, Drew RAL, Brochu M (2011) Synthesis and consolidation via spark plasma sintering of nanostructured Al-5356/B<sub>4</sub>C composite, *Materials Science and Engineering A* 528:4395-4407.
- 4.24. Chaim R, Margulis M (2005) Densification maps for spark plasma sintering of nanocrystalline MgO ceramics, *Materials Science and Engineering A* 407:180-187.
- 4.25. Xie G, Ohashi O, Yamaguchi N, Wong A (2003) Effect of surface oxide films on the properties of pulse electric-current sintered metal powders, *Metallurgical and Materials Transactions A* 34:2655-2661.
- 4.26. Jayatilaka A De S, Trustrum K (1977) Statistical approach to brittle fracture, *Journal of Materials Science* 12:1426-1430.

## Chapter 5 Investigating the Thermal Stability of Cryomilled Al-Mg-Er Powders

### 5.1. Introduction

In this chapter, the thermal stability of cryomilled Al-5Mg-Er powders is investigated. The Er content was changed from ~ 0.1 wt.% to 0.5 wt.% to observe the possible effects of Er on grain growth behavior. The microstructure of the milled powders with increasing temperature was investigated by differential scanning calorimetry (DSC) with various annealing treatments followed by X-ray diffraction (XRD) and electron microscopy analysis. Prolonged milling led to significant oxygen pick-up in the powders. Overall thermal stability in the Al-Mg-Er powders is attributed to the combined effects of solute/impurity drag and second phase pinning (nanoscale oxides, nitrides, oxy-nitrides) that impede grain boundary motion. Improved thermal stability was observed in the 0.5 Er powder, with as milled grain sizes maintained up to  $\sim 0.8T_m$ . This behaviour is attributed to the higher oxide content within the powders.

### 5.2. Background

Solute/impurities and nanoscale inclusions, such as nitrides and oxides introduced during the milling process, interfere with boundary mobility and reduce grain growth in milled Al alloy powders [5.1-5.4]. In order to improve grain size stability in milled Al alloy powders, research into the addition of alloying elements such as Sc has been conducted. Sc exhibits slow diffusion kinetics in Al. Sc also forms nanoscale, coherent  $L_{12}$  trialuminide  $Al_3Sc$  precipitates that are able to pin grain boundaries and substructures, and shows some promise as seen with the delay of recrystallization in cryomilled Al-Mg-Sc powders [5.5]. Typically, Sc additions give the most efficient improvement per weight percent added. Even though dilute (<0.12 at. %, 0.2 wt. %) additions are commonly made, the high cost of Sc (i.e.: \$1400/100g [5.6]) limits its widespread usage. Less costly trialuminide phase forming alternatives to Sc include

lanthanide elements such as Er (\$540/100g [5.6]). Additions of Er (< 1 wt.%) to wrought Al-Mg series alloys have been investigated [5.7-5.10]. Similarly, to Sc effects, Er addition retards the recrystallization of deformed structures in Al-Mg alloys. However, limited studies at the nanocrystalline regime have been done to date.

### **5.3. Al-Mg-Er powders**

#### **5.3.1. Atomized Al-Mg-Er powders**

The composition of the atomized powders, as determined from ICP and IGA analysis, is presented in Table 5.1. Both powders contain similar levels of Mg in the atomized form, with 5.3 – 5.4 wt.% Mg. The Er content was determined to be approximately 0.12 wt.% for the 0.1 Er powder and 0.55 wt.% for the 0.5 Er powder. The content of impurity solutes in the atomized powders was reduced with increased Er addition. This trend has also been found in literature where the levels of Fe and Si impurity in an Al 5052 alloy were reduced by Er addition due to Er combining with Si and Fe in the melt [5.11]. XRD spectra of the atomized powders indicate an  $\alpha$ -Al solid solution as shown in Figure 5.1; Si peaks are from the added crystallographic standard powder to correct peak position. Due to the higher concentration of Mg versus Er in the alloy, the changes in Al lattice parameter are attributed to the Mg solutes. Analysis of XRD peak shifts gives a lattice parameter of  $\sim 4.0633 \text{ \AA}$  for both powders, which indicates approximately 4.5 at.% ( $\sim 5 \text{ wt.}\%$ ) Mg is captured in solid solution. This is a marked increase from the equilibrium solubility in the Al-Mg system which is about 1 at.% Mg [5.12]. The data from XRD peak analysis of the atomized powders are compiled in Table 5.2 including lattice parameter, solid solubility extension, minimum average crystallite size and micro strain.

Table 5.1 Composition of atomized and 30 hour milled powders (wt.%)

Element	Mg	Er	Ti	Fe	Ni	TI	Si	Sb	Zn	Cr
Atomized 0.1 Er	5.29	0.12	0.19	0.07	0.01	0.15	0.07	0.05	0.04	0.00
Atomized 0.5 Er	5.40	0.55	0.06	0.04	0.00	0.04	0.07	0.01	0.02	0.00
Milled 0.1 Er	4.65	0.08	0.26	0.39	0.17	0.06	0.05	0.03	0.02	0.04
Milled 0.5 Er	4.48	0.44	0.01	0.16	0.03	0.00	0.05	0.01	0.02	0.03

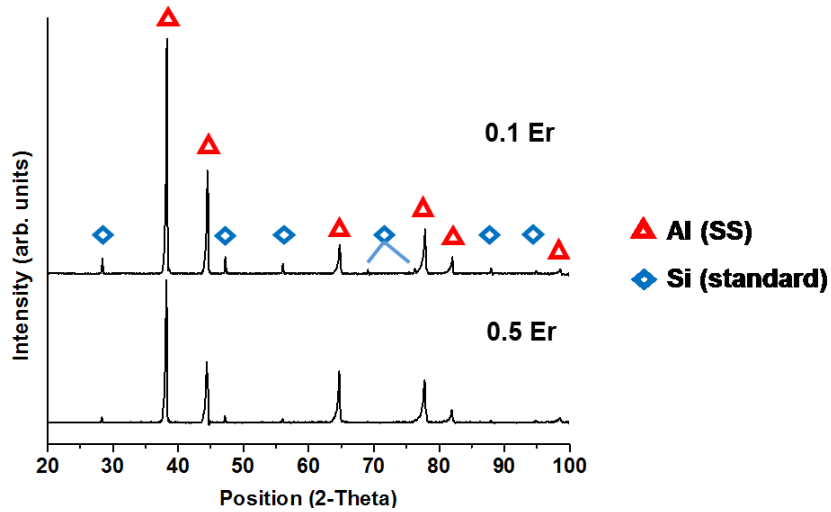


**Figure 5.1 XRD spectra of atomized Al-Mg-Er powders**

Back Scattered-SEM images taken of the cross-section of the atomized powders (Figure 5.2), show channeling contrast of the microstructure as well as the distribution of second phases in the powders. BSE images indicate a range of micron to nanoscale grains are present in the atomized powders. Nanoscale grains are observed mostly around the edges of the atomized powders, an example of which is shown in Figure 5.2 (c). XRD peak analysis also suggests the presence of nanocrystalline grains in the powders, with minimum crystallite sizes of 37 and 67 nm obtained in the 0.1 Er and 0.5 Er powders, respectively. Significant solute segregation was present in the 0.5 Er powder. An EDS element line scan across areas of micro-segregation in the 0.5 Er powders indicates co-segregation of Er and Mg as shown in Figure 5.2(c) and 5.2(d). Low strain values are obtained in the powders, with 0.048% and 0.059% in the 0.1 Er and 0.5 Er powders, respectively. The powders have 0.5 wt.% and 0.2 wt.% oxygen content in the 0.1 Er and 0.5 Er compositions, respectively, which can be attributed to the nanoscale oxide film on the powder surfaces.

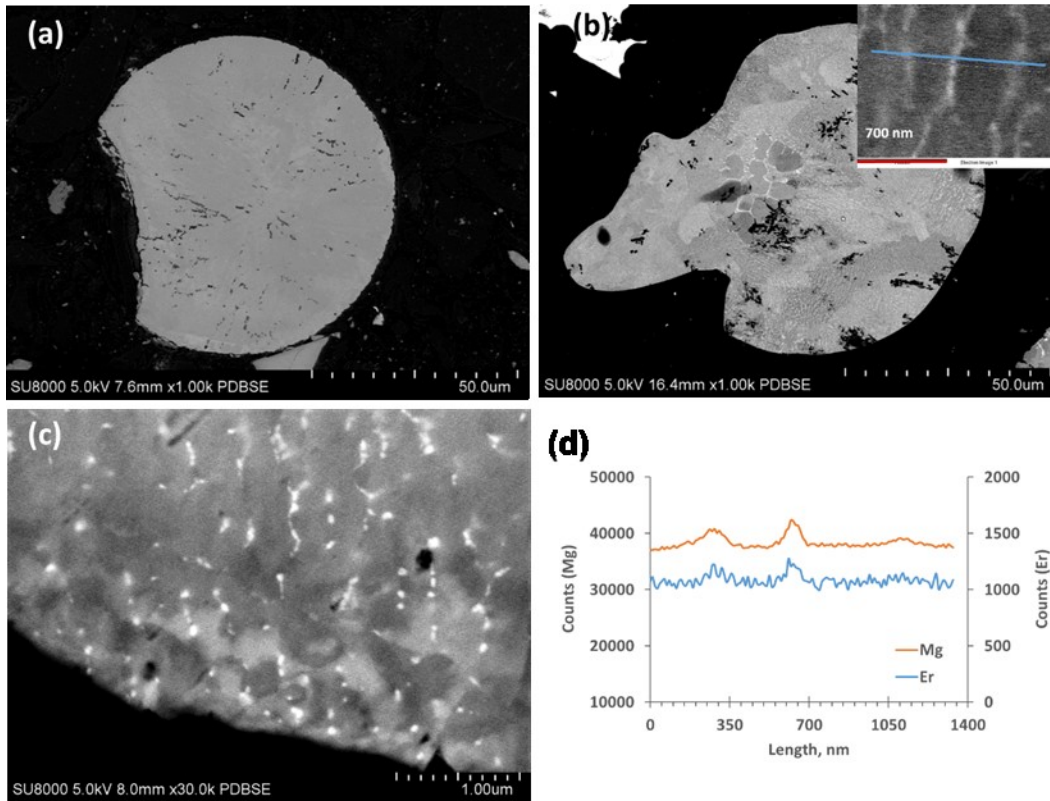


Figure 5.2 BSE images of atomized Al-Mg-Er powders: (a) 0.1 Er powder; (b) 0.5 Er powder with inset showing micro-scale segregation; (c) some nanoscale features in 0.5 Er powder; (d) EDS element line scan analysis from inset in (b) showing Mg and Er distribution.

Table 5.2 XRD results for atomized and 30 hour milled powders

Powder Condition	Lattice parameter (Å)	Mg in matrix (at.%)	Grain size, XRD (nm)	Microstrain (%)	Correlation coefficient, $R^2$	Grain size, TEM (nm)
Atomized, 0.1 Er	4.0633 ± 0.0011	4.52	37	0.048	0.91	-
Atomized, 0.5 Er	4.0637 ± 0.0003	4.62	67	0.059	0.92	-

Milled, 0.1	4.0662	5.26	22	0.094	0.92	16 ± 1
Er	± 0.0015					
Milled, 0.5	4.0647	4.87	19	0.106	0.93	17 ± 0
Er	± 0.0004					

### 5.3.2. Cryomilled powders

The composition of both powders is altered by the milling process as shown in Table 5.1. Changes in Mg and Er composition after milling in the 0.1 Er powders fall within the measurement uncertainty of the ICP technique. However, there is loss of Mg and Er content after milling in the 0.5 Er powder, likely due to oxidation during milling. The increased Fe, Ni and Cr content in both powders is a result of contamination from the milling equipment. After the two-stage milling procedure the powders contain 8.4 wt.% and 13 wt.% oxygen for the 0.1 Er and 0.5 Er milled powders, respectively. The significant oxygen levels in the final powders are attributed to oxygen pick up in situ and after the cryomilling process. Similar results were reported by Goujon *et al.* [5.13] for mechanically alloyed 5000 Al/AlN powders prepared by cryomilling. Up to 10 wt.% oxygen was obtained in the powders after 25 h of milling in liquid nitrogen [5.13]. Increase in nitrogen contamination in the 5000 Al/AlN powders was also reported. Initial nitrogen content for a 5000 Al/AlN mixture with 20 vol.% AlN content is 7.2 wt.%; the nitrogen concentration increases linearly up to approximately 9.5 wt.% after 26 hours of milling. It is likely that similar levels of nitrogen contamination (~ 2 wt.%) are present within the powder samples studied here.

Figure 5.3 displays the XRD spectra of both 30 h milled powders, with peaks identified as the  $\alpha$ -Al phase (Si is the standard) after cryomilling. Comparison of the  $\alpha$ -Al peaks of the as milled powders to those of atomized powders reveals (1) peak shifts to lower  $^{\circ}2\theta$  positions, indicating increased solubility from the starting condition, and (2) significant broadening – indicative of increased strain and grain refinement. Since the changes in the Al lattice parameter are attributed to the Mg solutes, the lattice parameters in this cryomilled Al-Mg-Er system are compared to those obtained for

mechanically milled pre-alloyed Al-Mg powders to determine solid solubility extensions. The results of Scudino *et al.* [5.14] are used to estimate the Mg in solution for the milled powders. Data extracted from the diffraction patterns of the milled powders are also compiled in Table 5.2 and grain size results from TEM image analysis are also included. Mg solubility in the matrix increases during the milling process. It is estimated that 5.26 at.% Mg and 4.87 at.% Mg is in solution in the 0.1 Er and 0.5 Er powders, respectively. Similar increases in solid solubility have been documented for other Al-Mg milled powder systems [5.3, 5.5].

An average minimum grain size of 22 nm and micro strain of 0.094% was determined for the 0.1 Er powder, while the 0.5 Er powder had a grain size of 19 nm and micro-strain of 0.106%. The grain size and micro strain obtained are similar to those previously reported for milled Al and Al-Mg systems [5.1-5.3]. After 8 hours of milling, Zhou *et al.* observed an average grain size of 25 nm in Al-7.5Mg-0.3Sc (wt.%) alloy powders [5.5], with TEM analysis showing an heterogeneous milled microstructure consisting of nanocrystalline equiaxed grains as well as elongated lamellar-type grains. In comparison, TEM images of the as milled powders in this study indicate only equiaxed nanocrystalline grains in the areas observed. Representative images are shown in Figure 5.3(b) and 5.3(c) with inset SAED patterns. The diffraction patterns contain rings which are indicative of nanocrystallinity and are indexed as the  $\alpha$ -Al phase by the blue arcs in the images. Cryomilling studies performed by Zhou *et al.* on Al-Mg-Sc powders indicate that grain refinement in the alloy is of the same grain sub-division mechanism observed in Al and Al-Mg powders during the cryomilling process [5.15, 5.16]. It is proposed that similar refinement mechanisms take place in these Al-Mg-Er powders during milling. The average grain size is determined by TEM image analysis to be  $16 \pm 1$  nm and 17 nm for 0.1 Er and 0.5 Er, respectively. The grain size distribution, shown in Figure 5.3(d), indicates 85% of the grains are below 30 nm for both samples; the frequency is shown on the left vertical axis, while the cumulative frequency curve corresponds to the right axis.

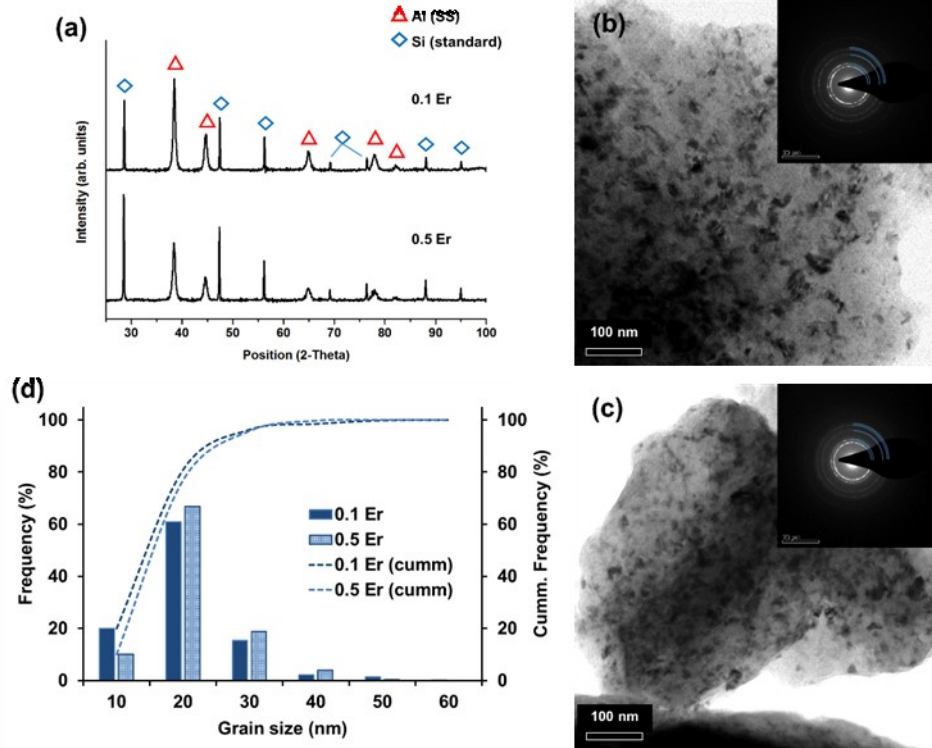


Figure 5.3 30 h milled powders with supersaturated  $\alpha$ -Al phase after milling (a); nanocrystalline grains as shown in Bright field TEM images of 0.1 Er (b) and 0.5 Er (c), both with inset SAED patterns taken from the areas shown; and the grain size distributions obtained from TEM image analysis (d). The nanocrystalline  $\alpha$ -Al phase is indicated by the blue arcs.

The thickness and composition of the oxide film, as well as the hydroxide film are determined via XPS analysis of the surface layers of the milled powders. The average thickness of the oxide film is estimated from the intensities of the Al 2p peaks obtained from the powders with the following equation from [5.17]

$$d = \lambda_o \sin\theta \ln \left[ \frac{C_m \lambda_m I_o}{C_o \lambda_o I_m} + 1 \right] \quad (5.6)$$

Where:  $I_m, I_o$  are the intensities (i.e.: peak areas) of the metal and oxide photoelectron peaks, respectively;  $C_m, C_o$  are the volume densities of metal atoms in the metal and oxide, respectively, taken as  $100.14 \text{ mole} \cdot \text{dm}^{-3}$  for Al metal and  $71.85 \text{ mole} \cdot \text{dm}^{-3}$  for the oxide from [5.18];  $\lambda_m, \lambda_o$  are the inelastic mean free paths (IMFPs) of the photoelectrons in the metal and oxide, respectively (in  $\text{\AA}$ );  $d$  is the oxide thickness (in  $\text{\AA}$ ); and  $\theta$  is the electron take-off angle (with respect to the sample surface). The use of effective attenuation lengths (EALs) rather than IMFPs is suggested since they take into account

the effect of elastic scattering [5.19]. Average EAL values are taken as  $\lambda_m = 2.39$  and  $\lambda_o = 2.92$  from reference [5.19].

The Al 2p peaks for both powders are shown in the first row of Figure 5.4. The oxide film is calculated as 52 Å (5.2 nm) for the 0.1 Er powder and 59 Å (5.9 nm) for the 0.5 Er. The thickness of the oxide films on the powders is also assessed from TEM micrographs of the powders as shown in Figure 5.5. The oxide measured in the HRTEM micrograph of the 0.1Er powder agrees with the XPS measurement, with a thickness of ~ 4 nm measured. However, the 0.5 Er powder shows varying oxide thickness, with thickness ranging from ~ 5 – 10 nm at various areas of the powder surface. The thickness of the hydroxide layer is estimated using the ratio of the OH<sup>-</sup> peak area to the total O peak area. The composition of the oxide film is determined from the intensities of the Al2p and Mg2p peaks. Fitting of the O1s, Al2p, Mg2p and valence bands is shown in Figure 5.4. Results of hydroxide layer and composition calculations are summarized in Table 5.3. The hydroxide film on the 0.5 Er increased compared to the 0.1 Er powders, increasing from a ratio of 17% to 19%. The 0.1 Er powder is estimated to have approximately 3% Mg in the oxide layer, while 0.5 Er has 4% Mg.

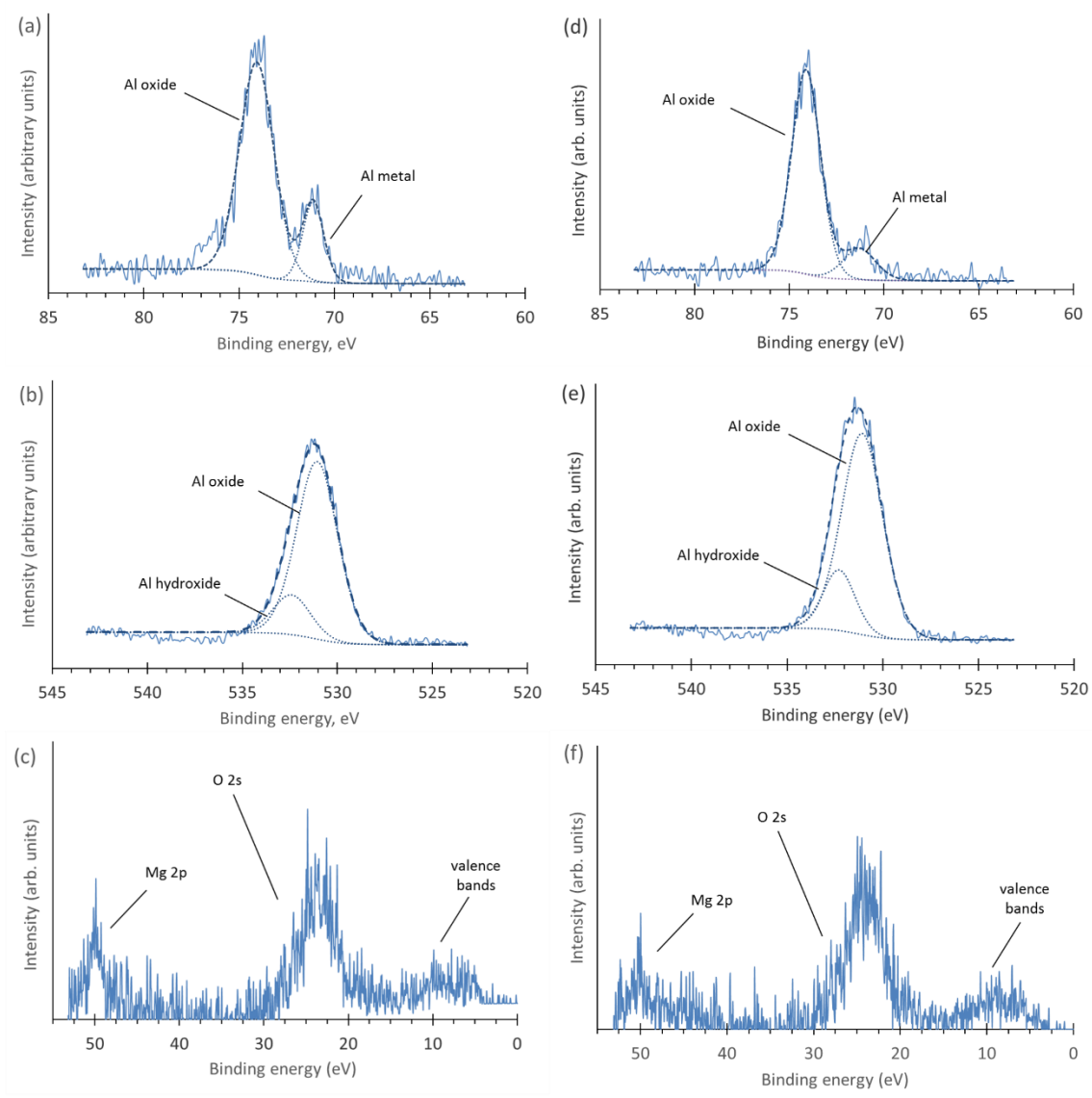


Figure 5.4 XPS analysis of the oxide film on 0.1 Er (a – c) and 0.5 Er (d – f) powders: Al2p peaks (a,d); O1s peaks (b,e); valence region with Shirley background subtracted (c,f).

Table 5.3 Oxide composition from XPS peak analysis

Powder	Thickness, XPS (Å)	Al2p	Mg2p	$\frac{OH^-}{[O^{2-} + OH^-]}$
0.1 Er	52	0.97	0.03	0.17
0.5 Er	59	0.96	0.04	0.19

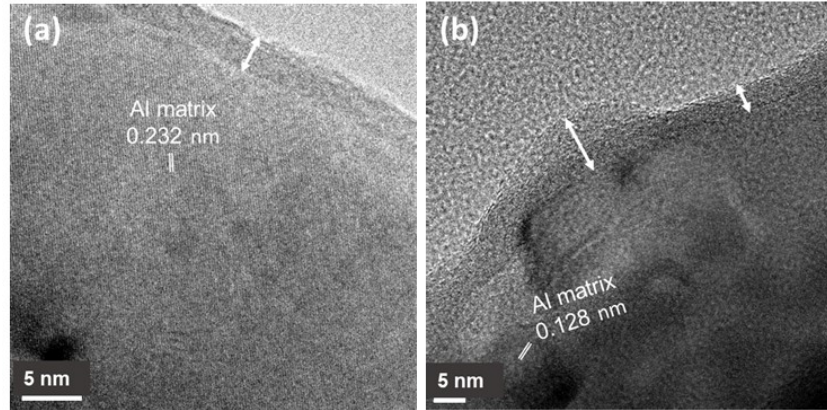


Figure 5.5 HRTEM images of (a) 0.1 Er and (b) 0.5 Er powders showing the oxide film (indicated by arrows) and the crystalline Al matrix:  $d \approx 0.232$  nm ( $d_{111} = 0.2338$  nm) and  $d \approx 0.128$  nm ( $d_{311} = 0.1221$  nm)

#### 5.4. DSC analysis of milled Al-Mg-Er powders

The thermal stability of the powders was studied with linear DSC traces. The  $10 \text{ K}\cdot\text{min}^{-1}$  scans from  $30 \text{ }^\circ\text{C}$  to  $750 \text{ }^\circ\text{C}$  of both milled powders is shown in Figure 5.6. According to FactSage calculations for the Al-5Mg-(0.1 – 1)Er system (wt.%), the bulk solidus and liquidus temperatures are approximately  $575 \text{ }^\circ\text{C}$  and  $635 \text{ }^\circ\text{C}$ , respectively; therefore, it is assumed that events prior to  $575 \text{ }^\circ\text{C}$  are unique to the microstructure of the powders. The scans here show exothermic events at approximately  $160 \text{ }^\circ\text{C}$  (A) and  $475 \text{ }^\circ\text{C}$  (B), with bulk melting events at  $650 \text{ }^\circ\text{C}$  (C).

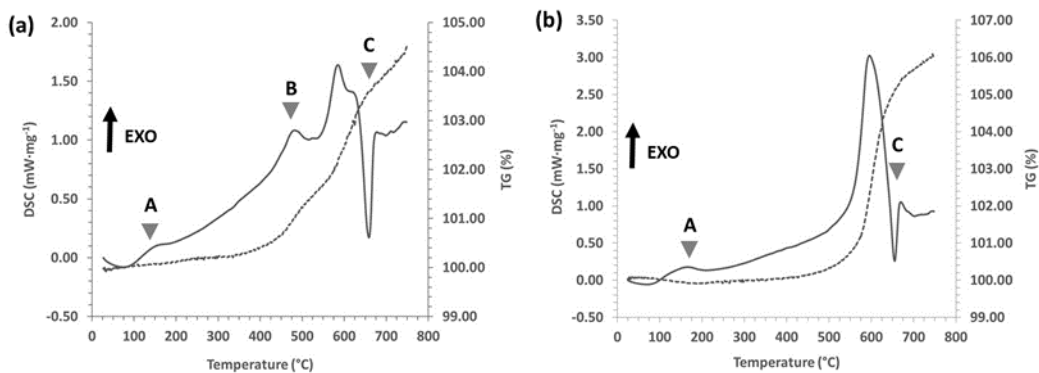
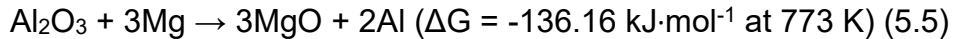
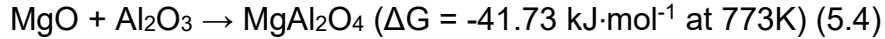


Figure 5.6 DSC traces (solid lines) and TG traces (dotted lines) of 0.1 Er and 0.5 Er powders at heating rate of  $10 \text{ K}\cdot\text{min}^{-1}$  under flowing argon: exothermic events A and B, and endothermic event C.

Milled Al-Mg systems typically exhibit recovery or grain boundary restructuring events below 200 °C [5.3-5.5]. A study on the thermal behavior of milled Al 5083 powder identified a grain boundary reordering event at approximately 158 °C [5.4], while recovery events were observed around 164 °C in milled Al-7.6Mg (at.%) [5.3] and 172 °C in Al-7.5Mg-0.3Sc (wt.%) [5.5]. These results suggest that the event marked A is a recovery event. Although both milled Al-7.6Mg (at.%) and Al-7.5Mg-0.3Sc (wt.%) exhibited recrystallization events around 330 °C [5.3,5.5], no exothermic peaks are observed in either DSC trace around this temperature range. The study on milled Al-7.5Mg-0.3Sc reported an exothermic peak at approximately 450 °C, which was interpreted as a precipitation peak for the Al<sub>3</sub>Sc phase [5.5]. However, the weight gain observed here in the TG curve, starting at 350 °C, suggests that the exothermic peak B is an oxidation event. Similarly, TG tests on cryomilled Al-7.6Mg powders have shown the onset of oxidation in milled powders beginning at 350 °C [5.3]. Another study on the oxidation behavior of milled Al-Mg powders with compositions ranging from Al<sub>0.95</sub>Mg<sub>0.05</sub> to Al<sub>0.5</sub>Mg<sub>0.5</sub> has shown that oxidation proceeds in two stages in an oxygen atmosphere with the onset of oxidation observed over the range of 525-570 °C due to the selective oxidation of Mg. [5.20].

Oxidation of Al-rich Al-Mg alloys at high temperatures is dependent on the Mg and oxygen diffusion through the amorphous oxide layer and subsequent reactions at the oxide-gas and oxide-metal interfaces. The oxide films which developed on an Al-4.2 wt.% Mg at high temperatures consisted of two types of MgO, primary and secondary oxides, which were dependent on the mechanism of formation [5.21]. Primary oxidation is the direct reaction at the oxide/metal interface between Mg from the alloy substrate with oxygen to form MgO. Secondary oxidation is the solid-state reduction of the original air-formed amorphous  $\gamma$ -Al<sub>2</sub>O<sub>3</sub> film by Mg from the alloy substrate to form MgO [5.21]. Although the powder annealing is done under a flowing argon atmosphere, complete removal of oxygen from the DSC chamber is not assured. Therefore, there is the possibility of both primary and secondary oxidation occurring during the DSC run and subsequent annealing processes.

Crystalline spinel phases could be formed by reduction reactions - (1) between Mg and the nanoscale oxides inside the milled powder, (2) between Mg and the oxide film at particle surfaces. Spinel and periclase (MgO) particles can form from several solid-state reduction reactions [5.22]:



Spinel formation due to solid-state reactions between the periclase and alumina particles will be dependent on the proximity of the MgO particles to the alumina oxide film/particles within the powders. The diffusivity of Mg will also affect the reduction reactions. Spinel formation is more thermodynamically favored to form at 500 °C as seen in the reactions presented above.

One hour anneals are carried out to determine the nature of the events observed during the scans, up to 580 °C. Temperatures are chosen at points before/after and during events A, B and C. Temperatures selected for the 0.1 Er powder are 150 °C, 180 °C, 250 °C, 330 °C, 500 °C and 580 °C; while 150 °C, 250 °C, 400 °C, 450 °C, 500 °C, and 580 °C are selected for the 0.5 Er powder. XRD patterns are collected after each anneal and the microstructure is also observed by TEM. The results of the annealed 0.1 Er powders are presented in the next section of this chapter and the 0.5 Er results in the subsequent section.

## **5.5. Annealing behavior of 0.1 Er powder**

### **5.5.1. XRD results of 0.1 Er powder**

Normalized XRD patterns of the as milled and annealed 0.1 Er powders are presented in Figure 5.7. The lattice parameter, estimated Mg in solid solution, grain size and micro strain calculated from the XRD patterns are summarized in Table 5.4; the average grain size from TEM image analysis is also included. Grain size distributions from annealing

at selected temperatures are shown in Figure 5.8; the largest grain size observed at each temperature is also included in the figure.

The major phase observed in the powders, marked in Figure 5.7, is the  $\alpha$ -Al phase. At 500 °C and 580 °C, peaks associated with the  $\text{MgAl}_2\text{O}_4$  spinel phase are also identified indicating the formation of crystalline oxide phases. Shifting of the  $\alpha$ -Al peak positions indicates changes in the Mg solubility with increasing temperature. Milling created a supersaturated solid solution of 5.26 at.% Mg in the matrix, which decomposed after low temperature annealing. After annealing at 150 °C, the estimated Mg in the matrix is 3.05 at.%, higher than the equilibrium value of  $\approx 2.5$  at.% observed in the Al-Mg phase diagram [5.12]. At 180 °C, the matrix content further reduces to 2.08 at.% and remains fairly constant thereafter with increasing annealing temperature, where 2.11 at.% is still in solution after the anneal at 500°C. Decreasing Mg supersaturation without the appearance of  $\beta$  or  $\beta'$  phase reflections in the XRD patterns suggests low volume of second phase precipitates but could also be an indication of Mg segregation to the grain boundary. Straumal *et al.* [5.23] found that partial decomposition of supersaturated solid solutions in Al-5Mg and Al-10Mg alloys after high pressure torsion (HPT) at room temperature resulted in nanoscale  $\beta$  precipitation (of less than 1 vol. %). However, Sauvage *et al.*'s study of an Al-5.7Mg-0.4Mn-0.32Sc (wt.%) alloy processed by HPT showed that decomposition of the solid solution and segregation of Mg clusters to the grain boundary occurred during processing at room temperature and 200 °C [5.24].

General sharpening of the  $\alpha$ -Al peaks from the as milled state with increasing temperature is indicative of (1) reducing micro strain in the powders and (2) increasing crystallite/grain size. XRD analysis indicates a linear increase in the average grain size from 22 nm in the as milled powder to a grain size of 50 nm at 500 °C. However, the micro strain in the 0.1 Er powder exhibits unexpected trends. Although the anneal at 150 °C resulted in reduced micro strain to 0.041%, similar values are obtained in the as milled condition and at 180 °C at 0.094% and 0.09%, respectively. Additionally, the micro strain increases from 0.052% at 330 °C to 0.087% after annealing at 500 °C.

The uncharacteristic changes in micro strain could be due to non-homogeneous solute distributions in the milled powders. Peak broadening due to solute effects as well as grain size and micro strain contributions was observed in milled Ni-15 at.% W powder [5.25]. Rane *et al.* [5.25] concluded that concentration inhomogeneity affected the micro strain obtained from the annealed Ni-W powders. Fluctuating micro strain values were obtained in the milled Ni-W powders with increasing temperature and annealing time. This behaviour was attributed to lattice broadening due to inhomogeneous distribution of W solutes in the Ni grains that may overshadow strain reduction resulting from microstructural relaxations. It is possible that similar conditions may occur in these milled Al-Mg-Er powders, where inhomogeneous distribution of Mg in the Al grains may contribute to the variations in micro strain obtained from the annealed powders.

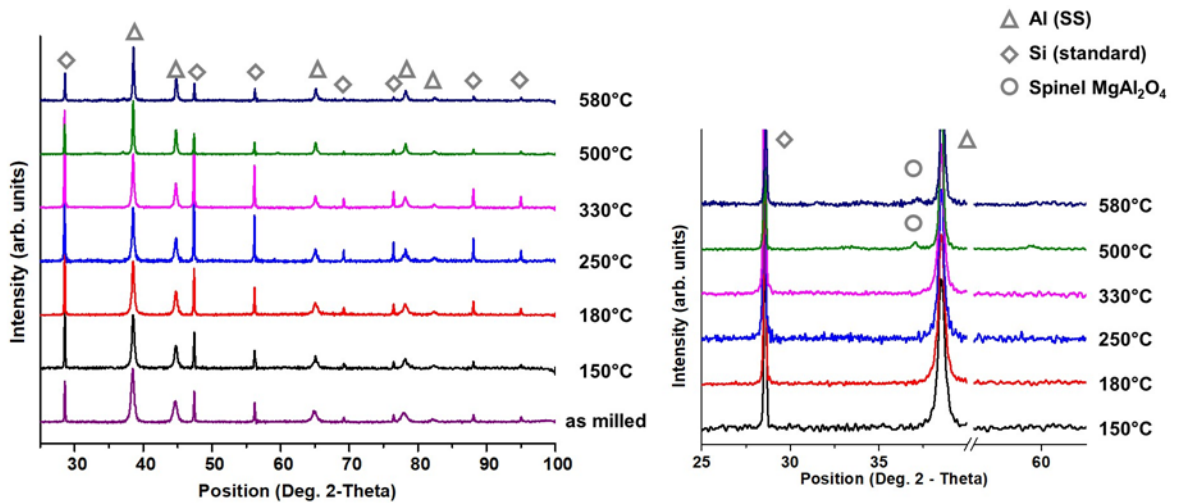


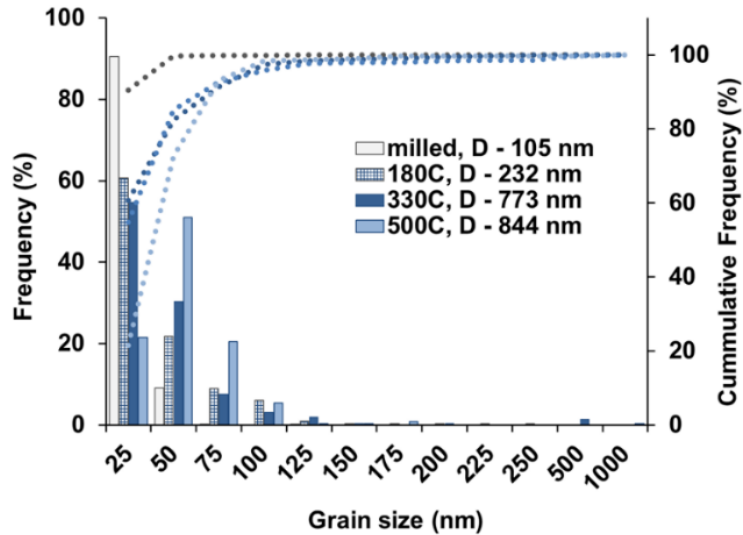
Figure 5.7 XRD patterns of the annealed 0.1 Er powders with major phases labelled; 25 to 60 Deg. 2-Theta inset shows minor crystalline oxide peaks.

Table 5.4 XRD results and TEM grain size for the 0.1 Er annealed powders

Powder sample	Lattice parameter (Å)	Mg in matrix (at.%)	Grain size, XRD (nm)	Micro strain (%)	R <sup>2</sup>	Grain size, TEM (nm)	Number of grains, N
Milled	4.0662 ± 0.0015	5.26	22	0.094	0.92	16 ± 1	592
150 °C	4.0575 ± 0.0004	3.05	24	0.041	0.97	23 ± 1	325
180 °C	4.0537 ± 0.0007	2.08	26	0.09	0.97	32 ± 3	313
250 °C	4.0549 ± 0.0002	2.39	32	0.076	0.99	32 ± 3	318
330 °C	4.0552 ± 0.0002	2.46	34	0.052	0.95	37 ± 4	665
500 °C	4.0538 ± 0.0004	2.11	50	0.087	0.86	45 ± 5	390

### 5.5.2. TEM results of 0.1 Er powder

Although some changes in the grain size distribution occur at 150 °C, significant grain growth (normal and abnormal) is not observed until 180 °C. As shown in Figure 5.8, 90% of the grains remain below 100 nm at 180 °C and there is growth into the UFG regime as seen with the largest grain size of 232 nm observed. The average grain size from TEM analysis changes from 16 ± 1 nm to 23 ± 1 nm to 32 ± 3 nm for powder as milled, at 150 °C and at 180 °C respectively, which agrees well with the grain sizes obtained from XRD.



**Figure 5.8 Grain size distributions obtained from TEM image analysis for selected 0.1 Er annealed powders. D is the largest grain size observed at temperature.**

The microstructure evolution in annealed 0.1 Er powders is presented in Figure 5.9. Figure 5.9(a) and 5.9(b) shows the typical nanocrystalline regions in the powders annealed at 150 °C and 180 °C, respectively; the diffraction rings in the inset SAED patterns are characteristic of the nanocrystalline structure. Other areas in the 0.1 Er powders annealed at 180 °C exhibit a bimodal microstructure with a representative image shown in Figure 5.9(c). Similar to the microstructure of the powders annealed at 250 °C, powders annealed at 330 °C exhibit abnormal grain growth with large ultra-fine grains nestled within nanocrystalline regions; images representative of the microstructure at 330 °C are shown in Figure 5.9(d) and 5.9(e). The average grain size from TEM analysis is constant at an average of 32 nm (within standard deviation) from 250 °C to 330 °C, which agrees well with the XRD results. However, the largest observed grain diameter continues to increase from 232 nm at 250 °C up to 773 nm at 330 °C. The grain size distribution changes significantly at 500 °C when the mode size shifts to 25 – 50 nm, as seen in Figure 5.8. From TEM image analysis, the average grain size increases from  $37 \pm 4$  nm at 330 °C to  $45 \pm 5$  nm at 500 °C, with the maximum grain size growing closer to 1  $\mu$ m (Figure 5.9(g)).

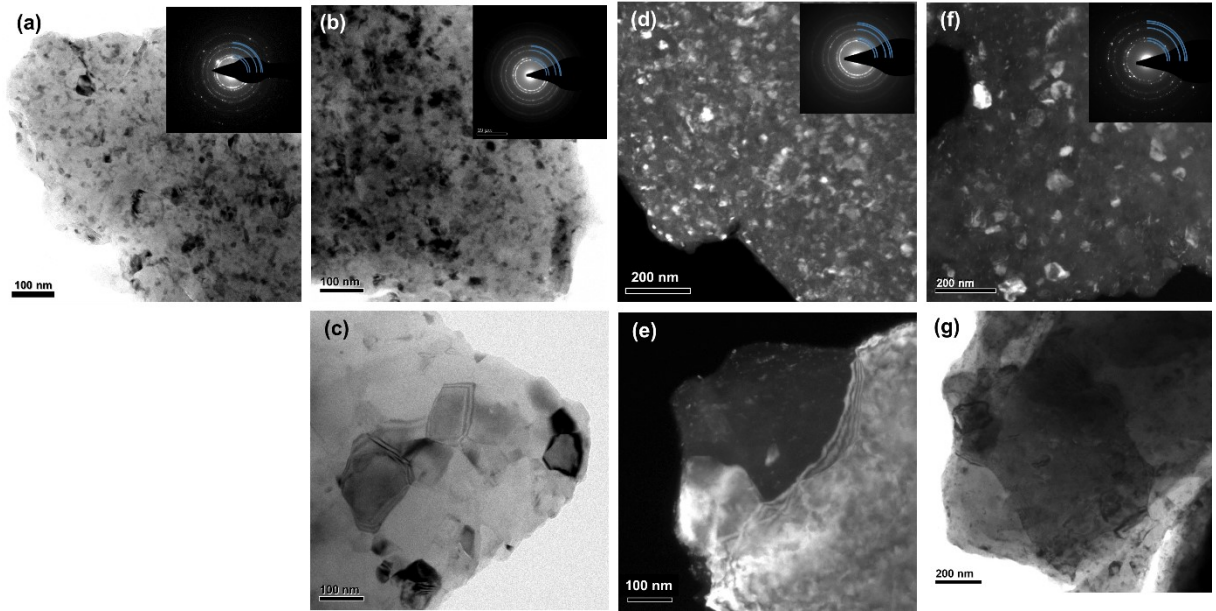


Figure 5.9 TEM images of 0.1 Er powder annealed at 150 °C (a), 180 °C (b,c), 330 °C (d,e) and 500 °C (f,g); top row – nanocrystalline regions; bottom row - abnormal grain growth. Nanocrystalline  $\alpha$ -Al phase is indexed with the blue arcs.

SAED patterns from the larger grained areas shown in Figure 5.9 are presented in Figure 5.10. The diffraction patterns contain diffraction spots consistent with single crystals, and rings indicating the presence of nanoscale second phases in the regions. Evidence of second phases is only observed in areas with grain sizes larger than 100 nm. The main spot diffraction patterns are indicated by small circles, while the diffraction rings are indicated by the arrows in the figure. The spot diffraction patterns correspond to Al crystals imaged from the  $[\bar{1}03]$  direction (Figure 5.10(a)), the  $[112]$  direction (Figure 5.10(b)), and the  $[121]$  direction (Figure 5.10(c)). Second phases observed in some of the large grains in powders annealed at 330 °C are shown in Figure 5.10(d). The lattice spacing corresponding to the diffraction rings from the SAED patterns in Figure 5.10 are calculated as  $d \approx 2.09 \text{ \AA}$  and  $d \approx 1.49 \text{ \AA}$ .

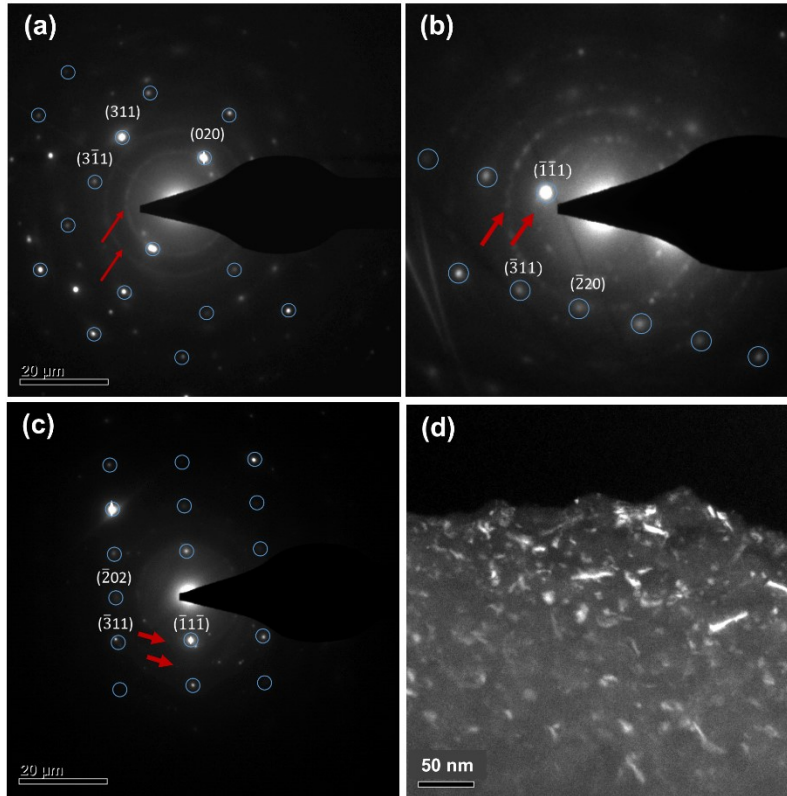


Figure 5.10 Indexed SAED patterns from the large grained regions shown in the previous figure: Al grains viewed from (a)  $B = [\bar{1}03]$  direction at 180 °C, (b)  $B = [112]$  direction at 330 °C, and (c)  $B = [121]$  direction at 500 °C; (d) second phase particles observed in powders annealed at 330 °C. The small circles indicate the spot diffraction pattern and rings (indicated by arrows) are produced by nanoscale phases in the imaged regions.

Although nanoscale  $\text{Al}_3\text{Sc}$  precipitates were observed in a milled Al-Mg-Sc powder after annealing at 200 °C [5.5] and studies on the precipitation behavior of  $\text{Al}_3\text{Sc}$  indicate Mg addition may accelerate the formation of these precipitates [5.26], the SAED patterns of Figure 5.10 do not exhibit  $L_{12}$  superlattice reflections. Also DSC and TEM studies on precipitation in coarse grained Al-16Mg alloys by Starink and Zahra [5.27, 5.28] identified temperatures 180 °C – 290 °C as the temperature range for  $\beta'$  precipitation. And the study by Straumal *et al.* [5.23] showed that a small fraction of nanoscale  $\beta$  precipitates formed in room temperature HPT formed nanograined Al-5Mg and Al-10Mg alloys. However, the diffraction rings observed would correspond to peaks of lower intensity, while the highest intensity ring (i.e.:  $d = 2.395 \text{ \AA}$ ) is absent.

The lattice measurements of Figure 5.10 can be indexed to the 200 ( $d = 2.11 \text{ \AA}$ ) and 220 ( $d = 1.492 \text{ \AA}$ ) planes of the MgO phase. In previous studies, Mg(O,N) dispersoids have been observed in an UFG Al-Mg-Sc alloy produced by milling and ECAP consolidation [5.29]. Results of STEM analysis of the milled powders annealed at 330 °C also indicates the presence of some Al-Mg-O ( $\sim 30 - 40 \text{ nm}$ ) phases as shown in Figure 5.11. These results suggest that the nanoscale particles observed after annealing at 180 °C, 330 °C and 500 °C are likely nanoscale MgO particles. Al-Fe phases ( $\sim 80 \text{ nm}$ ) phases were also observed in the powders, also shown in Figure 5.12. The Al-Fe precipitates observed in the powders could correspond to the  $\text{Al}_6\text{Fe}$  phase. Nanoscale precipitates of the metastable  $\text{Al}_6\text{Fe}$  phase were observed after one hour of annealing at 330 °C, and both  $\text{Al}_6\text{Fe}$  and the equilibrium phase  $\text{Al}_{13}\text{Fe}_4$  after annealing at 500 °C in a milled  $\text{Al}_{93}\text{Fe}_3\text{Cr}_2\text{Ti}_2$  alloy [5.30]. At 370 °C, the  $\text{Al}_6\text{Fe}$  particles were 15 – 30 nm in size, increasing to 15 – 50 nm after annealing at 450 °C.

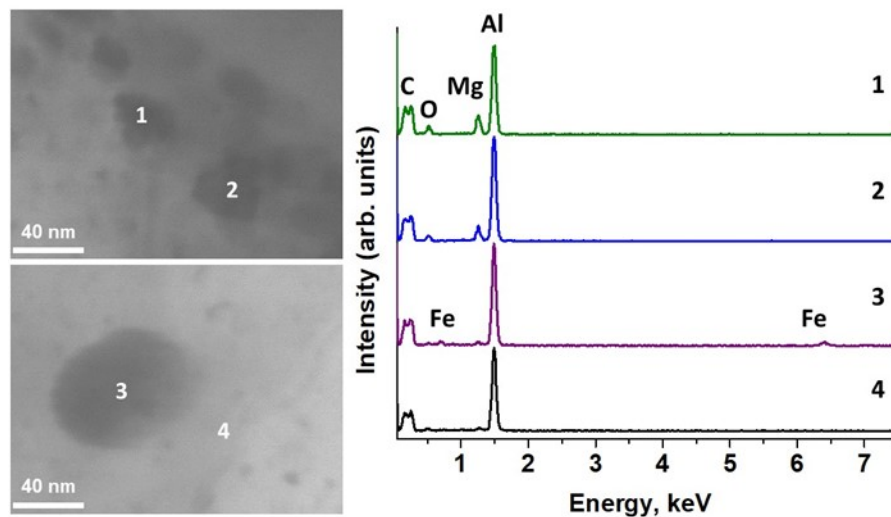


Figure 5.11 STEM-EDS analysis of some nanoscale phases observed in the powders annealed at 330 °C.

## 5.6. Annealing behavior of 0.5 Er powder

### 5.6.1. XRD results of 0.5 Er powder

Normalized XRD patterns of the as milled and annealed 0.5 Er powders are presented in Figure 5.12. The lattice parameter, estimated Mg in solid solution, grain size and

micro strain calculated from the XRD patterns are summarized in Table 5.5; average grain sizes from TEM image analysis are also included in the table. Grain size distributions after anneals at selected temperatures are shown in Figure 5.13; the largest grain size observed at each temperature is also given in the figure. The major phase in the powders, marked in Figure 5.12, corresponds to the  $\alpha$ -Al phase. Reflections from the  $\text{MgAl}_2\text{O}_4$  spinel phase are identified at 500 °C and 580 °C.

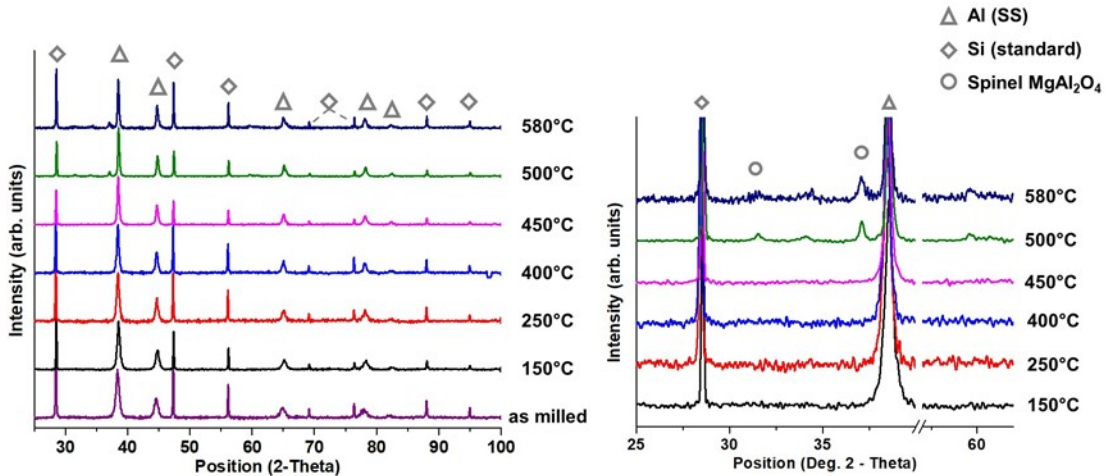


**Figure 5.12 XRD patterns of the annealed 0.5 Er powders with major phases labelled; 25 to 60 Deg. 2-Theta inset showing minor crystalline oxide peaks**

General sharpening of the  $\alpha$ -Al peaks from the as milled state with increasing temperature is indicative of (1) reducing micro strain in the powders and (2) grain growth. Shifts in the peak positions are observed indicating changes in the Mg solubility. The milling process created a supersaturated solid solution of Mg in the matrix of 4.87 at.%. With increasing temperature, there is decomposition of the solid solution and reducing Mg in the matrix. At 150 °C the Mg in the matrix is estimated to reduce to 2.72 at.%, approximately the equilibrium solubility of  $\sim 2.5$  at.% Mg [5.12]. With further annealing at higher temperatures the Mg content in the matrix approaches  $\sim 2$  at.%. From the as milled state till annealing at 450 °C, the average grain size remains below 30 nm in the 0.5 Er powder. However, a grain size of 41 nm is obtained at 500 °C, similar to the findings in the 0.1 Er powder at high temperature.

The micro strain decreases in the 0.5 Er powder after annealing, from 0.106% in the as milled state to 0.066% after annealing at 150 °C. The micro strain is ~ 0.06% until annealing at 450 °C when it increases. A micro strain of 0.089% is obtained at 450 °C, before reducing to 0.078% at 500 °C. As can be observed in Table 5.5, the micro strain in the powder increases as the Mg content in the matrix increases with temperature. The Mg content in the matrix increases with the solid solubility limit of the Al-Mg system, which increases from ~ 1 at.% at room temperature to 18.9 at.% at 450 °C. Due to the larger size of Mg atoms compared to Al atoms, it is possible that the increased amount and inhomogeneous distribution of Mg could also contribute to the changes observed in the micro strain.

**Table 5.5 XRD results and TEM grain size for the 0.5 Er annealed powders**

<b>Powder sample</b>	<b>Lattice parameter (Å)</b>	<b>Mg in matrix (at.%)</b>	<b>Grain size, XRD (nm)</b>	<b>Micro strain (%)</b>	<b>R<sup>2</sup></b>	<b>Grain size, TEM (nm)</b>	<b>Number of grains, N</b>
Milled	4.0647 ± 0.0004	4.87	19	0.106	0.93	17 ± 0	657
150 °C	4.0562 ± 0.0025	2.72	21	0.066	0.89	22 ± 1	468
250 °C	4.0519 ± 0.0004	1.62	23	0.054	0.94	18 ± 1	372
400 °C	4.0530 ± 0.0006	1.90	27	0.06	0.97	18 ± 1	328
450 °C	4.0544 ± 0.0006	2.26	35	0.089	0.93	32 ± 2	301
500 °C	4.0537 ± 0.0005	2.08	41	0.078	0.85	54 ± 4	300

### 5.6.2. TEM results of 0.5 Er powder

XRD analysis of the 0.5 Er powder indicated an increase in the average grain size after the first DSC event from 19 nm in the as milled powder to 23 nm at 250 °C. However, TEM image analysis reveals that grain size distributions at 150 °C and 250 °C are identical to the as milled condition, with more than 95% of the grains remaining below 100 nm as shown in Figures 5.13 and 5.14; the average grain size remains at  $18 \pm 1$  nm average. SAED patterns taken from the nanostructure indicate only the  $\alpha$ -Al phase. Extra reflections from nanoscale second phase precipitates are not observed in the diffraction patterns.

TEM image analysis indicates the grain size distribution remains constant and the average is  $18 \pm 1$  nm up to 400 °C, with onset of appreciable growth (normal and abnormal) at 450 °C. The average grain size roughly doubles to  $32 \pm 2$  nm and the maximum grain size at 450 °C is 280 nm. As seen in Figure 5.13, the mode grain size changes at 500 °C, with grain growth in the ultra-fine regime. TEM images of powders annealed at 400 °C, 450 °C and 500 °C are presented in Figure 5.15. The nanocrystallinity at 400 °C can be seen in Figure 5.15(a), while the onset of abnormal grain growth at 450 °C is shown in Figure 5.15(b), the increase in grain size at 500 °C is shown in Figure 5.15(c) with the accompanying SAED pattern shown in Figure 5.15(d). SAED patterns taken at 500 °C indicate the presence of the  $\alpha$ -Al (blue arcs) and  $\text{MgAl}_2\text{O}_4$  spinel phases.

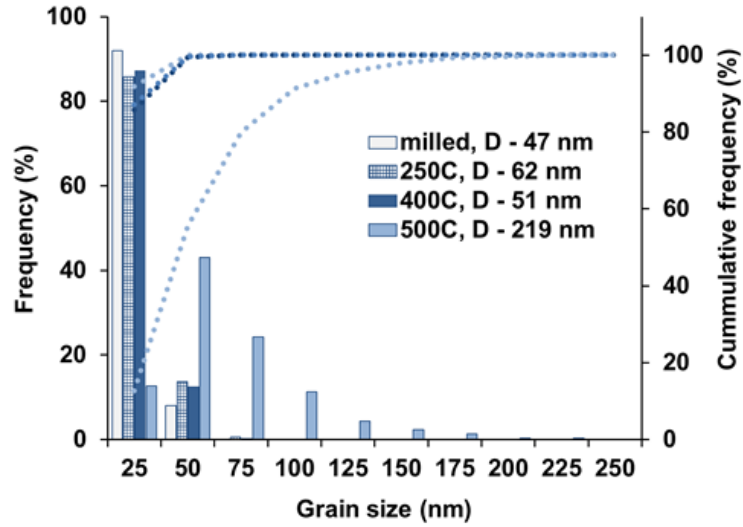


Figure 5.13 Grain size distribution obtained from TEM image analysis for selected 0.5 Er annealed powders. D is the largest grain size observed at temperature.

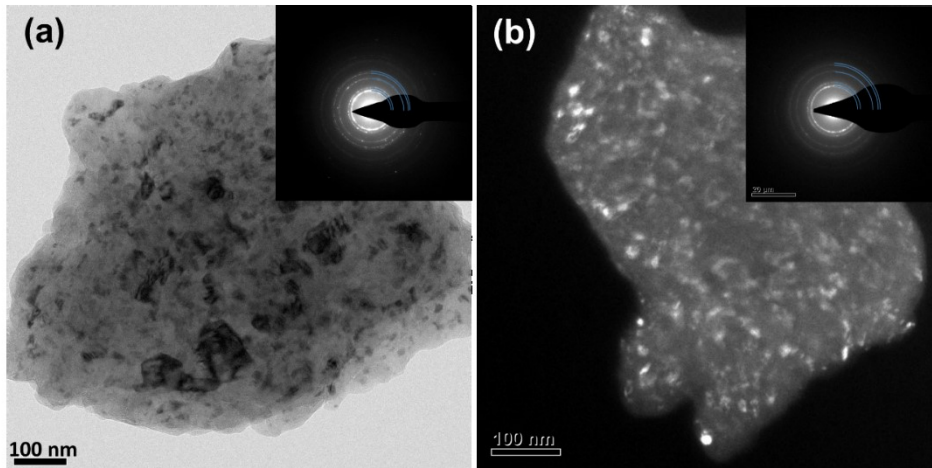


Figure 5.14 Nanocrystalline grains after annealing of 0.5 Er powders at 150 °C (a) and 250 °C (b). Nanocrystalline  $\alpha$ -Al phase is indexed with blue arcs

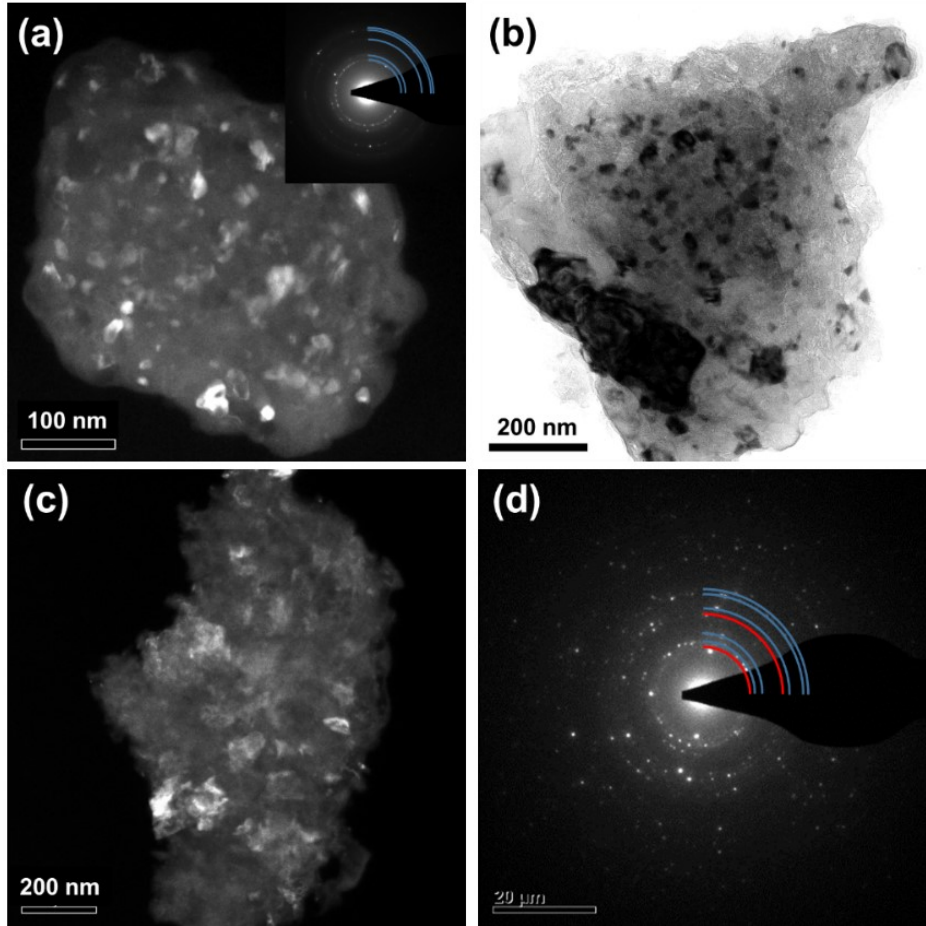


Figure 5.15 TEM images of the 0.5Er powders after various anneals: nanocrystalline regions after annealing at 400 °C (a); the onset of abnormal grain growth at 450 °C (b); grain growth at 500 °C (c) with corresponding diffraction pattern (d). Nanocrystalline  $\alpha$ -Al and  $MgAl_2O_4$  are indicated by the blue and red arcs, respectively

### 5.7. Grain size stability

In cryomilled powders, there are two defined grain growth regimes, with the transition temperature  $T_c$  observed at  $\sim 0.78T_m$  [5.1]. Below  $T_c$  the average grain size is fairly stable, but with increasing temperature the grain growth becomes more pronounced.  $T_c$  can be affected by many factors including solute impurities and highly stable nanoscale nitrides and oxides that are introduced into the powder during the milling process and are said to inhibit the mobility of the grain boundaries and prevent grain growth [5.1-5.5]. Previous studies on cryomilled Al systems and specifically Al-Mg and Al-Mg-Sc systems

have shown these trends [5.1-5.5]. The Al-Mg-Er powder systems here show similar behavior. The 0.5 Er powder maintains the as-milled grain size up till  $0.8T_m$  ( $\approx 400$  °C), at which grain sizes are similar to those observed in the 0.1 Er composition and literature values for milled Al and Al-Mg powders.

### 5.7.1. Activation energy for grain growth

In milled Al-Mg systems two sets of activation energies  $Q$  are typically reported – a lower  $Q$  for low temperature growth, and at higher temperatures  $Q$  values closer to that of self or impurity diffusion in Al. In Telkamp *et al.*'s study of a milled Al 5083 alloy powder,  $Q \approx 5.6$  kJ·mol<sup>-1</sup> was reported for the low temperature regime ( $T < 654$  K), while  $Q \approx 142$  kJ·mol<sup>-1</sup> was reported for the higher temperature regime ( $T > 654$  K) [5.4]. Another study on a bulk UFG Al 5083 alloy reported  $Q = 25 \pm 5$  kJ·mol<sup>-1</sup> for the low temperature regime, while  $Q = 124 \pm 5$  kJ·mol<sup>-1</sup> was found for higher temperatures ( $T > 573$  K) [5.31]. Roy *et al.* [5.31] suggest that the low activation energy at low temperatures is indicative of highly unstable and non-equilibrium grain boundaries. Unstable grain boundaries could require smaller driving force for rearrangement of the grains and grain boundaries, while non-equilibrium boundaries may possess greater atomic mobility due to excess dislocations [5.31].

In order to determine the activation energy for the peak event A, linear DSC scans are run at multiple heating rates from 5 K·min<sup>-1</sup> to 40 K·min<sup>-1</sup> under a flowing nitrogen atmosphere. The activation energy was determined using the KAS (Kissinger-Akahira-Sunose) method as described in [5.32] and shown below in Eq. 5.2.

$$\ln\left(\frac{\beta}{T_f^\kappa}\right) = -\frac{E_a}{RT_f} + C \quad (5.2)$$

Where  $\beta$  is the heating rate used,  $T_f$  is the peak temperature of the event,  $E_a$  is the associated activation energy,  $R$  is the gas constant,  $C$  is a constant, and  $\kappa$  is a constant which is set to 1.95. The activation energies were determined as  $Q_{0.1Er} = 18$  kJ·mol<sup>-1</sup> and  $Q_{0.5Er} = 17.7$  kJ·mol<sup>-1</sup>. The activation energies obtained here ( $\approx 20$  kJ·mol<sup>-1</sup>) are

comparable with those found for the low temperature kinetic regime ( $T < 600$  K) and lie between the energies obtained for milled Al 5083 powder and bulk UFG Al 5083. The activation energy of  $5.6 \text{ kJ}\cdot\text{mol}^{-1}$  was determined for milled Al 5083 powder where there is no strain relaxation. Similarly, to the findings of Roy *et al.* [5.31], the increase in activation energy of the Al-Mg-Er powders compared to the milled Al 5083 powder could be attributed to some strain relaxations taking place with increased temperature. Annealing at  $150 \text{ }^\circ\text{C}$  resulted in limited grain growth in both powders (Figures 5.9 and 5.14) and reduced micro strain from the as-milled state (i.e.:  $0.041\%$  in  $0.1 \text{ Er}$  and  $0.066\%$  in  $0.5 \text{ Er}$ ). The microstructure and reduced micro strain, in addition to the low activation energies obtained suggests a stress relaxation takes place in the low temperature regime ( $\sim 150 \text{ }^\circ\text{C}$ ); that results in reduced strain in the material and reordered grain boundaries.

### 5.7.2. Er effect on grain growth

Er addition to the Al-Mg system could potentially contribute to grain size control via either kinetic or thermodynamic means. In the work done by Murdoch and Schuh [5.33], their model generated moderate grain boundary segregation enthalpies for both Mg and La solutes ( $0 - 25 \text{ kJ}\cdot\text{mol}^{-1}$ ) in a binary Al-based system, suggesting they could be effective as grain boundary stabilizers for a nanocrystalline Al matrix. If Er atoms have similar potential as La atoms in Al, considering the atomic size mismatch and the low solubility in the Al matrix of both lanthanide elements, then Er content could reduce the grain boundary energy and therefore reduce the driving force for grain growth. According to Darling *et al.* [5.34], true thermodynamic stabilization is defined by the reduction of grain boundary energy to zero. Based on this definition, the stability of binary systems based on various solute and solvent combinations were evaluated. According to their evaluations (for global concentrations less than  $10 \text{ at.}\%$ ), for the stabilization of a grain structure with  $25 \text{ nm}$  grains at  $0.6T_m$  ( $396 \text{ }^\circ\text{C}$ ) in binary Al based systems, Er is not a candidate for thermodynamic stabilization. Although the material systems studied here are more complex, consideration of the results of Darling *et al.*

[5.34] and the Er content in the milled powders (< 0.1 at.%) suggest that Er does not contribute to a thermodynamic stability of the grain boundaries.

Considering kinetic effects on the grain growth, Er can contribute via either solute drag or second phase pinning of grain boundaries by nanoscale Al<sub>3</sub>Er phases. Both homogeneous and heterogeneous precipitation of Al<sub>3</sub>Sc nanoscale phases were observed in cryomilled Al-7.5Mg-0.3Sc after annealing at 400 °C for one hour, with precipitates approximately 5 nm in size observed within grains or along grain boundaries [5.5]. Compared to precipitation in Al-Sc alloys, the Al<sub>3</sub>RE (Er, Yb) phase have been observed to have the tendency to nucleate heterogeneously due to the small chemical driving force for precipitation and to possess higher coarsening rates due to the higher diffusivities of RE atoms in Al and the larger  $\alpha$ -Al/Al<sub>3</sub>RE interfacial energy [5.35]. Therefore, decomposition of the solid solution in this Al-Mg-Er nanocrystalline system should produce coarser precipitates of the Al<sub>3</sub>Er phase. However, the absence of L<sub>12</sub> phase reflections in the SAED patterns of the powders suggests the Er may remain in solute form in the powders and therefore contribute to the solute/impurity drag alongside with Mg and other impurity atoms.

### 5.7.3. Oxide contributions to grain size control

Due to the significant oxide content in the milled Al-Mg-Er powders, and their likely presence as nanoscale disperoids, grain growth can be affected by second phase pinning forces (i.e.:  $P_{Zener} = \frac{3f\gamma}{2r}$ ) [5.36]. Dispersoids formed in cryomilled ODS Al powders during milling were reported as being aluminum oxy-nitride particles 2 – 10 nm in size [5.37], and platelets of aluminum-nitrogen and aluminum-oxygen content a few atomic layers thick and 10 – 15 nm in two-dimensions [5.38]. If the volume fraction of the oxide is calculated by assuming that all of the oxygen atoms are present as oxide, and taking the average oxide/oxy-nitride particle to be 5 nm in size, it is possible to estimate the Zener limit grain size due to second phase pinning forces. Table 5.5 shows the reported oxygen content, calculated volume fraction of oxide and the Zener limit

grain size ( $D_{Zener} = \frac{4r}{3f}$ ) for the 0.1 Er, 0.5 Er and milled Al alloys. Up to 13 vol.% and 20 vol.% of nanoscale oxide particles could be present in the 0.1 Er and 0.5 Er powders, respectively, compared to the 2 vol.% in typical milled Al powders.

The Zener limit grain size  $D_{Zener}$  for both Al-Mg-Er milled powders match well with the grain sizes observed after 1 h anneals below 450 °C; this strongly supports the possibility of grain pinning by ultrafine oxide particles. However, grain growth in milled Al-7.6 at.% Mg powder and 0.1 Er powder are almost identical despite there being a difference in oxygen content by more than a factor of 10 between both powders. Oxygen content in the Al-7.6 at.% Mg was reported as ~0.3 wt.% [5.3], while the 0.1 Er powder here contains 8 wt.% oxygen. From 100 °C to 300 °C, the grain size changes from 26 to 40 nm after 1 h anneals in Al-7.6 at.% Mg [5.3], almost identical to the grain size observed in the 0.1 Er powders changing from 23 nm at 150 °C to 37 nm at 330 °C. Thus, the grain size stability is not controlled by second phase pinning alone, but likely from a combination of solute/impurity drag and second phase pinning forces. However, for the 0.5 Er powder, maintenance of the as-milled grain size up to  $T_c$  is likely due to the increased oxide content, with grain growth at higher temperatures controlled by a combined solute and second phase drag.

**Table 5.6 Volume fraction of nanoscale oxides and Zener limit grain size**

Composition	Oxygen content (wt.%)	Oxide volume fraction, F	Grain size, $D_{Zener}$ (nm)	Grain size below $T_c$ (nm)
Milled Al alloys [5.39]	0.3 – 1.5	0.4 – 2.2	150	40
0.1 Er	8.4	12.7	26	37
0.5 Er	13	20.4	16	18

## 5.8. Possible Er contributions to oxidation behaviour

As observed in literature, extended milling time increases the potential for contamination in the milled powders. The study by Goujon *et al.* [5.13] on 5000 Al/AlN powders showed that oxygen and nitrogen contamination both increase with long milling times in liquid nitrogen. Up to 10 wt.% oxygen was present in mechanically alloyed 5000 Al/AlN powders after 25 hours of milling, while Nitrogen concentration increased by ~ 2 wt.% after 26 hours of milling [5.13]. The increased oxygen content in the Al-Mg-Er powders has been attributed to pick up in situ and after the cryomilling process. It is likely that similar levels of Nitrogen contamination observed in literature (i.e.: ~ 2 wt.%) are also present within the powder samples studied here.

In addition to the extended milling time, the powder composition may also have played a role in the oxygen content observed after milling. Atomized Al 5083 powder milled in the Union Process HD-01 Lab Attritor had an oxygen concentration of 3.7 wt.% after 8 hours (as measured by IGA analysis provided by SGS Canada Inc.). The oxygen content doubles to 8.4 wt.% in the 0.1 Er powders after 30 h of milling, similar to the oxygen levels observed by Goujon *et al.* [5.13] in 5000 Al/AlN. However, the oxygen content approximately quadruples to 13.0 wt.% in the 0.5 Er powder after 30 hours of milling. These results suggest that the increase in oxide contamination during the process could be related to the increased Er content of the powders. Er has a high affinity for oxygen, with Er oxides having lower free energy of formation (per mole of oxygen) than Mg oxides [5.40]. Studies have also shown that Er can increase the oxide scale thickness on Al based alloys. Oxidation studies at 600 °C showed that ~100 nm thick film develops after 65 minutes, compared to the ~35 nm Al<sub>2</sub>O<sub>3</sub> oxide film on pure Al [5.41]. Therefore, it is possible that the Er content enhanced the oxygen contamination during milling.

The presence of Er could also influence the structure of the oxides formed in Al-Mg-Er powders, and subsequent phase transformations. In a study on the structural effects of lanthanide (Ln) doping of alumina, five possible locations were determined for the Lanthanide dopants to be present:

- (1) Within the alumina lattice, substituting some Al cations
- (2) Creating  $\text{LnAlO}_3$  or  $\text{Ln}_2\text{O}_3$  phases
- (3) Forming a  $\text{LnAlO}_3$  or  $\text{Ln}_2\text{O}_3$  shell around the alumina core particle
- (4) Occupying vacant tetrahedral or octahedral sites of the alumina lattice, or
- (5) Located at the grain boundaries of the alumina lattice

In the same study, it was observed that the addition of Ln elements influenced the phase transformations in  $\text{Al}_2\text{O}_3$  [5.42]. Dilute doping of  $\text{Al}_2\text{O}_3$  with Ln elements (400 ppm) affected the structural phase transformations of  $\text{Al}_2\text{O}_3$  from  $\theta \rightarrow \alpha$  phases [5.42]. With Er-dopants specifically (400 ppm, 0.033wt%), the transformation temperature increased to 1325 °C from 1280 °C in pure  $\text{Al}_2\text{O}_3$  [5.42]. It was proposed that the dopants changed the basic structure of the host lattice such that structural rearrangements for the phase transformations of  $\theta\text{-Al}_2\text{O}_3$  to  $\alpha\text{-Al}_2\text{O}_3$  required more thermal energy, leading to a phase transformation temperature increase [5.42]. It was proposed that the Ln dopants occupy the vacant octahedral sites in the  $\text{Al}_2\text{O}_3$  lattice, as the small dimensions of the tetrahedral sites can not accommodate the large  $\text{Ln}^{3+}$  dopants [5.42].

It is possible that, similar to these findings in literature, Er changes the structure of the oxides in the 0.5 Er powders and affects subsequent crystallization and spinel formation. In Figure 5.6, the DSC trace exhibited an oxidation peak at 475 °C in the 0.1 Er powder, which was not observed with the 0.5 Er powders. But both powder compositions exhibit oxide (spinel) peaks in the XRD analysis of anneals at 500 °C and higher, suggesting the oxidation event is delayed in the 0.5 Er powders. This behaviour is observed again during the TSS-SPS processes, with the absence of spinel phases/XRD peaks during sintering with the 500 TSS 20 process (i.e.: 500 °C for 1 minute), but prolific presence of crystalline spinel phases after sintering with the 550 TSS 20 process (i.e.: 550 °C for 30 seconds) in the 0.5 Er samples. It may be that the oxide particles in the milled 0.5 Er powders possess some Er content, which may cause a delay in the crystalline spinel formation.

Oxide particles may also contribute to some strength increase in the Al-Mg-Er powders. UFG Al-Mg-Sc alloys, produced by cryomilling and consolidation by HIP

followed by extrusion or dual mode dynamic forging, contained large  $\text{Al}_3\text{Sc}$  precipitates ( $\sim 154$  nm) as well as nanoscale Mg-O/N dispersions ( $\sim 4$  nm) [5.43]. The Mg-O/N dispersion strengthening and Hall-Petch mechanisms were reported as the main strengthening contributions for these Al-Mg-Sc alloys [5.43]. Similarly, the oxide particles and nanocrystalline grain sizes will contribute to the hardness of the Al-Mg-Er powders and the final strength of the sintered Al-Mg-Er materials.

## 5.9. Summary

Atomized Al-Mg-Er powders, 0.1 Er and 0.5 Er, were cryogenically milled for 30 hours in liquid nitrogen. A super-saturated  $\alpha$ -Al solid solution phase was obtained in both powders. Due to prolonged milling time a substantial amount of oxygen contamination was observed in the final milled powders with 8.4 wt.% and 13 wt.% oxygen detected in the 0.1 Er and 0.5 Er powders, respectively. The thermal stability of the microstructure was investigated by DSC; isothermal annealing at selected temperatures was followed by XRD and TEM analyses. The DSC traces exhibited a recovery event at  $\sim 160$  °C. An activation energy of  $\sim 20$   $\text{kJ}\cdot\text{mol}^{-1}$  was determined for the recovery event in both powders by the KAS method using heating rates of 5 – 40  $\text{K}\cdot\text{min}^{-1}$ . This is similar to activation energies reported for the low temperature regime in milled Al 5083 material and attributed to the presence of highly unstable and non-equilibrium grain boundaries.

Overall thermal stability in the Al-Mg-Er powders was attributed to the combined effects of solute/impurity drag and second phase pinning (nanoscale oxides, nitrides, oxy-nitrides) that impede grain boundary motion. The 0.1 Er powder exhibited grain growth behavior similar to other milled Al-Mg powders reported in literature, with abnormal grain growth observed after annealing at 180 °C. The 0.5 Er powder showed improved thermal stability at low temperatures with as milled grain size of  $\sim 20$  nm maintained till 400 °C ( $0.8T_m$ ). Controlled grain growth at higher temperatures resulted in an average grain size of 55 nm and a maximum observed grain size of  $\sim 200$  nm after one hour of annealing at 500 °C.

Second phase particles of Al-Mg-O (~ 40 nm) and Al-Fe (~ 80 nm) were observed in the annealed 0.1 Er powders by STEM analysis. SAED patterns from powders annealed at 180 °C, 330 °C, and 500 °C could be indexed to nanocrystalline MgO phases. Crystalline spinel phases were detected by XRD in powders annealed at temperatures of 500 °C and higher. Detection of Nitrogen-containing particles was not possible due to limitations of the equipment used, however, it is highly likely that nanoscale dispersoids of oxynitrides are also present in the milled powders. Evidence of nanoscale  $L1_2$   $Al_3Er$  precipitation, from x-ray or electron diffraction techniques, was not found in either powder composition.

## 5.10. References

- 5.1. Zhou F, Lee J, Lavernia EJ (2001) Grain growth kinetics of a mechanically milled nanocrystalline Al, *Scripta Materialia* 44:2013-2017.
- 5.2. Zhou F, Lee J, Dallek S, Lavernia EJ (2001) High grain size stability of nanocrystalline Al prepared by mechanical attrition, *Journal of Materials Research* 16:3451-3458.
- 5.3. Zhou F, Liao XZ, Zhu YT *et al.* (2003) Microstructural evolution during recovery and recrystallization of a nanocrystalline Al-Mg alloy prepared by cryogenic ball milling, *Acta Materialia* 51:2777-2791.
- 5.4. Tellkamp VL, Dallek S, Cheng D, Lavernia EJ (2001) Grain growth behavior of a nanostructured 5083 Al-Mg alloy, *Journal of Materials Research* 16:938-944.
- 5.5. Zhou F, Lee Z, Lavernia EJ, Nutt, SR (2005) The influence of Sc on thermal stability of nanocrystalline Al-Mg alloy processed by cryogenic ball milling, *Metallurgical Materials Transactions A* 36:1587-1594.
- 5.6. Chemicool Periodic Table. 1/31/2017. <http://www.chemicool.com/>.

- 5.7. Xu G, Mou S, Yang J *et al.* (2006) Effect of trace rare earth element Er on Al-Zn-Mg alloy, Transactions of Nonferrous Metals Society of China 16:598-603.
- 5.8. Wen SP, Xing ZB, Huang H, Li BL (2009) The effect of erbium on the microstructure and mechanical properties of Al-Mg-Mn-Zr alloy, Materials Science and Engineering A 516:42-49.
- 5.9. Meng G, Li B, Li H, Huang H, Nie Z (2009) Hot deformation behavior of an Al-5.7 wt.%Mg alloy with erbium, Materials Science and Engineering A 516:131-137.
- 5.10. Lin S, Nie Z, Huang H, Li B (2010) Annealing behaviour of a modified 5083 aluminum alloy, Materials and Design 31:1607-1612.
- 5.11. Zhang J, Zhao JJ, Zuo RL (2015) Microstructure and mechanical properties of micro-alloying modified Al-Mg alloys, International Conference on Power Electronics and Energy Engineering (PEEE 2015):153-156.
- 5.12. Okamoto H (1998) Al-Mg (Aluminum-Magnesium), Journal of Phase Equilibrium 19:598.
- 5.13. Goujon C, Goeuriot P, Delcroix P, Le Caër G (2001) Mechanical alloying during cryomilling of a 5000 Al alloy/AlN powder: the effect of contamination, Journal of Alloys and Compounds 315:276-283.
- 5.14. Scudino S, Sakaliyska M, Surreddi KB, Eckert J (2009) Mechanical alloying and milling of Al-Mg alloys, Journal of Alloys and Compounds 483:2-7.
- 5.15. Zhou F, Witkin D, Nutt SR, Lavernia EJ (2004) Formation of nanostructure in Al produced by a low-energy ball milling at cryogenic temperature, Materials Science and Engineering A 375-377:917-921.
- 5.16. Zhou F, Nutt SR, Bampton CC, Lavernia EJ (2003) Nanostructure in an Al-Mg-Sc alloy processed by low-energy ball milling at cryogenic temperature, Metallurgical and Materials Transactions A 34:1985-1992.

- 5.17. Seah MP in: Briggs D, Seah MP (Eds.): Practical Surface Analysis, 2nd edn., vol. 1, Wiley, Chichester. 1990, p. 201-255.
- 5.18. Jeurgens LPH, Sloof WG, Tichelaar FD *et al.* (1999) Determination of thickness and composition of aluminum-oxide overlayers on aluminum substrates. Applied Surface Science 144-145:11-15.
- 5.19. Alexander MR, Thompson GE, Zhou X *et al.* (2002) Quantification of oxide film thickness at the surface of aluminum using XPS. Surface and Interface Analysis 34:485-489
- 5.20. Schoenitz M, Dreizin E (2004) Oxidation processes and phase changes in metastable Al-Mg alloys, Journal of Propulsion and Power 20:1064-1068.
- 5.21. Field DJ, Scamans GM, Butler EP (1987) The high temperature oxidation of Al-4.2 wt pct Mg alloy. Metallurgical Transactions A 18:463-472
- 5.22. Chen PC, Shih TS, Wu CY (2009) Thermally formed oxides on Al-2 and 3.5 mass % Mg alloys heated and held in different gases, Materials Transactions 50:2366-2372.
- 5.23. Straumal BB, Baretzky B, Mazilkin AA *et al.* (2004) Formation of nanograined structure and decomposition of supersaturated solid solution during high pressure torsion of Al-Zn and Al-Mg alloys, Acta Materialia 52:4469-4478.
- 5.24. Sauvage X, Enikeev N, Valiev R *et al.* (2014) Atomic-scale analysis of the segregation and precipitation mechanisms in a severely deformed Al-Mg alloy, Acta Materialia 72:125-136.
- 5.25. Rane GK, Apel D, Welzel U, Mittemeijer EJ (2013) The microstructural evolution and thermal stability of nanocrystalline ball-milled Ni-15at.%W powder, Journal of Materials Research 28:873-886.
- 5.26. Marquis EA, Seidman DN (2004) Nanostructural evolution of Al<sub>3</sub>Sc precipitates in an Al-Mg-Sc alloy by three-dimensional atom probe microscopy, Surface and Interface Analysis 36:559-563.

- 5.27. Starink MJ, Zahra AM (1997) Low-temperature decomposition of Al-Mg alloys: Guinier-Preston zones and L<sub>12</sub> ordered precipitates, *Philosophical Magazine A* 76:701-714.
- 5.28. Starink MJ, Zahra AM (1998)  $\beta'$  and  $\beta$  precipitation in an Al-Mg alloy studied by DSC and TEM, *Acta Materialia* 46:3381-3397.
- 5.29. Harrell TJ, Topping TD, Wen H, Hu T *et al.* (2014) Microstructure and strengthening mechanisms in an ultrafine grained Al-Mg-Sc Alloy produced by powder metallurgy. *Metallurgical and Materials Transactions A* 45:6329-6343.
- 5.30. Shaw L, Luo H, Villegas J, Miracle D (2003) Thermal stability of nanostructured Al<sub>93</sub>Fe<sub>3</sub>Cr<sub>2</sub>Ti<sub>2</sub> alloys prepared via mechanical alloying, *Acta Materialia* 51:2647-2663.
- 5.31. Roy I, Chauhan M, Lavernia EJ, Mohamed FA (2006) Thermal stability in bulk cryomilled ultrafine-grained 5083 Al alloy, *Metallurgical and Materials Transactions A* 37:721-730.
- 5.32. Starink MJ (2004) Analysis of aluminium based alloys by calorimetry: quantitative analysis of reactions and reaction kinetics, *International Materials Reviews* 49:191-226.
- 5.33. Murdoch HA, Schuh CA (2013) Estimation of grain boundary segregation enthalpy and its role in stable nanocrystalline alloy design. *Journal of Materials Research* 28: 2154-2163
- 5.34. Darling KA, Tschopp MA, VanLeeuwen BK *et al.* (2014) Mitigating grain growth in binary nanocrystalline alloys through solute selection based on thermodynamic stability maps. *Computational Materials Science* 84:255-266.
- 5.35. van Dalen ME, Karnesky RA, Cabotaje JR *et al.* (2009) Erbium and ytterbium solubilities and diffusivities in aluminum as determined by nanoscale characterization of precipitates. *Acta Materialia* 57:4081-4089.

- 5.36. Smith CS (1948) Grains, phases and interfaces: An interpretation of microstructure. Transactions of AIME. 175:15-51. (private communication from Zener C)
- 5.37. Luton MJ, Jayanth CS, Disko MM, Matras S and Vallone J (1988) Cryomilling of nano-phase dispersion strengthened aluminum, Proceedings of Materials Research Society (MRS), 132:79-86.
- 5.38. Susegg O, Hellum E, Olsen A, Luton MJ (1993) HREM study of dispersoids in cryomilled oxide dispersion strengthened materials, Philosophical Magazine A, 68:2, 367-380.
- 5.39. Witkin DB, Lavernia EJ (2006) Synthesis and mechanical behavior of nanostructured materials via cryomilling, Progress in Materials Science 51:1-60.
- 5.40 Hirota K, Okabe TH, Saito F *et al.* (1999) Electrochemical deoxidation of RE-O (RE = Gd, Tb, Dy, Er) solid solutions, Journal of Alloys and Compounds 282:101-108.
- 5.41 Akashev LA, Popov NA, Kochedykov VA, Shevchenko VG (2011) Elipsometric study of the surface oxidation of Aluminum-Heavy REM alloys, Russian Metallurgy 2011:744-747.
- 5.42 Patel K, Blair V, Douglas J, Dai Q *et al.* (2017) Structural Effects of Lanthanide Dopants on Alumina, Scientific Reports 7:39946:1-9.
- 5.43 Harrell TJ, Topping TD, Wen H, Hu T *et al.* (2014) Microstructure and Strengthening Mechanisms in an Ultrafine Grained Al-Mg-Sc Alloy Produced by Powder Metallurgy, Metallurgical and Materials Transactions A 45:6329:6343.

## Chapter 6 Consolidation of Cryomilled Al-Mg-Er Powders by Two-Stage (TSS) SPS Sintering Processes

### 6.1. Introduction

In this chapter, the investigation of the consolidation of milled Al-Mg-Er powders with TSS sintering schedules is presented. As shown in chapter 4, a two-step sintering process improved the consolidation of milled conventional Al 5356 alloy powders, with the 500 TSS 20 sintering schedule producing the best consolidation as determined from the Weibull modulus analysis. However, significant increase in oxygen content was observed in the Al-Mg-Er powders after long milling times as presented in chapter 5. The high oxygen content increases the hardness and decreases the compressibility of the powders making it difficult to obtain dense parts during sintering. Difficulties in densification can be improved by using higher sintering temperatures and pressures. Higher temperatures will soften the powder making them easier to compact, while increasing the sintering pressure will improve particle rearrangement and deformation [6.1]. Higher sintering pressure will also improve removal of the oxide layer [6.2].

Two TSS schedules, 500 TSS 20 and 550 TSS 20, are tested to obtain dense compacts of the milled Al-Mg-Er powders. The best densification was achieved using the 550 TSS 20 sintering schedule with a heating rate of  $300\text{ }^{\circ}\text{C}\cdot\text{min}^{-1}$  and maximum pressure of 60 MPa. Average densities of ~98% and ~93% were obtained in the 0.1 Er and 0.5 Er samples, respectively. Decomposition of the solid solution, second phase precipitation, as well as reduction reactions were observed after the TSS sintering of the Al-Mg-Er powders. Nanoscale oxide crystallization also occurred during sintering and was dependent on  $T_1$  in the TSS schedule.

### 6.2. Phases in sintered Al-Mg-Er compacts

#### 6.2.1. XRD results

As shown in the previous chapter, a supersaturated  $\alpha$ -Al solid solution was formed in both powders during milling with a final lattice parameter of 4.0662 Å and 4.0647 Å in

the 0.1 Er and 0.5 Er powders, respectively. It was assumed that the lattice expansion is attributed solely to Mg in the matrix. Using the work of Scudino *et al.* [6.3] on mechanically milled Al-Mg alloys as a reference for lattice expansion, the supersaturated solid solution in the milled powders was estimated at 5.26 at.% and 4.87 at.% Mg for the 0.1 Er and 0.5 Er powders, respectively. Decomposition of the supersaturated solid solution and crystalline oxide formation have been observed in the Al-Mg-Er powders after annealing at elevated temperatures. Loss of supersaturated solid solution and the precipitation of  $\beta$ -Al<sub>3</sub>Mg<sub>2</sub> and other Mg containing phases were observed during TSS sintering of milled Al 5356 powders in Chapter 4. Similar processes have been observed during field-assisted sintering of Al alloys in literature [6.4, 6.5]. Reduction reactions resulted in MgAl<sub>2</sub>O<sub>4</sub>, MgO, or a mixture of both oxides formed at inter-particle contacts in Al-Mg alloys during field-assisted sintering [6.4]. The oxide phase was dependent on the alloy composition and the sintering temperature [6.4].

Upon consolidation, the sintered samples show peaks corresponding to the  $\alpha$ -Al and MgAl<sub>2</sub>O<sub>4</sub> phases (Si peaks are from the standard) as shown in the XRD spectra for the 500 TSS 20 and 550 TSS 20 sintered samples in Figure 6.1. No peaks corresponding to the Al<sub>3</sub>Er phase were observed. No second phase peaks are observed in the 0.1 Er 550 TSS 20 and 0.5 Er 500 TSS 20 samples. However, the absence of additional peaks could be due to a low volume fraction of the phases in the sample. The lattice parameters obtained from the sintered samples also indicate a loss in solute supersaturation during sintering. The results from XRD peak analysis of the milled powders and the sintered samples is presented in Table 6.1. It is estimated that 1.57 at.% Mg is left in the matrix after the 500 TSS 20 consolidation of the 0.1 Er powders, near equilibrium levels as determined from the Al-Mg phase diagram. However, a supersaturated solid solution is still maintained in the 550 TSS 20 sample with 2.59 at.% Mg left in the matrix. In chapter 5, an oxide forming event was observed at  $\sim 475$  °C from the DSC traces of the 0.1 Er powder. The lower Mg content measured in the 500 TSS 20 sample could be attributed to reduction reactions occurring during the T<sub>1</sub> hold at 500 °C. For the 0.5 Er samples, a supersaturated solid solution is maintained after

sintering with both conditions. 3.68 at.% and 2.44 at.% Mg is estimated in the matrix of the 500 TSS 20 and 550 TSS 20 samples, respectively.

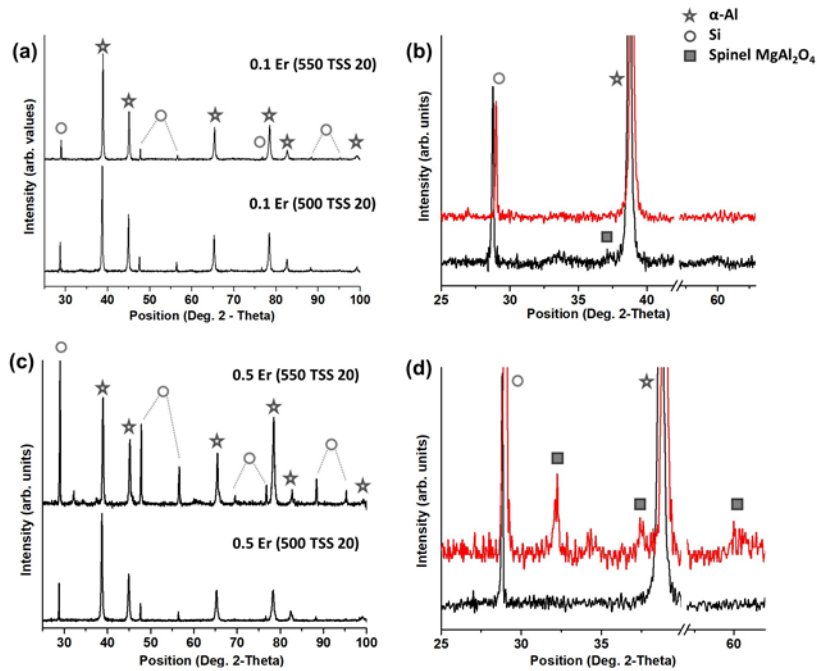


Figure 6.1 XRD spectra of samples sintered by TSS schedules for 0.1 Er (a, b) and 0.5 Er (c, d): full spectra (a, c) and close up of small peaks (b, d). Peaks are normalized.

Table 6.1 XRD peak analysis for milled powders and sintered bulks

Sample Condition	Lattice parameter (Å)	Mg in matrix (at.%)
Milled 0.1 Er	4.0662 ± 0.0015	5.26
0.1 Er (500 TSS 20)	4.0517 ± 0.0004	1.57
0.1 Er (550 TSS 20)	4.0557 ± 0.0009	2.59

Milled 0.5 Er	4.0647 ± 0.0004	4.87
0.5 Er (500 TSS 20)	4.0600 ± 0.0008	3.68
0.5 Er (550 TSS 20)	4.0551 ± 0.0009	2.44

### 6.2.2. TEM results

X-ray microanalysis of the sintered samples is carried out to determine the distribution of solutes and the composition of second phases. Higher Mg, O and N content are detected in the nanocrystalline regions of the sintered samples. The distribution of Er and Fe solutes is similar in the nanocrystalline and coarse-grained regions, while the Cu signal is produced from the TEM sample holder. No signal from Ni or Ti solutes is detected in the samples. A representative result is shown in Figure 6.2 by the X-ray spectrum produced from a 0.1 Er 550 TSS 20 sample. SAED patterns taken from the nano-grained regions of the 0.1 Er samples are shown in Figure 6.3. The SAED patterns of the 0.1 Er samples consist of ring diffraction patterns indicative of nanocrystallinity (Figure 6.3(b) and 6.3(d)). The SAED patterns can be indexed to the  $\alpha$ -Al phase with extra reflections in the 500 TSS 20 sample measured as  $d \approx 2.62 \text{ \AA}$  and  $d \approx 1.53 \text{ \AA}$ . Considering the results of the X-ray spectrums taken from the nanocrystalline regions, the extra rings can be indexed to the spinel  $\text{MgAl}_2\text{O}_4$  phase. These results reflect the oxidation behaviour observed in the 0.1 Er powders in Chapter 5, where the first oxidation peak event occurs at  $\sim 475 \text{ }^\circ\text{C}$ .

SAED patterns from the nanocrystalline regions of the 0.5 Er samples are shown in Fig 6.4. The 500 TSS 20\* condition (Figure 6.4(a) and 6.4(b)) was sintered with a heating rate of  $300 \text{ }^\circ\text{C}\cdot\text{min}^{-1}$  under 60 MPa. Akin to the 500 TSS 20 sample ( $100 \text{ }^\circ\text{C}\cdot\text{min}^{-1}$  and 50 MPa) the 500 TSS 20\* exhibited only  $\alpha$ -Al peaks from XRD analysis. Similarly, no extra phase rings were detected in the SAED patterns taken from the nanocrystalline regions as shown in Figure 6.4(b). However, the 0.5 Er powder

processed at 550 TSS 20 (Figure 6.4(c) and 6.4(d)) shows the prolific presence of nanoscale second phases within the nanocrystalline regions. An SAED pattern taken from the nanocrystalline region (Figure 6.4(d)) is indexed to the  $\alpha$ -Al, spinel  $\text{MgAl}_2\text{O}_4$  and  $\gamma$ - $\text{Al}_2\text{O}_3$  phases. Phases in the nanocrystalline region of the 0.5 Er 550 TSS 20 sample were further analyzed by TEM with HRTEM imaging and X-ray elemental mapping, results of which are shown in Figures 6.5 through 6.8.

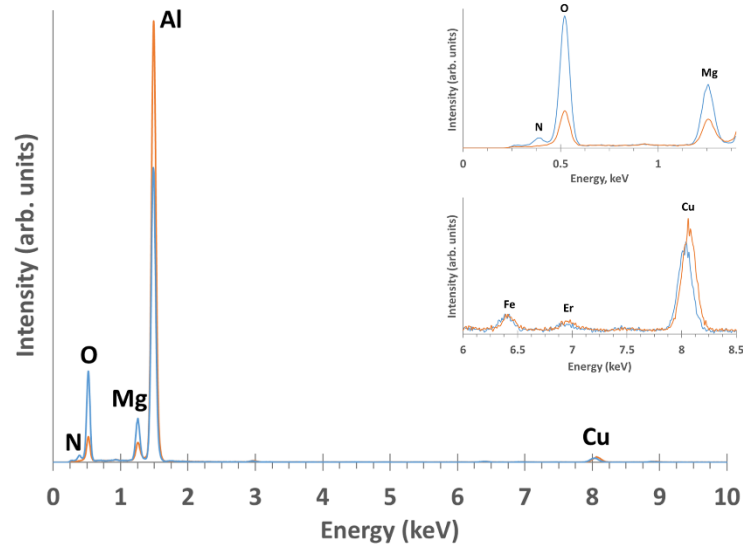


Figure 6.2 X-ray spectrums taken from the nanocrystalline (blue line) and coarse grained (orange line) in the 0.1 Er 550 TSS 20 sample.

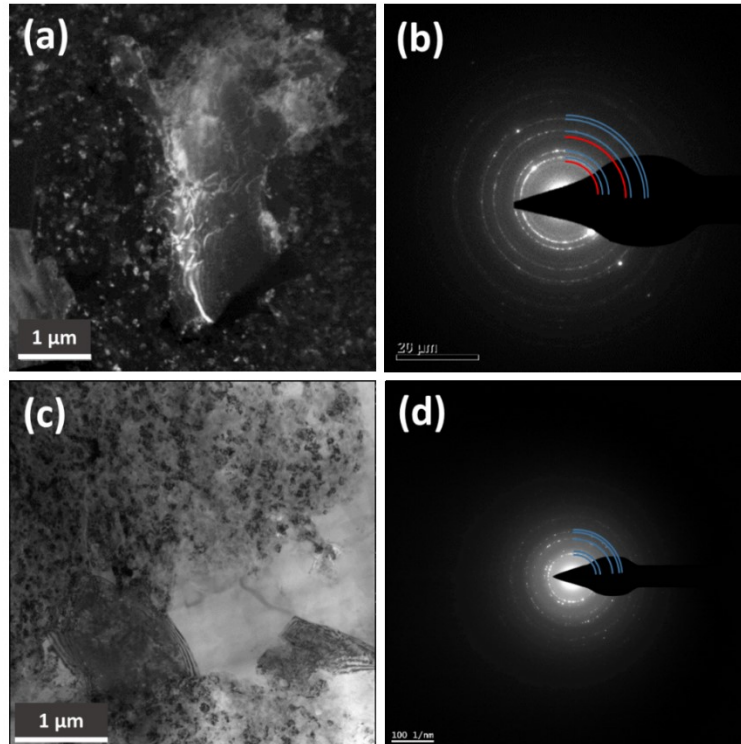
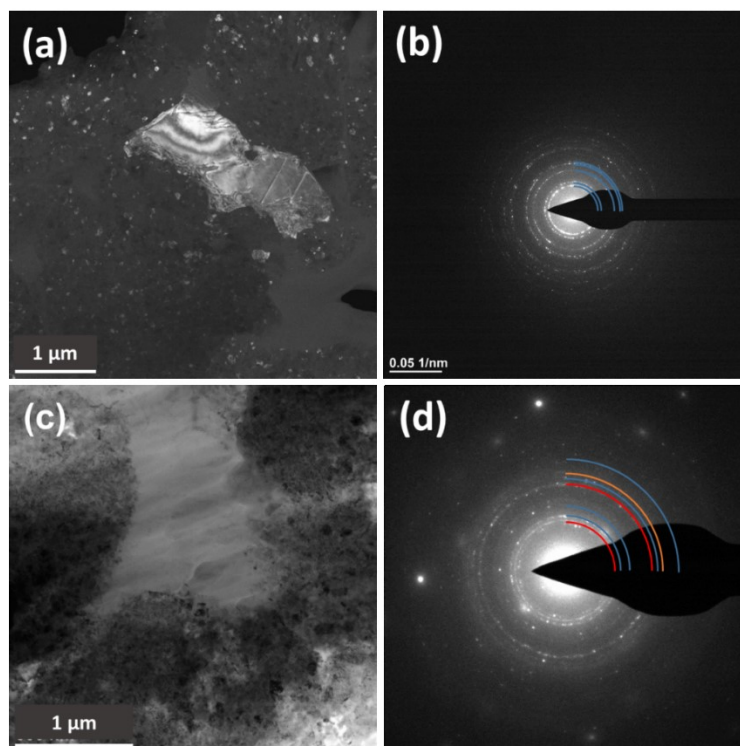
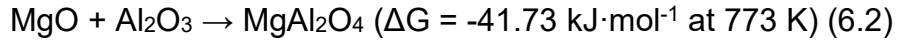


Figure 6.3 Typical results from sintered 0.1 Er samples (a,b – 500 TSS 20; c,d – 550 TSS 20): bimodal microstructure (a,c). Typical SAED patterns taken from the nanocrystalline regions (b,d). SAED patterns are indexed as  $\alpha$ -Al (blue arcs) and  $\text{MgAl}_2\text{O}_4$  (red arcs) phases.



**Figure 6.4 Microstructure in sintered 0.5 Er pucks (a,b – 500 TSS 20\*; c,d – 550 TSS 20): bimodal microstructure (a,c). Typical SAED patterns taken from nanocrystalline regions (b,d). SAED patterns are indexed as  $\alpha$ -Al (blue arcs),  $\text{MgAl}_2\text{O}_4$  (red arcs), and  $\gamma$ - $\text{Al}_2\text{O}_3$  (orange arc).**

Regions of the sintered 0.5 Er 550 TSS 20 sample are shown in Figure 6.5, with X-ray spectrums and TEM images of the marked particles presented in Figure 6.6 to 6.8. Mg, Al, O signals are detected in the particles, along with N, Er and Fe. The Cu signal is obtained from the sample holder. Lattice measurements from the particles in Figure 6.7 are close to the d-spacings for the  $\text{MgAl}_2\text{O}_4$  phase ( $d_{111} = 4.6477 \text{ \AA}$ ,  $d_{220} = 2.8461 \text{ \AA}$ ,  $d_{400} = 2.0125 \text{ \AA}$ ). Literature reports that oxide, oxynitride and aluminum nitride nanoparticle inclusions are present in Al powders produced by cryomilling [6.6, 6.7]. Despite similarities between the lattice parameters of  $\text{MgAlON}$  and  $\text{MgAl}_2\text{O}_4$  spinel-type structures, it is not certain that the level of N detected is sufficient to classify the particles as oxynitrides. As discussed in the previous chapter, crystalline oxide phases may be formed as a result of reduction reactions between Mg and the nanoscale oxides within the milled powder, as well as the oxide film at particle surfaces. Spinel and periclase ( $\text{MgO}$ ) particles can form from several solid-state reduction reactions as given below [6.8]:



Spinel formation due to solid-state reactions between the periclase and alumina particles will also be dependent on the proximity of the MgO particles to the alumina oxide film/particles within the powders.

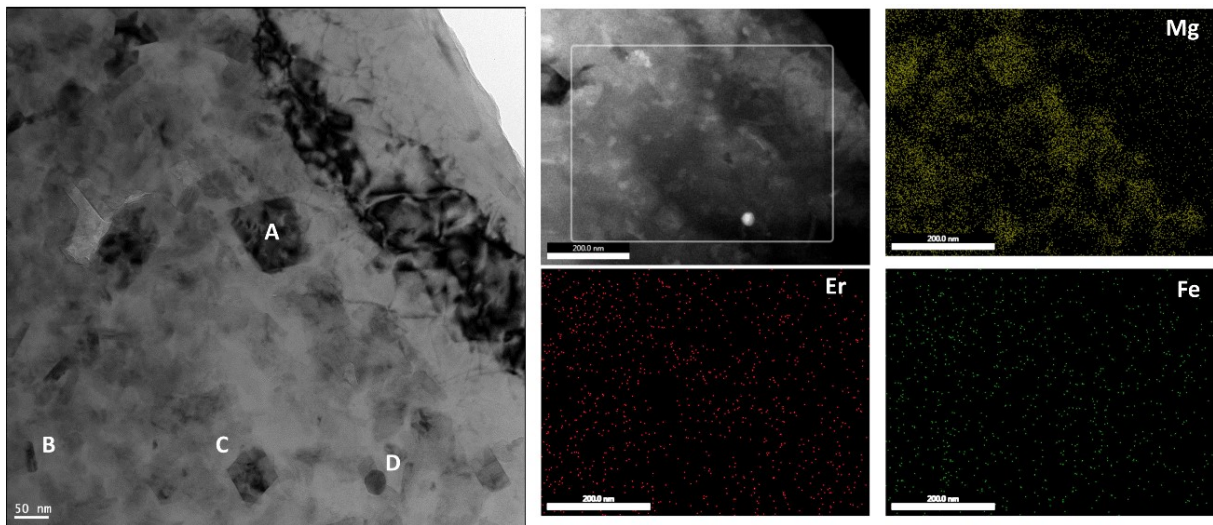


Figure 6.5 X-ray elemental maps of 0.5 Er 550 TSS 20 sample showing distribution of Mg, Er, and Fe solutes in the sintered sample.

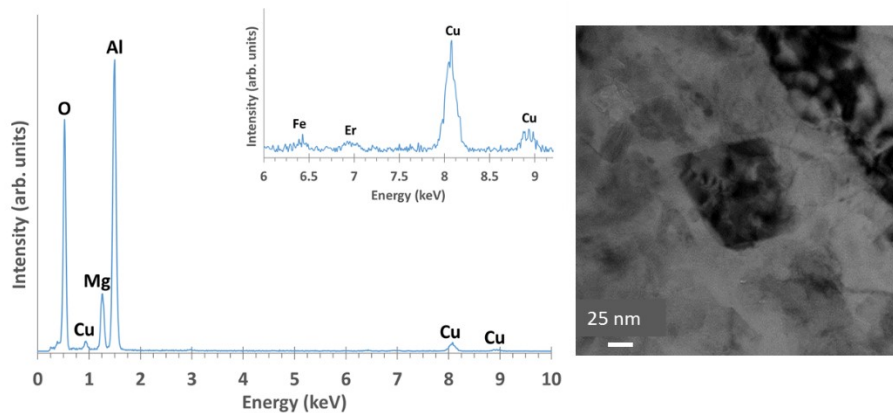


Figure 6.6 X-ray spectrum and TEM image of Al-Mg-Er-Fe-O particle from Region A

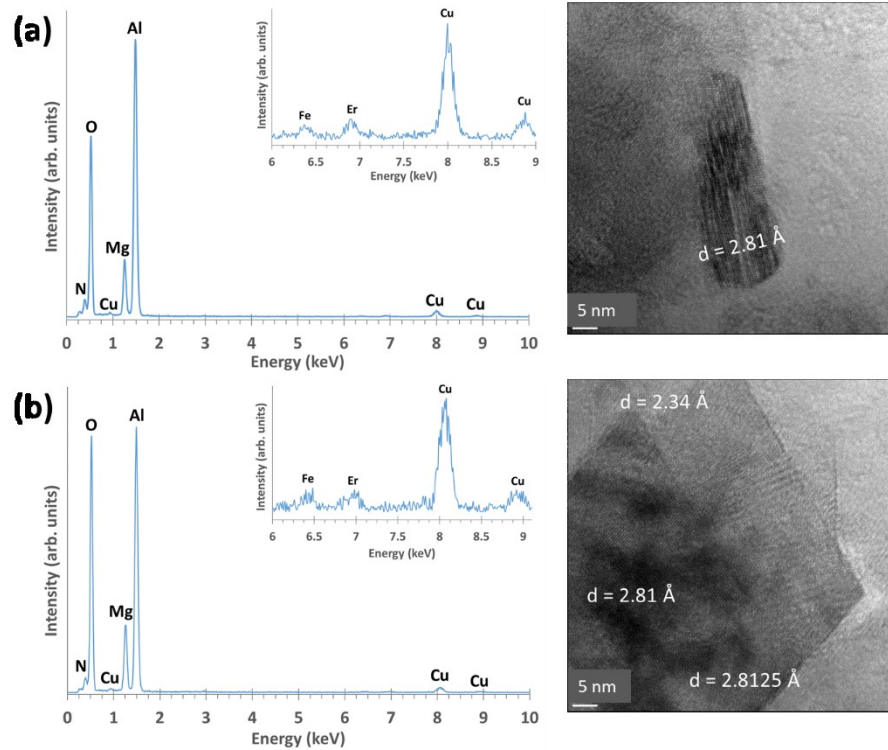


Figure 6.7 X-ray spectrums and HRTEM images of Al-Mg-Er-Fe-O-N particles from (a) Region B and (b) Region C

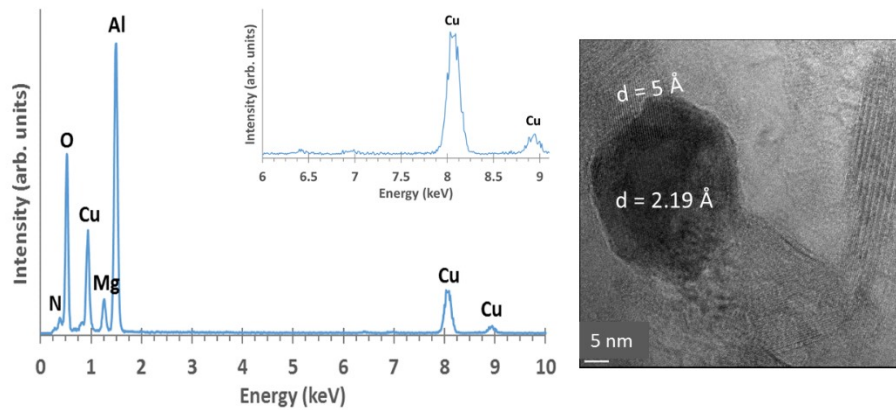


Figure 6.8 X-ray spectrum and HRTEM image of Al-Mg-O-N particles from Region D

### 6.3. Microstructure and grain size distribution

Grain size and micro-strain in the consolidated materials were determined from XRD peak broadening and the results of the analysis are presented in Table 6.2. TEM image analysis was used to confirm the grain size. The standard deviation and 95%

confidence interval (CI) for the grain size measurements are also reported in the Table; the CI values are in round brackets. As milled grain sizes of 22 nm and 19 nm were determined for the 0.1 Er and 0.5 Er powders, respectively; these values are comparable to the grain size of ~20 nm reported in literature for milled Al and Al-Mg alloys [6.9-6.11]. Grain size results from TEM image analysis were  $16 \pm 1$  nm and 17 nm in the 0.1 Er and 0.5 Er powders, respectively, in agreement with measurements from XRD.

**Table 6.2 Grain size and micro-strain data**

<b>Sample Condition</b>	<b>Grain size, XRD (nm)</b>	<b>Micro-strain (%)</b>	<b>Grain size, TEM (nm)</b>	<b>R<sup>2</sup></b>
Milled 0.1 Er	22	0.094	$16 \pm 1$	0.92
0.1 Er (500 TSS 20)	57	0.069	$72 \pm 42$ (4)	0.95
0.1 Er (550 TSS 20)	48	0.088	$86 \pm 52$ (5)	0.99
Milled 0.5 Er	19	0.106	$17 \pm 0$	0.93
0.5 Er (500 TSS 20)	28	0.08	-	0.99
0.5 Er (550 TSS 20)	35	0.047	$50 \pm 21$ (2)	0.92

Upon consolidation, the average minimum grain size in the 0.1 Er samples were 57 nm and 48 nm for the 500 and 550 TSS 20 samples, correspondingly, which agreed

well with the TEM results of  $72 \pm 42$  nm and  $86 \pm 52$  nm. The 0.5 Er sample produced by the 550 TSS 20 schedule has a grain size of 35 nm according to XRD measurement which is also in agreement with the TEM result of  $50 \pm 21$  nm. In the 0.1 Er samples, the micro-strain decreased from 0.094% in the milled powder to 0.069% and 0.088% after the 500 and 550 TSS 20 sintering schedules, in turn. In the 0.5 Er sintered samples, the micro-strain decreased from 0.106% to 0.08% and 0.047% after the 500 and 550 TSS 20 schedules, respectively. These values are similar to those observed in the milled Al-Mg-Er powders after one hour of annealing at 500 °C, with micro-strain levels of 0.092% and 0.062% in the 0.1 Er and 0.5 Er powders, respectively. The micro-strain in the sintered pucks may be influenced by the Mg content in the matrix in addition to the contributions from lattice defects.

Grain size distributions determined via TEM image analysis are presented in Figure 6.9 for the 0.1 Er 500 and 550 TSS 20 samples, and the 0.5 Er 550 TSS 20 sample. The grain size distribution from the 500 TSS 20 sintered Al 5356 alloy is also included in the figure. The distributions were identical for both Al 5356 and 0.1 Er powders processed by the 500 TSS 20 process, with 80% of the measured grains in the nanocrystalline range. After the 550 TSS 20 sintering condition, 65% of the measured grains were below 100 nm in size. In the 0.5 Er 550 TSS 20 sample over 90% of the measured grains were under 100 nm.

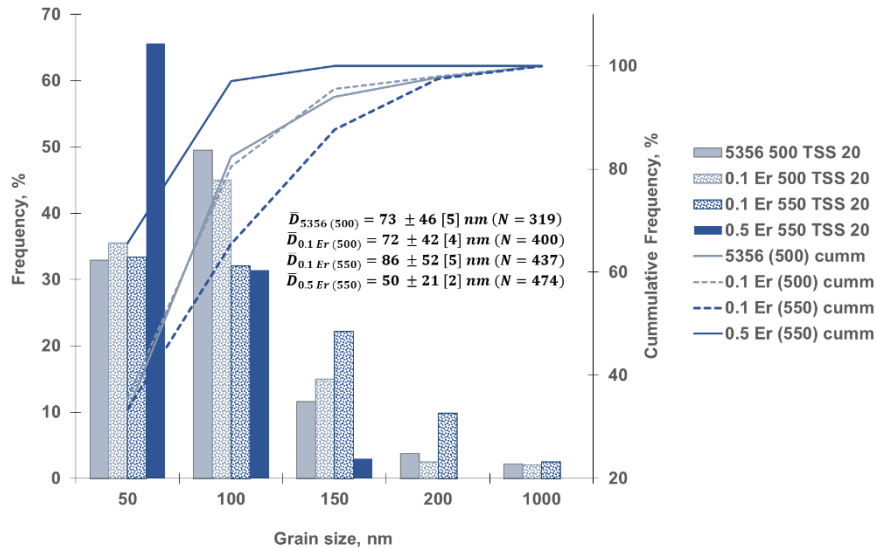


**Figure 6.9 Grain size distribution in TSS sintered Al 5356, 0.1 Er and 0.5 Er samples**

Previous researchers have reported a bimodal microstructure in SPS consolidated cryomilled Al powders [6.12-6.14] and similar results were observed here. Representative microstructures of the sintered bulks are shown in Figure 6.10. Similar to the TSS results of the Al 5356 milled powders, regions of coarse grains ( $\approx 1 - 3 \mu\text{m}$ ) were observed within a matrix of nanocrystalline grains in the sintered samples. Two types of boundaries are generally observed around the coarse grains in the 0.1 Er sintered samples – irregular shaped boundaries and linear boundaries. The large grains also often contain dislocation structures, similar to results of the 500 TSS 20 sintered Al 5356 samples. However, the coarse grains observed in the 0.5 Er 550 TSS 20 samples have irregular shaped boundaries. These large grains are observed between clusters of nanocrystalline grains, suggesting they result from abnormal grain growth at inter-particle regions (Figure 6.10(c)).

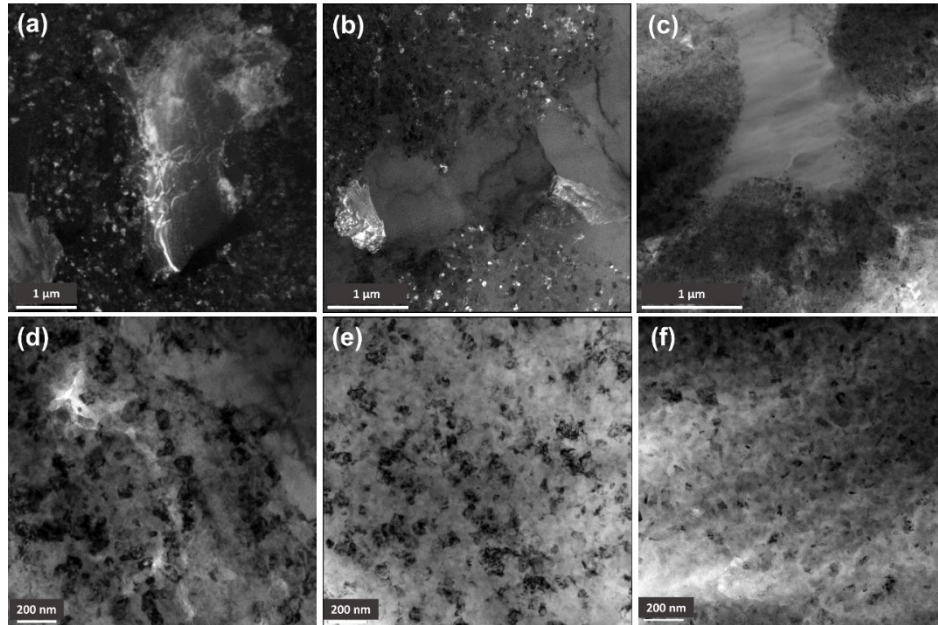


Figure 6.10 Dark field and bright field images of the microstructure in the 0.1 Er 500 TSS 20 (a,d), 0.1 Er 550 TSS 20 (b, e) and 0.5 Er 550 TSS 20 (c,f).

#### 6.4. Grain growth during consolidation

In this powder system, the starting microstructure of the milled powders was observed to be fairly homogeneous, with no observations of the elongated lamellar grains or dislocation networks typically reported in milled Al systems [6.9-6.11]. This suggests the bimodal microstructure obtained in the final sintered materials is gained mainly during the SPS processing, and not as a result of pre-existing heterogeneity. The bimodal microstructure in the sintered compacts could be attributed to a few factors: uneven distribution of solutes and pinning phases [6.15]; heterogeneous temperature distribution during SPS causing abnormal growth or local melting at particle contacts [6.15].

Similar bimodal microstructures to those observed in the Al-Mg-Er sintered material have been observed in ODS Fe-Al alloys produced by SPS. In ODS ( $Y_2O_3$ ) strengthened Fe-40Al milled alloy, several types of microstructures are observed in the SPS consolidated material: large grains that contain no oxide particles or yttrium [6.15], grains with very square-like boundaries, and grains with more irregular shaped

boundaries. Square-like boundaries were attributed to regions of insufficient incorporation of oxides within the powder; while the large irregular grains, which are often bordered by large oxide particles, were proposed to correspond to areas where local melting occurred [6.15]. The bimodal microstructures were largely attributed to the heterogeneous temperature distribution often encountered during SPS processing.

Results of SPS modelling show local increase in temperature, stress, and current density during initial heating when the contact points/necks between particles are very small [6.16]. The appearance of the coarse-grained regions in the 0.5 Er 550 TSS 20 sample (Figure 6.10(c)) supports the notion of enhanced growth at inter-particle contacts. Although irregular grain boundaries and the presence of oxide particles at the interfaces between coarse grains and nanocrystalline regions is suggestive of local melting during sintering, the presence of alloying elements in both coarse and nanocrystalline regions suggests that melting does not occur. These large grains with irregular grain boundaries could correspond to regions in the samples where heterogeneous temperature and strain distributions during the sintering process enhance grain growth.

Previously, the grain growth during the TSS procedures was estimated using the general grain growth equation:

$$D^{1/n} - D_0^{1/n} = kt \quad (6.4)$$

where:  $D$  is the average grain size,  $D_0$  is the starting grain size,  $k$  is the kinetic parameter and  $t$  is time. The average nanocrystalline grain growth during sintering can be estimated using the kinetic parameters from the thermal behavior of cryomilled Al powders [6.9]: where  $n = 0.28$  and  $Q = 112 \text{ kJ}\cdot\text{mol}^{-1}$  for  $T > 450 \text{ }^\circ\text{C}$ , and  $n = 0.05$  and  $Q = 79 \text{ kJ}\cdot\text{mol}^{-1}$  for  $T = 350 - 450 \text{ }^\circ\text{C}$ . From the results of Chapter 4, it is observed that most of the grain growth occurs during the  $T_1$  hold, so isothermal grain growth is estimated for the time duration at  $500 \text{ }^\circ\text{C}$  and  $550 \text{ }^\circ\text{C}$ . A grain size of  $\sim 50 \text{ nm}$  is estimated after one minute hold at  $T_1$  for the 500 TSS 20 schedule, while a grain size of  $\sim 60 \text{ nm}$  is estimated after a 30 second hold at  $T_1$  for 550 TSS 20. In the 0.1 Er powders the grain growth after both 500 and 550 TSS 20 schedules is larger than the estimated

value by ~ 20 nm, but grain growth in the 0.5 Er sample is less than predicted. As previously discussed, heterogeneous temperature distributions during sintering may lead to inhomogeneous grain growth in the sintered compacts. Unaccounted grain growth may also occur during the heating segment up to  $T_1$ .

As discussed in Chapter 5, grain growth behavior in these milled Al-Mg-Er powder systems was attributed to combined solute/impurity drag and pinning by (oxide) second phase particles typical to that observed in cryomilled Al powders. Burke's model considers the effect of drag/pinning forces on grain growth under the assumption that the drag forces are independent of the average grain size [6.17]. This can be true if the volume fraction and size distribution of the inclusions are fixed. The drag forces due to solutes, second phases or sample thickness are represented by a maximum grain size in the system [6.17]. Burke's model of grain growth is given as

$$\frac{(D_0 - D)}{D_{max}} + \ln\left(\frac{D_{max} - D_0}{D_{max} - D}\right) = \frac{kt}{D_{max}^2} \quad (6.5)$$

where:  $D_0$  is the initial grain size,  $D$  is the grain size,  $D_{max}$  is the maximum grain size in the system,  $k$  is a product of boundary mobility  $m_b$  and grain boundary energy  $\gamma$ , and  $t$  is time. Essentially Burke's model estimates the drag force from second phases and impurities as a maximum grain size in the system, such that Burke's model can be written as

$$\frac{dD}{dt} = k\left(\frac{1}{D} - \frac{1}{D_{max}}\right) \quad (6.6)$$

Hence the driving force for grain growth in the system is supplied by the difference between the average grain size and the Zener limit grain size.

The grain growth in the Al-Mg-Er powders can be estimated using Burke's model and replacing the mobility term with an estimated reduced mobility due to solute drag in the system. The effect of solute content is typically assessed by a solute drag approach [6.18,6.19]. Recently a new solute drag model was proposed based on a solute pinning approach [6.20], which was then expanded to accommodate the effects of different types of solutes in solution by [6.21]. From their treatment, the boundary velocity can be expressed as

$$v = m_b \cdot P = \frac{1}{\frac{1}{M^{int}} + \frac{1}{M_A^{ext}} + \frac{1}{M_B^{ext}}} \cdot P \quad (6.7)$$

where:  $v$  is the boundary velocity,  $m_b$  is the boundary mobility due to solute drag,  $P$  is the driving pressure,  $M^{int}$  is the intrinsic mobility of the grain boundary,  $M_A^{ext}$  is the mobility of the grain boundary loaded with solute A, and  $M_B^{ext}$  is the mobility of the grain boundary loaded with solute B. The expression can be expanded to accommodate for  $n$  number of solutes in the material system.

The mobility of the grain boundary loaded with impurities A,  $M_A^{ext}$ , is defined as:

$$M_A^{ext} = \frac{2}{nb^3} \frac{\Gamma_A b^4 v_D}{kT c_A} e^{-\frac{(2U_A^0 + U_A^s)}{kT}} \quad (6.8)$$

where:  $\Gamma_A$  is a constant,  $b$  is the burger's vector of the matrix Al,  $v_D$  is the Debye frequency,  $U_A^0$  is the interaction energy between the solute atoms and the grain boundary,  $U_A^s$  is the activation energy for (volume) diffusion of the solute atom,  $nb$  is the number of atomic sites per unit area inside the matrix, and  $c_A$  is the volume impurity concentration of solute. The available atomic sites at the grain boundary for solute adsorption is taken as one monolayer of  $1.885 \cdot 10^{-5} \text{ mol/m}^2$ . The activation energies for volume diffusion used for the calculations for  $m_b$  for Mg, Er, Ti, Fe and Ni in Al are shown in Figure 6.11. The base interaction enthalpy is calculated using the suggested method by Lucke and Stuwe which is approximately  $6 \text{ kJ}\cdot\text{mol}^{-1}$  for the Al grain boundary. Diffusion coefficients and activation energy for Er diffusion in Al were not found in the literature. However, due to the similarities of diffusion behaviour in Al across the lanthanide series the diffusion parameters of Sc in Al were used as an approximation for Er behaviour. The diffusion parameters for Sc diffusion in Al were taken from the results of Kerkove *et al.* [6.22] for a dilute Al-Sc system. Considering the absence of Ni and Ti signals in the X-ray microanalysis results, these solutes are not used in the boundary mobility calculations.

A plot of the boundary mobilities in Al-5Mg, 0.1 Er and 0.5 Er compositions calculated with eq. 6.7 and 6.8 are shown in Figure 6.11. The boundary mobility is reduced in the Al-Mg-Er compositions in comparison to a binary Al-5Mg system, but the

mobilities in both the 0.1 Er and 0.5 Er compositions are comparable. A plot using just Fe content in the system shows that the mobility of the Al-Mg-Er powders is highly influenced by the Fe solute content. The difference in grain growth in both powder systems is then dependent on the temperature dependent Zener limited grain size and grain boundary mobility during stage one of the TSS process. Using eq. 6.5, an estimation of the grain growth in the 0.1 Er and 0.5 Er systems is made for both 500 TSS 20 and 550 TSS 20 schedules as shown in Figure 6.12(a). Considering the experimental SPS results,  $D_{\max}$  in the 0.1 Er powders is taken as 75 nm and 85 nm for the 500 TSS 20 and 550 TSS 20 schedules, respectively.  $D_{\max}$  in the 0.5 Er system is taken to be 50 nm. As observed in Figure 6.12, with boundary mobility controlled by just Mg solutes, the experimental grain size is achieved in under 10 seconds at  $T_1$ . However, the grain growth during the  $T_1$  hold is underestimated with the Al-Mg-Er compositions. It is possible that other factors during the process, such as the applied pressure, may influence the grain growth observed during sintering. Molecular dynamics simulations on nanocrystalline Pd have shown that external stress affects grain growth by acceleration of both grain boundary migration and grain rotation events [6.24].

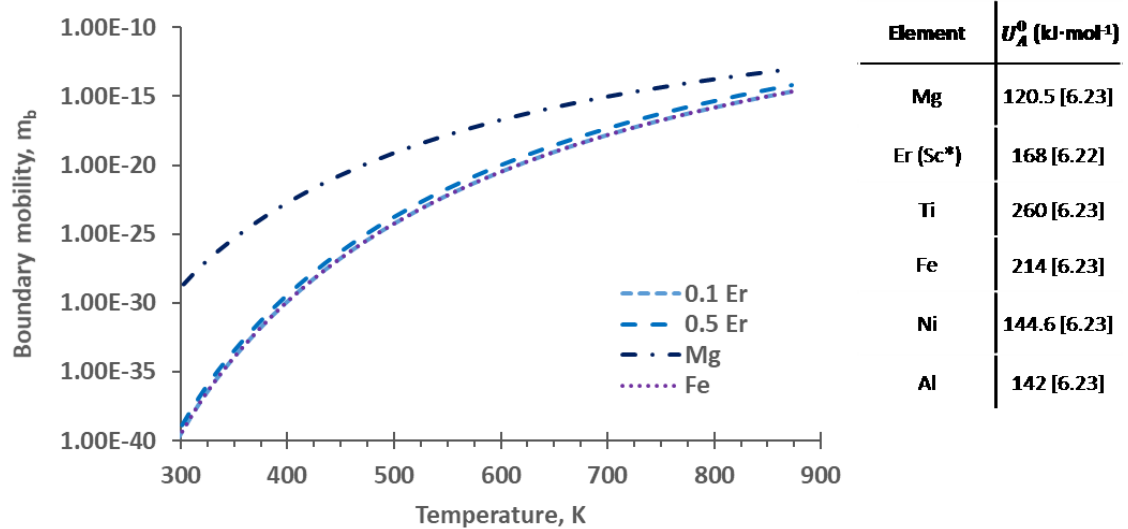


Figure 6.11 Estimated boundary mobilities

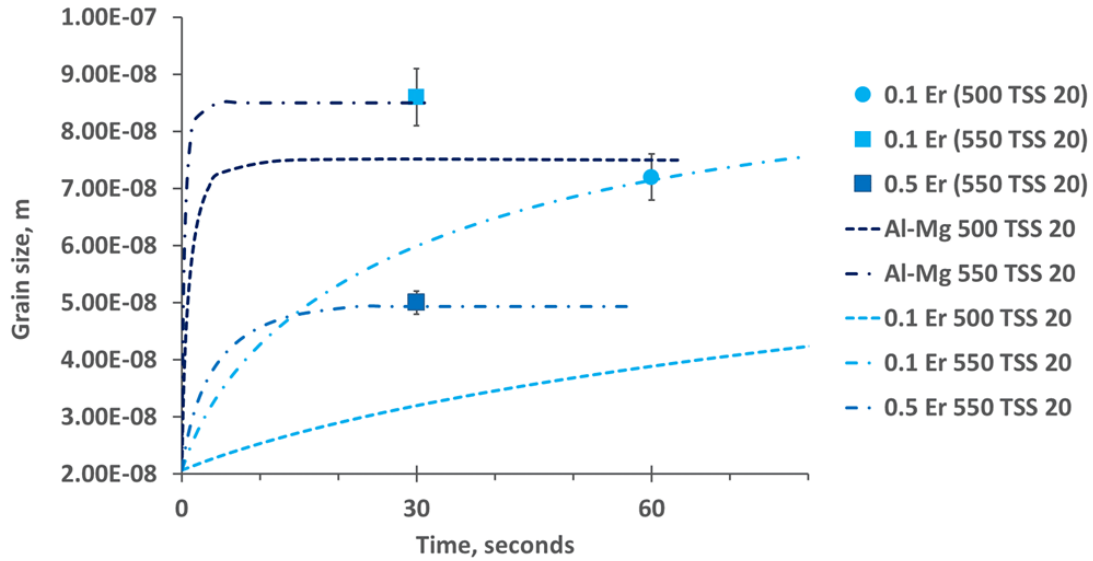


Figure 6.12 Estimated and experimental grain growth during TSS schedules

### 6.5. Effect of heating rate on consolidation

The consolidation issues of the milled Al-Mg-Er powders was addressed by using higher sintering temperature  $T_1$ , higher pressure and higher heating rates during the sintering process. These changes have a significant effect on the density and properties of the sintered materials as shown in Table 6.4. For the 0.5 Er compacts sintered with the 500 TSS 20 schedule, the density improved from 69% to 76% when a heating rate of  $300\text{ }^\circ\text{C}\cdot\text{min}^{-1}$  and 60 MPa was used. Densities above 90% were achieved when the  $T_1$  was also increased to  $550\text{ }^\circ\text{C}$ . A density of 93% was obtained for the 0.5 Er pucks with the 550 TSS 20 schedule. Densities of the 0.1 Er pucks were improved from 92% to 98% with the 500 TSS 20 and 550 TSS 20 schedules, respectively. Higher oxide content in the 0.5 Er powders (versus 0.1 Er powders) results in increased hardness of the powders and therefore lower densities after sintering at 550 TSS 20. The density results for the 0.1 Er 500 TSS 20 samples are similar to those of mechanically alloyed Al-Al<sub>2</sub>O<sub>3</sub> nanocomposites, with Al<sub>2</sub>O<sub>3</sub> particles of 150 nm, consolidated by SPS. Saheeb et al observed that sintering at  $550\text{ }^\circ\text{C}$  with 50 MPa and a heating rate of  $200\text{ }^\circ\text{C}\cdot\text{min}^{-1}$  resulted in densification of 91% with 15 vol.% Al<sub>2</sub>O<sub>3</sub> [6.25].

The consolidated bulks were further examined by testing the mechanical properties. Three-point flexural strength and micro-hardness of the sintered samples are compiled in Table 6.3. For the 0.1 Er composition, bend strength of ~ 440 MPa and ~ 550 MPa was achieved with 500 TSS 20 and 550 TSS 20 schedules, respectively. Concerning the 0.5 Er powders, samples were poorly sintered at 500 TSS 20 conditions and fractured during preparation for mechanical testing. As such testing was conducted only for the 550 TSS 20 samples of the 0.5 Er from which a bend strength of ~ 400 MPa was obtained. Hardness values of 166 HV and 210 HV were obtained in the 500 TSS 20 and 550 TSS 20 sintered 0.1 Er samples, respectively. Similarly, 167 HV was obtained for the 0.5 Er powders sintered with 550 TSS 20 schedule.

**Table 6.3 Mechanical properties of sintered samples**

<b>Sintered Condition</b>	<b>Composition</b>	<b>Density (% theor.)</b>	<b>3-point flexural strength (MPa)</b>	<b>Hardness (HV<sub>50gf</sub>)</b>
<b>500 TSS 20</b>	0.1 Er	91.5 ± 6.4	440 ± 216	166 ± 39
	0.5 Er	68.9 ± 0.2	-	-
<b>500 TSS 20*</b>	0.5 Er	76	-	-
<b>550 TSS 20</b>	0.1 Er	97.6 ± 0.9	556 ± 142	210 ± 10
	0.5 Er	93.0 ± 1.8	402 ± 127	167 ± 18

Due to the high oxide content, these Al-Mg-Er powder compacts are similar to Al-Al<sub>2</sub>O<sub>3</sub> nanocomposite materials and have similar bulk mechanical properties. Similar consolidation issues were observed during the processing of Al-Al<sub>2</sub>O<sub>3</sub> powders produced by high energy milling in a SPEX mill [6.26,6.27]. Al-Al<sub>2</sub>O<sub>3</sub> composites with Al<sub>2</sub>O<sub>3</sub> reinforcement phases varying from 50 nm to 5 µm in size and in volume fractions of 5 to 50 % were synthesized by milling for 20 hours. The final composite powders had

increased hardness which made consolidation to full density difficult to achieve. Al-Al<sub>2</sub>O<sub>3</sub> composite powders with 10 vol.% of 50 nm sized oxide particles were consolidated to full density by a combination of vacuum hot pressing and hot isostatic pressing giving rise to tensile and compressive strengths of 515 MPa and 628 MPa, respectively [6.27]. These values are comparable to the flexural strengths of ~ 550 MPa obtained in this study with the 550 TSS 20 processed 0.1 Er powders; oxide content is estimated as ~ 12 vol.% oxide by assuming all oxygen atoms are present as oxide within the powder.

Densification curves were plotted for both TSS schedules and powder compositions. The densification occurs during the ramping stage of the SPS process. The changes in density with respect to the time and temperature are shown in Figure 6.13. Similar to the observations of Milligan [6.28] and Ye et al [6.12], both TSS schedules shows a quick increase in densification at the beginning of the ramping segment. This increase has been attributed to plastic yielding at the onset of the process [6.12, 6.28]. However, densification behaviour differs between the two TSS processes. While the 500 TSS 20 curves exhibit continuous increase in density with temperature and time, the 550 TSS 20 processes show ~10 – 15% jumps in density during the ramping process, indicated by the arrows in the figure. Density jumps occur at ~200 °C and ~350 °C for the 0.1 Er powder, and at ~250 °C and ~400 °C for the 0.5 Er powders during the 550 TSS 20 process.

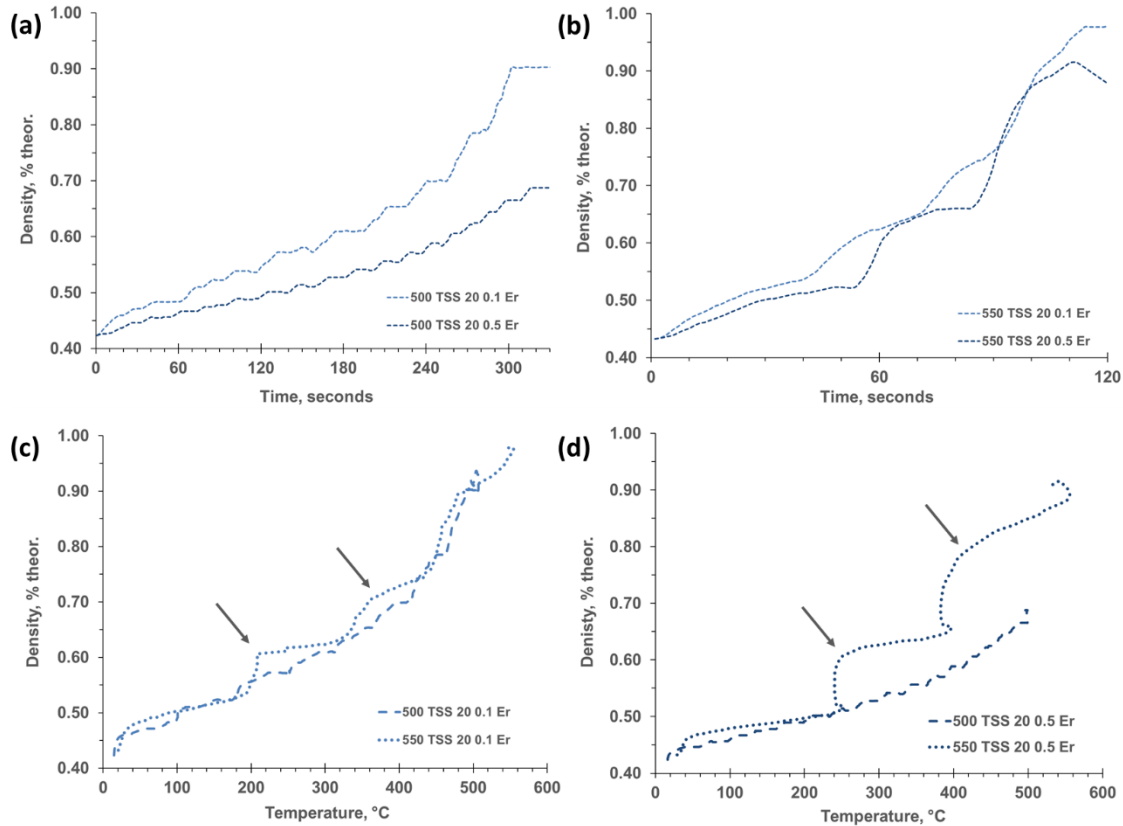


**Figure 6.13 Densification curves for (a) 500 TSS 20 and (b) 550 TSS 20 processes; (c) 0.1 Er and 0.5 Er powders**

As seen in Figure 6.14, the temperature profile is different for both TSS schedules. While the 500 TSS 20 has a linear temperature profile, the 550 TSS 20 schedule shows multiple jumps in the temperature during the ramping segment. The current profile also shows that multiple high amplitude (i.e.: ~ 1000 A) current pulses are applied during the 550 TSS 20 process, compared to the ~ 600 A applied once during the 500 TSS 20 process. Due to the instantaneous densification effect of plastic yielding, the altered temperature profile likely causes the changes observed in the densification curve. Since Joule heating effects are related to current intensity, the current profile applied during the TSS ramping segment can also enhance densification due to plastic yielding. Olevsky and Froyen [6.29] proposed that Joule heating effects, i.e.: high local temperatures at particle contacts, enhanced plastic yielding and contribute to densification during the initial stages of sintering [6.12,6.30].

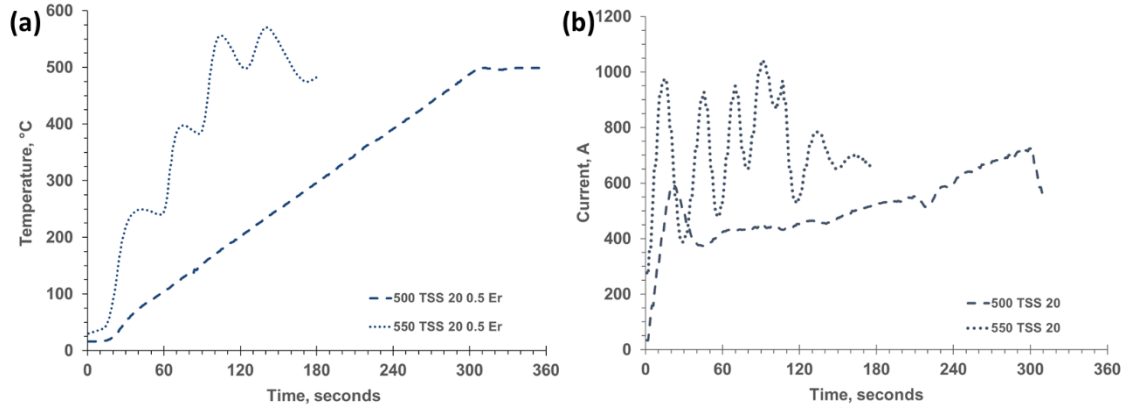


**Figure 6.14 (a) SPS temperature profiles and (b) SPS current profiles during TSS sintering of 0.5 Er powders**

The densification curves can be modelled utilizing MATLAB software. The pressure profile is programmed to match the test conditions of the SPS. Similar to the approach of Milligan [6.28], the (local) temperature profile is adjusted to obtain the experimental densification curve. Contribution of plastic yielding to densification can be calculated using equations 6.9 and 6.10 from [6.1]. At densities lower than 90% ( $\rho \leq 0.9$ ), densification can be calculated with equation 6.9, while at densities above 90% ( $\rho > 0.9$ ) equation 6.10 can be used as shown below:

$$\rho_{Yield} = \left( \frac{(1-\rho_0)P}{1.3\sigma_y} + \rho_0^3 \right)^{\frac{1}{3}} \quad \rho \leq 0.9 \quad (6.9)$$

$$\rho_{Yield} = 1 - \exp\left(-\frac{3P}{2\sigma_y}\right) \quad \rho > 0.9 \quad (6.10)$$

Where  $\rho_{Yield}$  is the density resulting from plastic yielding,  $\rho_0$  is the starting density, P is the applied pressure and  $\sigma_y$  is the yield strength at temperature.

The behaviour of the yield strength of cryomilled Al-7.5Mg with temperature was investigated by Han & Lavernia [6.31] and their results were suitably used by Milligan [6.28] in modeling the SPS densification of cryomilled Al-Si powders. However, if the oxygen content in the Al-Mg-Er powders is taken as present in oxide form, then the effect of temperature on the yield strength of a milled Al-Mg alloy composite material is more suitable for use here. Ye et al [6.32] have studied the effect of temperature on the compressive yield strength of a trimodal milled Al 5083 with 10wt.% B<sub>4</sub>C. Although the

composite alloy is not identical to the material studied here, the high reinforcement volume, base alloy composition, and temperature range tested are similar to the conditions studied here. The data of Ye *et al.* [6.32] is fitted to obtain equation 6.11 where T is temperature in Kelvin and  $\sigma_y$  is in MPa:

$$\sigma_y = 47.5 + \frac{1375}{1 + 10^{-0.0065(385-T)}} \quad (6.11)$$

The contribution of plastic yielding to densification with changing sintering temperature can then be incorporated into equations 6.9 and 6.10.

Shrinkage kinetics during SPS can be described by equations 6.12 – 6.15 [6.33]. Shrinkage rate components associated with grain boundary diffusion mechanisms include  $\dot{\epsilon}_{gbx}^{load}$ ,  $\dot{\epsilon}_{gbx}^{em}$ , and  $\dot{\epsilon}_{gbx}^{st}$  due to the external load, electromigration, and conventional sintering stresses, respectively. Power-law creep shrinkage contribution is given by equation 6.15 [6.33].

$$\dot{\epsilon}_{gbx}^{load} = \frac{\delta_{gb} D_{gb}}{kT} \frac{\Omega}{(G+r_p)} \frac{\bar{\sigma}_x}{G^2} \quad (6.12)$$

$$\dot{\epsilon}_{gbx}^{em} = -\frac{\delta_{gb} D_{gb}}{kT} \frac{Z^* e_q}{(G+r_p)^2} \frac{U}{l} \quad (6.13)$$

$$\dot{\epsilon}_{gbx}^{st} = -\frac{3\delta_{gb} D_{gb}}{kT} \frac{\Omega}{(G+r_p)^2} \frac{\alpha}{G} \left[ \frac{1}{r_p} - \frac{1}{2G} \right] \quad (6.14)$$

$$\dot{\epsilon}_{crx} = -\left[ \left( \frac{3\theta}{2} \right)^{\frac{3}{2}} \left( \frac{3\alpha}{2G} (1-\theta)^2 - \bar{\sigma}_x \right) / A (1-\theta)^{\frac{5}{2}} \right]^{\frac{1}{m}} \quad (6.15)$$

Where  $\delta_{gb} D_{gb}$  is the grain boundary diffusion coefficient,  $\Omega$  is the atomic volume,  $\sigma_x$  is the applied pressure, k is the Boltzmann's constant, T is the temperature, G is the grain size,  $r_p$  is the pore radius, m is the power-law creep exponent, A is the power-law creep frequency factor,  $Z^* e_q$  is the effective charge,  $U/l$  is the applied field and  $\alpha$  is the surface tension, and  $\theta$  is the porosity. The total shrinkage rate during SPS is obtained by summing the individual contributions from equations 6.12 to 6.15. The total shrinkage rate is converted to densification rate by equation 6.17, with overall change in density as a function of time described by equation 6.18, with  $\Delta t$  being the set time step.

$$\dot{\epsilon}_{total} = \dot{\epsilon}_{gbx}^{load} + \dot{\epsilon}_{gbx}^{em} + \dot{\epsilon}_{gbx}^{st} + \dot{\epsilon}_{crx} \quad (6.16)$$

$$\dot{\theta} = -(1 - \theta)\dot{\epsilon}_{total} = -(1 - \theta)(\dot{\epsilon}_{gbx}^{load} + \dot{\epsilon}_{gbx}^{em} + \dot{\epsilon}_{gbx}^{st} + \dot{\epsilon}_{crx}) \quad (6.17)$$

$$\rho(t) = \dot{\theta} \cdot \Delta t + \Delta\rho_{yield}(\sigma_y) \quad (6.17)$$

Fitting of the experimental curves requires altered temperature profiles as shown in Figure 6.15(a) and 6.15(b). Various researchers have shown that local temperatures may be different from the macroscopic temperature during the SPS process, due to the inhomogeneous temperature distribution at the stage of neck formation [6.28,6.34,6.35]. Local temperature differences of 100 – 300 °C are obtained during the ramping segments. Similar to the results obtained here, Milligan [6.28] observed that a local temperature difference upwards of 200 °C could exist at the initial sintering stage for Al-Si powders sintered at similar heating rates of 100 °C·min<sup>-1</sup>. Increased instances of locally high temperatures are observed during the 550 TSS 20 versus 500 TSS 20 process.

Fitted TSS densification curves for the 0.5 Er powder are presented in Figure 6.15(c) and 6.15(d). Ye *et al.* determined that plastic yielding dominated densification during the initial heating stages of SPS, but power law creep and diffusion become more significant during the latter heating stages and during the isothermal hold [6.12]. Modeling by Olevsky and Froyen [6.33] also showed that electromigration can become the dominant densification mechanism during SPS of aluminum at lower porosity values. Similar trends are observed for the modeling results here. As observed in Figure 6.15, plastic yielding is the main contributor to densification during both TSS processes, especially during the initial stages of sintering. Electromigration contributions become more significant with increasing temperature and reducing porosity. The jumps in density at the onset of sintering and during the ramp (i.e.: at ~ 250 °C and ~400 °C) can be mainly ascribed to plastic yielding effects and coincide with periods of high local temperature. These density jumps are more pronounced during sintering of the 0.5 Er sample versus the 0.1 Er sample, as observed in Figure 6.13. This could be due to differences in how yield strength  $\sigma_y$  changes with temperature in the two alloys.

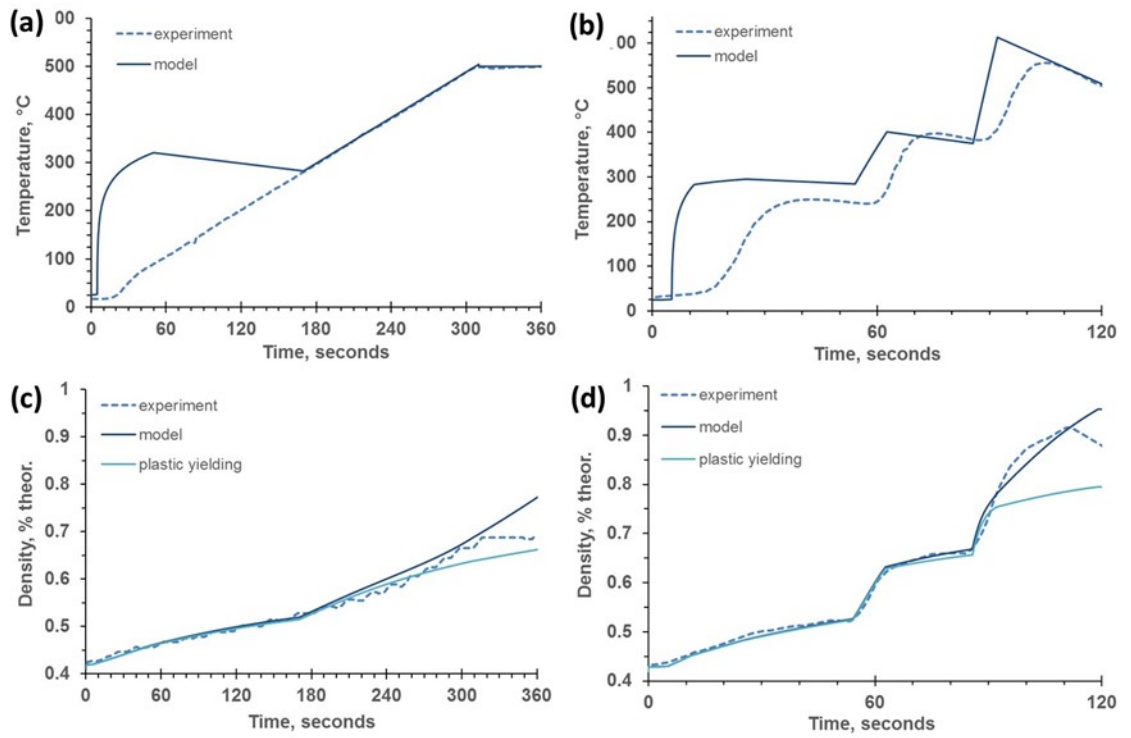


Figure 6.15 Temperature profiles (a,b) and fitted densification curves (c,d) obtained for 500 TSS 20 (left column) and 550 TSS 20 (right column) sintering of 0.5 Er powders

Table 6.4 Aluminum material properties used for the model

Crystallographic Data	
Atomic Volume, $\Omega$ ( $\text{cm}^3 \cdot \text{mol}^{-1}$ )	10.00 [6.36]
Burger's vector, $b$ (m)	$2.86 \times 10^{-10}$ [6.37]
Shear modulus, $\mu_0$ (MPa)	$2.64 \times 10^4$ [6.38]
Surface tension, $\alpha$ ( $\text{J} \cdot \text{m}^{-2}$ )	1.1 [6.1]
Diffusion Data	
Volume diffusion - Pre-exponential, $D_{0v}$ ( $\text{m}^2 \cdot \text{s}^{-1}$ )	$2.0 \times 10^{-4}$ [6.1]
Grain boundary diffusion – Pre-exponential, $D_{0b}$ ( $\text{m}^3 \cdot \text{s}^{-1}$ )	$3.0 \times 10^{-14}$ [6.1]
Volume diffusion - Activation energy, $Q_v$ ( $\text{kJ} \cdot \text{mol}^{-1}$ )	142 [6.1]
Grain boundary diffusion – Activation energy, $Q_{gb}$ ( $\text{kJ} \cdot \text{mol}^{-1}$ )	60 [6.1]
Power-law creep	
Exponent, $m$	4.4 [6.39]
Dorn Constant, $A$	$3.4 \times 10^6$ [6.39]
Creep activation energy, $Q_{cr}$ ( $\text{kJ} \cdot \text{mol}^{-1}$ )	120 [6.39]
SPS Process Data	
Applied Pressure, $P$ (MPa)	50, 60
Particle size, $G$ (m)	$7.5 \times 10^{-6}$

## 6.6. Summary

Improved densification and consolidation of the milled Al-Mg-Er powders was obtained with the 550 TSS 20 sintering schedules with 60 MPa pressure and a heating rate of  $300\text{ }^{\circ}\text{C}\cdot\text{min}^{-1}$ . Faster heating rates resulted in a non-linear temperature profile during SPS. Modeling showed densification increase during the 550 TSS 20 process coincides with occurrences of local temperature increase which enhanced the plastic yielding contributions. Sintered samples with 98% density, flexural strength of  $\sim 550\text{ MPa}$ , and hardness of 210 HV are obtained for the 0.1 Er composition, while 93% dense samples with flexural strength of  $\sim 400\text{ MPa}$  and hardness of 167 HV are obtained for the 0.5 Er compositions.

A bimodal microstructure is observed in both sintered Al-Mg-Er bulks. Average grain sizes in all the sintered compacts was maintained below 100 nm with the tested sintering conditions. A final grain size of  $72 \pm 42\text{ nm}$  and  $86 \pm 52\text{ nm}$  is obtained in the 0.1 Er powder after the 500 TSS 20 and 550 TSS 20 schedules, respectively. The average grain size and distribution is similar in the 0.1 Er and Al 5356 alloys processed at 500 TSS 20, with 80% of the grain below 100 nm. In the 550 TSS 20 sample, 60% of the grains remain below 100 nm. The final grain size of the 0.5 Er 550 TSS 20 sample was  $50 \pm 21\text{ nm}$ , with over 90% of the grains below 100 nm.

Crystalline oxides were formed in the 0.1 Er sample during the 500 TSS 20 schedule, but not the 550 TSS 20, where-as opposite conditions were observed for the 0.5 Er powder with extensive crystalline oxide formation observed in the 550 TSS 20 processed samples. Nanocrystalline phases, indexed by SAED patterns, were determined as  $\alpha\text{-Al}$ ,  $\text{MgAl}_2\text{O}_4$ , and  $\gamma\text{-Al}_2\text{O}_3$ . The nanoscale oxide particles were analyzed by HRTEM, X-ray mapping and SAED patterns. Particles with Al-Mg-Er-Fe-O, Al-Mg-Er-Fe-O-N, and Al-Mg-O-N composition were observed.

## 6.7. References

- 6.1. German RM: Powder Metallurgy & Particulate Materials Processing, MPIF, New Jersey. 2005, p.181-220.
- 6.2. Xie G, Ohashi O, Song M *et al.* (2003) Behavior of oxide film at the interface between particles in sintered Al powders by pulse electric-current sintering, Metallurgical and Materials Transactions A 34:699–703.
- 6.3. Scudino S, Sakaliyska M, Surreddi KB, Eckert J (2009) Mechanical alloying and milling of Al-Mg alloys, Journal of Alloys and Compounds 483:2-7.
- 6.4. Xie G, Ohashi O, Song M, Mitsuishi K, Furuya K (2005) Reduction mechanism of surface oxide films and characterization of formations on pulse electric-current sintered Al–Mg alloy powders, Applied Surface Science 241:102-106.
- 6.5. Sasaki TT, Mukai T, Hono K (2007) A high-strength bulk nanocrystalline Al–Fe alloy processed by mechanical alloying and spark plasma sintering, Scripta Materialia 57:189-192.
- 6.6. Luton MJ, Jayanth CS, Disko MM, Matras S and Vallone J (1988) Cryomilling of nano-phase dispersion strengthened aluminum, Proceedings of Materials Research Society (MRS), 132:79-86.
- 6.7. Susegg O, Hellum E, Olsen A, Luton MJ (1993) HREM study of dispersoids in cryomilled oxide dispersion strengthened materials, Philosophical Magazine A 68:367-380.
- 6.8. Chen PC, Shih TS, Wu CY (2009) Thermally formed oxides on Al-2 and 3.5 mass % Mg alloys heated and held in different gases, Materials Transactions 50:2366-2372.
- 6.9. Zhou F, Lee J, Lavernia EJ (2001) Grain growth kinetics of a mechanically milled nanocrystalline Al, Scripta Materialia 44:2013-2017.

- 6.10. Zhou F, Lee J, Dallek S, Lavernia EJ (2001) High grain size stability of nanocrystalline Al prepared by mechanical attrition, *Journal of Materials Research* 16:3451-3458.
- 6.11. Zhou F, Liao XZ, Zhu YT *et al.* (2003) Microstructural evolution during recovery and recrystallization of a nanocrystalline Al-Mg alloy prepared by cryogenic ball milling, *Acta Materialia* 51:2777-2791.
- 6.12. Ye J, Ajdelsztajn L, Schoenung J (2006) Bulk nanocrystalline aluminum 5083 alloy fabricated by a novel technique: Cryomilling and spark plasma sintering, *Metallurgical and Materials Transactions A* 37:2569-2579.
- 6.13. Rana JK, Sivaprahasam D, Raju KS, Sarma VS (2009) Microstructure and mechanical properties of nanocrystalline high strength Al-Mg-Si (AA6061) alloy by high energy ball milling and spark plasma sintering, *Materials Science and Engineering A* 527:292-296.
- 6.14. Roy I, Chauhan M, Lavernia EJ, Mohamed FA (2006) Thermal stability in bulk cryomilled ultrafine-grained 5083 Al alloy, *Metallurgical and Materials Transactions A* 37:721-730.
- 6.15. Ji G, Grosdidier T, Bozzolo N, Launois S (2007) The mechanisms of microstructure formation in a nanostructured oxide dispersion strengthened FeAl alloy obtained by spark plasma sintering, *Intermetallics* 15:108-118.
- 6.16. Xiong Y, Liu D, Li Y *et al.* (2012) Spark plasma sintering of cryomilled nanocrystalline Al alloy - part I: Microstructure evolution, *Metallurgical and Materials Transactions A* 43:327-339.
- 6.17. Burke JE (1949) Some factors affecting the rate of grain growth in metals, *Transactions of the Metallurgical Society of AIME*, 180:73-91.
- 6.18. Cahn JW (1962) The impurity-drag effect in grain boundary motion, *Acta Metallurgica* 10:768-798.
- 6.19. Lücke K and Stüwe HP (1971) On the theory of impurity controlled grain boundary motion, *Acta Metallurgica* 19:1087-1099.

- 6.20. Hersent E, Marthinsen K and Nes E (2013) The effect of solute atoms on grain boundary migration: A solute pinning approach, *Metallurgical and Materials Transactions A* 44:3364-3375.
- 6.21. Hersent E, Marthinsen K, Nes E (2014) A solute pinning approach to solute drag in multi-component solid solution alloys, *Modeling and Numerical Simulation of Material Science* 4:8-13.
- 6.22. Kerkove MA, Wood TD, Sanders PG *et al.* (2014) The diffusion coefficient of scandium in dilute aluminum-scandium alloys, *Metallurgical and Materials Transactions A* 45:3800-3805.
- 6.23. Du Y, Chang YA, Huang B, Gong W *et al.* (2003) Diffusion coefficients of some solutes in fcc and liquid Al: critical evaluation and correlation, *Materials Science and Engineering A* 363:140-151.
- 6.24. Haslam AJ, Yamakov V, Moldovan D, Wolf D *et al.* (2004) Stress-enhanced grain growth in nanocrystalline materials by molecular-dynamics simulations, *Advances in Science and Technology* 44:1-8.
- 6.25. Saheb N, Khan MS, Hakeem AS (2015) Effect of processing on mechanically alloyed and spark plasma sintered Al-Al<sub>2</sub>O<sub>3</sub> nanocomposites, *Journal of Nanomaterials* 1-13
- 6.26. Prabhu B, Suryanarayana C, An L, Vaidyanathan R (2006) Synthesis and characterization of high volume fraction Al–Al<sub>2</sub>O<sub>3</sub> nanocomposite powders by high-energy milling, *Materials Science and Engineering A* 425:192–200.
- 6.27. Suryanarayana C (2008) Recent developments in mechanical alloying, *Reviews on Advanced Materials Science* 18:203-211.
- 6.28. Milligan J (2013) Surface modification of heat treatable Al components using cryomilled and rapidly solidified Al-Si, Ph.D. Thesis, McGill University, Montreal, QC, Canada, 2013.
- 6.29. Olevsky EA, Froyen L (2009) Impact of thermal diffusion on densification during SPS. *Journal of the American Ceramic Society* 92:S122–S132

- 6.30. Xie G, Ohashi O, Yamaguchi N, Wang A (2003) Effect of surface oxide films on the properties of pulse electric-current sintered metal powders, *Metallurgical and Materials Transactions A* 34:2655-2661.
- 6.31. Han BQ, Lavernia EJ (2005) High-temperature behaviour of a cryomilled ultra-fine grained Al-7.5% Mg alloy, *Materials Science and Engineering A* 410-411:417-421.
- 6.32. Ye J, Han BQ, Lee Z *et al.* (2005) A tri-modal aluminum based composite with super-high strength, *Scripta Materialia* 53:481-486.
- 6.33. Olevsky E, Froyen L (2006) Constitutive modeling of spark-plasma sintering of conductive materials, *Scripta Materialia* 55:1175-1178.
- 6.34. Kuz'mov AV, Olevskii EA, Aleksandrova EV (2013) Effect of micrononuniform heating of powder in field-assisted sintering on shrinkage kinetics, *Powder Metallurgy and Metal Ceramics* 51:657-665.
- 6.35. Xiong Y, Liu D, Li Y *et al.* (2012) Spark plasma sintering of cryomilled nanocrystalline Al alloy - part I: microstructure evolution, *Metallurgical and Materials Transactions A* 43:327-339.
- 6.36. Singman CN (1984) Atomic Volume and Allotropy of the Elements, *Journal of Chemical Education* 61:137-142.
- 6.37. A Handbook of Lattice Spacings and Structures of Metals and Alloys Volume 4. Pearson WB: Chapter 7 – Tabulated Lattice spacings and data of the elements, p124, 1958
- 6.38. ASM Handbook Volume 2 Properties and Selection: Nonferrous Alloys and Special-Purpose Materials, 5083, p363.
- 6.39. Frost HJ, Ashby MF, *Deformation-Mechanism Maps*, Pergamon Press, NY, 1982.

## Chapter 7 Multi-stage SPS Processing of 0.1 Er Cryomilled Powder

### 7.1. Introduction

Processing of the Al-Mg-Er powders by the TSS schedules in the previous chapter showed that conventional SPS processing parameters ( $100\text{ }^{\circ}\text{C}\cdot\text{min}^{-1}$  and 50 MPa) produced poorly consolidated material with wide variations in 3-point flexural strength. In this chapter improved consolidation of the 0.1 Er powders is achieved by testing conventional SPS parameters with multi-stage sintering schedules (MSS), where  $T_1 < T_2 < T_3$  for isothermal hold times of 5 to 10 minutes. More uniform consolidation and grain growth is observed under the MSS conditions versus TSS conditions. Although longer holds at high temperatures in the MSS schedules have no significant effect on the average grain size of the samples, increased variability (i.e.: standard deviation) of the mechanical properties is observed. Ideal sintering conditions are obtained with the 350 MSS 5 sintering schedule. The minimal grain growth observed during sintering is attributed to second phase pinning forces and the resultant temperature-dependent Zener limit grain size which controls the driving force for grain growth.

### 7.2. Background

Reddy *et al.* [7.1,7.2] have shown that multi-stage sintering of nanocrystalline alumina powders with SPS leads to better consolidated material with uniform mechanical properties and unimodal grain growth. Improved consolidation was achieved in their study when a three-stage (MSS) sintering process was used as opposed to two-stage (TSS) and single stage (SSS) schedules. Reddy *et al.* [7.1] attributed the improvement in consolidation of alumina with their multi-stage sintering to the high current discharge applied at each new sintering stage, which they claimed promoted new necking events due to surface cleaning by the spark discharge. Similarly, studies in AlN have shown that current-assisted sintering promotes oxide removal by “surface cleaning” resulting from spark discharge within the powder bed [7.3]. Multi-stage SPS sintering of the 0.1

Er powders could therefore enhance the consolidation due to increased oxide removal during the additional sintering stages.

A three-step (MSS) process where the temperature schedule is  $T_1 < T_2 < T_3$  was selected. Prolonged sintering at high temperatures will encourage grain growth in the nanocrystalline system. As discussed in Chapter 5, the grain growth in the 0.1 Er powder is influenced by drag/pinning forces due to solute/impurity content and oxide dispersoids within the powders. In addition, grain growth can be hindered or controlled by the precipitation of second phases. It has been shown in the work of Ferry *et al.* [7.4] that grain coarsening in an ultrafine grained Al-Sc alloy, produced by ECAP, was controlled by the coarsening of the nanoscale  $\text{Al}_3\text{Sc}$  precipitates in the alloy. Likewise, the presence of nanoscale  $\text{Al}_3\text{Er}$  could contribute to the drag/pining effects in the 0.1 Er powders.

Previous studies have shown that the average radius of homogeneously precipitated  $\text{Al}_3\text{Er}$  is 1.5 nm after 10 minutes of ageing at 350 °C in a coarse-grained Al-0.04 at.%Er alloy [7.5], with coarsening of the precipitate phase to 12 nm after ageing for 65 hours. Although precipitation of nanoscale  $\text{Al}_3\text{Er}$  phases was not observed after annealing of the 0.1 Er powders, precipitation may occur during sintering due to SPS processing conditions such as fast heating rates and the presence of an electric field. Literature has shown that precipitation of  $\text{L}_{12}$  phases is affected by the heating rate to the ageing temperature. Deschamps *et al.* [7.6] observed that the heating rate to the ageing temperature affects the size of the  $\text{Al}_3(\text{Sc,Zr})$  precipitates obtained in an Al-Sc-Zr alloy. Larger precipitates almost 200 nm in size are obtained when the heating rate is increased from 10 °C·min<sup>-1</sup> to 430 °C·min<sup>-1</sup> for ageing at 450 °C [7.6]. Onodera and Hirano [7.7] have also shown that DC current density  $j$  has an effect on the ageing process in an Al-4 wt.% Cu alloy. Although the influence of current density on the aging kinetics varied with the aging temperature, in general for  $j > 10^3 \text{ A}\cdot\text{cm}^{-2}$  the current enhanced the aging rate, but the aging process was slightly retarded when  $j < 10^3 \text{ A}\cdot\text{cm}^{-2}$ . Therefore, heating rates and current density conditions in the powder bed may enhance the ageing kinetics of the  $\text{Al}_3\text{Er}$  phase.

MSS sintering temperatures were selected as 350 °C ( $T_1 = 0.6T_m$ ), 450 °C ( $T_2 = 0.8T_m$ ), and 500 °C ( $T_3 = 0.9T_m$ ); holding times were varied from 5 to 10 minutes. The first sintering temperature is set to 350 °C to obtain slow grain growth kinetics during the initial consolidation step and encourage heterogeneous precipitation of nanoscale  $Al_3Er$  phase within the powder compact. Sintering temperatures of 450 °C and 500 °C are then selected to improve densification and promote faster precipitation and growth of the  $Al_3Er$  precipitates. Effects of the MSS schedules on sintering and grain growth of the 0.1 Er powders are compared to those of the TSS process in this chapter.

### **7.3. Phases in sintered samples**

#### **7.3.1. XRD results**

As detailed in Chapter 5, a supersaturated solid solution was formed in the 0.1 Er powders during milling with a final lattice parameter of 4.0662 Å. During SPS sintering, solid-state reduction reactions and decomposition of the solid solution occur. XRD spectra for the sintered samples are presented in Figure 7.1. Minor peaks corresponding to the spinel  $MgAl_2O_4$  phase was observed in both the 500 TSS 20 and 350 MSS 10 processed samples. However, lattice parameters obtained from the sintered samples indicate a loss of solute supersaturation occurred under all sintering conditions. A summary of the results from XRD analysis of the milled powders and the sintered samples is presented in Table 7.1. It is estimated that near room temperature equilibrium levels of Mg are left in the matrix after consolidation, with 1.57 at.%, 2.11 at.% and 1.50 at.% in the 500 TSS 20, 350 MSS 5 and 350 MSS 10 samples, respectively.

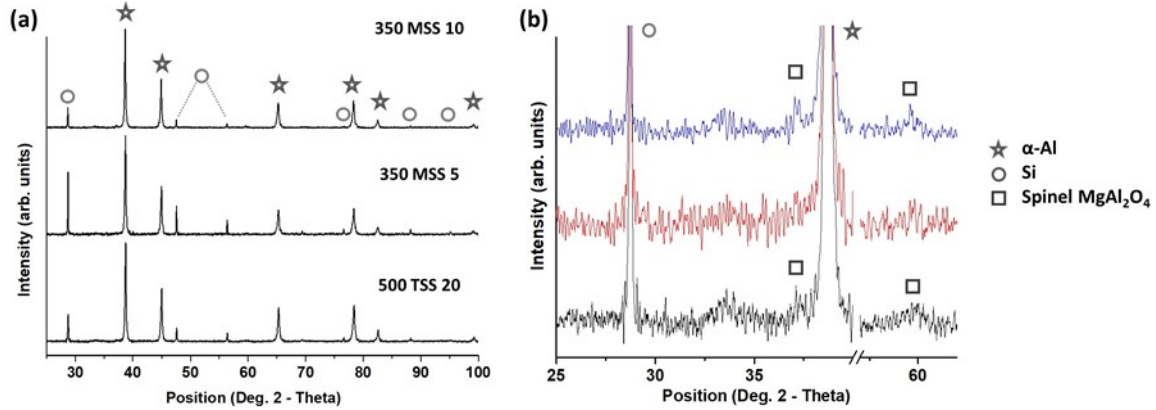


Figure 7.1 (a) XRD spectra of the TSS and MSS sintered samples; (b) close-up of minor peaks in XRD spectra. Peaks have been normalized.

Table 7.1 XRD results for milled powders and sintered pucks

Powder Condition	Lattice parameter (Å)	Mg in matrix (at.%)
Milled powder	$4.0662 \pm 0.0015$	5.26
500 TSS 20	$4.0517 \pm 0.0004$	1.57
350 MSS 5	$4.0538 \pm 0.0003$	2.11
350 MSS 10	$4.0514 \pm 0.0011$	1.50

### 7.3.2. TEM results

X-ray microanalysis was used to observe the distribution of elements in the coarse-grained and nanocrystalline regions of the sintered microstructure. Representative X-ray microanalysis of the TSS and MSS (350 MSS 5) samples is presented in Figure 7.2. These X-ray spectra indicate higher levels of O in the nanocrystalline regions compared to the coarse grains. Although there is Mg enrichment in the nanocrystalline regions in the MSS sample, Mg distribution is similar in coarse and nanocrystalline grained regions in the TSS sample. Signals for Er and impurity elements (i.e.: Ti, Fe, Ni) are not

generally detected in the MSS samples, but small peaks are detected in the TSS sample as shown in the insets. The Cu peaks detected in the samples comes from the TEM sample holder. Representative images taken from the 350 MSS 5 sample are presented in Figure 7.3. Diffraction patterns taken from the nanocrystalline regions (Figure 7.3(a) and 7.3(b)) consist of rings that are indexed to the  $\alpha$ -Al (blue) and  $\text{MgAl}_2\text{O}_4$  spinel (red) phases. Some coarse-grained regions show contrast suggestive of second phase precipitation or crystal imperfections (Figure 7.3(c) and 7.3(d)). However, the absence of  $L1_2$  superlattice reflections in the inset diffraction pattern suggests the observed contrast is due to the presence of crystal imperfections. Similar features (i.e.: nanocrystalline SAED patterns, contrast features in large grains) are observed in the 500 TSS 20 and 350 MSS 10 samples.

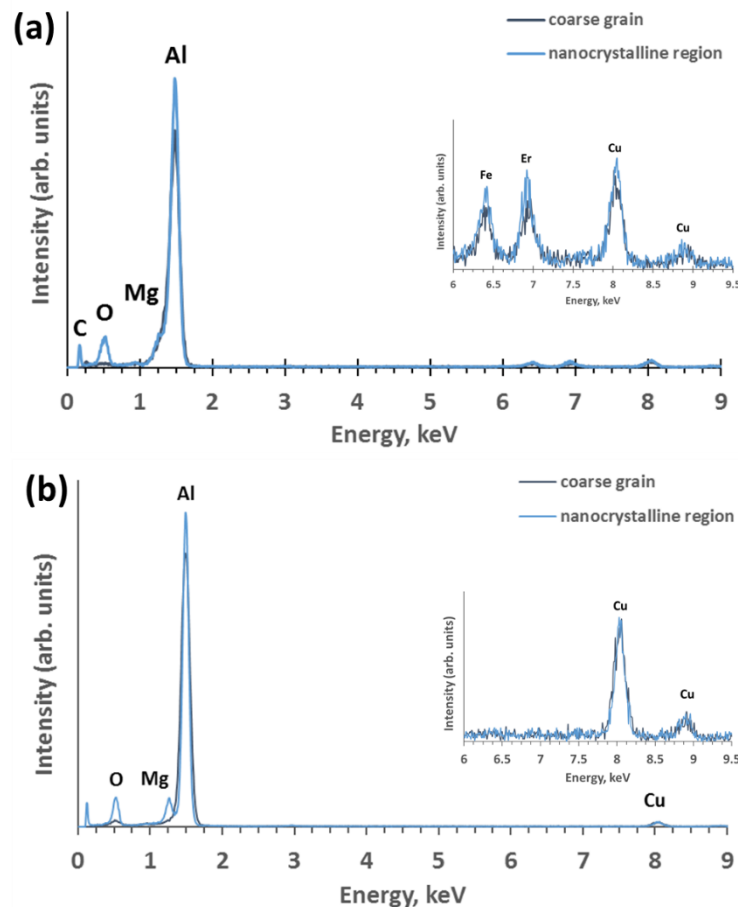


Figure 7.2 X-ray spectrums taken from nanocrystalline and coarse-grained regions of (a) 500 TSS 20 and (b) 350 MSS 5 samples showing distribution of solute elements.

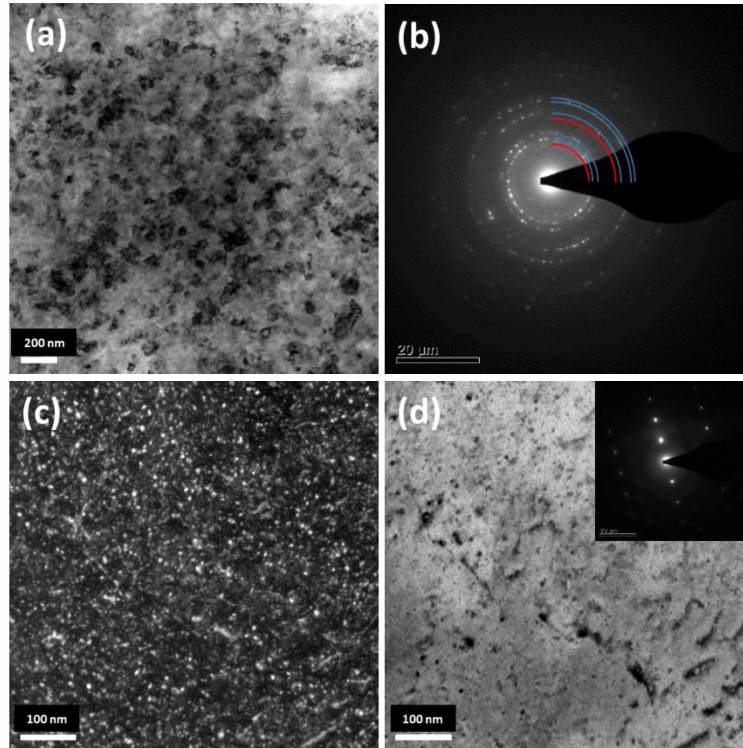
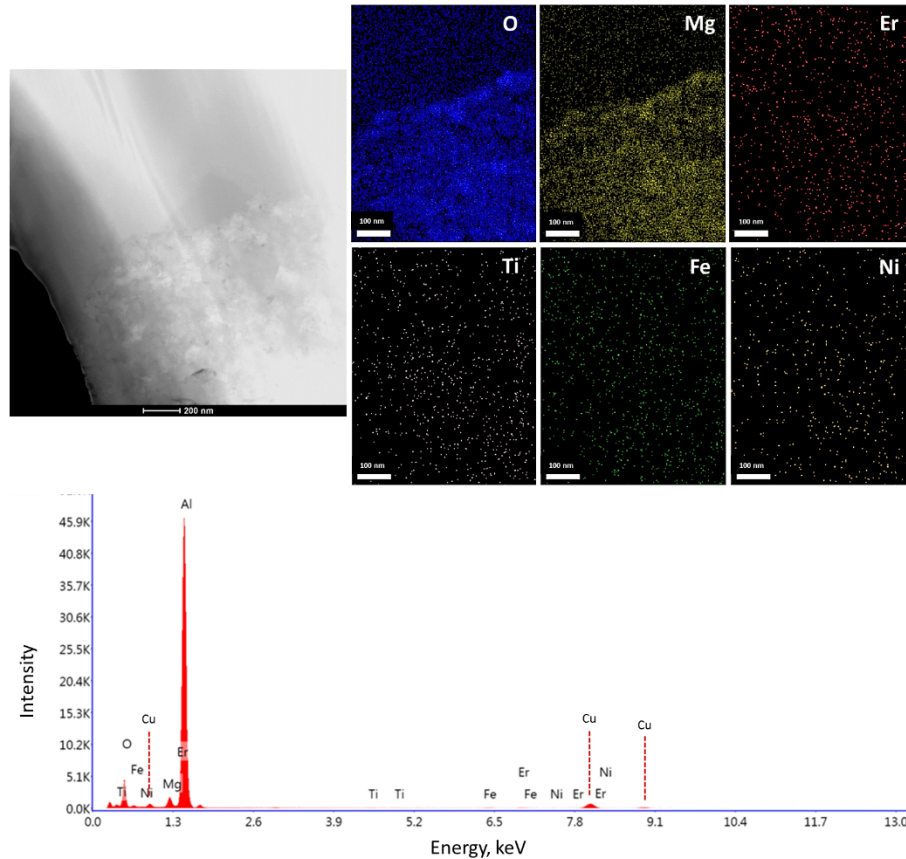


Figure 7.3 TEM analysis of phases in the 350 MSS 5 sample: (a) nanocrystalline region imaged in BF mode; (b) corresponding diffraction pattern from area shown in (a) indexed with colored arcs – Al (blue) and  $\text{MgAl}_2\text{O}_4$  (red); coarse grain imaged in DF (c) and BF (d) mode with inset SAED pattern indexed as Al from  $B = [121]$  direction.

X-ray elemental maps of the 350 MSS 5 sample are presented in Figure 7.4. Mg and O enrichment in the nanocrystalline regions compared to the coarse-grained region is observed, similar to the results from the EDS spot analysis. X-ray spectrum collected from the mapping area show no signal from Er or the impurity elements Ti, Fe and Ni. Mg and O rich regions ( $\sim 50$  nm) are observed at the interface between coarse and nanocrystalline grains, suggesting the presence of nanoscale oxides at the interface. Concentrated regions of Mg and O atoms, interpreted as oxide particles, are also infrequently observed within the nanocrystalline regions.



**Figure 7.4 X-ray elemental maps of the 350 MSS 5 sample showing higher concentrations of Mg and O in the nanocrystalline regions. X-ray spectrum collected from the mapping area showing the elements present**

X-ray elemental maps of the 350 MSS 10 samples are shown in Figure 7.5 to 7.7. Similar to the results of the 350 MSS 5 sample higher Mg and O concentrations are observed in the nanocrystalline regions (Figure 7.5). Highly concentrated regions of Mg and O atoms within the nanocrystalline regions are more frequently observed in the 350 MSS 10 samples as shown in Figures 7.6 and 7.7. Fe-rich clusters of approximately 30 nm in size (Figure 7.5), and Fe and Ni rich clusters of approximately 200 – 300 nm in size were also observed within the nanocrystalline regions (Figure 7.6 and 7.7).

Second phase precipitation of Al-Fe phases in milled Al systems was observed after SPS sintering. In milled Al-5 at.% Fe Sasaki et al [7.8] observed that SPS consolidation of as-milled nanocrystalline  $\alpha$ -Al solid solution resulted in a mixture of  $\alpha$ -Al and Al<sub>6</sub>Fe grains of ~80 nm in the nanocrystalline regions [7.8]. As shown previously in Chapter 5, precipitation of Al-Fe phases occurs during annealing. Nanoscale Al-Fe

precipitates of ~80 nm size were observed in the 0.1 Er powder after annealing at 330 °C for 1 hour, almost twice the 30 nm size of Al-Fe ( $\text{Al}_6\text{Fe}$ ) reported in literature [7.9]. It was observed that deformation affects the precipitation of Al-Fe phases in an Al-0.03 wt.% Fe alloy [7.10]. In a 65% cold-drawn specimen, the time-temperature-precipitation (TTP) curve shows that metastable  $\text{Al}_6\text{Fe}$  phase forms in the low temperature range, while the equilibrium  $\text{Al}_3\text{Fe}$  phase forms in the high temperature range. It is suggested that the metastable phase can precipitate when dislocation substructures are remaining; and the stable precipitate is formed after dislocation substructures have been annealed out [7.10]. The simple crystal structure of the  $\text{Al}_6\text{Fe}$  phase (orthorhombic, 28 atoms) allows it to nucleate and grow easier than  $\text{Al}_3\text{Fe}$  phase (monoclinic, 102 atoms), especially in strained regions around dislocations or cell walls [7.10]. It is possible that the precipitate observed in the 350 MSS 10 sample is the  $\text{Al}_6\text{Fe}$  phase, as  $\text{Al}_6\text{Fe}$  precipitation can occur in ~ 10 minutes at 450 °C according to the TTP from [7.10].

In alloys with Fe and Ni solutes, the formation of  $\text{Al}_9\text{FeNi}$  phases is most probable at higher Fe content when Fe-Ni ratio  $\approx 1$ . Typically these aluminide particles form by a peritectic reaction during solidification of an alloy but can be modified during subsequent processes.  $\text{Al}_9\text{FeNi}$  particles were observed in an Al-Cu-Mg-Fe-Ni-Sc alloy produced by cryomilling and SPS consolidation [7.11]. The  $\text{Al}_9\text{FeNi}$  particles were originally observed in the atomized powder, but were then broken down during milling to UFG – micron size particles; these particles then coalesced to larger sizes during sintering at 400 °C [7.11]. However, another study of  $\text{Al}_{80}\text{Fe}_{10}\text{Ti}_5\text{Ni}_5$  (at%) powder mixture showed that a supersaturated solid solution (SSS), nanocrystalline  $\text{Al}_9\text{FeNi}/\text{Al}_3\text{Ti}$  (~ 7 nm) and amorphous phases are formed during mechanical milling [7.12]. The SSS and amorphous phases are then transformed to  $\text{Al}_9\text{FeNi}/\text{Al}_3\text{Ti}$  intermetallic compound upon annealing of the milled powders [7.12]. It is possible that the 200 – 300 nm Al-Fe-Ni clusters, observed in the nanocrystalline regions of the 350 MSS 10 sample, could form during SPS due to coalescence of pre-existing nanocrystalline  $\text{Al}_9\text{FeNi}$  phases or direct transformation from the SSS Al matrix.

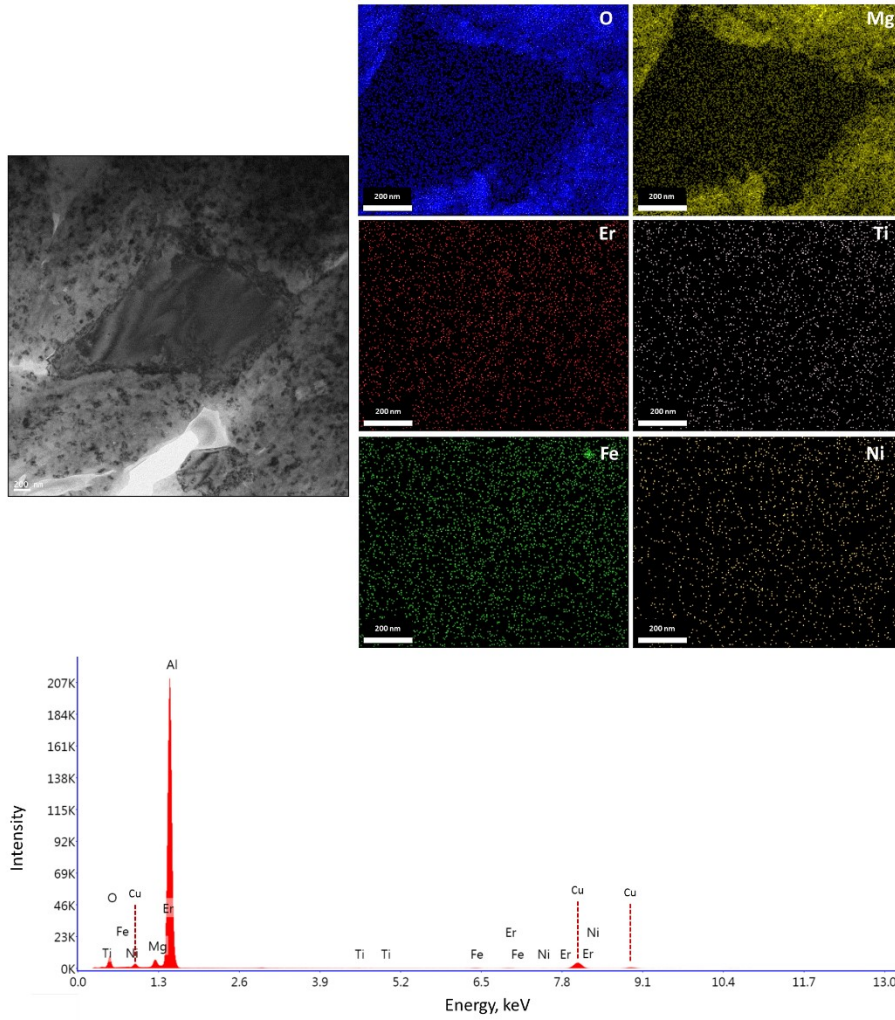


Figure 7.5 X-ray elemental maps of the 350 MSS 10 sample showing higher concentrations of Mg and O within the nanocrystalline regions. X-ray spectrum collected from the mapping area showing the elements present.

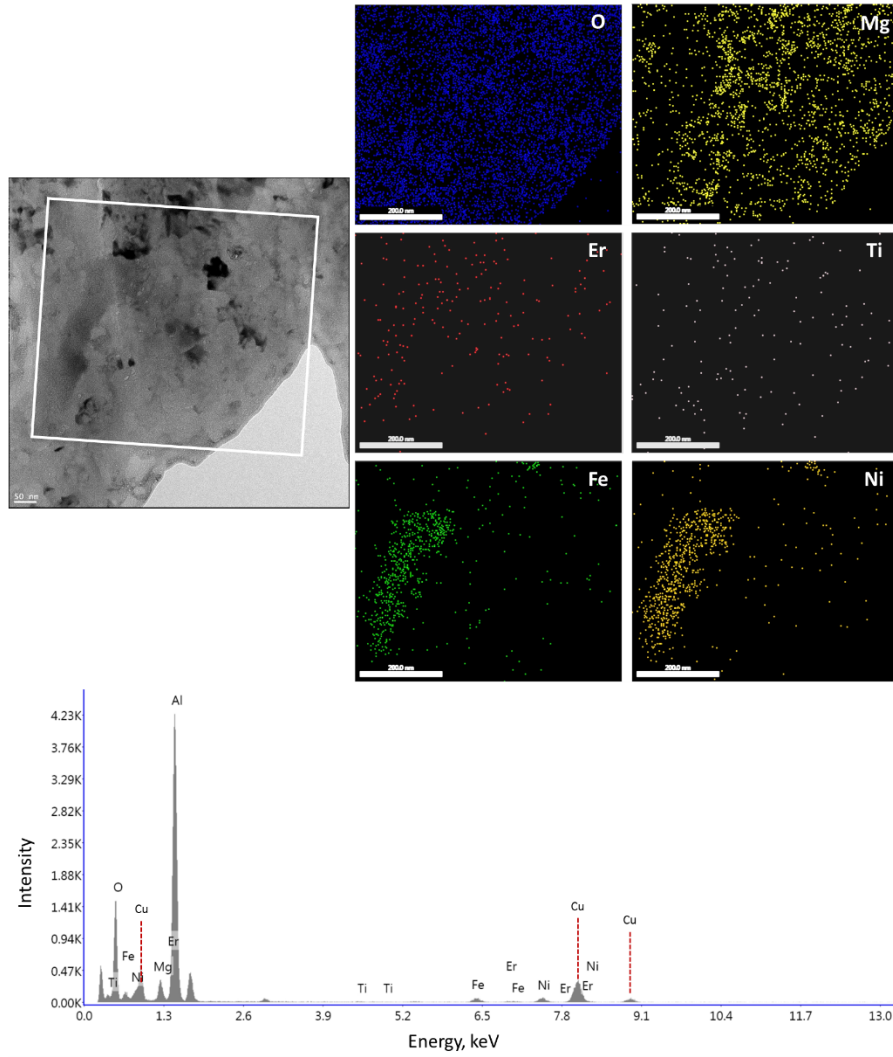
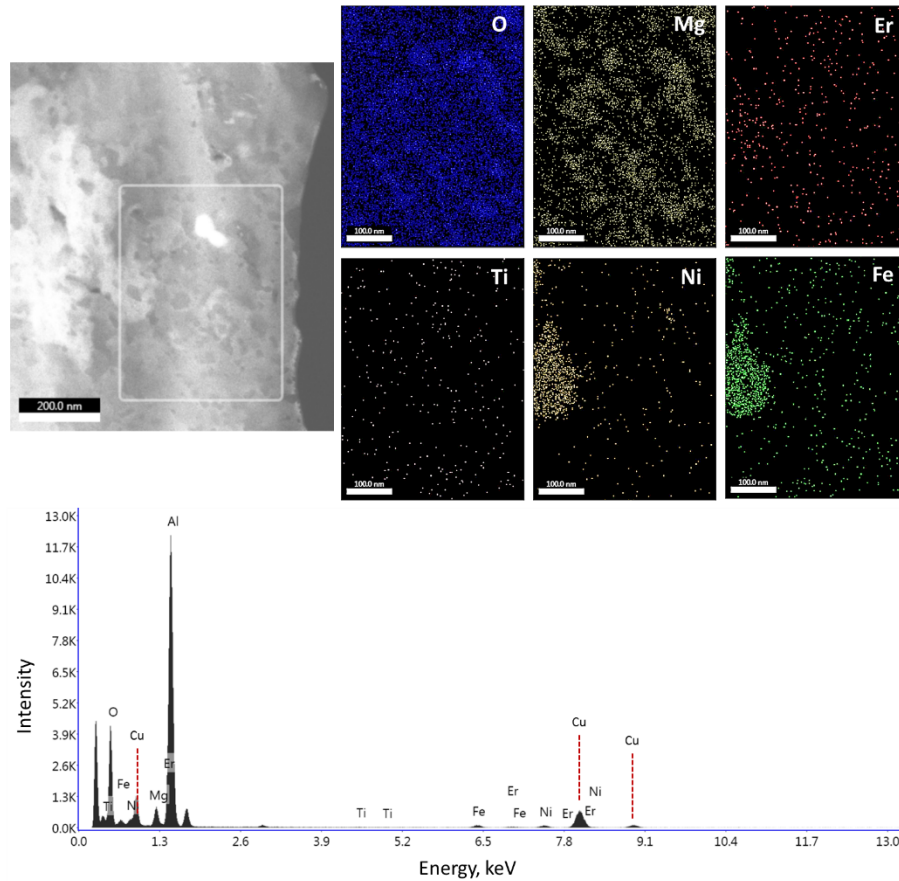


Figure 7.6 X-ray elemental maps of a nanocrystalline region in the 350 MSS 10 sample showing Fe and Ni rich clusters of ~ 300 nm size suggesting the presence of Al-Fe-Ni precipitates. X-ray spectrum collected from the mapping area showing the elements present.



**Figure 7.7 X-ray elemental maps of a nanocrystalline region in the 350 MSS 10 sample showing clusters of Mg and O atoms. Fe and Ni rich clusters of ~ 200 nm size suggest the presence of nanoscale Al-Fe-Ni precipitate. X-ray spectrum collected from the mapping area shows the elements present.**

Similarly to the 350 MSS 5 and 350 MSS 10 samples, X-ray elemental mapping of the 500 TSS 20 sample (Figure 7.8) shows Mg and O clusters suggesting the presence of nanoscale oxides within the nanocrystalline regions. The 500 TSS 20 sample shows no clustering of Fe or Ni solutes, but instead some clustering of Er and Ti solutes is observed in the nanocrystalline regions. This suggests nanoscale Al-Er-Ti precipitates around 100 nm in size. These types of phases were rarely observed within the sample. Similar sized precipitates have been observed in Al-Mg-Sc alloys [7.13]. UFG Al-Mg-Sc alloys, produced by cryomilling and consolidated by HIP followed by extrusion or dual mode dynamic forging, contained ~ 154 nm Al<sub>3</sub>Sc precipitates [7.13]. However, literature shows that homogeneously precipitated Al<sub>3</sub>Er is 1.5 nm after 10

minutes of ageing at 350 °C in an Al-0.04 at.%Er alloy with coarsening to a size of 12 nm observed after ageing for 65 hours [7.5]. It is possible that the sintering conditions – such as fast heating rates, locally high current densities, high temperature  $T_1$  – may enhance the precipitation kinetics within the compact, resulting in larger precipitates than those commonly observed in literature.

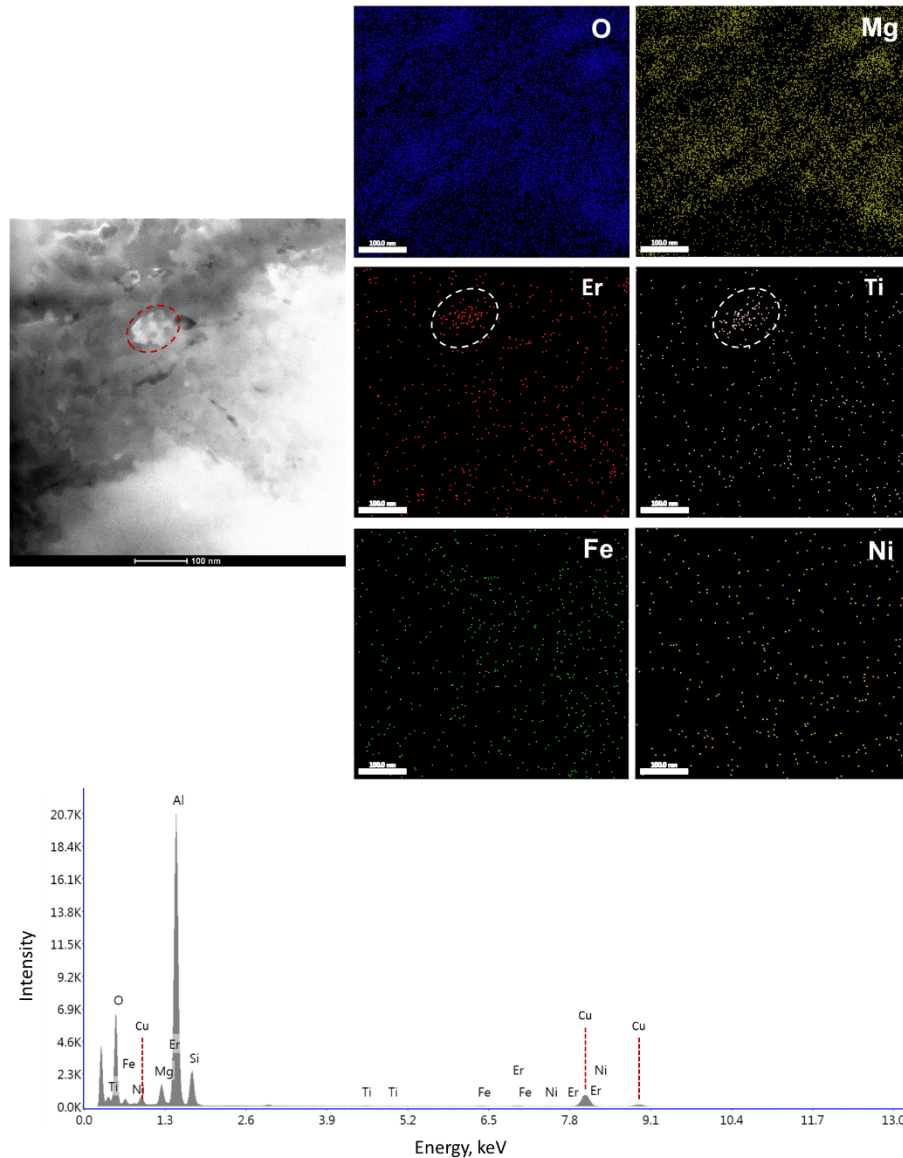


**Figure 7.8 X-ray elemental maps of the 500 TSS 20 sample showing higher concentrations of Mg and O in the nanocrystalline regions and possible clustering of Er and Ti atoms. X-ray spectrum collected from mapping area showing the elements present.**

#### 7.4. Microstructure and grain size analysis

The microstructure of the consolidated material is examined in this section. The grain size and micro-strain in the cryomilled powder were determined from XRD peak broadening. TEM image analysis was also used to confirm the average grain size in the sintered samples. Results of these analysis are compiled in Table 7.2, with standard deviation of the TEM grain size reported and the 95% CI given in the round brackets. In the 0.1 Er milled powder, grain size was determined to be 22 nm, with a micro-strain of 0.094% after 30 hours of milling. TEM image analysis were in agreement with the XRD results, with the average grain size measured as  $16 \pm 1$  nm. Analysis of grain size distribution showed that all grains observed were below 100 nm in size with a narrow size distribution. Upon SPS consolidation, the micro-strain decreased to 0.078% and 0.082% after the 350 MSS 5 and 350 MSS 10 schedules, respectively. Micro-strain is higher in the MSS samples compared to the TSS sample with 0.069% strain after the 500 TSS 20 process. Samples produced by the MSS schedules have similar XRD grain sizes with 55 nm and 51 nm obtained for the 350 MSS 5 and 350 MSS 10 schedules, respectively. The XRD grain size is 57 nm for the 500 TSS 20 sample. The TEM grain sizes are in good agreement with the XRD measurements, with  $56 \pm 21$  nm,  $59 \pm 25$  nm and  $72 \pm 42$  nm obtained for the 350 MSS 5, 350 MSS 10 and 500 TSS 20 samples, respectively.

Table 7.2 Grain size and microstrain data

Powder Condition	Grain size, XRD (nm)	$G_{N'}$ , TEM (nm)	Microstrain (%)	$R^2$
Milled powder	22	$16 \pm 1$	0.094	0.92
500 TSS 20	57	$72 \pm 42$ (4)	0.069	0.95
350 MSS 5	55	$56 \pm 21$ (2)	0.078	0.86
350 MSS 10	51	$59 \pm 25$ (2)	0.082	0.84

Representative images of the microstructures in the sintered bulks are shown in Figure 7.9. Images in the left column of the figure shows the bimodal microstructure obtained regardless of the sintering schedule used; the middle column shows the nanocrystalline grains, while the right column shows the corresponding SAED patterns taken from the nanocrystalline regions. The diffraction patterns from all the nanocrystalline regions are identical, showing the characteristic Al rings and additional rings which were indexed to  $\text{MgAl}_2\text{O}_4$  spinel phase. The bimodal microstructure obtained is similar to those previously reported in literature [7.14-7.16]. Regions of coarse grains ( $\approx 1 - 3 \mu\text{m}$ ) were observed within a matrix of nanocrystalline grains in the sintered samples. Grain size distributions determined for the sintered samples are shown in Figure 7.10. The grain size distributions differed between the TSS and MSS schedules. In the MSS samples, greater than 90% of the measured grains were finer than 100 nm, with a standard deviation of  $\sim \pm 20$  nm around the average grain size. In the TSS sample, 80% of the measured grains were finer than 100 nm with a standard deviation of  $\sim \pm 40$  nm around the average grain size. The standard deviation in the MSS samples is about half that encountered in the TSS sample, suggesting the MSS sample exhibits more unimodal growth. Under similar one-stage SPS sintering conditions, the average grain size in the fine grained regions of sintered Al alloys was reported as between 100 - 150 nm [7.17,7.18].

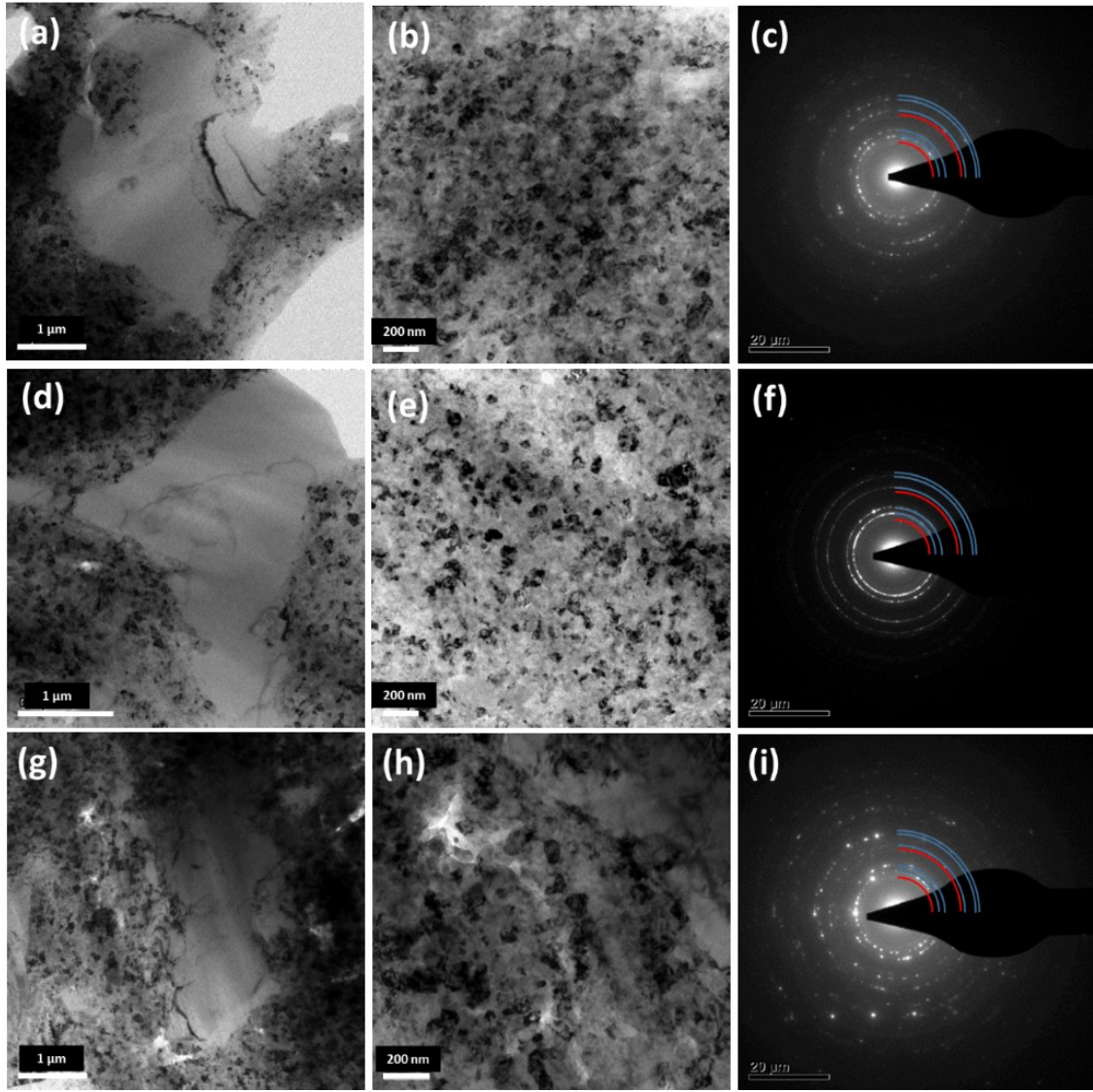


Figure 7.9 As sintered microstructure of 350 MSS 5 (first row), 350 MSS 10 (second row) and 500 TSS 20 (third row): Bimodal microstructure in sintered samples (a,d,g); BF images of nanocrystalline regions (b,e,h); corresponding SAED patterns (c,f,i) indexed with colored arcs – Al (blue arcs) and  $MgAl_2O_4$  (red arcs) phases.

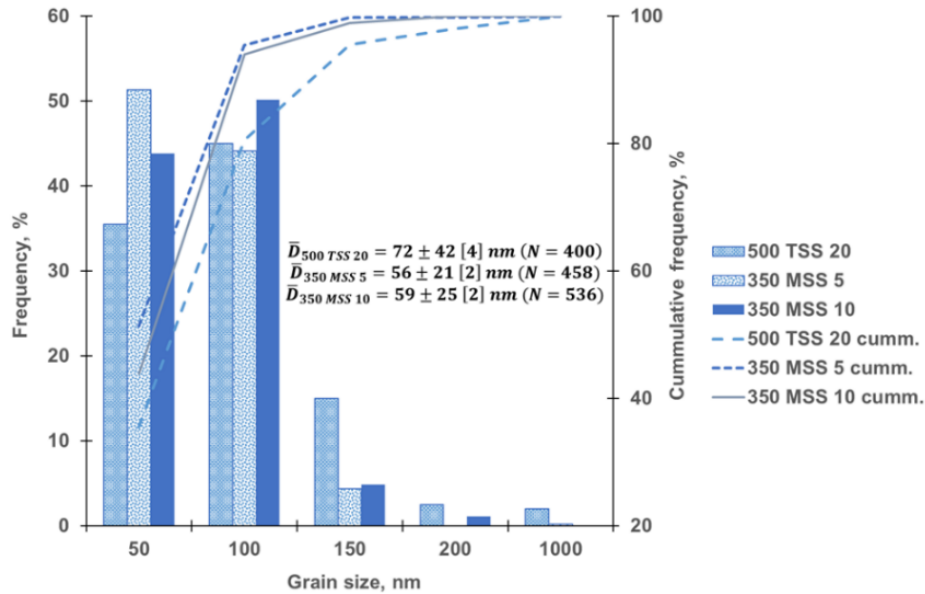


Figure 7.10 TEM grain size distributions in TSS and MSS sintered samples

## 7.5. Grain growth during consolidation

As discussed in Chapter 5 grain growth behavior in the milled Al-Mg-Er powder systems was attributed to combined solute/impurity drag and pinning by second phase particles. Isothermal annealing at 500 °C resulted in a grain size of 50 nm after one hour. While the MSS samples exhibit a similar average grain size of ~ 60 nm after 5 to 10 minutes of sintering at 500 °C, TSS samples show grain growth up to 72 nm after one minute at 500 °C. The differences in the grain growth behaviour may be related to the modes of pressure and temperature profile during the two processes.

Both experimental work [7.19,7.20] and molecular dynamics simulations [7.21] have shown that external stress affects grain growth in nanocrystalline materials. Cryomilled Al sintered by SPS under high pressure (i.e.: 300 MPa) exhibited increased grain growth due to grain rotation and coalescence [7.19]. Yao *et al.* [7.20] suggest that grain growth during hot forging of a trimodal Al composite may be influenced by the stored energy due to the large deformations during the process. Molecular dynamics simulations reveal that external stress affects grain growth by increasing both grain

boundary migration and grain rotation and coalescence events, possibly due to the enhancement of driving forces and/or grain boundary mobility [7.21]. Although pressures investigated in these references are much higher than present conditions (i.e.: 0.3 – 1 GPa versus 50 MPa), the application of an external stress could still provide some enhancement to grain boundary migration during SPS sintering, albeit at a lower magnitude.

Enhanced grain growth during SPS could be limited to the pressure ramping segment and initial isothermal hold during the SPS process. Yao et al [7.20] proposed that stored deformation energy during hot forging could drive the grain growth. Absorption of excess dislocations by the grain boundaries could cause local changes in the surface energy, leading to changing triple point angles and grain growth through strain induced grain boundary migration [7.20]. It is possible that stored deformation energy from the ramping segment of the SPS enhances grain growth during the stage one hold, with mainly curvature-driven grain growth during subsequent sintering stages. Thus, grain growth could be enhanced at 500 °C in a TSS sample. While grain growth in the MSS samples could be enhanced at 350 °C, but be mainly curvature-driven at 450 °C and 500 °C.

Burke's model [7.22] is given as

$$\frac{(D_0 - D)}{D_{max}} + \ln\left(\frac{D_{max} - D_0}{D_{max} - D}\right) = \frac{kt}{D_{max}^2} \quad (7.1)$$

where:  $D_0$  is the initial grain size,  $D$  is the average grain size,  $D_{max}$  is the Zener limit grain size in the system,  $k$  is a product of boundary mobility  $M_b$  and grain boundary energy  $\gamma$ , and  $t$  is time. Using the treatment of Hersent *et al.* [7.23], the boundary velocity can be expressed as

$$v = m_b \cdot P = \frac{1}{\frac{1}{M^{int}} + \frac{1}{M_A^{ext}} + \frac{1}{M_B^{ext}}} \cdot P \quad (7.2)$$

where:  $v$  is the boundary velocity,  $m_b$  is the boundary mobility due to solute drag,  $P$  is the driving pressure,  $M^{int}$  is the intrinsic mobility of the grain boundary,  $M_A^{ext}$  is the mobility of the grain boundary loaded with solute A, and  $M_B^{ext}$  is the mobility of the grain

boundary loaded with solute B. The mobility of the grain boundary loaded with impurities A,  $M_A^{ext}$ , is defined as:

$$M_A^{ext} = \frac{2}{nb^3} \frac{\Gamma_A b^4 v_D}{kT c_A} e^{-\frac{(2U_A^0 + U_A^s)}{kT}} \quad (\text{eq. 7.3})$$

where:  $\Gamma_A$  is a constant,  $b$  is the burger's vector of the matrix Al,  $v_D$  is the Debye frequency,  $U_A^0$  is the interaction energy between the solute atoms and the grain boundary,  $U_A^s$  is the activation energy for (volume) diffusion of the solute atom,  $nb$  is the number of atomic sites per unit area inside the matrix, and  $c_A$  is the volume impurity concentration of solute. The available atomic sites at the grain boundary for solute adsorption is taken as one monolayer of  $1.885 \cdot 10^{-5} \text{ mol} \cdot \text{m}^2$ . The activation energies for volume diffusion used for the calculations for  $m_b$  for Mg, Er, Ti, Fe and Ni in Al are shown in Table 7.3. The base interaction enthalpy is calculated using the suggested method by Lucke and Stuwe which is approximately  $6 \text{ kJ} \cdot \text{mol}^{-1}$  for the Al grain boundary. Diffusion coefficients and activation energy for Sc in Al were used as an approximation for Er behaviour in Al. The diffusion parameters for Sc in Al were taken from the results of Kerkove *et al.* [7.24] for a dilute Al-Sc system.

Grain growth during the 500 °C hold of the MSS schedule estimated by eq. 7.1 is shown in Figure 7.11. The limiting grain size  $D_{max}$  is taken as 60 nm. Starting grain size of 50 nm is based on the work of Ye *et al.* on SPS of cryomilled Al 5083 at 350 °C under 50 MPa and with  $100 \text{ }^\circ\text{Cmin}^{-1}$  heating rate [7.14]. Experimental results from the MSS schedules are fit well with eq. 7.1. These results suggest that the grain growth at 500 °C is curvature-driven during the MSS processes.

Table 7.3 Diffusion data for boundary mobility calculations

Element	Mg	Er (Sc*)	Ti	Fe	Ni	Al
$U_A^0$ (kJ·mol <sup>-1</sup> )	120.5	168	260	214	144.6	142
Ref.	[7.25]	[7.24]	[7.25]	[7.25]	[7.25]	[7.26]

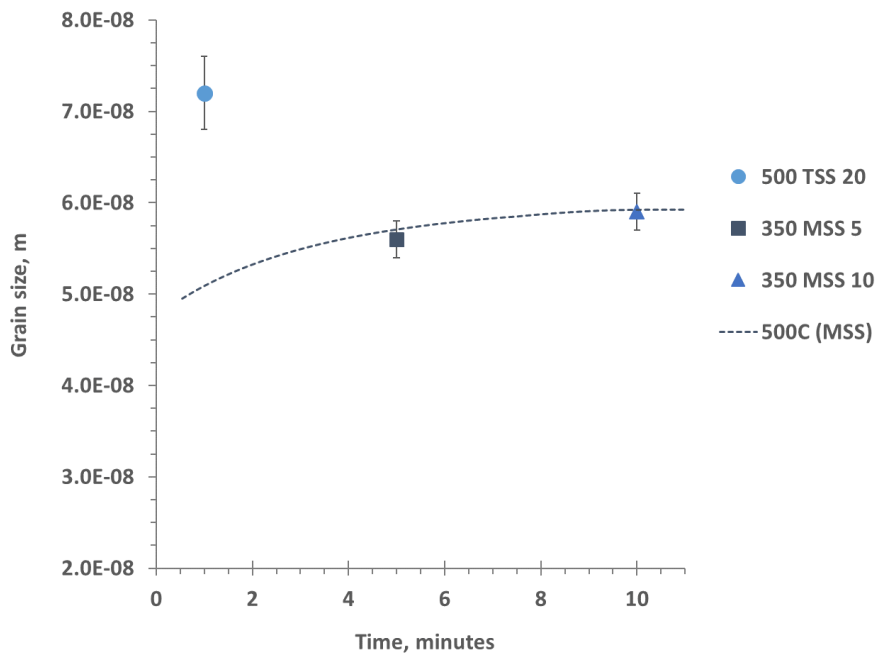


Figure 7.11 Estimation of grain growth during the TSS and MSS schedules using Burke's model with estimated boundary mobility  $m_b$

## 7.6. Consolidation in multi-stage sintered samples

Consolidation of the powders sintered by TSS and MSS schedules was determined by the final density and mechanical properties of the sintered pucks. Results are compiled in Table 7.4. Consolidation of the milled 0.1 Er powders is improved under MSS conditions compared to the TSS conditions. TSS samples have an average density of ~

92%, bend strength of  $440 \pm 216$  MPa, and hardness of  $166 \pm 39$  HV. A final density of 98% with a bend strength of 624 MPa and hardness of 183 HV was obtained for the 350 MSS 5 samples. An average density of 97% with bend strength of 567 MPa and hardness of 180 HV was obtained in the 350 MSS 10 samples. Fracture strengths of  $\sim 600$  MPa obtained in the MSS samples are comparable to the properties of Al-Al<sub>2</sub>O<sub>3</sub> composite powders, with 10 vol.% of 50 nm sized oxide particles, consolidated to full density by a combination of vacuum hot pressing and hot isostatic pressing [7.27] with tensile and compressive strengths of 515 MPa and 628 MPa, respectively. However, differences in the average value and standard deviation between the two MSS conditions indicates that more uniform consolidation is obtained with the 350 MSS 5 sintering schedule. The standard deviation for flexural strength doubles from  $\pm 76$  to  $\pm 173$  MPa, and hardness from  $\pm 5$  to  $\pm 31$  HV from the 350 MSS 5 to 350 MSS 10 conditions.

**Table 7.4 Properties of Multi-stage SPS sintered bulks**

Sintering Schedule	Density (% theor.)	3-point flexural strength (MPa)	Micro-hardness (HV <sub>50gf</sub> )
500 TSS 20	$91.5 \pm 6.4$	$440 \pm 216$	$166 \pm 39$
350 MSS 5	$97.8 \pm 1.0$	$624 \pm 76$	$183 \pm 5$
350 MSS 10	$97.1 \pm 3.0$	$567 \pm 173$	$180 \pm 31$

The densification curves for the MSS and TSS schedules are presented in Figure 7.12. Densification curves are obtained using the final density and dimensions of the sintered sample as well as the ram position monitored by the SPS apparatus. As previously shown in Chapter 4, most of the densification during the TSS schedule

occurs during the ramp up to  $T_1$ ; whereas in the MSS schedules, a step-wise densification occurs during each ramp between isothermal sintering stages. Density increases to 75% during the ramp to  $T_1 = 350$  °C with no macroscopic improvement observed by the continued hold at  $T_1$ . With increase to  $T_2 = 450$  °C a density of 85% is reached and the remaining densification is obtained during the final ramp to  $T_3 = 500$  °C. Single stage sintering at 350 °C and 450 °C corroborate the values from the densification curves, with ~75% theoretical density obtained after a 10 minute hold at 350 °C and ~88% obtained after a 20 minute hold at 450 °C.

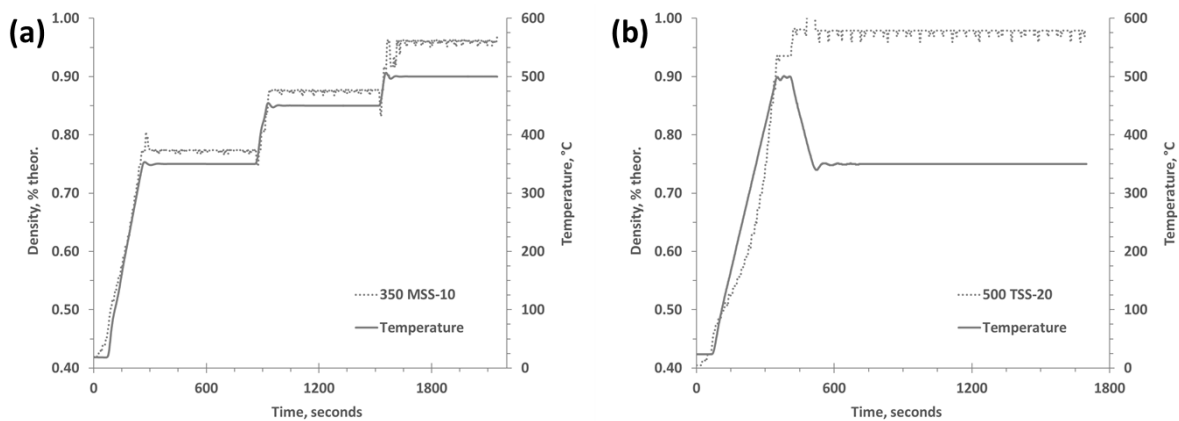


**Figure 7.12** Plotted densification curves for the (a) MSS and (b) TSS schedules

Removal of the oxide layer at particle interfaces will enhance consolidation of the powder compact. Oxide breakdown during current-assisted sintering of Al occurs mainly due to plastic deformation, with the effects of pressure being amplified by Joule heating within the powder bed leading to preferential heating at interfacial regions of particles and high temperatures at contact points [7.28,7.29]. It has also been proposed that the electric field can assist in removal of the oxide layer through discharges in micro-gaps in the powder bed [7.3]. These phenomena can be operative during both TSS and MSS sintering processes.

Increased oxide removal may occur during the MSS process due to the density of the powder bed at the different isothermal stages. Zadra *et al.* [7.30] observed improved consolidation of sintered Al powders, as determined by improved ductility, when pressure was applied at high temperature during SPS. One of the factors proposed for the improved consolidation was the density state of the powder bed. Zadra

*et al.* [7.30] proposed that the sample is subjected to a higher electrical field as a result of higher resistivity of the powder bed due to the loose powder. The high electric field then enhances atomic mobility and diffusion. Also due to low powder bed density there is a greater possibility of cleaning the powder surfaces due to sparks and/or higher local temperatures between the particles. Longer holding times are spent at lower powder bed density in the MSS versus TSS schedules, i.e.: 10 minute hold at 75% density and 5 – 10 minute holds at 85%. The holds at  $T_1$  and  $T_2$  in the MSS schedules could therefore provide increased opportunities for breakdown/removal of the oxide layer which will improve the final consolidation.

While the average density, flexural strength and hardness of the sintered compacts were similar for both MSS conditions, the longer holds at 450 °C and 500 °C during 350 MSS 10 lead to wider standard deviations in the properties. The cause of this decrease in consolidation quality with longer sintering time is unclear. However, one factor could be the increase of crystalline oxide (spinel) particles in the samples. Minor peaks associated with the spinel phase can be detected in the XRD spectrum obtained from the 350 MSS 10 sample but are absent for the 350 MSS 5 sample (see Figure 7.1). The presence of these peaks indicates growth of crystalline oxides during sintering. Prabhu [7.31] showed that for an alumina reinforced ODS Al alloy an increase in the oxide particle size from 50 nm to 150 nm reduced the tensile strength from 515 to 461 MPa, respectively, at 10 vol.% addition. Similarly, an increase in the oxide particle size with longer sintering time may adversely affect the fracture strength of the sintered MSS samples.

## 7.7. Summary

Cryomilled 0.1 Er powders were consolidated using multi-stage SPS schedules. Improved powder consolidation was observed with the MSS schedules compared to the TSS schedule. Although a bimodal microstructure was still obtained, average grain size and standard deviation was reduced from  $72 \pm 42$  nm in the TSS sample to  $56 \pm 21$  nm and  $59 \pm 25$  nm in the MSS samples. The average grain size of  $\sim 60$  nm was maintained after up to 10 mins of sintering at 500 °C ( $0.9 T_m$ ). Unlike the TSS results,

grain growth during the MSS schedules was suitably fitted using Burke's model, suggesting that the grain growth during MSS schedules is mainly curvature-driven. It is proposed that stored deformation energy due to applied external stress may enhance grain growth at high temperatures during TSS.

The best consolidation was obtained with the 350 MSS 5 schedule with sintered pucks of 98% theoretical density, flexural strength of  $624 \pm 76$  MPa and hardness of  $183 \pm 5$  HV. Although 350 MSS 10 samples showed similar (mean) mechanical properties, the standard deviations were wider and similar to those obtained for the 500 TSS 20 samples. Improved consolidation with the MSS versus TSS schedules could be due to improved cleaning of the powder surfaces due to longer hold times spent at low powder bed density. The holds at  $T_1$  and  $T_2$  at 75% and 85% density, respectively, could provide increased opportunities for breakdown/removal of the oxide layer due to discharges and/or higher local temperatures between the particles.

Second phase precipitation and nanocrystalline oxide formation were observed after sintering. XRD and SAED patterns showed the presence of  $\alpha$ -Al and spinel  $MgAl_2O_4$  phases. X-ray elemental maps revealed higher oxide content within the nanocrystalline regions of the sintered materials. X-ray elemental mapping revealed Al-Fe and Al-Fe-Ni rich clusters sized  $\sim 30$  nm and  $\sim 200 - 300$  nm size, respectively, in the 350 MSS 10 sample. Er and Ti rich clusters of  $\sim 150$  nm size were observed in the 500 TSS 20 sample.

## 7.8. References

- 7.1. Reddy KM, Kumar N, Basu B (2010) Innovative multi-stage spark plasma sintering to obtain strong and tough ultrafine-grained ceramics, *Scripta Materialia* 62:435-438.
- 7.2. Reddy KM, Kumar N, Basu B (2010) Inhibition of grain growth during the final stage of multi-stage spark plasma sintering of oxide ceramics, *Scripta Materialia* 63:585-588.

- 7.3. Groza JR, Garcia M, Schneider JA (2001) Surface effects in field assisted sintering, *Journal of Materials Research* 16:286-292.
- 7.4. Ferry M, Hamilton NE, Humphreys FJ (2005) Continuous and discontinuous grain coarsening in a fine-grained particle-containing in Al-Sc alloy, *Acta Materialia* 53:1097-1109.
- 7.5. Wen SP, Gao KY, Li Y, Huang H, Nie ZR (2011) Synergetic effect of Er and Zr on the precipitation hardening of Al-Er-Zr alloy. *Scripta Materialia* 65:592-595.
- 7.6. Deschamps A, Bley F, Lae L, Dumont M, Perrard F (2006) Characterisation and modelling of non-isothermal precipitation in metallic systems, *Advanced Engineering Materials* 8:1236-1239.
- 7.7. Onodera Y, Hirano KI (1976) The effect of direct electric current on precipitation in a bulk Al-4 wt% Cu alloy, *Journal of Materials Science* 11:809-816.
- 7.8. Sasaki TT, Mukai T, Hono K (2007) A high-strength bulk nanocrystalline Al-Fe alloy processed by mechanical alloying and spark plasma sintering, *Scripta Materialia* 57:189-192.
- 7.9. Shaw L, Luo H, Villegas J, Miracle D (2003) Thermal stability of nanostructured  $Al_{93}Fe_3Cr_2Ti_2$  alloys prepared via mechanical alloying, *Acta Materialia* 51:2647-2663.
- 7.10 Yamamoto A, Kato T, Tsubakino H (2004) Precipitation in an Al-300 ppm Fe alloy, *Materials Transactions* 45:3106-3113.
- 7.11 Zuniga A, Ajdelsztajn L, Lavernia EJ (2006) Spark Plasma Sintering of a Nanocrystalline Al-Cu-Mg-Fe-Ni-Sc Alloy, *Metallurgical and Materials Transactions A* 37:1343-1352.
- 7.12 Tavoosi M (2017) Fabrication and thermal characterization of amorphous and nanocrystalline Al<sub>9</sub>FeNi/Al<sub>3</sub>Ti compound, *Materials Chemistry and Physics* 186:44-51.

- 7.13. Harrell TJ, Topping TD, Wen H, Hu T *et al.* (2014) Microstructure and Strengthening Mechanisms in an Ultrafine Grained Al-Mg-Sc Alloy Produced by Powder Metallurgy, *Metallurgical and Materials Transactions A* 45:6329-6343.
- 7.14. Ye J, Ajdelsztajn L, Schoenung J (2006) Bulk nanocrystalline aluminum 5083 alloy fabricated by a novel technique: cryomilling and spark plasma sintering, *Metallurgical and Materials Transactions A* 37:2569-2579.
- 7.15. Rana JK, Sivaprahasam D, Raju KS, Sarma VS (2009) Microstructure and mechanical properties of nanocrystalline high strength Al-Mg-Si (AA6061) alloy by high energy ball milling and spark plasma sintering, *Materials Science and Engineering A* 527:292-296.
- 7.16. Roy I, Chauhan M, Lavernia EJ, Mohamed FA (2006) Thermal stability in bulk cryomilled ultrafine-grained 5083 Al alloy, *Metallurgical and Materials Transactions A* 37:721-730.
- 7.17. Zuniga A, Ajdelsztajn L, Lavernia EJ (2006) Spark plasma sintering of an Al-Cu-Mg-Fe-Ni-Sc alloy, *Metallurgical and Materials Transactions A* 37:1343-1352.
- 7.18. Chen H, Taq K, Yang B, Zhang J (2009) Nanostructured Al-Zn-Mg-Cu alloy synthesized by cryomilling and spark plasma sintering, *Transactions of Nonferrous Metals Society of China* 19:1110-1115.
- 7.19. Liu D, Wen H, Zhang D *et al.* (2014) Stress-enhanced grain growth in a nanostructured aluminium alloy during spark plasma sintering, *Philosophical Magazine Letters* 94:741-748.
- 7.20. Yao B, Simkin B, Majumdar B, Smith C *et al.* (2012) Strain-induced grain growth of cryomilled nanocrystalline Al in trimodal composites during forging, *Materials Science and Engineering A* 536:103-109.
- 7.21. Haslam AJ, Yamakov V, Moldovan D, Wolf D *et al.* (2004) Stress-enhanced grain growth in nanocrystalline materials by molecular-dynamics simulations, *Advances in Science and Technology* 44:1-8.

- 7.22. Burke JE (1949) Some factors affecting the rate of grain growth in metals, Transactions of the Metallurgical Society of AIME, 180:73-91.
- 7.23. Hersent E, Marthinsen K, Nes E (2014) A solute pinning approach to solute drag in multi-component solid solution alloys, Modeling and Numerical Simulation of Material Science 4:8-13.
- 7.24. Kerkove MA, Wood TD, Sanders PG *et al.* (2014) The diffusion coefficient of scandium in dilute aluminum-scandium alloys, Metallurgical and Materials Transactions A 45:3800-3805.
- 7.25. Du Y, Chang YA, Huang B, Gong W *et al.* (2003) Diffusion coefficients of some solutes in fcc and liquid Al: critical evaluation and correlation, Materials Science and Engineering A 363:140-151.
- 7.26. German RM: Powder Metallurgy & Particulate Materials Processing, MPIF, New Jersey. 2005, p.181-217.
- 7.27. Suryanarayana C (2008) Recent developments in mechanical alloying, Reviews on Advanced Materials Science 18:203-211.
- 7.28. Xie G, Ohashi O, Song M, Furuya K, Noda T (2003) Behavior of oxide film at the interface between particles in sintered Al powders by pulse electric-current sintering, Metallurgical and Materials Transactions A 34:699–703.
- 7.29. Nagae T, Yokota M, Nose M, *et al.* (2002) Effects of pulse current on an aluminum powder oxide layer during pulse current pressure sintering, Materials Transactions 43:1390–1397.
- 7.30. Zadra M, Casari F, Girardini L, Molinari A (2007) Spark plasma sintering of pure aluminium powder: Mechanical properties and fracture analysis, Powder Metallurgy 50:40–45.
- 7.31. Prabhu B. Microstructural and mechanical characterization of Al-Al<sub>2</sub>O<sub>3</sub> nanocomposites synthesized by high-energy milling. M.S. Thesis, University of Central Florida, Orlando, FL, USA, 2005.

## Chapter 8 Summary, Contributions, and Future Work

### 8.1. Summary

This section contains a summary of the previous chapters.

1. The consolidation of cryomilled Al-Mg powders under two-stage versus one-stage sintering processes was investigated. A two-stage sintering process, with properly selected parameters  $T_1$  and  $T_2$  (TSS:  $T_1 > T_2$ ) allowed for enhanced sintering while avoiding excessive grain growth. The increased duration of the second hold (from 5 to 20 minutes) marginally increased the Weibull Modulus, from 23 to 25. Final average grain size was maintained below 100 nm.
2. Atomized Al-Mg-Er powders were cryogenically milled for 30 hours in liquid nitrogen. Two powder compositions were investigated - Al-4.65Mg-0.08Er (0.1 Er) and Al-4.48Mg-0.44Er (0.5 Er). Prolonged milling time resulted in substantial oxygen contamination in the final milled powders. Recovery events were observed in both powders. Grain growth was observed at 180 °C in the 0.1 Er powder, but the as milled grain size of ~ 20 nm was maintained till 400 °C (0.8  $T_m$ ) in the 0.5 Er powders. Evidence of nanoscale  $L_{12} Al_3Er$  precipitation was not observed. Crystalline oxides (spinel) were observed by XRD for powders annealed at 500 °C and higher.
3. Densification and consolidation of the milled Al-Mg-Er powders with two-stage sintering processes (TSS:  $T_1 > T_2$ ) was dependent on the sintering temperature, maximum pressure and heating rate. Crystalline oxide formation (spinel) during sintering was dependent on the powder composition and selection of  $T_1$ . The average nanocrystalline grain size after sintering was maintained below 100 nm. Bulk sintered nanocrystalline Al-Mg-Er possessed mechanical properties similar to that of oxide-dispersion strengthened (ODS) Al alloys with similar oxide content. Oxide particles with Al-Mg-Er-Fe-O, Al-Mg-Er-Fe-O-N, and Al-Mg-O-N composition were observed in the 0.5 Er samples sintered with  $T_1$  of 550 °C.

4. Three-stage sintering (MSS:  $T_1 < T_2 < T_3$ ) and two-stage sintering (TSS:  $T_1 > T_2$ ) processes were investigated for consolidation of the cryomilled Al-4.65Mg-0.08Er (0.1 Er) powder. MSS schedules produced more uniform sintering compared to the TSS schedule as exhibited in the higher fracture strength and hardness, and the reduced standard deviations. MSS sintering schedules also limited grain growth at an average grain size of  $\sim 60$  nm after 30 minutes of sintering, with a final sintering stage of 10 minutes at 500 °C (0.9 Tm). Smaller grain size standard deviation was observed with the MSS versus TSS results. Nanoscale Al-Fe and Al-Fe-Ni phases were observed in MSS samples after 30 minutes of sintering. Nanoscale clustering of Er and Ti is observed in the TSS sample.

## 8.2. Contributions to original knowledge

The most important contributions to scientific literature from this research are detailed in this section:

1. First study on two-stage sintering of cryomilled Al-Mg (5356) alloy powders using Spark Plasma Sintering.
  - a. Improved sintering of milled Al 5356 with a two-stage SPS schedule as shown by the increasing Weibull modulus (i.e.:  $m = 13$  (500 OSS) to  $m = 25$  (500 TSS 20))
  - b. Obtained bulk NS Al-Mg alloy, average nanocrystalline grain size of  $\sim 70$  nm, with two-stage SPS schedule
2. Preliminary study on cryomilling of Al-Mg powder micro-alloyed with erbium (up to 0.5 wt.%)
  - a. As milled grain size maintained up to  $T_c \approx 400$  °C – 450 °C in Al-5Mg-0.5Er powders
  - b. Activation energy of recovery events in milled Al-Mg-Er powders was determined as  $\sim 20$  kJ·mol<sup>-1</sup> by DSC analysis

3. Initial study on bulk nanocrystalline Al-Mg alloys micro-alloyed with erbium (up to 0.5 wt.%) produced by Spark Plasma Sintering (two-stage sintering)
  - a. Model suggested improved densification under heating rate of  $300\text{ }^{\circ}\text{C}\cdot\text{min}^{-1}$  and 60 MPa was mainly due to enhanced plastic yielding contributions during the initial ramping segment of the SPS process.
  - b. Nanocrystalline oxide particles with Al-Mg-Er-Fe-O, Al-Mg-Er-Fe-O-N, and Al-Mg-O-N composition were detected in Al-5Mg-0.5 Er samples sintered with a maximum temperature of  $550\text{ }^{\circ}\text{C}$ .
  
4. First study on bulk nanocrystalline Al-Mg alloys micro-alloyed with Erbium (0.1 wt.%) produced using multi-stage Spark Plasma Sintering (two-stage and three-stage sintering)
  - a. Three-stage SPS schedules (i.e.: 350 MSS 5) improves sintering of milled Al-Mg powders, i.e.: better density, larger flexural strength and hardness, lower grain growth and smaller standard deviation in the aforementioned properties.
  - b. Bulk NS Al-Mg alloy with average nanocrystalline grain size of  $\sim 60\text{ nm}$  obtained with three-stage SPS schedule
  - c. Nanoscale ( $\sim 150\text{ nm}$ ) clustering of Er and Ti atoms in nanocrystalline regions of TSS sintered samples

### **8.3. Recommendations for future work**

The following recommended studies could contribute to a fuller understanding of this work:

1. Further DSC studies on the milled Al-Mg-Er powders
  - a. Possible (exothermic) events in the  $500\text{ }^{\circ}\text{C}$  to  $630\text{ }^{\circ}\text{C}$  temperature range
  - b. Oxidation behaviour of the milled Al-Mg-Er powders

2. Modelling of the XRD patterns from annealed powders to better determine possible sources of micro strain contribution
3. Further analysis of second phases in the milled powders and sintered bulk materials:
  - a. Nature of oxide dispersoids in the as-milled powders
  - b. Second phases in the sintered materials.